

Bubble guts

**Controlling apical membrane morphology
in the *C. elegans* intestine**

Sanne Remmelzwaal

DOI: <https://doi.org/10.33540/1128>

ISBN: 978-90-393-7442-9

Printed by Ridderprint

Cover, design and layout by Sanne Remmelzwaal

Copyright © 2022 by S. Remmelzwaal
All rights reserved.

Bubble guts—Controlling apical membrane morphology in the *C. elegans* intestine

Bubble guts—Regulatie van apicale membraanmorphologie in de darm van *C. elegans*
(met een samenvatting in het Nederlands)

Proefschrift

ter verkrijging van de graad van doctor aan de Universiteit Utrecht op gezag van de rector magnificus, prof. dr. H.R.B.M. Kummeling, ingevolge het besluit van het college voor promoties in het openbaar te verdedigen op 9 maart 2022 des ochtends te 10.15 uur

door

Susanne Maartje Remmelzwaal

geboren op 14 februari 1994 te Rheden

Promotoren:

Prof. dr. M. Boxem

Prof. dr. S.J.L. van den Heuvel

*„Ihr habt den Weg vom Wurm zum Menschen gemacht,
und Vieles ist in euch noch Wurm.“*

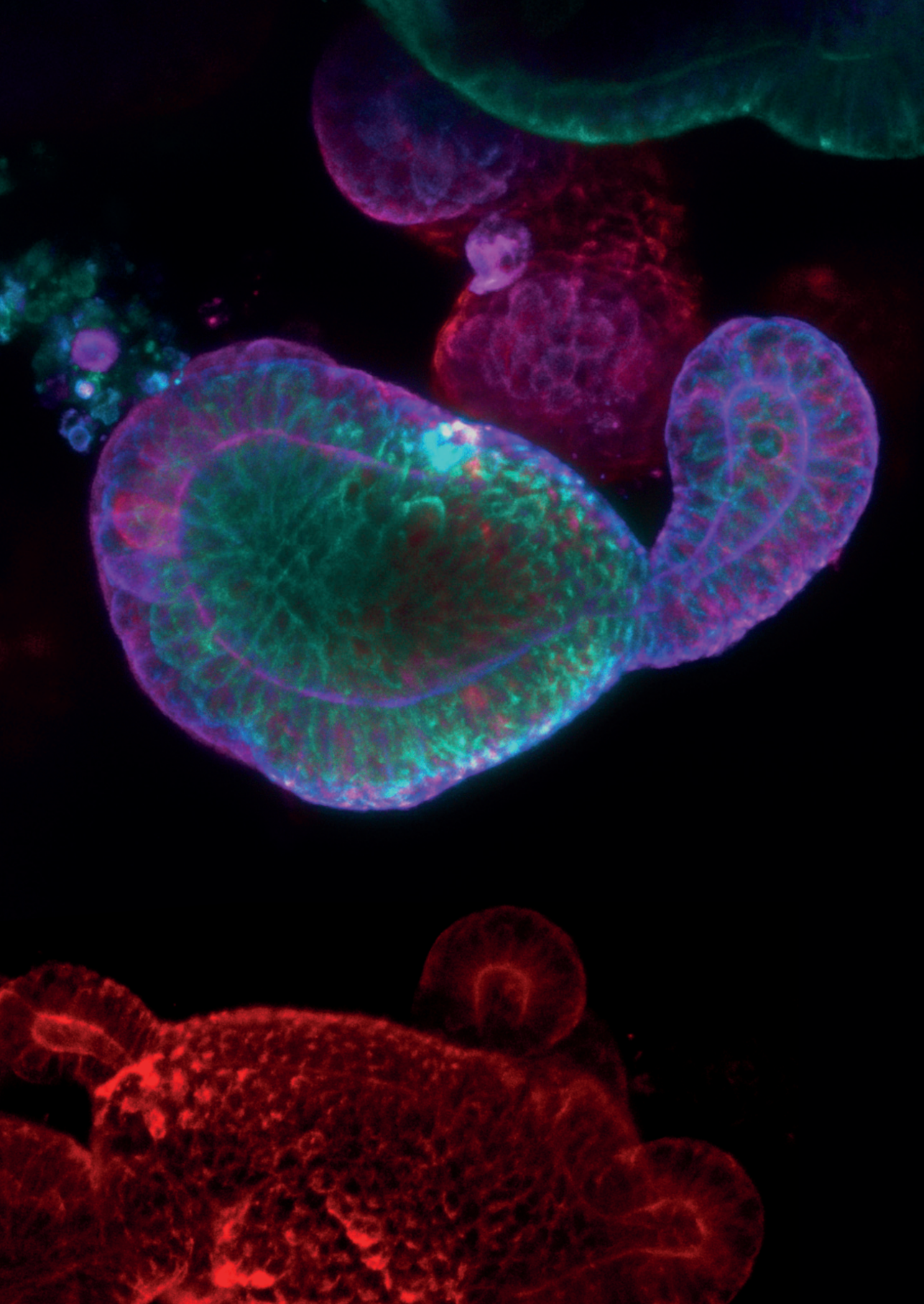
*“You have evolved from worm to man,
but much within you is still worm.”*

*“U bent de weg van worm tot mens gegaan,
en veel in U is nog worm.”*

– Friedrich Nietzsche

Table of contents

Chapter 1	General introduction	9
	Outline of this thesis	23
Chapter 2	Protein interactome mapping in <i>Caenorhabditis elegans</i>	27
Chapter 3	CeLINC, a fluorescence-based protein-protein interaction assay in <i>C. elegans</i>	41
Chapter 4	BBLN-1 is essential for intermediate filament organization and apical membrane morphology	73
Chapter 5	A possible link between BBLN-1 and vacuolar H⁺-ATPases in regulating lumen morphology	127
Chapter 6	Perturbed intermediate filament regulation causes aggregate toxicity	155
Chapter 7	Optogenetically-controlled localization of the apical polarity protein PAR-6	177
Chapter 8	General discussion	199
Appendix	References	210
	Nederlandse samenvatting	236
	Curriculum vitae	240
	List of publications	241
	Acknowledgments (Dankwoord)	242



Chapter 1

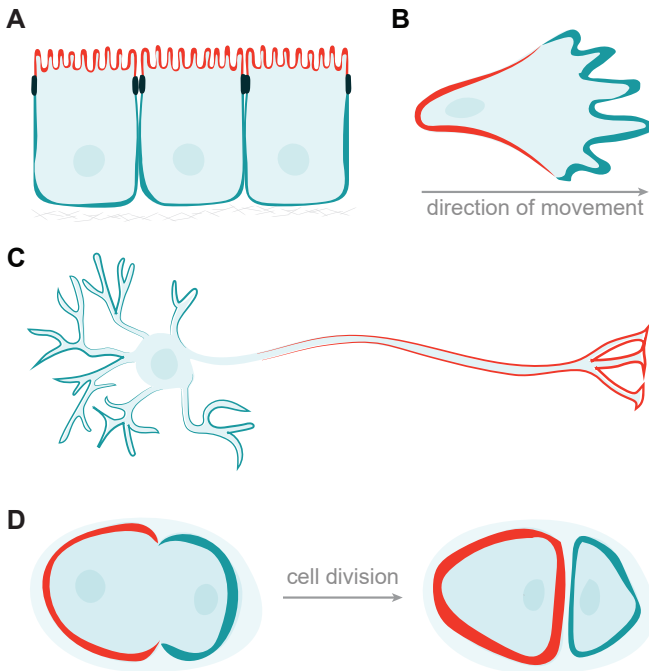
General introduction

Biological tubes

At the root of the complexity of multicellular animals lies the capacity to develop tubes. With animal evolution came an impressive increase in body size, and with that the need of a network to transport and exchange molecules, gases, and fluids throughout the body. Tubes are therefore a fundamental unit of tissue organization and most of our major organs including the lung, kidney, and blood vessels are composed primarily or exclusively of tubes (Iruela-Arispe and Beitel, 2013; Lubarsky and Krasnow, 2003). Biological tubes come in various shapes, sizes, and complexities, ranging from simple unicellular tubes, such as the roundworm excretory (renal) cell (Buechner et al., 2020); to multicellular highly branched networks that span the entire body, like the human circulatory system. Despite these varieties, they all share common features and are built of the same type of cell: the epithelial cell.

Epithelial cells

Epithelial cells are one of the defining features of animals and build one of the body's major tissue type. They have the unique ability to form a sheet of interconnected cells that line the inner and outer surfaces of the entire body. This unique position situates epithelial cells at the interface of the internal and external environment where they face challenges to maintain organismal and tissue homeostasis and integrity. Epithelial cells therefore function as barriers



while simultaneously controlling the selective transport of nutrients. These seemingly contradictory tasks require epithelial cells to establish molecularly and structurally specialized cell domains.

Polarity

Cell polarity refers to the uneven distribution of proteins, shapes and functions along an axis, that creates distinct subcellular domains. It allows cells to produce diverse cell morphologies optimized for distinct tasks. Although an incredible range of cell types establish cellular polarity (Figure 1), decades of research

Figure 1. Examples of polarized cell types. Functionally and structurally distinct domains are indicated in different colors. A) Epithelial cells. B) Migrating cell. C) Neuron. D) The *C. elegans* zygote during asymmetric cell division.

have uncovered common principles that underlie the generation and maintenance of cellular asymmetry (Campanale et al., 2017; Riga et al., 2020; Rodriguez-Boulan and Macara, 2014). An initial symmetry-breaking event (e.g. external signals like sperm entry (Goldstein and Hird, 1996; Munro et al., 2004), intrinsic biochemical phase transitions (Goryachev and Leda, 2017), or cell geometry (M. Friedrich and A. Safran, 2012)) defines a new axis. This often local and transient cue is subsequently amplified to establish stable and global asymmetry. The amplification involves mutually antagonistic interactions and positive feedback loops between groups of cortically localized polarity proteins that lead to the formation of molecularly distinct membrane domains along specified axes.

Epithelial cells are the paradigm of a polarized cell type and polarize along an apical-basal axis (Riga et al., 2020; Rodriguez-Boulan and Macara, 2014; Roignot et al., 2013). Apical cell membranes contact the external environment, lateral membranes seal epithelial cells to other epithelial cells, and the basal membranes connect to the extracellular matrix (Figure 2). Multiprotein complexes, collectively known as intercellular junctions, separate the apical and basolateral domains. These complexes act as diffusion barriers between apical and basolateral membrane domains, provide structure and integrity, and govern intra- and intercellular communication. Cell junctions are anchored to and established by the cytoskeleton: a filamentous network composed of actin, microtubules and intermediate filaments. The cytoskeleton is involved in critical steps of cell polarity and performs vital functions in generating and maintaining tissue architecture (Figure 2 and 3).

ACTIN – The actin cytoskeleton is assembled from actin monomers that polymerize into polarized actin filaments (Figure 3A; reviewed by Pollard, 2016). By regulation of the many actin binding proteins the network exhibits diverging dynamics and shapes to perform a wide variety of functions, ranging from cell motility to molecular organization. In transporting epithelia, the actin microfilaments are

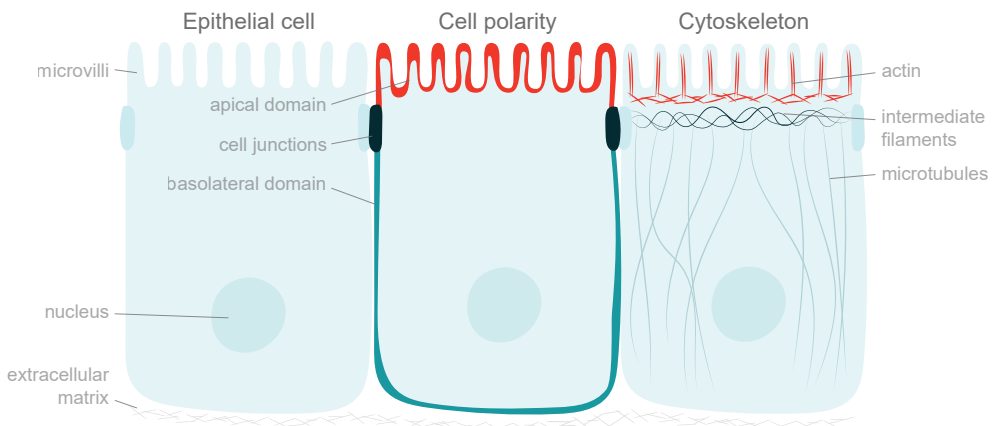


Figure 2. Structure of an epithelial cell. Organization of a typical epithelial cell.

linked to the junctions to build a comb-like framework for the apical membrane to form finger-like protrusions called microvilli (Sauvanet et al., 2015).

MICROTUBULES – Microtubules have fundamental roles in many essential biological processes, including cell division and intracellular transport. They are structured as hollow cylinders that undergo a continuous cycle of assembly and disassembly by the polymerization of tubulin heterodimers (Figure 3B; reviewed by Aher and Akhmanova, 2018). The dimers associate in a head-to-tail fashion, making microtubules intrinsically polarized with two structurally and functionally different ends. Their organization and dynamics are controlled by a huge variety of microtubule-associated proteins, and many proteins additionally exploit microtubule polarity for intercellular directional transport. In epithelia, microtubules organize from the apical to basal domain to provide structure and perform essential roles in cellular trafficking (Müsch, 2004).

INTERMEDIATE FILAMENTS – Cytoplasmic intermediate filament (IF) proteins and their nuclear counterparts, the lamins, all share similar α -helical rod domains, flanked by more varied head and tail domains (Figure 3C; reviewed by Herrmann and Aebi, 2016). Through a series of homo- and heterodimerization, and -multimerization reactions, IF proteins assemble into long filaments and filamentous networks. In an isolated system *in vitro*, IFs spontaneously assemble into simple, stable filaments (Herrmann et al., 2004). *In vivo*, IFs form remarkably morphologically and dynamically diverse networks, suggesting that additional factors modulate filament assembly in their native environment. Indeed, post-translational modifications such as phosphorylation or sumoylation functionally regulate IFs (Kaminsky et al., 2009; Snider and Omary, 2014). However, little potential cofactors have been found to date.

IFs show no intrinsic polarity and, unlike actin and microtubules, are therefore not primarily used in cellular transport. With their extreme viscoelasticity, flexibility and great tensile strength, IFs rather serve to provide structural support. By connecting to actin and cell-cell or cell-matrix contacts, IFs transmit mechanical forces, affect cell shape and establish tissue integrity. In the intestinal cells of mammals and the nematode *Caenorhabditis elegans*, but not *Drosophila*, intermediate filaments anchor at the junctions to form a flexible sheet underneath the actin cytoskeleton (Carberry et al., 2009; Coch and Leube, 2016b; Etienne-Manneville, 2018; Sanghvi-Shah and Weber, 2017).

Morphogenesis

Organisms and their organs develop shape through a combination of biological processes summarized as morphogenesis. The process controls the spatial organization of cells in which every step is highly coordinated. This includes the specialization of generic cell types into more specialized cell types, driven by cell-fate-specific changes in gene expression. Cells migrate, divide, rearrange and undergo cell death in order to build the appropriate tissue and body shape. Morphogenesis is generally regarded as an embryonic process driving organism shape throughout development, however, the process also takes place in the mature organism to maintain tissue homeostasis and regenerate injured tissues.

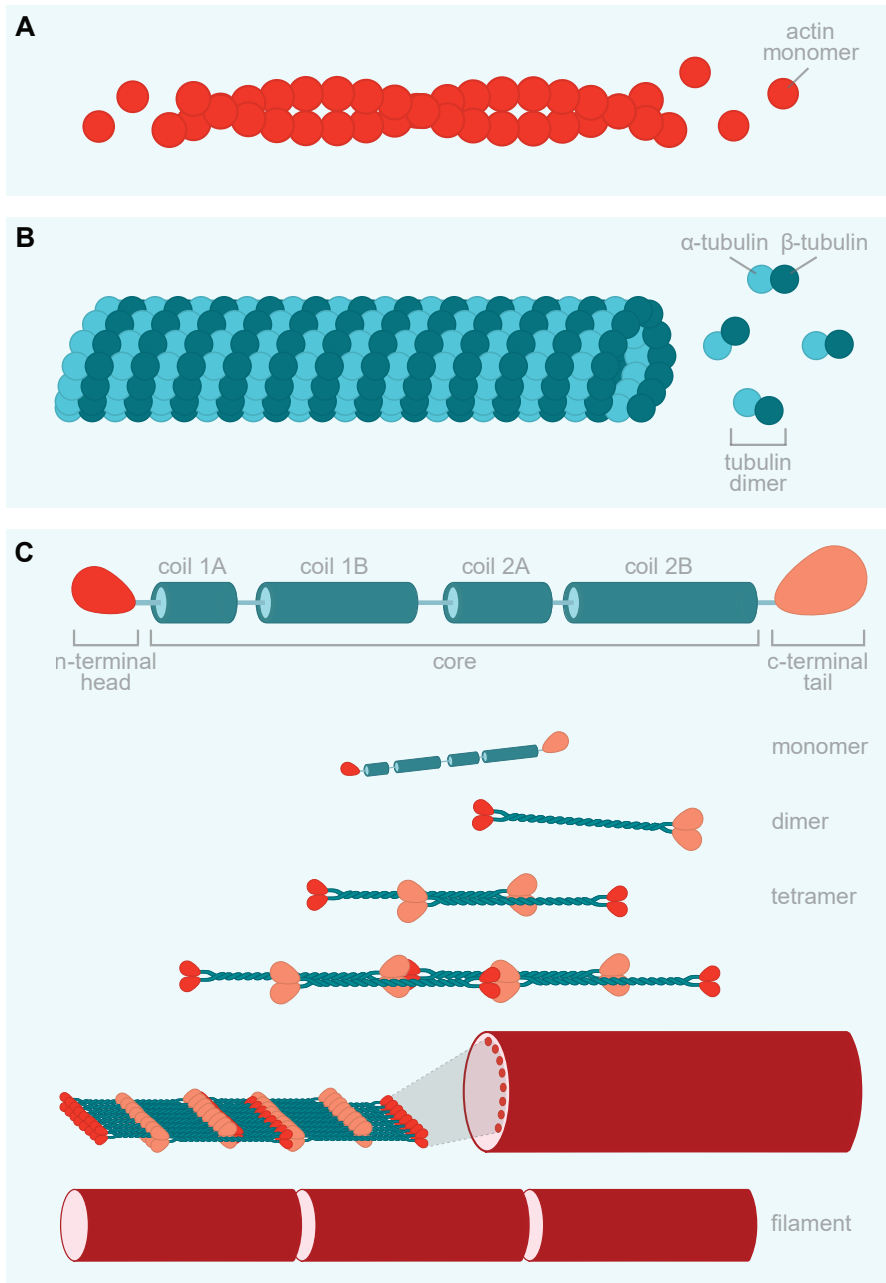


Figure 3. The cytoskeleton. A) Actin microfilaments assemble from actin monomers. B) Microtubules assemble from tubulin dimers, made up from α -tubulin and β -tubulin monomers. C) Intermediate filaments assemble from monomers into dimers. Through interactions between their head, rod, and tail domains they form sheaths that roll up into filaments.

Lumenogenesis – how epithelial cells form tubes

In a specialized class of morphogenic processes, called lumenogenesis, cells form a hollow space or a lumen to form a tube. Cells have developed a number of diverse mechanisms to deliver the astonishing variety in tube morphologies. Despite this diversity, lumenogenesis can generally be grouped in two categories: lumen formation from an already existing sheet of epithelial cells (budding, wrapping or entrapment) or *de novo* lumen formation, in which cells create a hollow space from scratch (hollowing, cavitation) (Iruela-Arispe and Beitel, 2013).

In nearly all cases, lumens are lined by the apical surfaces of the epithelial cells. The apical cell membranes are specialized to regulate the exchange of materials, such as the exchange of gasses in the lungs and nutrients in the intestine. The polarity proteins define the specialized apical surface upon which directed intracellular transport ensures the delivery of new membrane. Importantly, cells must coordinate the orientation of their apical surfaces to face the lumen, which requires interaction of the cell with other cells and specialized extracellular molecules called the extracellular matrix (ECM) (Datta et al., 2011).

Lumen positioning

Typically, lumens form at a shared position between neighboring cells. Cells position the lumen by sensing their neighbors and environment via cell-cell and cell-ECM contacts. In the latter, extracellular ECM proteins connect to transmembrane receptor proteins to provide molecular cues, and thus spatial coordinates for the generation and positioning of apical and basolateral membranes (Bryant et al., 2014; Myllymäki et al., 2011; Overeem et al., 2015). The cell division process is often linked to the first signs of apicobasal polarity and describes a typical example of cell-cell recognition. When a non-polarized cell divides, a protein structure forms at the intersection of both daughter cells to coordinate their final abscission (Pohl, 2017; Wang et al., 2014). This structure, called the midbody, is left behind to function as a spatial cue to attract polarity proteins to create the apical membrane (Bryant et al., 2010; Wang et al., 2014).

Lumen initiation

Once newly polarized cells recognize the ECM and their neighbors, luminal space can be generated. During the hollowing process of *de novo* lumen formation, a luminal domain is generated by directed delivery of apical membrane components to an apical landmark such as the midbody (Andrew and Ewald, 2010; Lubarsky and Krasnow, 2003; Sigurbjörnsdóttir et al., 2014). Fusion of the trafficked membrane vesicles with either the existing apical membrane (cord hollowing) or with each other in the cell's cytoplasm (cell hollowing) expands the apical domain to generate the lumen. In cavitation, interior cells that are not in contact with the ECM fail to receive polarizing signals and undergo cell death to clear the lumen (Andrew and Ewald, 2010; Lubarsky and Krasnow, 2003; Sigurbjörnsdóttir et al., 2014). It is important to note that these and other mechanisms of *de novo* lumen formation are not mutually exclusive; different processes are combined to fine tune tube morphologies, and when one mechanism falls short another can compensate to ensure the proper outcome (Martín-Belmonte et al., 2008).

Inflating the lumen

Tubes are generally very small when they form and must therefore expand to their mature, functional size and shape. Luminal expansion is established by the generation of forces such as electrostatic repulsion and hydrostatic pressure (Chan and Hiragi, 2020; Jewett and Prekeris, 2018; Khan et al., 2013; Luschnig and Uv, 2014; Strilić et al., 2010). Cells generate electrostatic repulsion to not only initiate but also maintain lumen expansion. On the extracellular side of their apical membrane, cells display negatively charged molecules to repel similar molecules on the opposing cells. Hydrostatic pressure is achieved through the delivery of apical membrane components and the activation of pumps and channels. Liquid efflux into the luminal space subsequently drives luminal expansion. The transport of apical components is additionally accompanied by the delivery of new membrane that in its turn contributes to increased apical size and therefore lumen. Interestingly, as the lumen inflates, cell volume decreases, suggesting that the volume between cells and lumen is conserved (Ferrari et al., 2008).

Stop, or it might pop

Tubular tissue and organ function are highly dependent on lumen size, since this dictates their flow properties. How cells sense lumen diameter is poorly understood, however, several mechanisms controlling tube size have been characterized (Andrew and Ewald, 2010; Jewett and Prekeris, 2018; Lubarsky and Krasnow, 2003; Mailleux et al., 2008). For example, in the cavitation model, cells divide until the tissue reaches the appropriate proportions, which is followed by regulated cell death of the inner cells to generate the desired lumen diameter. In other lumenogenesis processes, cells may regulate tube size by adjusting the membrane trafficking and pressure machinery, or by adjusting the composition of the luminal matrix. Although these mechanisms are similar to the processes that drive tube formation, multiple mutations are known to exclusively affect tube size maintenance, but not establishment. Several studies describing such regulators of lumen maintenance are performed in the excretory canal and intestine of the small roundworm *C. elegans* (see below).

***C. elegans* as a model to study complex biology**

In the 1970s, Sydney Brenner started using *C. elegans* as a model to study animal genetics and neurobiology (Brenner, 1974), but the nematode has since been at the forefront of developmental and cell biological research. The animal has extensively been used to study subjects ranging from host-microbe interactions (Kumar et al., 2020) to the modelling of various human diseases (Markaki and Tavernarakis, 2020).

C. elegans are self-fertilizing hermaphrodites, that develop from embryos to full adulthood in only 2 to 3 days depending on the environment. Under stress conditions, males can arise, leading to sexual reproduction. The *C. elegans* genome is relatively small which facilitated it becoming the first multicellular eukaryote to have its entire genome sequenced, and since then it has been extensively curated. An adult hermaphrodite is approximately 1 mm long, consists of only

959 somatic cells, and due to excellent reproducibility of cell division timing and placement, the cell lineage has been fully characterized. The *C. elegans* body is transparent and has a simple anatomy with surprisingly similar characteristics to higher order organisms. Collectively, these features make the nematode the ideal model organism for genetic manipulation (forward/reverse genetics, CRISPR/Cas9), analysis of developmental processes at single-cell resolution, and high-quality imaging.

C. elegans body plan

The *C. elegans* body consist of four major epithelial tissues: the pharynx, hypodermis, excretory system and intestine. The pharynx is a neuromuscular pump that drives the food towards the intestine for digestion. The outer epithelial layer forms the hypodermis, a tissue that secretes a protective layer of specialized ECM to build the cuticle. The excretory system includes a single cell that extends four tubes anteriorly and posteriorly forming an H-shape flanking both lateral sides along the entire length of the animal.

The *C. elegans* intestine

As an epithelial tube that forms a lumen *de novo*, and with its cells highly resembling its vertebrate analogs, the *C. elegans* intestine deserves little more attention. The tissue consists of a single layer of only 20 cells, divided over 9 rows in which generally two cells face each other with their apical membranes, enveloping a central ellipse-shaped lumen (Leung et al., 1999). All cells develop during embryogenesis and do not renew during the lifetime of the nematode. The tissue makes up a substantial part of the animal's body, spanning more than three quarters of its body length. Its size facilitates multiple essential functions such as absorbing and storing nutrients, hosting an innate immune system, and providing yolk for oocyte development.

Despite the simplicity of the tissue, the architecture of the *C. elegans* intestinal cell is remarkably similar to our own enterocytes. On the apical side, it forms a microvillar brush border, shaped by bundles of actin microfilaments that are connected to the membrane by the ezrin-radixin-moesin homolog ERM-1 (Göbel et al., 2004). The actin bundles are tightly connected to the underlying electron-translucent terminal web. This structure is mostly devoid of cell organelles and consist primarily of actin bundles and its associated proteins. Subapical of the terminal web lies a structure that in nematodes is referred to as the endotube. This electron-dense network is formed by a sheet of IFs and associated proteins that provide support for the apical surface (Carberry et al., 2009; Coch and Leube, 2016). Both the terminal web and the endotube are connected to the *C. elegans* apical junctions (CeAJs) that connect adjacent and opposing cells. The CeAJs span along the length of the intestine in a characteristic ladder-like structure when viewed by fluorescence microscopy and form a single, electron dense structure when observed by electron microscopy on a single cell level. Nevertheless, it has proven to consist of two distinct macromolecular subdomains: the apical cadherin-catenin complex that provides cell adhesion, and the DLG-1/AJM-1 complex that presumably controls intercellular barrier function (Armenti and Nance, 2012).

C. elegans intestinal lumenogenesis

The intestinal cells derive from a single progenitor cell E during *C. elegans* embryogenesis (Leung et al., 1999). When this cell has divided into 16 descendants (the E16 stage), 10 cells are organized in two dorsal rows and 6 cells in two ventral rows. At this point, the nuclei and centrosomes of the cells start to migrate to the future apical side, soon whereafter vesicle trafficking follows (Feldman and Priess, 2012; Leung et al., 1999). Membrane-associated polarity proteins such as the apical partitioning-defective (PAR) complex are assumed to define the domains, upon which polarized vesicular trafficking directs membrane components to their corresponding domain (Achilleos et al., 2010a; Sundaram and Buechner, 2016). During lumenogenesis, the vesicles are continuously present at the intestinal midline and are therefore likely the key drivers of a cord-hollowing process of lumen formation (Leung et al., 1999).

This hypothesis is supported by analogous mechanism in excretory canal tubulogenesis. The apical PAR proteins and ERM-1 are among the earlier markers at the apical domain and are essential for lumen formation. In excretory canal morphogenesis, the PAR proteins concentrate exocytosis-driving exocyst proteins at the apical membrane (Armenti et al., 2014). Luminal extension is then driven by ERM-1-dependent apical recruitment of the actin protein ACT-5 for exocytic vesicle fusion, and the aquaporin AQP-8 for water-channel fluid efflux (Khan et al., 2013).

Tube growth control

C. elegans has proven an ideal model for studying tube growth control *in vivo*. Mutations in multiple genes have been found to affect the size and shape of excretory canals and intestinal lumens. Canal mutant animals display enlarged tubules, sometimes swelling so dramatically that it fills the entire width of the animal and pushes aside other tissues. Mutant animals with intestinal phenotypes show luminal widening or herniations from hatching that may increase in size during development. Often a single mutation affects both tissues and effectively all dilated phenotypes are assigned to defects of the apical cytoskeleton or luminal matrix.

A recent study links all three cytoskeletal components in excretory canal lumen morphogenesis, showing that actin and microtubules guide lumen-inflating vesicles to the apical membrane, while IFs regulate vesicle access to restrain lateral lumen expansion (Khan et al., 2019). This nominates IFs as credible candidates for key regulators of lumen size maintenance.

Of the three cytoskeletal networks, IFs are by far the least well understood in terms of filament assembly and organization. Unicellular organisms and insects mostly lack cytoplasmic IFs, precluding these models for *in vivo* IF function research. On the other hand, mammals have over 70 cytoplasmic IFs, divided over several IF families, hindering dissection of the system's function and organization by redundancy and intricacy (Etienne-Manneville, 2018). However, *C. elegans* does host cytoplasmic IFs and with only 11 IF isotypes it provides a simplified system for studying IFs *in vivo* (Carberry et al., 2009).

The *C. elegans* intestine expresses six cytoplasmic IF proteins, all of which localize almost exclusively to the electron-dense endotube structure (Bossinger et al., 2004; Carberry et al., 2009; Coch and Leube, 2016; Geisler et al., 2020; Karabinos et al., 2002, 2004). The intestinal isotypes IFB-2, IFC-1, IFC-2, IFD-1, IFD-2 and IFP-1 all homo- or heteropolymerize with each other, but preferably with the most abundant intestinal IF, IFB-2 (Karabinos et al., 2017). Few proteins have been shown to organize the network and loss of each of them leads to deformations of the endotube and compromises intestinal lumen morphology (Bossinger et al., 2004; Carberry et al., 2012; Estes et al., 2011; Geisler et al., 2016). The MAP kinase 7 orthologue SMA-5 controls intestinal tube stability by affecting IF network phosphorylation (Geisler et al., 2016). *sma-5* mutant animals show dilated intestinal lumens by the formation of bubble-shaped cytoplasmic membrane invaginations. Since *sma-5* mutants paradoxically have increased levels of IF phosphorylation this appears to be an indirect effect of the enzyme. Loss of the IF organizer IFO-1 leads to a similar, but more dramatic phenotype in which the entire intestinal IF network aggregates at cell-cell junctions (Carberry et al., 2012). IFO-1 is a small, histidine-rich coiled-coil protein that putatively acts to anchor the IF sheet to the adjacent actin network (Carberry et al., 2012). IFO-1 shows structural similarities to filaggrin, a protein that is synthesized as a giant precursor protein before it is proteolysed into multiple monomeric units (Carberry et al., 2012; Lynley and Dale, 1983; Sandilands et al., 2009). Filaggrin monomers interact with IFs but not any other components of the cytoskeleton and promotes the parallel alignment of keratin IFs by initiating their aggregation (Sandilands et al., 2009).

Disorganization of the IF network is often associated with phenotypes of altered lumen morphology. Pathogenic invasion of the *C. elegans* intestine induces lesions in the actin and IF apical network, and gives rise to luminal dilations that progress through the course of infection (Estes et al., 2011a; Troemel et al., 2008). Alternatively, loss of ACT-5 or its regulators leads to dramatic widening of the lumen after hatching (Bernadskaya et al., 2011; Croce et al., 2004; Göbel et al., 2004; MacQueen et al., 2005), often accompanied by altered IFB-2 organization. Moreover, direct loss of IF isotypes has been shown to induce luminal widening and endotube aggregates (Geisler et al., 2020; Hüsken et al., 2008). Surprisingly, animals largely tolerate all these IF network defects under normal conditions, but are dramatically more susceptible to biotic and abiotic stresses (Geisler et al., 2019).

In humans, aggregation of IF proteins is a hallmark of “IF-pathies”: over 80 different IF-associated disorders that range from skin problems to neurological diseases (Omary, 2009; Omary et al., 2004). In, for instance, the skin blistering disease epidermolysis bullosa simplex, keratin intermediate filament aggregates are hypothesized to induce uncoupling of the keratin filament network from the desmosomal cell-cell junctions which makes the epidermis highly vulnerable to mechanical stresses (Quinlan et al., 2017). Furthermore, changes in phosphorylation state and structure of the keratin 8 IF protein is known to be associated with liver disease (Ku and Omary, 2006). IF structure

is highly regulated *in vivo* by post-translational modifications, but the function and regulation of IF phosphorylation is poorly understood. Besides, relatively few IF-associated proteins are identified while there are several examples of mutations in genes encoding known IF-associated proteins leading to these IF-pathies.

Techniques to exploit the multifaceted animal model

As illustrated by the lumenogenesis research discussed above, *C. elegans* offers relatively simple examples of animal biology. Nearly all aspects of animal biology are therefore covered by studying the nematode (Corsi, 2015). Further virtues of using *C. elegans* for biological research is that it is easily grown in the lab with its minimal nutritional and growth requirements and rapid reproduction cycle. Since the introduction of *C. elegans* as a model system, many approaches have therefore been and are continued to be developed to exploit the ease of working with this versatile animal.

Forward genetics

Most of the discussed lumen morphology mutants came about from forward genetic experiments. These molecular genetic approaches serve to identify genes that are responsible for a phenotype. There are multiple ways to mutagenize an animal. In a chemical mutagenesis screen, a compound is used to stably and randomly induce mutations in the genome. The most commonly used mutagen in *C. elegans* research is ethyl methanesulfonate (EMS) (Kutscher and Shaham, 2014). Treatment with EMS generally adds an ethyl group to guanine, that in subsequent replications will inappropriately pair with thymine, resulting in G/C to A/T transitions. EMS mutagenesis therefore typically generates new stop codons, often leading to complete or partial disruption of gene function.

C. elegans are conveniently visualized on a simple microscope, which allows for easy identification of mutant animals. Screens are designed to identify mutants with altered body shape, movement, development, or altered levels or location of fluorescent protein expression. There are different strategies to determine the mutant genes ranging from crosses with strains carrying known genetic markers or deletion chromosomes, to performing single-nucleotide polymorphism (SNP) mapping. In SNP mapping, single nucleotide differentiations between *C. elegans* strains are exploited to identify regions linked to the mutant phenotype. Once the mutation is mapped to a region where a candidate gene is found, the causative mutation can be identified by gene sequencing and confirmed by the introduction of the wild-type gene to rescue the mutant phenotype or by RNAi delivery to phenocopy the mutant phenotype. Over the past few years, it has also become increasingly accessible to directly perform whole genome sequencing on mutants to identify the causative mutation. Even though mutagenesis produces many irrelevant mutations, it is fairly easy to pinpoint the causative mutation due to the relatively small genome size of *C. elegans*—which makes it the ideal model organism for genetic screens.

Reverse genetics

Reverse genetics is used to help understand gene function by analyzing the phenotype that is caused by genetically manipulating the gene. While forward genetics aims to find the genetic basis of a phenotype, reverse genetics researches what phenotypes are controlled by particular genes.

Before the introduction of rapid methods for genetic analysis, it was difficult to identify the gene affected by the mutation that caused the phenotype. This was often overcome by performing an RNA interference (RNAi) screen, which uses targeted gene inactivation by sequence-specific suppression of messenger RNA (mRNA). In *C. elegans*, delivery of double stranded RNA (dsRNA) by multiple means can trigger the RNAi response. The easiest way of dsRNA delivery is by simply feeding the nematodes with dsRNA encoding bacteria. Standard feeding plates are covered with dsRNA transcribing *Escherichia coli*, the desired stage and number of *C. elegans* are placed on the plates, and they or their offspring are analyzed after the appropriate time upon ingestion (often a few days). The method is further facilitated by the availability of multiple "libraries" containing frozen dsRNA transcribing *E. coli* that cover the entire *C. elegans* genome (Kamath et al., 2003a; Lamesch et al., 2004).

By inactivating the entire mRNA, RNAi methods often do not allow to partially disrupt a gene's function. To specifically alter a gene, researchers increasingly resort to CRISPR/Cas9-mediated genome editing. In brief, CRISPR/Cas9 causes double-strand breaks within the genome at specific sites. Cellular repair machinery repairs the DNA by homologous recombination events or by base insertion or deletions, which can be exploited to include sequences of interest. Recent advances in CRISPR/Cas9-mediated genome editing has greatly improved the efficiency of generating mutant *C. elegans* strains (Ghanta and Mello, 2020; Waaijers and Boxem, 2014). An additional exceptionally useful application of the method is the integration of fluorescent protein sequences to endogenous genes of interest.

CRISPR/Cas9-based applications of protein manipulation

Fluorescent proteins have revolutionized molecular research as they are easy to use for protein tagging, fluoresce without fixation or permeabilization, and thus, enable live imaging of proteins *in vivo*. They have been extensively used to study gene expression, characterization of protein (co)localization, and for unravelling cellular signaling pathways. Fluorescent proteins were traditionally introduced in *C. elegans* using transgenic overexpression. Although easy to implement, transient overexpression systems might not recapitulate the endogenous expression of proteins, which could be remarkably low in a cell, and therefore lead to problems such as protein misfolding, false localization, and nonspecific protein-protein interactions. CRISPR/Cas9-mediated genome editing has made it an increasingly straightforward task to generate endogenous *C. elegans* protein reporter lines, making it now possible to visualize your new fluorescent strain under the microscope in less than a week (Ghanta and Mello, 2020).

Besides the addition of fluorescent proteins, a wide range of proteins and protein sequences from various models are adopted for use in equally diverse model systems. In auxin-inducible degradation (AID) (Zhang et al., 2015), a plant-derived protein degradation system is exploited for conditional protein depletion in various experimental models. In *C. elegans*, the modified *Arabidopsis* TIR1 F-box protein is expressed under the control of endogenous (tissue-specific) gene promoters to drive auxin-dependent depletion of degron-tagged targets. CRISPR/Cas9-mediated genome editing allows the endogenous tagging of any target protein of interest by the degron. Degradation of the target protein in the generated lines is then initiated by simply adding auxin to the system (i.e. plates or growth medium). The AID system therefore provides a powerful tool for spatially- and temporally-controlled regulation of protein function.

Developed to control and monitor neuronal activity with light, optogenetics has provided powerful techniques for the neurobiology field. However, optogenetic tools have also been used to manipulate proteins in other systems. These techniques make use of proteins that undergo a conformational shift in the presence of light that—generally in non-neuronal systems—allows them to participate in protein-protein interactions. By attaching these proteins to target proteins, one can force their activation, inactivation or localization. Due to its transparency and susceptibility to genetic manipulation, *C. elegans* proves an ideal subject for optogenetic techniques (Dong et al., 2021; Fielmich et al., 2018; Harterink et al., 2016). New light-based methods are regularly emerging, expanding the toolbox of *C. elegans* research.

Protein-protein interaction assays

Most biological functions are mediated by interactions between proteins, and mapping these interactions is therefore one of the key approaches to understand the functions of gene products and the relationships between them. Protein-protein interaction assays can additionally be exploited to identify new components involved in distinct molecular processes. Protein interaction mapping techniques are therefore an often indispensable approach in biomolecular research.

All protein-protein interactions that take place in an organism or cell are described in the 'interactome'. *C. elegans* has been on the forefront of proteome-wide interactome research (reviewed in Chapter 2) due to a plethora of advantages that comes with using a genetically and developmentally traceable organism. One of the many advantages is that interactions can be mapped in a spatiotemporal manner using a wide variety of experimental techniques. For example, methods like co-fractionation, proximity labeling, and tissue-specific protein purification not only identify protein-protein interactions, but have the potential to provide crucial insight into when and where interactions take place. These are all well-established techniques, but the field continues to develop and improve protein interaction mapping approaches for *C. elegans* to overcome current limitations and contribute to elucidating the nematode's interactome. Recently, a split-intein mediated protein ligation for detection of interacting protein pairs (Yao et al., 2020) has been adapted for use in *C. elegans*. Despite

these endeavors, the total interactome is estimated to be an order of magnitude larger than the number of protein-protein interactions currently identified. Continued efforts are therefore needed to elucidate the *C. elegans* interactome and advanced techniques will aid in bringing new insights and advantages in protein-protein interaction mapping.

C. elegans as a model for human diseases

Translating fundamental research questions and findings into applied sciences often requires studying human or closely related models. There are, however, practical and ethical limitations in investigating higher order organisms, and *in vitro* cell culture generally does not fully simulate organismal physiology. However, genes linked to human diseases usually function in evolutionarily conserved pathways, which can be readily dissected in simple model organisms. The number of human disease-related genes that share at least simple homology with *C. elegans* genes has often been estimated and ranges between 40 and 75% (Silverman et al., 2009). This number includes genes associated with metabolic diseases, cancers and many neurodegenerative diseases like Alzheimer's disease (Pir et al., 2017), Parkinson's disease (Cooper and Van Raamsdonk, 2018), or Amyotrophic lateral sclerosis (ALS) (Therrien and Parker, 2014). One strength of using *C. elegans* for modelling human diseases is that beyond the shared homology, it is possible to express human genes and disease-related gene variants in the nematode (Li and Le, 2013). The flexibility and ease of transgenesis in *C. elegans* allows the investigation of basic cellular mechanisms in the context of expressed gene-variants and expands the use of the nematode in human-disease research beyond more obviously related pathologies like host-pathogen interactions. (Humanized) *C. elegans* models therefore offer a good balance between the ability to simulate many aspects of human disease, while offering an abundance of powerful, cost effective and rapid tools.

Outline of this thesis

As described above, establishment and maintenance of tissue morphogenesis are key processes in building a functional organism's body. In this thesis, I have used *C. elegans* as a model to broaden our understanding of the maintenance of tube morphogenesis *in vivo*—with a special role for protein-protein interactions.

In **chapter 2** we provide a timeline of old and recent advances in the identification of the *C. elegans* protein interactome. We describe commonly used techniques and shine light on recent innovations.

Chapter 3 describes the implementation of a novel protein-protein interaction assay in *C. elegans* to investigate whether pairs of proteins interact *in vivo*. *C. elegans* light-induced co-clustering (CeLINC), is based on trapping fluorescently-tagged bait protein into artificial clusters to subsequently observe whether candidate interacting prey proteins co-cluster with the bait protein. The method is light inducible and can be widely applied, as a single set of universal plasmids can be used on existing strains that express fluorescently-tagged proteins of interest.

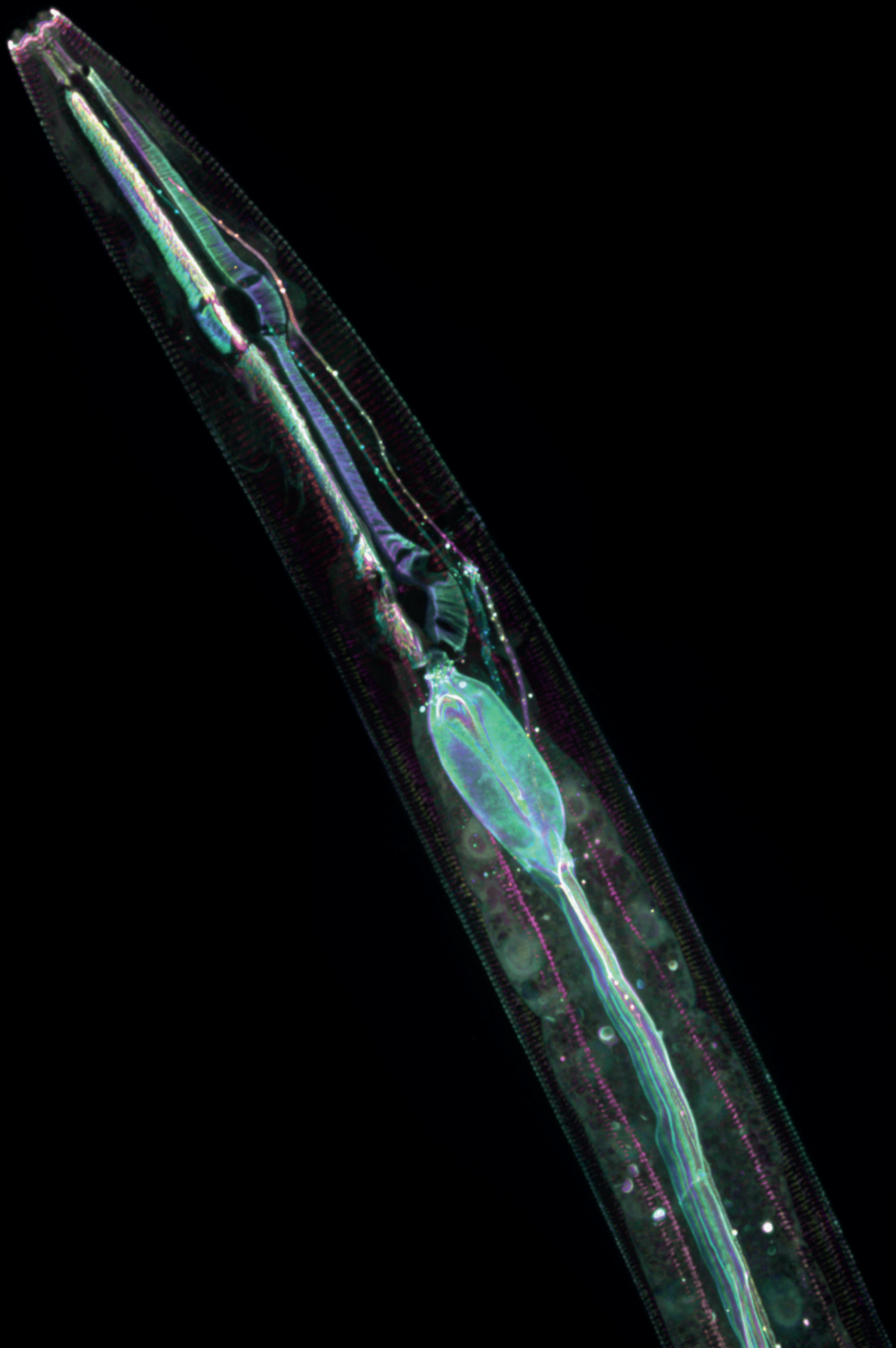
In **chapter 4** we identify a novel regulator of intestinal lumen morphology. By performing an EMS mutagenesis screen we generated a mutant that formed dramatic, bubble-shaped protrusions of the apical membrane into the cytoplasm of the intestinal cells. SNP mapping combined with whole genome sequencing revealed that this phenotype was caused by a mutation in the previously uncharacterized gene C15C7.5, that we called *bbln-1* for bulges budding from the intestinal lumen. Loss of BBLN-1 leads to the aggregation of the IF network into bundles, that subsequently causes the cytoplasmic invaginations. We go on to show that bublin (BBLN) is the mammalian ortholog of BBLN-1.

In chapter 4 we revealed a potential interaction between BBLN-1 and subunits of the Vacuolar-type H⁺ ATPase (V-ATPase) by pull down combined with mass spectrometry experiments. **Chapter 5** exploits CeLINC to invigorate the identified protein-protein interaction. We further address their molecular link and show that loss of V-ATPase function can result in bubble-shaped membrane protrusions in the *C. elegans* intestine.

In **chapter 6** we investigate how IFs and MAPK signalling shape the *C. elegans* intestinal lumen. Loss of SMA-5 has previously been shown to cause bubble-shaped apical membrane protrusions (Geisler et al., 2016 and Chapter 4) and we here link the MAP kinase's function to the IF polypeptide IFB-2. IFB-2 proved to be the main effector of the *sma-5* phenotype, highlighting the tight linkage between the IF cytoskeleton and signaling.

In **chapter 7** we manipulate intestinal polarity protein localization using optogenetic techniques in the endeavor of establishing ectopic lumens laterally. However, we conclude that optogenetic relocation of PAR-6 alone is insufficient to manipulate apical-basal polarity in the fully established epithelium of the *C. elegans* intestine.

Finally, in **chapter 8** I discuss and connect the results described in this thesis. I also provide suggestions for future directions.



Chapter 2

Protein interactome mapping in *Caenorhabditis elegans*

Sanne Remmelzwaal and Mike Boxem

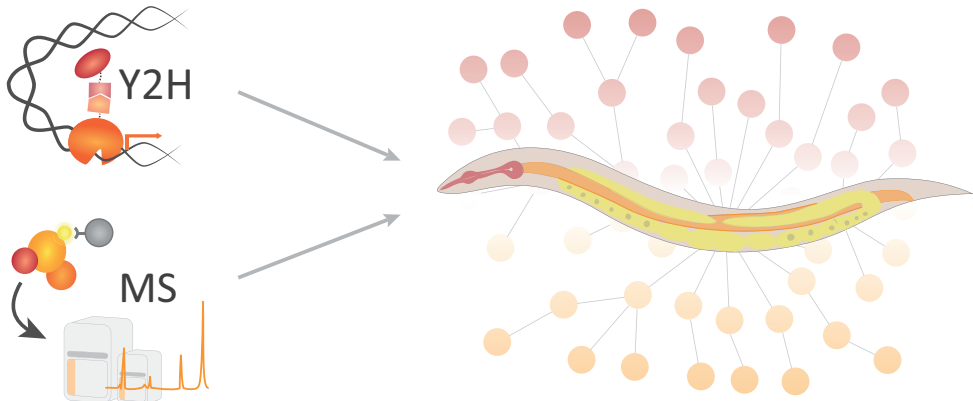
Developmental Biology, Institute of Biodynamics and Biocomplexity, Department of Biology,
Faculty of Science, Utrecht University, Padualaan 8, 3584 CH, Utrecht, The Netherlands.

This chapter is published:

Remmelzwaal, S., & Boxem, M. (2019). Protein interactome mapping in
Caenorhabditis elegans. *Current Opinion in Systems Biology*, 13, 1-9.

Abstract

The systematic identification of all protein-protein interactions that take place in an organism (the 'interactome') is an important goal in modern biology. The nematode *Caenorhabditis elegans* was one of the first multicellular models for which a proteome-wide interactome mapping project was initiated. Most *C. elegans* interactome mapping efforts have utilized the yeast two-hybrid system, yielding an extensive binary interactome, while recent developments in mass spectrometry-based approaches hold great potential for further improving our understanding of protein interactome networks in a multicellular context. For example, methods like co-fractionation, proximity labeling, and tissue-specific protein purification not only identify protein-protein interactions, but have the potential to provide crucial insight into when and where interactions take place. Here we review current standards and recent improvements in protein interaction mapping in *C. elegans*.



Graphical abstract.

Introduction

Since the advent of whole-genome sequencing, high-throughput (HT) approaches are increasingly important for our efforts to understand the functions of all gene products and the relationships between them. Interactions between proteins represent a large part of the interactions between macromolecules in our cells, and several HT protein-protein interaction (PPI) mapping techniques have been developed to systematically map these interactions. HT-PPI mapping technologies were initially employed to map the interactomes of single cell systems, but efforts quickly expanded to model organisms, to investigate PPI networks on a multicellular level.

The mapping of the *C. elegans* interactome has been dominated by binary interaction mapping using the yeast two-hybrid (Y2H) system (Figure 1). *C. elegans* was the first multicellular organism to have its entire genome sequenced and annotated (*C. elegans* Sequencing Consortium, 1998). This gave the roundworm an advantage for pioneering Y2H-based PPI mapping approaches, such as the development of complete ORFeome collections to facilitate screening efforts (Lamesch et al., 2004; Reboul et al., 2003), and the integration of interactome maps with phenome and transcriptome data to improve the predictive capabilities of interactome networks (Boulton et al., 2002; Gunsalus et al., 2005; Tewari et al., 2004; Walhout et al., 2002). The procedures and improvements developed in *C.*

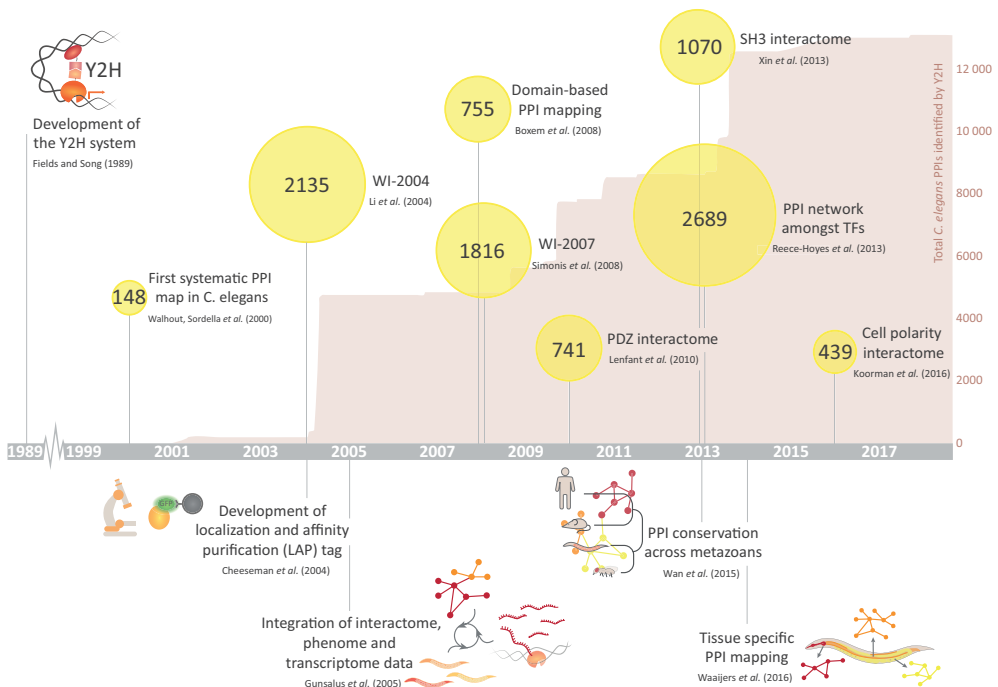


Figure 1. Chronological presentation of landmark publications for protein interactome mapping in *C. elegans*. Yellow circles depict number of high-confidence interactions reported in key Y2H studies. Graph represents total *C. elegans* PPIs identified by Y2H curated in IntAct.

C. elegans have served as a template for similar Y2H-based interactome mapping efforts in other organisms, including human (*Arabidopsis* Interactome Mapping Consortium, 2011; Dreze et al., 2010; Rolland et al., 2014; Rual et al., 2005).

Mass spectrometry (MS)-based protein complex mapping approaches have made more modest contributions to the *C. elegans* interactome, though recently thousands of candidate *C. elegans* protein-protein associations were identified by co-fractionation (Figure 1) (Wan et al., 2015). MS-based techniques like tissue-specific protein purification and proximity labeling enable the addition of spatiotemporal information to interactome networks, a critical step towards understanding protein-protein interactions in the context of a multicellular organism such as *C. elegans*. Here, we review the state of interactome mapping in *C. elegans*, and discuss recent developments that are likely to improve protein interaction mapping efforts in this organism in the coming years.

Binary interactome mapping - *C. elegans* as a model for genome-scale Y2H mapping

The most widely-used binary interaction assay is the Y2H system, which is based on the reconstitution of a transcription factor through binding of two hybrid proteins: one fused to a DNA binding (DB) domain, and one fused to an activation domain (AD) (Fields and Song, 1989). A major advantage of the Y2H system is its simplicity: only yeast and DNA clones need to be handled, making the Y2H system highly scalable.

The elucidation of the *C. elegans* protein interactome by Y2H took off discretely, with the mapping of a network of 148 interactions centered around proteins involved in vulval development (Walhout et al., 2000a). While small in size, this study produced the first interaction network for a multicellular organism and pioneered several approaches that remain current to date. One of these was the development of Gateway recombinational cloning, which was later used to generate a genome-scale resource of *C. elegans* open reading frames (ORFs) (the ORFeome) (Hartley et al., 2000; Lamesch et al., 2004; Reboul et al., 2003). Another was the use of matrix experiments, in which all pairwise combinations of proteins are tested. While labor intensive, the advantage of this approach is that the search space of protein pairs tested is known precisely. Matrix screens using ORFeome collections were used to map a significant fraction of the *C. elegans* binary interactome, and form the backbone of current efforts to map the human interactome by Y2H (Dreze et al., 2010; Rolland et al., 2014; Rual et al., 2005; Simonis et al., 2009).

The first truly large-scale interaction map for *C. elegans* was published in 2004 (Li et al., 2004). Using 1,873 metazoan-specific proteins as baits in library screens, a total of 2,135 protein-protein interactions were uncovered, and the quality of the data set was verified by co-affinity purification. Together with a large scale Y2H interaction map of *Drosophila* published just weeks prior (Giot et al., 2003), this publication heralded the first proteome-scale interaction maps for multicellular organisms. In 2009, the *C. elegans* ORFeome collection, which by then covered

some 10,000 genes, was used in matrix Y2H screens to expand the interactome to 3,864 interactions among 2,528 proteins (the Worm Interactome version 8, or WI8) (Simonis et al., 2009). The largest single addition to the *C. elegans* binary interactome since WI8 was made by Reece-Hoyes *et al.*, who combined PPI mapping by Y2H with protein–DNA interaction (PDI) mapping by yeast one-hybrid (Y1H) in a comprehensive study of *C. elegans* transcription factor (TF) network evolution (Reece-Hoyes et al., 2013). Over 2500 PPIs were uncovered between TFs or between TFs and transcriptional cofactors, and analysis of the PPI and PDI networks showed unexpectedly rapid rewiring of transcriptional networks, with even highly similar TFs often having different interaction profiles (Reece-Hoyes et al., 2013).

Most recent binary interactome mapping efforts by Y2H have focused on specific biological processes and novel applications of the Y2H system. An example is the use of the Y2H system to map interaction domains by testing different fragments of a protein for their ability to interact. This approach was first used at large scale in *C. elegans* to generate a domain-based interactome network for proteins involved in early-embryonic development (Boxem et al., 2008). The network contained 731 interactions and defined minimal interacting regions for >200 proteins. The interacting regions identified proved to be highly accurate, with 90% matching prior information in the literature, and the approach increased the sensitivity of the Y2H system, resulting in a more complete interactome network. The domain-based interactome network yielded novel insights into the assembly of the nuclear pore complex as well as the centrosome assembly pathway (Boxem et al., 2008).

The ability of the Y2H system to accurately map interactions with protein domains was also exploited in two *C. elegans* studies that mapped interactions involving the two most common peptide recognition domains: the Src homology 3 (SH3 domain) and the PSD-95/Discs-large/ZO-1 (PDZ) domain (Lenfant et al., 2010; Xin et al., 2013). Both studies generated extensive domain-centric PPI datasets that provide novel insights into the potential biological functions of proteins harboring these domains. The PDZ-domain screens uncovered an unexpectedly high frequency of non-canonical interactions, not involving the C-terminus of the protein partner, many of which were confirmed by co-immunoprecipitation (Lenfant et al., 2010). Comparison of the *C. elegans* SH3 domain interactome with similar networks generated for budding yeast indicated that, while the repertoire of ligand binding motifs is conserved, the actual wiring of the network evolved rapidly, with almost no SH3 domain interactions between orthologous proteins being conserved between worm and yeast (Xin et al., 2013).

Integrating functional genomic and protein interactome data

One of the advantages of a genetically tractable organism like *C. elegans* is that physical interaction mapping can be combined with phenotypic analysis to yield more meaningful hypotheses regarding the *in vivo* roles of protein interactions. The value of integrating interactome and phenotypic data was first demonstrated in a study of the *C. elegans* DNA damage response (DDR) (Boulton et al., 2002).

Each of 192 proteins in a DDR interactome network generated by Y2H was investigated for a role in the response to g-irradiation, and 23 genes required for DDR were identified, of which 11 were novel in any system (Boulton et al., 2002). Two later studies expanded upon this theme. The first added integration of transcriptomic data to identify 10 novel interactions between germline proteins likely to be functionally relevant (Walhout et al., 2002), and the second combined a transforming growth factor b (TGFb) interactome with single and double genetic perturbations to generate an integrated network of protein-protein and genetic interactions (Tewari et al., 2004). In a landmark study, Gunsalus *et al.* generated an extensive integrated network of *C. elegans* early embryonic development that incorporated three high-quality datasets: 6,572 binary physical interactions between 3,848 *C. elegans* proteins, a compendium of *C. elegans* microarray profiles, and a series of detailed microscopy observations of phenotypes caused by RNA-mediated inactivation of 661 early embryogenesis genes (Gunsalus et al., 2005). The integrated network was very effective at predicting two types of molecular assemblies required for embryogenesis: multi-protein complexes like the ribosome or anaphase-promoting complex – supported by PPI and phenotypic data – and highly connected subnetworks of proteins acting in distinct but functionally interdependent processes – supported by phenotypic and expression correlations (Gunsalus et al., 2005).

The relative ease with which phenotypic screens can be performed in *C. elegans* by RNAi continues to make integration of interactomic and phenotypic data attractive. We recently combined Y2H-based interactome mapping with phenotypic profiling to generate an integrated network of *C. elegans* cell polarity proteins (Koorman et al., 2016). We identified 100 physically interacting protein pairs for which RNAi-mediated depletion caused a defect in the same polarity-related process (Koorman et al., 2016). Moreover, by using a fragment-based approach we were able to delineate the regions that mediate the identified interactions, and used this information to demonstrate that an interaction between PAR-6 and PAC-1 is essential for the establishment of radial polarity (Koorman et al., 2016).

Protein complex mapping in *C. elegans* – MS-based technologies add spatiotemporal information to interactome networks

The most commonly used mass spectrometry (MS)-based protein complex mapping approach is affinity purification followed by mass spectrometry (AP-MS) (Dunham et al., 2012). Although the number of *C. elegans* PPIs identified by AP-MS is relatively low, smaller scale studies have yielded numerous biological insights and several noteworthy innovations have been developed in *C. elegans*.

The earliest AP-MS studies in *C. elegans* used custom antibodies directed against a specific protein (Chan et al., 2003; Desai et al., 2003; Duchaine et al., 2006; Srinivasan et al., 2003). Most affinity purifications, however, utilize proteins fused to a tag that is recognized by a common affinity reagent. A common type of tag is the tandem affinity purification (TAP) tag, which incorporates two affinity purification tags separated by a protease cleavage site (Rigaut et al.,

1999). The original TAP tag, developed for use in yeast, contained protein A and the calmodulin-binding peptide (CBP) as the affinity tags (Rigaut et al., 1999). This combination has drawbacks in other cell types than yeast, however, and several alternative TAP tags have been developed (see Table 1 for an overview *C. elegans* TAP tags). A very useful improvement pioneered in *C. elegans* was the inclusion of the green fluorescent protein (GFP). In a study of the composition of the kinetochore, Cheeseman *et al.* developed the Localization and Affinity Purification (LAP) tag, consisting of GFP, a TEV protease cleavage site, and the S peptide (Cheeseman and Desai, 2005; Cheeseman et al., 2004). The LAP tag enabled *in vivo* visualization of novel candidate kinetochore components, as well as the identification of interacting proteins by AP-MS. This tag was later also used in a large-scale analysis of human protein complexes involved in mitosis (Hutchins et al., 2010).

While greatly reducing background, the high stringency of tandem purifications makes it difficult to identify transient or weak interactions (Dunham et al., 2012). With the development of quantitative MS techniques and sophisticated algorithms to distinguish true interactors from background proteins, single-step affinity purification has become the current AP-MS method of choice. For single-step purifications, GFP remains a very attractive tag. Nanobody-based GFP purification reagents (*e.g.*, GFP-Trap) enable efficient purification. Moreover, novel developments expand the uses of GFP-tagged proteins. Recently, a method was developed that enables spatiotemporally controlled degradation of GFP-tagged proteins in *C. elegans* (Wang et al., 2017). The method is based on a fusion between a GFP-targeting nanobody and a SOCS-box containing ubiquitin ligase adaptor, which can be expressed from tissue-specific or heat shock promoters. A single transgenic strain can thus be used to visualize a protein, identify binding partners by AP-MS, and characterize the role of the tagged protein in specific tissues.

Tissue-specific complex mapping

Many proteins are expressed in a subset of cells or are part of multiple distinct complexes that reflect the needs of specific cell types. Yet when we lyse an animal for affinity purification, the proteins from all tissues become mixed, diluting the relative levels of the targeted protein, and mixing the complexes from different cells. To circumvent these problems, tissue specific protein complex purification approaches are needed. The physical isolation of large numbers of cells from *C. elegans* remains challenging. Efforts to date have instead made use of tissue-specific protein tagging based on the Avi tag, a 15 amino acid sequence that can be biotinylated *in vivo* by the BirA biotin ligase from *Escherichia coli* (de Boer et al., 2003; Schäffer et al., 2010; Schatz, 1993; Waaijers et al., 2016). This enables purification through a biotin-streptavidin interaction, one of the strongest non-covalent interactions known. Since biotinylation of the Avi tag depends on the expression of the BirA, biotinylation can be restricted to specific cell types by expressing BirA from tissue-specific promoters.

Two affinity purification tags incorporating the Avi tag have been developed for *C. elegans*. Schäffer *et al.* created the SnAvi TAP tag containing GFP, a new epitope (SB1) recognized by a publicly available monoclonal antibody, and the Avi tag (Schäffer *et al.*, 2010). The suitability of the SnAvi tag for protein complex purification was demonstrated by purifying the E3/E4 ubiquitin-protein ligase CHN-1 expressed in body-wall muscle cells. This resulted in the identification of multiple known and novel interactions, one of which was further investigated and confirmed in independent experiments (Schäffer *et al.*, 2010). In collaboration with the group of B. Tursun, we developed the GTA TAP tag, containing GFP and the Avi tag separated by a TEV cleavage site (Waijers *et al.*, 2016). We generated several driver lines expressing BirA in specific tissues and demonstrated that GTA-tagged proteins are indeed biotinylated specifically in the targeted tissue. We further demonstrated the efficacy of the approach by purifying known interactors of the basolateral polarity regulator LGL-1 using tissue-specific BirA expression (Waijers *et al.*, 2016).

A drawback of biotinylation-based systems is that endogenously biotinylated proteins bind to the affinity reagent as well. This necessitates the use of a TEV cleavage step to release the tagged protein and associated proteins from the purification reagent. An attractive alternative is the use of Cre/lox or FLP/Frt to couple a tag to a protein of interest (Muñoz-Jiménez *et al.*, 2017; Schwartz and Jorgensen, 2016). The tag is initially separated from the protein coding sequence by a lox- or Frt-flanked “off cassette”. Expression of Cre or FLP, which can be spatiotemporally controlled, excises the cassette sequence, directly linking the tag and gene coding sequences. This approach should enable improved tissue-specific purification of protein complexes in a single-step procedure.

Complex mapping by co-fractionation

The need to individually tag and purify each protein makes AP/MS a time-consuming approach. Co-fractionation offers an alternative in which large numbers of candidate protein interactions are inferred from a limited number of mass spectrometry runs (Havugimana *et al.*, 2012; Kirkwood *et al.*, 2013; Kristensen *et al.*, 2012; Wan *et al.*, 2015). In co-fractionation, lysates are subjected to extensive biochemical fractionation followed by quantitative MS, and protein complex memberships are determined based on similarities in elution profile. Recently, Wan *et al.* used co-fractionation to investigate the evolutionary conservation of protein complexes (Wan *et al.*, 2015). From biochemical fractionations of 9 species, including worm, fly, mouse, and human cells, 16,655 co-complex interactions were derived that were conserved between human and at least one of the other species. The projected complexes tended to group into ‘new’ complexes, which were smaller and made up of metazoan-specific proteins, and ‘old’ complexes, which consisted mainly of proteins conserved across eukaryotes. Of the 16,655 interactions, 10,256 were conserved in *C. elegans*, and three inferred *C. elegans* complexes were experimentally verified in AP-MS experiments. This represents the largest collection of MS-derived interactions in *C. elegans* to date.

The main drawback of co-fractionation is that interactions are inferred rather than directly detected. Nevertheless, the increase in scale offered by co-fractionation makes it possible to address questions that cannot easily be addressed using conventional AP-MS approaches. One attractive application is the elucidation of spatiotemporal dynamics of protein interactions. For example, co-fractionation was used to determine changes in the interactome of human cells upon epidermal growth factor (EGF) stimulation (Kristensen et al., 2012). Co-fractionation could similarly be used in *C. elegans* to detect changes in complex composition during development, under different mutant conditions, or in response to different environmental cues.

Adding spatial information by proximity labeling

To understand the roles of a protein-protein interaction *in vivo*, it is important to know in which tissues and at which subcellular location the interaction takes place. Proximity labeling is an MS-based PPI-mapping approach that utilizes enzymes that promiscuously attach a reactive label, usually biotin, to any proteins nearby (generally within a ~20 nm radius) (Kim and Roux, 2016). The biotinylated proteins can then be purified using standard methods and characterized by MS. Proximity labeling therefore not only identifies candidate interaction partners but provides information on the subcellular location of interactions as well: if the 'bait' protein localization is known, any labeled proteins are presumably localized nearby. The two most common approaches are Biotin Identification (BioID), in which a promiscuous biotin ligase is attached to a protein of interest, and engineered ascorbate peroxidase (APEX), which uses a peroxidase instead of a biotin ligase (Kim and Roux, 2016). The main drawback of these approaches is that any proteins within the labeling radius, including those not physically interacting, will be labeled. Neither approach has been used yet in *C. elegans* to identify candidate interacting proteins, but an improved variant of BioID, termed TurboID, was recently reported to be able to biotinylate proteins in *C. elegans* embryos (Branon et al., 2017).

Completing the *C. elegans* interactome

Two of the largest PPI curation databases, BioGRID and IntAct, currently list 5,805 and 13,273 PPIs for *C. elegans* respectively (Chatr-Aryamontri et al., 2017; Licata and Orchard, 2016), while the full *C. elegans* interactome is estimated to contain between 100,000 and 260,000 PPIs (Simonis et al., 2009; Stumpf et al., 2008) – a number that is likely an underestimate when taking into account that different protein isoforms can have distinct interaction profiles (Yang et al., 2016). We are therefore at least an order of magnitude away from producing a complete map of all protein interactions that take place in *C. elegans*. How are we to fill this gap? In the short term, the most expedient way will be to renew efforts using improved variants of the Y2H system and AP-MS. Both are tried-and-true technologies that are highly effective at mapping protein-protein interactions. AP-MS approaches benefit from continuous developments in mass spectrometers and computational algorithms that increase the fraction of true interactions that can be detected (sensitivity) as well as the ability to distinguish

true interactors from contaminants (specificity) (Dunham et al., 2012a; Oeffinger, 2012). Moreover, endogenously tagged *C. elegans* lines, which are most likely to accurately reflect normal protein levels and localization patterns, can now readily be generated using CRISPR/Cas9. Since AP-MS has not been applied at large scale in *C. elegans*, there is tremendous opportunity to use this technology to expand the interactome.

For binary interactome mapping by Y2H, several improvements can be implemented. First, using multiple protein fragments in addition to full-length clones greatly increases the sensitivity (Boxem et al., 2008; Waaijers et al., 2013). Not all fusion constructs are functional – for example when steric hindrance impedes formation of a functional Gal4p transcription factor – and using multiple fragments increases the chances an interaction can be detected. Second, sensitivity can be optimized by combining multiple variations of the Y2H system (Caufield et al., 2012), as the vector backbone (low or high copy), the linker length between the fusion protein and the AD and DB domains, and the location of the tag (N-terminal vs. C-terminal) all affect the detectability of interactions. Implementing these improvements would substantially increase the scale at which Y2H screens need to be performed. One way to accomplish this is to use next-generation DNA sequencing to reduce the amount of colony picking and PCR amplification required (Weimann et al., 2013; Yachie et al., 2016; Yu et al., 2011). Yachie *et al.* recently developed a Cre-mediated recombination approach that generates fused DNA barcodes from the Gal4 AD and DB plasmids in each yeast cell, which can subsequently be isolated from pools of yeast and quantified by next-generation sequencing (Yachie et al., 2016). Their approach improved the efficiency of matrix Y2H screens while maintaining a quality similar to current high-quality Y2H implementations (Yachie et al., 2016).

Notwithstanding technological improvements, multiple PPI mapping techniques will ultimately need to be applied to complete the *C. elegans* interactome. For example, the Y2H system is not able to detect interactions that take place at the plasma membrane, or that require specific posttranslational modifications, and AP-MS approaches have difficulty detecting weak or transient interactions. Numerous alternative binary and complex mapping approaches have been developed to complement such blind spots. A split-ubiquitin system was designed to identify binary interactions at the plasma membrane (Snider et al., 2010; Stagljar et al., 1998). This system was recently used to reveal physical interactions between transmembrane proteins involved in *C. elegans* sperm maturation (Marcello et al., 2018). Other binary PPI mapping approaches, including the Mammalian Protein-Protein Interaction Trap (MAPPIT), the co-immunoprecipitation-based LUMIER system, and Bimolecular fluorescence complementation (BiFC) assays, make use of other host cells than yeast to better mimic the natural environment of the proteins investigated (Barrios-Rodiles et al., 2005; Lievens et al., 2016; Miller et al., 2015; Taipale et al., 2014). Several alternatives to AP-MS also exist (Mehta and Trinkle-Mulcahy, 2016; Smits and Vermeulen, 2016). The proximity labeling approaches discussed above covalently label proteins *in vivo*, and are able to detect lower affinity interactions

and interactions involving insoluble proteins (Kim and Roux, 2016). Cross-linking mass spectrometry physically links amino acids that are in close proximity, which improves the detectability of weak or transient interactions, and provides valuable information on the topology of protein complexes (Liu and Heck, 2015).

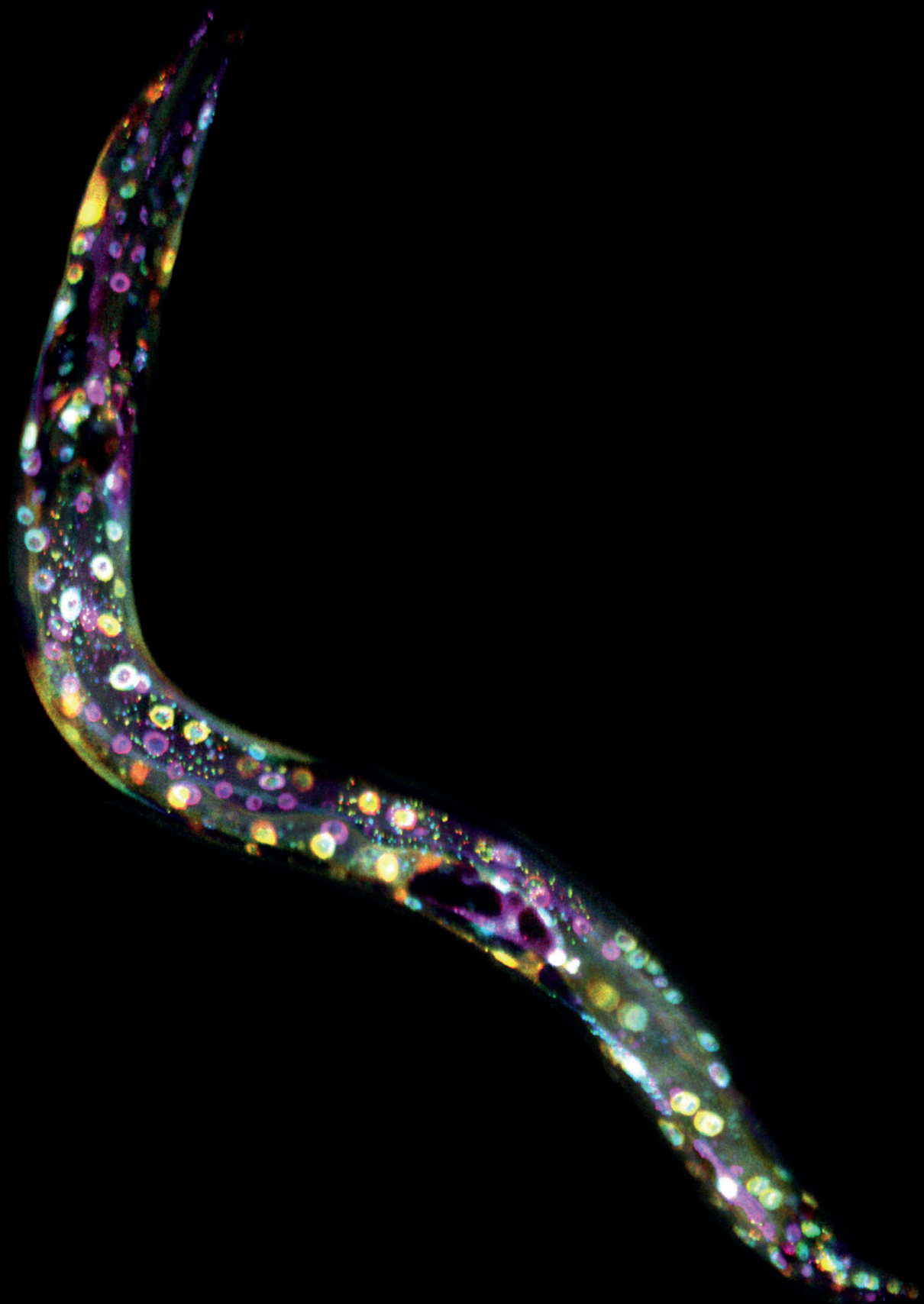
The data obtained from all these different experimental sources will need to be integrated, which poses both challenges and opportunities. Datasets cannot simply be added together due to the presence of false positives. As the interactome becomes more complete, each additional dataset will only add a limited number of true interactions. False positives, however, tend to be random proteins pairs, and will therefore be overrepresented in the 'novel' interactions added. Thus, more sophisticated approaches are needed. In general, a safe assumption is that an interaction reported in multiple experimental datasets is more likely to be true. Using computational algorithms based on intimate knowledge of the methods used, combining multiple data sources can greatly increase the accuracy of the interactome. For example, by taking into account the number and type of assays in which a binary interaction has been observed, it is possible to derive a confidence score for each interaction (Braun et al., 2009). Similarly, a recent integration and re-analysis of three MS-based datasets (two AP-MS and one co-fractionation) used machine learning algorithms to produce a network with both better coverage and accuracy than the original datasets (Drew et al., 2017). Finally, specialized databases such as STRING (Szklarczyk et al., 2017) integrate different sources of interaction data, including direct physical evidence and indirect evidence such as genetic interactions or co-expression, and attach a confidence score to each interaction.

Conclusion

The efforts and techniques discussed here have made great inroads in elucidating the protein interactome of *C. elegans*. Nevertheless, the total interactome is estimated to be an order of magnitude larger than the number of PPIs currently identified. Hence, redoubled efforts using classic approaches like the Y2H system and AP/MS, in combination with novel techniques will be necessary if we are to identify the full complement of PPIs that can take place in this model organism. Moreover, it is ultimately not sufficient to know that an interaction can take place. It is also necessary to understand when, where, and under what circumstances the interaction occurs. In the past years, several MS-based approaches have been developed that make strides in this direction. Co-fractionation and tissue-specific complex purification have already been shown to work in *C. elegans*, and proximity labeling techniques are likely to be tested in the near future. These technologies still have to come into their own in *C. elegans*, and a key challenge for the future will be to successfully develop and apply these and other approaches at large scale in *C. elegans*.

Acknowledgements

We thank P. Porras Millán for his assistance in querying the IntAct database. Research in the lab of MB is supported by grants from the Netherlands Organization for Scientific Research (NWO): earth and life sciences (ALW) Innovational Research Incentives Scheme grant 016.VICI.170.165 and chemical sciences (CW) ECHO grant 711.014.005, and by the European Union's Horizon 2020 research and innovation programme under the Marie Skłodowska-Curie grant agreement No 675407.



Chapter 3

CeLINC, a fluorescence-based
protein-protein interaction assay
in *C. elegans*

Jason R. Kroll, Sanne Remmelzwaal, and Mike Boxem

Developmental Biology, Institute of Biodynamics and Biocomplexity, Department of Biology, Faculty of Science, Utrecht University, Padualaan 8, 3584 CH, Utrecht, The Netherlands.

This chapter is published:

Kroll, J.R., Remmelzwaal, S., & Boxem, M. (2021). CeLINC, a fluorescence-based protein-protein interaction assay in *C. elegans*. *Genetics*.

Chapter image by: Jason R. Kroll

Abstract

Interactions among proteins are fundamental for life and determining whether two particular proteins physically interact can be essential for fully understanding a protein's function. We present *C. elegans* light-induced co-clustering (CeLINC), an optical binary protein-protein interaction assay to determine whether two proteins interact *in vivo*. Based on CRY2/CIB1 light-dependent oligomerization, CeLINC can rapidly and unambiguously identify protein-protein interactions between pairs of fluorescently tagged proteins. A fluorescently tagged bait protein is captured using a nanobody directed against the fluorescent protein (GFP or mCherry) and brought into artificial clusters within the cell. Co-localization of a fluorescently tagged prey protein in the cluster indicates a protein interaction. We tested the system with an array of positive and negative reference protein pairs. Assay performance was extremely robust with no false positives detected in the negative reference pairs. We then used the system to test for interactions among apical and basolateral polarity regulators. We confirmed interactions seen between PAR-6, PKC-3, and PAR-3, but observed no physical interactions among the basolateral Scribble module proteins LET-413, DLG-1, and LGL-1. We have generated a plasmid toolkit that allows use of custom promoters or CRY2 variants to promote flexibility of the system. The CeLINC assay is a powerful and rapid technique that can be widely applied in *C. elegans* due to the universal plasmids that can be used with existing fluorescently tagged strains without need for additional cloning or genetic modification of the genome.

Introduction

Interactions among proteins are critical for the functioning of the cell. Characterizing protein-protein interactions (PPIs) is therefore necessary to understand protein function, and numerous technologies have been developed to identify PPIs. One commonly used technique is the yeast two-hybrid system (Walhout et al., 2000b), which allows for high-throughput screening, but takes place in a context different from the original organism or cell type. Affinity purification combined with mass spectrometry can identify multiple targets interacting with a protein of interest (Dunham et al., 2012) but tissue-specific information is lost and animals are analyzed in bulk. PPI assays that can be applied *in vivo* often rely on split or complementary tags that assemble upon physical proximity of the two proteins to be tested (Bischof et al., 2018; Brückner et al., 2009; Hudry et al., 2011; Shyu et al., 2008), and generally require the generation of fusion proteins that have no uses outside of the interaction assay. To complement these existing assays, we have adapted a fluorescence-based PPI assay for use in *C. elegans*, CeLINC, that can utilize existing fluorescently tagged strains, is easily analyzed, and can be performed in single animals in any cell type of interest without using specialized equipment.

CeLINC is based on a method originally developed in mammalian cell culture (Taslimi et al., 2014) and is an extension of an optogenetic protein inhibition system called “light-activated reversible inhibition by assembled trap” (LARIAT). LARIAT can inhibit target proteins in living cells in a spatiotemporally controlled manner by sequestering the target protein into clusters (Lee et al., 2014). LARIAT elegantly exploits the cryptochrome 2 (CRY2) protein that homodimerizes and heterodimerizes with the cryptochrome-interacting basic-helix-loop-helix (CIB1) protein upon blue light exposure (Kennedy et al., 2010). By fusing a target protein to CRY2 or through the use of nanobodies, target proteins can be sequestered and inhibited in a light-dependent manner. Together, this system has been used to inhibit proteins in a variety of pathways (Asakawa et al., 2020; Nguyen et al., 2016; Qin et al., 2017, 2018) and to recently control mRNA localization (Kim et al., 2020a).

With the LARIAT system as the basis, light-induced co-clustering (LINC) has been developed as a binary PPI assay (Osswald et al., 2019; Taslimi et al., 2014; Ventura et al., 2020). In LINC, two proteins tagged with different fluorescent proteins are tested for their ability to co-cluster in the blue-light-induced CRY2/CIB1 clusters (Figure 1A). To modularize the assay, a GFP nanobody is attached to CRY2 to allow recruitment of any GFP-tagged bait protein to CRY2 clusters in blue light (Figure 1A). After cluster formation, co-clustering of a prey protein tagged with a differently colored fluorescent protein (*e.g.*, mCherry, mScarlet, BFP, or mKate2) is assessed. Proteins that show a positive protein interaction show co-localization in the clusters, while proteins that do not interact do not co-localize in the clusters (Figure 1B). LINC is analogous to a typical immunoprecipitation experiment but takes place within the living cell and allows for visual identification of the protein interaction. The assay therefore requires minimal equipment, only relies on fluorescent protein tags, can maintain cell type specificity, and can be easily

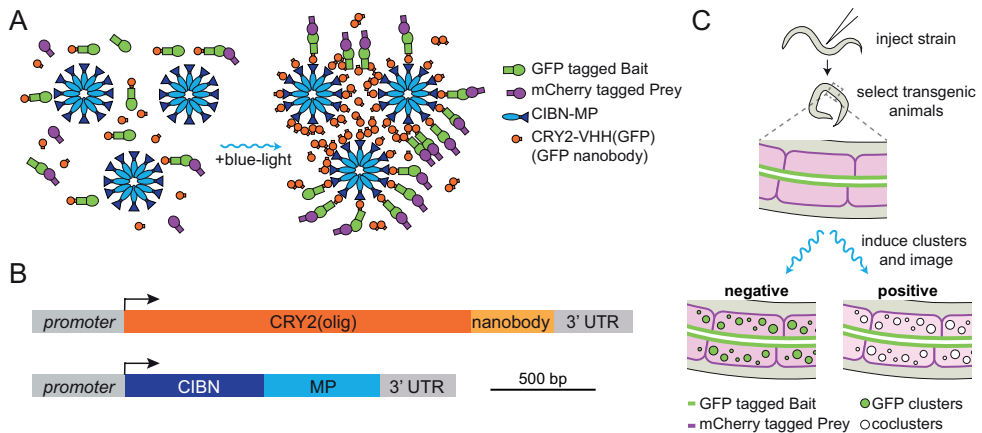


Figure 1. Overview of CeLINC. (A) Overview of CRY2/CIB1 light-induced co-clustering (LINC). Two proteins to be tested for interaction are tagged with fluorescent proteins (GFP and a second color fluorescent protein). In dark conditions, the CRY2::VHH(GFP nanobody) protein is mainly in the nonoligomerized form, and there is no to little association between CIBN with CRY2. Upon blue light exposure, CRY2 both homodimerizes and heterodimerizes with CIBN. The CIBN-MP protein forms a dodecamer that act as a scaffold to increase cluster size. GFP-tagged proteins bound to the nanobody are clustered, resulting in a bright and compact fluorescent signal. The second color fluorescent protein (mCherry in this example) is analyzed for colocalization in the clusters. (B) Diagram of the CeLINC expression constructs. (C) Overview of CeLINC. A strain with two tagged proteins to be tested for an interaction (GFP and mCherry in this example) is injected with plasmids to express the CRY2::VHH(GFP nanobody) and CIBN-MP proteins. Transgenic F1 animals carrying an extrachromosomal array are identified by the presence of a coinjection marker. After transgenic strains are established, clusters are induced by blue light exposure of the transgenic animals and imaged. Cells with GFP containing clusters are then analyzed for colocalization of the mCherry tagged protein.

scored without complex analysis. Additionally, the use of a nanobody gives the system flexibility since any fluorescently tagged protein with a suitable nanobody epitope can be used as the bait protein without additional modifications.

CRY2 based oligomerization and clustering has been used previously in *C. elegans* to induce aggregation of Amyloid- β to study how aggregates affect Alzheimer's disease pathologies, and to oligomerize UNC-40 to manipulate growth cone development, but not to investigate PPIs (Endo et al., 2016; Lim et al., 2020). We adapted LINC for *C. elegans* (CeLINC) and have validated its function and utility to investigate PPIs. First, we have adapted components of the system by codon-optimizing the proteins for use in *C. elegans* and have created expression plasmids that allow for expression of CRY2/CIB1 proteins in multiple tissues. Next, we have characterized CRY2/CIB1 clustering characteristics upon blue light exposure in various *C. elegans* tissues. We then tested CeLINC on various positive and negative reference protein pairs. Finally, we tested for interactions among cell polarity regulators due to their extensively studied nature and previously established protein interactions in other systems and *C. elegans*. We provide a plasmid toolkit to enable flexibility and adaptability of the CeLINC system for further studies and uses. Due to the universal nature of the plasmids and the

ability to use existing fluorescent strains, the CeLINC system is an extremely rapid and powerful way to characterize PPIs in *C. elegans*.

Materials and methods

Plasmid Cloning

Plasmid names and descriptions are available in File S2. Primer information is in File S3. SapTrap donor plasmid overhangs and assembly information are found in File S4. Annotated GenBank files of the plasmids are available in the GSA Figshare portal. Plasmids will be made available at Addgene (<https://www.addgene.org/>).

Sequences for CRY2(olig) (Taslimi et al., 2014), CIBN(1–170) (Lee et al., 2014), mCherry nanobody (RANbody2 mCherry nanobody variant) (Yamagata and Sanes, 2018), and MP (Lee et al., 2014) were codon-optimized using the *C. elegans* codon adapter tool (Redemann et al., 2011) and ordered as gBlocks Gene Fragments (IDT) with appropriate *SapI* restriction sites and overhangs flanking the sequences. The MP, CIBN, and CRY2(olig) sequences each contain one synthetic intron. A 3xFLAG tag and linker segment was added to the C-terminus of the CIBN sequence. The CRY2 variant used, CRY2(olig), contains an E490G mutation to increase clustering ability (Taslimi et al., 2014). The GFP nanobody (VHH(GFP)) sequence was PCR amplified from plasmid pVP130 (Vaart et al., 2020), which was codon-optimized from the original sequence (Wang et al., 2017). The *Pwrt-2* promoter was amplified from plasmid pRS177, the *Pelt-2* promoter was amplified from plasmid pSMR12, the *Phsp-16.48* promoter from plasmid pJRK83, and the *par-6* coding sequence from pJRK11. The *ajm-1* gene was cloned from a mixed-stage cDNA library. *SapI* restriction sites and overhangs for SapTrap assembly were included in the primers used for amplification. PCR amplicons and gBlock fragments were phosphorylated and cloned blunt-ended into the plasmid backbone pHSG298 digested with *Eco53KI*. Donor plasmids were combined as shown in File S4. The SapTrap assembly method (Schwartz and Jorgensen, 2016) was used to assemble donor plasmids to generate the final expression plasmids used for injections. Donor vector mixes were then combined with pMLS257 predigested and linearized with *SapI*. pMLS257 was a gift from Erik Jorgensen (Addgene plasmid # 73716) (Schwartz and Jorgensen, 2016). The plasmid pJRK86 for general AID::GFP expression was made by combining the donor plasmids pJRK1, pDD397, pJRK245, and pJRK150.

The co-injection plasmid pJRK248 was made by Gibson assembly (*Prps-0::HygR::unc-54 3'UTR; Psqt-1::sqt-1::sqt-1 3' UTR*) and contains the dominant markers HygR (Hygromycin resistance) and a *sqt-1* mutation (conferring Roller phenotype), and is a derivative of the plasmid pDD382. pDD382 was a gift from Bob Goldstein (Addgene plasmid # 91830). The plasmid pJRK259 (*Prps-0::mKate2::par-6(ΔPB1)::unc-54 3'UTR*) was made by Gibson assembly from the plasmid pJRK258 using PCR fragments that excluded the amino acids 15–28 of the *par-6* coding region. Plasmids pJRK260 and pJRK261, pJRK262, pJRK263,

and pJRK264 were made by Gibson assembly. The T2A segment and the empty promoter/SapI module were provided by gBlock Gene Fragments (IDT).

Strains and generation of extrachromosomal array strains

Strains are available upon request. The complete list of genotypes and strains used is in File S1. N2 was used as the wild-type strain. The *pkc-3(it309[gfp::pkc-3])* allele was linked to the *dpy-10(cn64)* allele in strain FT1991 and precluded efficient injection. Therefore, the strain was first crossed to N2 to isolate the *lgl-1(xn103[lgl-1::zfp1::mScarlet])* allele, and then was crossed to *pkc-3(it309[gfp::pkc-3])* to generate the strain BOX757.

Fluorescently tagged strains were first generated by crossing and then CeLINC plasmids were injected into the gonads of young adult worms to form extrachromosomal arrays. Injection mixes were made with the CRY2(olig)::nanobody and CIBN-MP plasmids at a concentration of 10 ng/μL, and the co-injection plasmid pJRK248 at 20 ng/μL. Strains with *mKate2::par-6::unc-54 3' UTR* or *mKate2::par-6(ΔPB1)::unc-54 3' UTR* were at a concentration of 10 ng/μL. Strains with *Pelt2::ajm-1::mCherry::unc-54 3' UTR* were at a concentration of 20 ng/μL and *Pelt2::dlg-1::GFP::unc-54 3' UTR* and *Pelt2::dlg-1(ΔL27)::GFP::unc-54 3' UTR* were used at 5 ng/μL. Negative reference pair control strains used injection mixes with 10 ng/μL of pJRK86 (*Prps-0::AID::GFP::unc-54 3' UTR*). Lambda DNA (Thermo Scientific) was used to bring the total concentration of DNA to 95 ng/μL for all injection mixes. Plasmids were isolated from bacteria using the HQ PureLink Mini Plasmid Purification Kit (Invitrogen) with an extra wash step. After injection, transgenic animals were identified by a Rol phenotype and/or resistance to hygromycin. For hygromycin selection, 300–400 μL of 5 mg/ml hygromycin B (Foremedium Ltd) dissolved in water was added to the plates 2–3 days after growth on the plate was established.

Animal handling

Animals were grown on standard nematode growth medium (NGM) agar plates at 20° seeded with OP50. Hermaphrodites in the L2–L4 larval stage were used for imaging. Animals grown in the ambient light condition were grown in the dark but mounted under a binocular microscope with normal white light illumination. Animals grown in the complete darkness condition were grown in the dark and mounted for microscopy in dark conditions with only the use of a green or red light in the room. The slide was then transported in aluminum foil to the spinning disk microscope. The animals were focused and moved into position on the microscope using the dimmest possible setting of a white light. For the heat shock experiment in Figure 6E–F, worms were either kept at 20° (-heat shock) or 30° (+heat shock) for two hours, and then imaged.

Imaging and blue light activation

Imaging was performed by mounting larvae on a 5% agarose pad in 1 mM levamisole solution in M9 buffer to induce paralysis. Images were taken with a Nikon Ti-U microscope driven by MetaMorph Microscopy Automation and Image Analysis Software (Molecular Devices) and equipped with a Yokogawa

CSU-X1-M1 confocal head and an Andor iXon DU-885 camera, using a 60× 1.4 NA objective and with 0.25 μm z-step intervals. Exposure settings were customized for each fluorescently tagged protein, due to wide variations in expression levels and signal intensities. To activate cluster formation with blue light from starting dark conditions, as in Figure 2, z-stacks were taken of the sample with the blue laser with 300ms exposure, 50% laser power, and 50–80 z-stacks (depending on the sample depth). For Figures 3–6, animals were mounted with white light therefore clusters were pre-activated before imaging. Animals were then directly imaged, and z-stacks were obtained with both green and blue lasers. Images were analyzed and processed with ImageJ/FIJI (Schindelin et al., 2012). Photoshop was used to non-destructively prepare images and Adobe Illustrator was used for figure preparation.

Half-life experiment & cluster quantification

For the experiment in Figure 2B and C, animals were grown and mounted in complete darkness. The animal was imaged first with the green laser to determine the baseline mKate2 signal (pre blue light). Next, the clusters were activated by imaging the z-stack with both green and blue lasers (300ms exposure, 50% laser power, and 89–105 z-stacks), corresponding to the 0 min time-point. After activation, the animal was imaged in 5-minute intervals for 25 minutes with only the green laser. Maximum projections of the z-stack were generated at each time point, and ComDet 0.5.4 plugin for ImageJ (<https://github.com/ekatruxha/ComDet>) was used to detect and count the number of clusters. The parameters used were: “include larger particles”-true, “segment larger particles”-false. In animals one and two, approximate particle size was set to 3.0, and intensity threshold (in SD) was set to 25. For animal three in the experiment, “include larger particles” was set to false, the approximate particle size was 2.0, and the intensity threshold (in SD) was increased to 35. Cluster numbers were normalized by subtracting the number of clusters identified in the pre-blue-light timepoint from the number of clusters in the following time-points to have a baseline corresponding to zero clusters. The maximum number of clusters identified in each sample was then used to determine the fraction of maximum clusters at every time point. The half-life was determined by solving the equation

$$N(t) = N_0 \left(\frac{1}{2} \right)^{\frac{t}{t_{1/2}}}$$

for $t_{1/2}$, where N_0 is the initial quantity, $N(t)$ is the remaining quantity after time t , and $t_{1/2}$ is the half-life. For Figure 1E and F, the following settings were used for the ComDet plugin: “include larger particles”-true, “segment larger particles”-false, approximate particle size was set to 2.0, and intensity threshold (in SD) was set to 5.

Quantitative image analysis

Quantification of the co-clustering of bait and prey proteins in the various protein pairs and negative control pairs (GFP) was performed by the ComDet 0.5.4 plugin for ImageJ (<https://github.com/ekatruxha/ComDet>). Images were prepared for analysis by generating a maximum z-stack projection and manually outlining the region(s) of analysis in the cell. Next, the ComDet plugin was used in colocalization mode with the following settings: “max distance between colocalizing particles”-3, “include larger particles”-false, “segment larger particles”-false, “approximate particle size”-3.0. “Intensity threshold (in SD)” was initially set to 1 standard deviation, and the analysis repeated with an intensity threshold increase of 1 until reaching the value of 25 standard deviations. In each animal, the percent of bait or prey proteins colocalizing was obtained from the generated results table. In some cases, very few spots were detected in the images (especially at higher threshold levels). To avoid bias in the percentage from a small number of clusters, threshold levels where fewer than 15 spots were detected in the image were not incorporated into the mean percentage calculation. Co-clustering curves were then generated showing the mean percentage value and 95% confidence intervals. Negative control pairs show flat or rapidly decreasing curves for both the prey and bait colocalization. In contrast, positive pairs show an increasing prey colocalization percentage. Image quantification data is available as File S5 in the GSA Figshare portal. For the graphs in Figure S3, maximum z-stack projections were analyzed with the ComDet plugin with the following settings: “max distance between colocalizing particles”-3, “include larger particles”-false, “segment larger particles”-false, “approximate particle size”-3.0. “Intensity threshold (in SD)”-25 standard deviations. The area of the cluster was obtained from the “Narea” column of the results table and the sum of the pixels in each cluster corrected to spot specific background was obtained from the “IntegrIntChX” column of the results table. Quantification data is available as File S6 in the GSA Figshare portal.

Data availability

Plasmids are available from Addgene (<https://www.addgene.org>, Addgene plasmids #173730-173755). Strains are available upon request. The complete list of genotypes and strains used is in File S1. Plasmid names and descriptions are available in File S2. Primer information is in File S3. SapTrap donor plasmid overhangs and assembly information are found in File S4. Annotated GenBank files of the plasmids and image quantification data (Files S5-S6) are available in the GSA Figshare portal: <https://doi.org/10.25386/genetics.16546098>. The authors affirm that all data necessary for confirming the conclusions of the article are present within the article, figures, and tables.

Results

Light-induced CRY2 clustering in *C. elegans*

We designed the CeLINC system as a two-vector system (Figure 1B). One vector expresses a fusion of a nanobody (VHH) with a variant of the CRY2 protein, CRY2(olig) (E490G), that increases oligomerization (Taslimi et al., 2014).

The other vector expresses the CIB1 N-terminal region (CIBN) fused to the multimerization domain (MP) of Ca²⁺/Calmodulin-dependent protein kinase II (CaMKII). Inclusion of MP enhances light-activated oligomerization and helps to increase cluster sizes by acting as a scaffold (Che et al., 2015; Lee et al., 2014). All of the components were codon optimized for expression in *C. elegans*. We first designed vectors for expression with a general promoter, *rps-0*, which expresses broadly in somatic cells including the intestine, muscle cells, and hypodermis. Constructs were assembled modularly with the SapTrap assembly system (Schwartz and Jorgensen, 2016) to allow for further flexibility and ease of use for future modifications or variants. To use CeLINC, in brief, animals expressing fluorescently tagged proteins to be tested for interaction are injected with the CeLINC plasmids to form extrachromosomal arrays (Figure 1C). Transgenic strains are established by selecting animals expressing a co-injection marker, and strains are established that reliably transmit the extrachromosomal array. Finally, animals are exposed to blue light and are imaged to determine whether the two fluorescently tagged proteins co-cluster in the cell types of interest or not, indicating a positive or negative protein interaction respectively (Figure 1C).

We first tested the ability for CRY2(olig) to form clusters in response to blue light. To directly visualize cluster formation, we tagged CRY2(olig) with the fluorescent protein mKate2. Worms were injected with two plasmids: mKate2::CRY2(olig)::VHH(GFP), and a protein fusion of CIBN::MP, both expressed from the *rps-0* general promoter and using the *unc-54* 3' UTR. We used a non-fluorescent co-injection marker that confers a Roller (Rol) phenotype and resistance to hygromycin to identify animals carrying extrachromosomal arrays. Transgenic strains were kept in complete darkness during development, mounted on slides under dark lighting conditions, and then placed on the spinning disk microscope in near darkness, with the dimmest amount of light possible to center the worm on the microscope and focus (dark lighting condition). Before blue light stimulation, few to no mKate2::CRY2(olig) clusters were apparent in the animals, but a diffuse mKate2 signal was detected, corresponding to mKate2::CRY2(olig) proteins in a non-oligomerized state (Figure 2A). Next, blue light was delivered in a series of pulses to the animal (see Methods). Immediately after this treatment, mKate2::CRY2(olig) was found to be highly clustered in the cell, indicating that the CRY2 clustering system responds to blue light activation and readily and rapidly forms clusters, as seen in other systems (Figure 2A). Both intestinal and muscle cells showed rapid cluster formation (Figure 2A), in addition to other cells in the animal. Clusters were visible and had formed in different compartments of the cell, such as the nucleus, cytoplasm, and alongside the plasma membrane (Figure 2A). Overall, cellular morphology in the animals appeared normal, and there were no apparent phenotypes observed in the transgenic progeny. Therefore, blue-light-activated CRY2 clusters form rapidly and readily in *C. elegans*, and there was little to no toxicity or lethality associated with expression of the constructs.

To determine the half-life of the CRY2(olig) clusters in *C. elegans*, we grew and mounted animals in dark conditions, stimulated cluster formation with blue

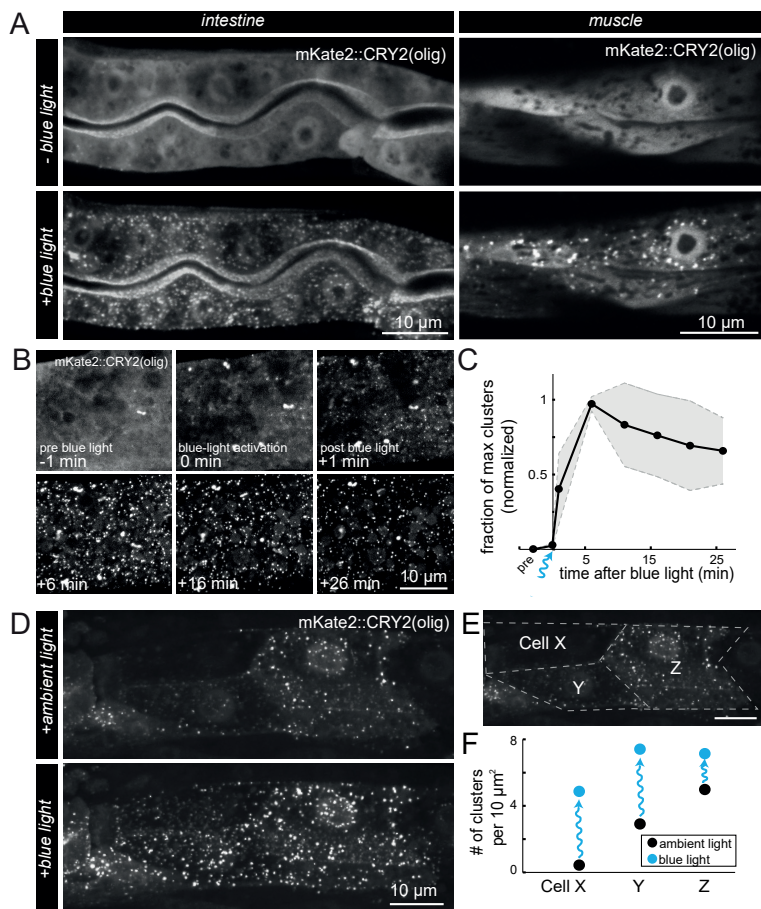


Figure 2. Behavior of CRY2(olig) clusters and light activation in *C. elegans*. (A) Fluorescent images (maximum z-stack projections) of intestine and muscle cells in transgenic animals expressing mKate2::CRY2(olig) and CIBN-MP before and after blue light exposure. mKate2 signal was diffuse before blue light exposure, while extensive clusters rapidly formed throughout the cytoplasm and in the nuclei upon exposure. Time between conditions was 1 min. (B) Maximum projections of a region of an intestinal cell taken before (-1 min), during (0 min), and after (+1 min to +26 min) blue light activation to quantify oligomerization and decay of mKate2::CRY2(olig) clusters. (C) Quantification of cluster number over time in intestinal cells before and after blue light exposure, N = 3 animals. Clusters were quantified with ComDet plugin for ImageJ/Fiji (see Materials and Methods). Black line indicates the mean fraction of clusters at a given time point, normalized to 0 before illumination and 1 at the point of maximum cluster formation. Gray shaded regions indicate the standard deviation. (D) Maximum projection images of the anterior portion of the intestine after ambient light exposure during mounting (normal binocular microscope with white light), and after additional blue light stimulation. (E) Schematic of the manual segmentation of the intestinal cells of the animal in (D) for quantification in (F). (F) The number of clusters per 10 μm^2 in each cell segmented in (E), in ambient light and blue light conditions. Clusters were quantified with ComDet plugin.

light, then imaged the animals over time with no further blue light stimulation (Figure 2B). We found that the maximum number of clusters was obtained six minutes after blue light exposure, and the decay in the number of clusters was slow, giving an estimated half-life of 34 min (Figure 2C). The rate of decay was roughly comparable to experiments in cell culture using a CRY2(olig)-mCherry construct, which showed a half-life of 23 min (Taslimi et al., 2014). These values are significantly longer than wild-type CRY2, for which a half-life of around 6 minutes has been reported (Bugaj et al., 2013; Lee et al., 2014). Therefore, CRY2(olig) clusters in *C. elegans* are relatively stable and allow ample time for animal manipulation and imaging.

Since it is inconvenient to manipulate animals in complete darkness and under special lighting conditions, in subsequent experiments we mounted animals on slides under ambient room lighting conditions and with white light from a binocular microscope. We expected this approach to pre-activate cluster formation before imaging. Pre-activation of clusters during mounting should also aid imaging, since animals and cells expressing the CeLINC constructs in the cell types of interest can be more quickly identified. In this condition, cells already displayed clustering of mKate2::CRY2(olig) before blue light stimulation, indicating that the white light received during mounting was sufficient to activate CRY2 oligomerization (Figure 2D). These animals were then subjected to blue light stimulation to determine whether additional oligomerization could be induced. Indeed, cells showed increased mKate2::CRY2(olig) clustering in response to blue light stimulation (Figure 2D). One such animal showed differing levels of mKate2::CRY2(olig) expression in three different intestinal cells, as determined by their level of diffuse mKate2 signal in the nucleus (Figure 2E, F). The cell with the weakest level of mKate2::CRY2(olig) expression showed no cluster formation under ambient light, but significant cluster formation after blue light stimulation, while the cells with higher amounts of mKate2::CRY2(olig) expression had less of a change after blue light exposure (Figure 2F). In addition, the area and number of clusters correlated to the mKate2::CRY2(olig) expression level (Figure 2F). Therefore, as seen in another study, higher expression levels induce clustering more readily than lower expression levels (Che et al., 2015). In summary, the blue-light-activated CRY2 based oligomerization behaves similarly to other systems, suggesting that the system is functional and suitable for use in *C. elegans*.

Use of CeLINC for identifying PPIs

Having established CRY2 functionality and cluster formation in *C. elegans*, we next tested the ability of the CeLINC assay to discriminate between positive and negative protein-protein interactions. We used the highly conserved and well-studied protein interaction between PKC-3 (aPKC) and PAR-6 (Par6). Both proteins are essential for polarization of cells in various tissues and form a complex through interaction of their PB1 domains (Li et al., 2010b). Mutations that delete this domain are lethal, highlighting the critical importance of this protein interaction during development and cell function (Li et al., 2010b).

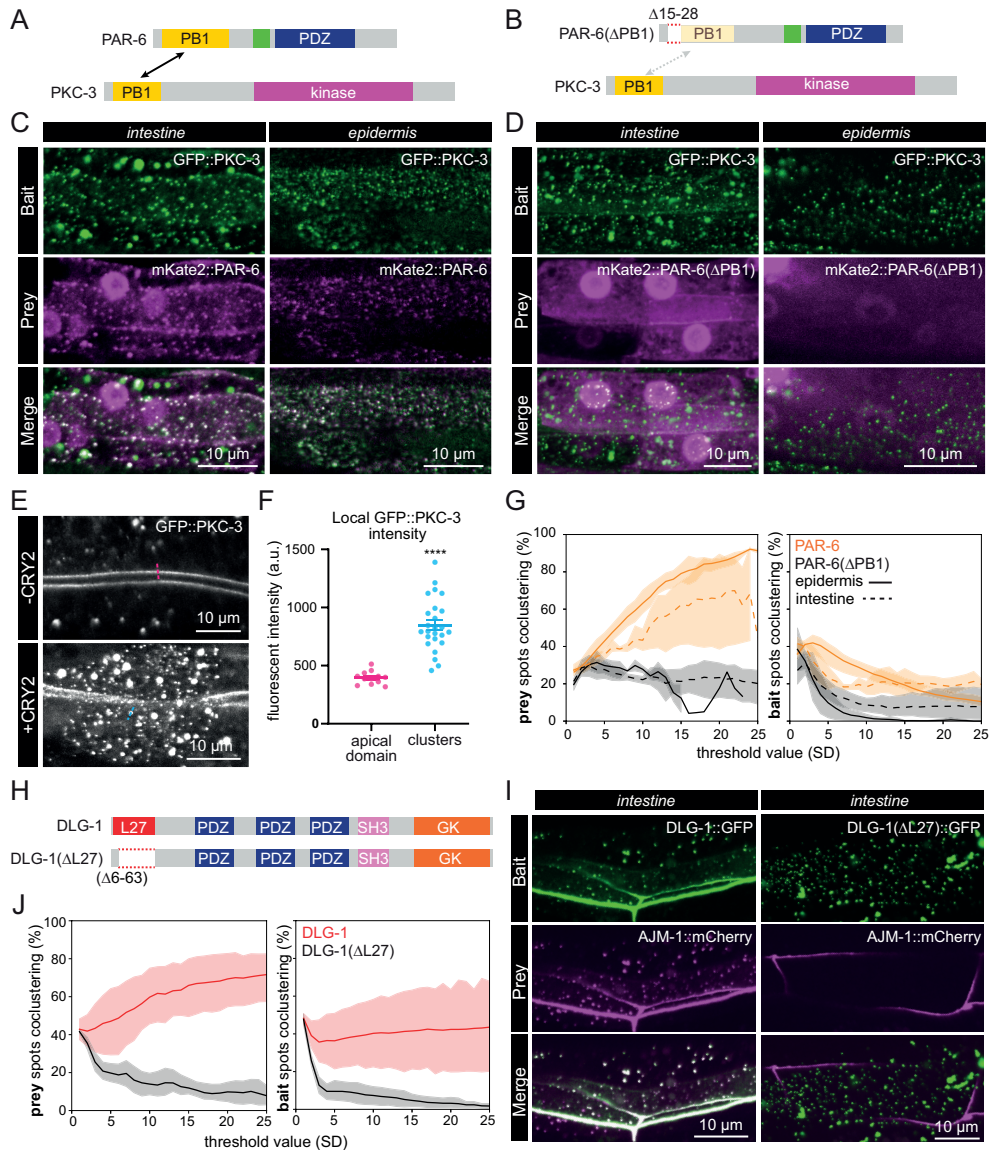


Figure 3. Interaction of PKC-3 with PAR-6 and an interaction defective PAR-6 variant assayed with CeLINC. (A) Schematic representation of the wild-type PKC-3 and PAR-6 proteins with labeled protein domains. Arrow indicates the PB1 domains that mediate the PPI. (B) Diagram of PKC-3 and mutant PAR-6(Δ PB1) proteins with their domains. Dashed protein region in PAR-6 (aa 15–28) is deleted to abolish the interaction with PKC-3 (indicated by dashed arrow). (C,D) Representative images of CeLINC interaction experiment for GFP::PKC-3 and mKate2::PAR-6 (C) or GFP::PKC-3 and mKate2::PAR-6(Δ PB1) (D) in the intestine and hypodermis. The GFP::PKC-3 bait protein is clustered by the nanobody fused to CRY2(olig). PAR-6 constructs were expressed from an extrachromosomal array while the GFP::PKC-3 allele is endogenous. CeLINC constructs were expressed from the *rps-0* promoter. Overlapping clusters are white in the merged image. For clarity, PAR-6 and PAR-6(Δ PB) are displayed at similar intensity levels. Unadjusted images showing high levels

of PAR-6(Δ PB) are depicted in Supplementary Figure S1. (E) Typical example of relative fluorescent intensity of GFP::PKC-3 at its native localization site at the apical membrane domain of the intestine (top) versus in clusters (bottom). (F) Quantification of GFP::PKC-3 fluorescent intensity. Data are represented as mean \pm SEM and analyzed with unpaired t-test; ****P < 0.0001. n = 12 measurements among 4 animals for the apical domain and n = 25 measurements among 5 animals for clusters. (G) Quantifications of coclustering in the wild-type and mutant mKate2::PAR-6 proteins with GFP::PKC-3 from (C,D). Left graph shows fraction of prey spots coclustering with bait spots, and right graph the fraction of bait coclustering with prey. Dark line indicates the mean value, while the shaded regions indicate the 95% confidence interval. Threshold value refers to the ComDet intensity threshold in SD for detecting a spot. n = 3 animals for wild-type and 4 animals for the mutant combination in the epidermis, and 3 animals for wild-type, 6 animals for mutant combination in intestine. (H) Schematic representation of the DLG-1 protein with labeled protein domains [L27, PDZ, SH3, and GK (guanylate kinase)]. The deletion of the L27 domain, responsible for binding with AJM-1, is indicated. (I) CeLINC interaction experiment between wild-type and binding mutant DLG-1::GFP and AJM-1::mCherry. Both fluorescently tagged proteins are expressed in the intestine from the *elt-2* promoter and CeLINC components are expressed from the *rps-0* promoter, all from an extrachromosomal array in a wild-type animal. Coclustering is readily detected in only the wild-type combination. Images are representative of multiple animals. (J) Quantification of prey and bait spot coclustering in the wild-type and mutant protein pair combinations of DLG-1/AJM-1 from (I). Dark line indicates the mean value, while the shaded regions indicate the 95% confidence interval. n = 7 wild-type combination animals and 5 mutant combination animals.

To test this protein pair for physical interaction, we used a strain with an endogenous CRISPR/Cas9 tagged *GFP::pkc-3* allele, and provided either *mKate2::par-6* or *mKate2::par-6(Δ PB1)*, containing a small deletion of the PB1 domain (amino acids 15–28), to test for positive and negative interactions, respectively (Figure 3A, B). Both *par-6* variants were expressed with a general promoter from an extrachromosomal array to circumvent the lethality of mutated *par-6* alleles. Unlabeled *CRY2(olig)::VHH(GFP)* and the *CIBN-MP* plasmids were injected alongside either *mKate2::par-6* or *mKate2::par-6(Δ PB1)*. Clusters were pre-activated with white light during mounting, and we analyzed both the epidermal and the intestinal tissues. We found the wild-type protein pair showed extensive co-localization of GFP and mKate2 signal in cytoplasmic clusters (Figure 3C), while there was clearly a lack of co-localization in the PAR-6 mutant protein pair, in which the mKate2 signal remained diffuse (Figure 3D). Additionally, GFP::PKC-3 containing clusters showed on average a more than two-fold higher signal than the endogenous fluorescent signal of GFP::PKC-3 at the apical intestine (Figure 3E, F). The concentration and increased signal of the fluorescent protein in the clusters is a significant benefit for the CeLINC system, since it increases the visibility and signal of weakly expressed proteins, allowing them to be more easily identified for co-localization analysis.

To be able to assess co-clustering in an unbiased fashion, we next tested the use of automated quantification using the spot detection ImageJ plugin ComDet (see Methods)(Figure 3G). Bait and prey clusters were identified in their corresponding maximum z-projections, and each cluster was scored for colocalization in the other channel. Since choosing a specific intensity threshold level for spot detection can be arbitrary, we used different thresholding levels and plotted the percent of total prey or bait spots found to co-cluster at different thresholds. Two co-clustering percentages can be derived from this approach: the fraction

of bait spots co-clustering with prey spots, and the fraction of prey spots co-clustering with bait spots. We found that the percent of prey spots co-clustering with bait spots was the most informative, with the percentage increasing with higher threshold levels for the positive protein pair, while the percentage for the negative control remained flat or decreased (Figure 3G). We used ComDet to quantify the co-clustering for all further CeLINC experiments performed. In addition, for all CeLINC experiments we included a control experiment using GFP only as the bait, to rule out the possibility that the prey protein is recruited to GFP clusters independently of an interaction with the bait protein.

Next, we tested an additional protein interaction pair: DLG-1 and AJM-1. These proteins localize to the junctions of *C. elegans* and physically interact via the L27 domain of DLG-1 (Köppen et al., 2001; Lockwood et al., 2008). Therefore, we generated a wild-type and a deletion construct removing the L27 domain that was previously shown to prevent binding of DLG-1 and AJM-1 (Figure 3H). We expressed the *CRY2(olig)::VHH(GFP)* and *CIBN-MP* plasmids along with fluorescently-tagged bait and prey plasmids in wild-type worms from extrachromosomal arrays and looked for co-clustering in the wild-type and mutant combinations. We found extensive co-clustering in the wild-type combination, while little co-clustering of AJM-1::mCherry was observed when DLG-1(Δ L27)::GFP was expressed as the bait (Figure 3I, J).

Therefore, the data above show that the CeLINC system can unambiguously identify and distinguish between well characterized positive and negative protein-protein interaction pairs in *C. elegans*.

Analysis of cortical cell polarity proteins with CeLINC assay

Next, we tested the assay with combinations of the apical polarity regulators PAR-3, PAR-6, and PKC-3 (aPKC) and the basolateral polarity regulators LGL-1, DLG-1, and LET-413. Each of these proteins was fluorescently tagged by CRISPR/Cas9 editing at the endogenous loci, preserving all aspects of normal localization and expression levels.

PAR-3, PAR-6, and PKC-3 are each localized to the apical membrane of intestinal cells and the junctional area of seam cells, among other epithelial tissues and cells types (Achilleos et al., 2010; Castiglioni et al., 2020; Li et al., 2010a; Nance et al., 2003; Welchman et al., 2007). PAR-3 is known to transiently, but not permanently, interact with the PAR-6/PKC-3 complex (Rodriguez et al., 2017). Testing the interaction of the PAR-6/PKC-3 complex with PAR-3 can determine whether CeLINC is able to detect more transient and dynamic protein interactions. We also tested the use of tissue-specific promoters directing the expression of the *CRY2(olig)* construct to the intestine and hypodermis, using the *elt-2* and *wrt-2* promoters, respectively. The *CIBN-MP* module was expressed from the *rps-0* general promoter. After light activation, the endogenously tagged PAR-6 and PKC-3 proteins showed extensive co-localization in cytoplasmic clusters in the intestine (Figure 4A and Figure S2A) and the hypodermis (Figure 4B and Figure S2A), as expected based on our results using expression of PAR-6::mCherry from

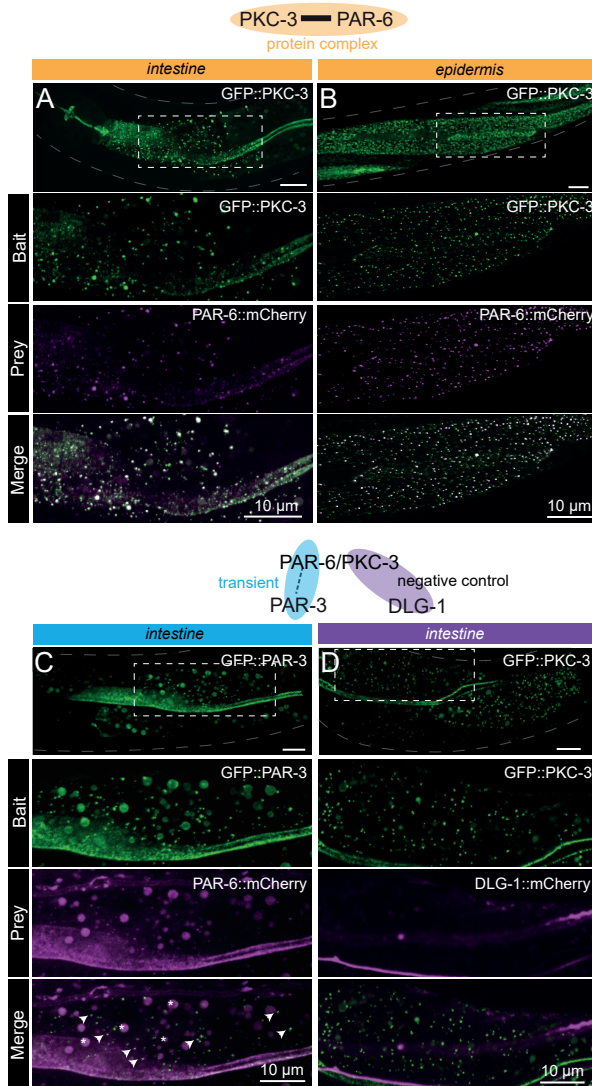


Figure 4. Interactions between apical cell polarity regulators assayed with CeLINC.

(A,B) Interaction between GFP::PKC-3 and PAR-6::mCherry using endogenously tagged alleles. The top panel shows the region of the worm examined and the area within the white dashed box is shown enlarged in the panels below. The CIBN-MP construct is expressed from the *rps-0* promoter. In (A), CRY2(olig)::VHH(GFP) is expressed from the *elt-2* promoter, while in (B), CRY2(olig)::VHH(GFP) is expressed from the *wrt-2* promoter to enable tissue-specific clustering. In all panels, the bait protein corresponds to the protein trapped by the CRY2-fused nanobody. (C) Interaction between GFP::PAR-3 and PAR-6::mCherry using endogenous alleles. PAR-6 is not present in every GFP containing cluster, but PAR-6::mCherry clusters overlap with PAR-3 clusters (white arrows indicate some of the co-clusters). Bigger round spheres in both the bait and prey channels correspond to autofluorescence from gut granules, which are marked with an asterisk in the merged image. CeLINC constructs are expressed from the *rps-0* promoter. (D) Negative control CeLINC assay between GFP::PKC and DLG-1::mCherry (endogenous alleles). See Supplementary Figure S2, A and C for quantifications of all pairs shown. All images are representative of multiple animals.

an array (Figure 3C, D). Next, we tested the interaction of PAR-3 with the PAR-6/PKC-3 complex using GFP::PAR-3 and PAR-6::mCherry using the general promoter *rps-0* to express the CeLINC proteins. We identified co-localization between the two proteins, but fewer GFP clusters contained the mCherry signal than with the interaction between PAR-6 and PKC-3 (Figure 4C and Figure S2A). This result is consistent with the previously described transient and dynamic nature of the interaction (Rodriguez et al., 2017). Little to no co-clustering was observed in a negative control protein pair consisting of GFP::PKC-3 and DLG-1::mCherry, a protein not expected to interact with PKC-3 (Figure 4D and Figure S2C). For all pairs, matching negative controls using GFP alone as the bait also showed little to no clustering (Figure S2A, C). We also tested an additional negative control pair, that of GFP::MAPH-1.1 and ERM-1::mCherry (Figure S2F), and saw little to no co-clustering, consistent with other negative controls.

The Scribble module proteins LGL-1 (Lgl), DLG-1 (Dlg), and LET-413 (Scrib) play conserved roles in promoting basolateral domain identity, in part by antagonizing aPKC (Stephens et al., 2018; Wen and Zhang, 2018). In *Drosophila*, Lgl, Scrib, and Dlg are interdependent for their localization to the basolateral membrane in multiple tissues and act in a common basolateral polarity pathway (Bilder, 2000; Bilder et al., 2003; Khoury and Bilder, 2020; Su et al., 2012). However, unlike the apical polarity determinants, evidence for physical interactions between Scribble module members remains limited. In the synapses of *Drosophila* neuron, Dlg was also shown to indirectly associate with Scrib through the linker protein GUK-holder (Gukh) (Caria et al., 2018; Mathew et al., 2002). In mammalian cells, Lgl2 may interact with the guanylate kinase domain of Dlg4 (Zhu et al., 2014), as well as with the LAP unique region of Scrib (Choi et al., 2019; Kallay et al., 2006). Recently, the LINC system was used in *Drosophila* follicular epithelial cells to show that Dlg and Scribble interact via Scribble's LRR domains (Ventura et al., 2020). However, the importance of these interactions for polarity establishment, and their conservation between organisms remains unclear.

Currently, there is no evidence in *C. elegans* that the basolateral proteins physically interact. Clarifying whether LGL-1, DLG-1, and LET-413 interact is important for understanding their function, and how their roles might differ between *C. elegans*, *Drosophila*, and mammals. LGL-1 and LET-413 have overlapping basolateral expression patterns in the intestine and the seam cells, whereas DLG-1 remains junctional in both cell types. We expressed CeLINC plasmids with general promoters and analyzed all combinations of the basolateral proteins with the CeLINC assay, but identified few to no co-clusters containing both signals, similar to negative controls (Figure 5A, B, D, E, Figure S2C-E). Specifically, in contrast to the *Drosophila* follicular epithelium (Ventura et al., 2020), we found no co-clustering of LET-413 and DLG-1, despite testing for interaction in both orientations by using each protein separately as the bait protein targeted by the nanobody (Figure 5A, B, Figure S2C, D). These results add to the body of evidence that LGL-1, DLG-1, and LET-413 do not belong to the same physical protein complex in *C. elegans* (Waaaijers et al., 2016). As a positive

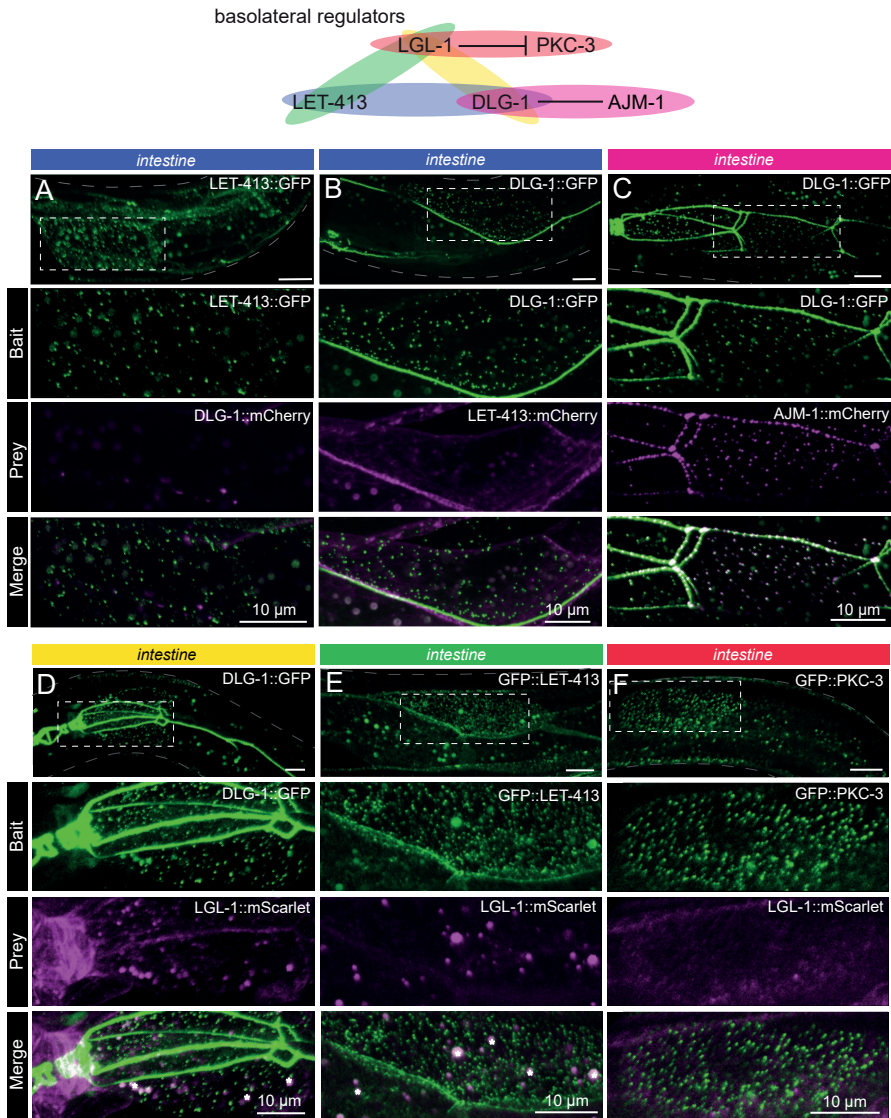


Figure 5. Basolateral cell polarity regulators assayed with CeLINC. (A–F) CeLINC experiments to investigate interactions among the basolateral cell polarity proteins LET-413, DLG-1, AJM-1, and LGL-1, and the apical protein PKC-3. All proteins are endogenously tagged, except for AJM-1::mCherry, which is expressed from an integrated multicopy array. The top panels show the region of the worm examined and the area within the white dashed box is shown enlarged in the panels below. Intestinal cells were analyzed, and all images represent maximum projections of a z-stack. The bait protein corresponds to the protein trapped by the CRY2 fused nanobody. All CeLINC constructs are expressed from the *rps-0* promoter, except in (E), which used the *elt-2* promoter. In (E), larger round spheres in both the bait and prey channels correspond to autofluorescence from gut granules, which are marked with an asterisk in the merged image. No physical interactions were detected in any of the basolateral protein pairs except for AJM-1 and DLG-1. See Supplementary Figure S2, B–E for quantifications. All images are representative of multiple animals.

control, we did identify an interaction between DLG-1::GFP (endogenous tag) and AJM-1::mCherry (multicopy insertion) (Figure 5C, Figure S2B).

Finally, we investigate the interaction between LGL-1 and PKC-3. In the one-cell embryo, LGL-1 and PKC-3 engage in mutually inhibitory interactions to localize to opposing poles and promote cell polarity (Beatty et al., 2010; Hoege et al., 2010). In addition, depletion of PKC-3 in the epidermal seam cells causes apical invasion of LGL-1 (Castiglioni et al., 2020). Despite their localization to opposing membrane domains, PKC-3 and LGL-1 co-immunoprecipitate together (Hoege et al., 2010; Waaijers et al., 2016), which led to a model where LGL-1 associates with PAR-6/PKC-3 at the boundary of their respective domains, becomes phosphorylated by PKC-3, and subsequently dissociates from PAR-6/PKC-3 (Hoege et al., 2010). Using the CeLINC assay, we found that in the intestine there was no significant co-clustering between the proteins (Figure 5F, Figure S2E). Therefore, while CeLINC can detect some transient interactions, not all transient interactions are identified by the technique.

Overall, the CeLINC system was able to trap all of the cell polarity proteins tested into ectopic clusters within the cytoplasm of the intestinal cells, even DLG-1, which is localized to the cell junctions. We found no false-positives between any of the negative reference protein pairs tested. In the positive reference pairs, we found that the interaction between PKC-3 and PAR-6 could be identified, and also prevented with a mutation of the PKC-3 binding site on PAR-6. Additionally, a more transient interaction, that of the PAR-6/PKC-3 complex and PAR-3, could also be identified with the assay.

Finally, we tested if bait clusters with higher fluorescence intensity or greater area would more effectively capture prey proteins. We used the GFP::PKC-3 and PAR-6::mCherry protein pair and analyzed the epidermis as an example (Figure 4B). We found that the sum of the pixel intensity of the bait and prey in co-clustering spots showed a tight correlation (Figure S3A), and larger bait spots were more likely to be identified as a co-clustering spot (Figure S3B), suggesting that larger and brighter clusters can recruit more prey protein, and therefore have a higher chance of being categorized as a co-cluster.

Generation of a CeLINC toolkit

To expand the potential use cases of CeLINC, we investigated the possibility of clustering proteins tagged with other fluorescent proteins than GFP. First, we tested a nanobody targeting the mCherry protein (Yamagata and Sanes, 2018). We confirmed that CRY2(olig)::VHH(mCherry) was able to induce clustering of an mCherry tagged protein (DLG-1::mCherry) but not a GFP tagged protein (PAR-6::mCherry) (Figure 6A, C), and that the mCherry nanobody could induce co-clustering of the positive reference pair PAR-6/PKC-3 (Figure 6B, C). The mCherry nanobody further expands the use of the system to allow for more proteins to be used as baits. Furthermore, if nanobodies against additional fluorescent proteins are developed they can be easily incorporated.

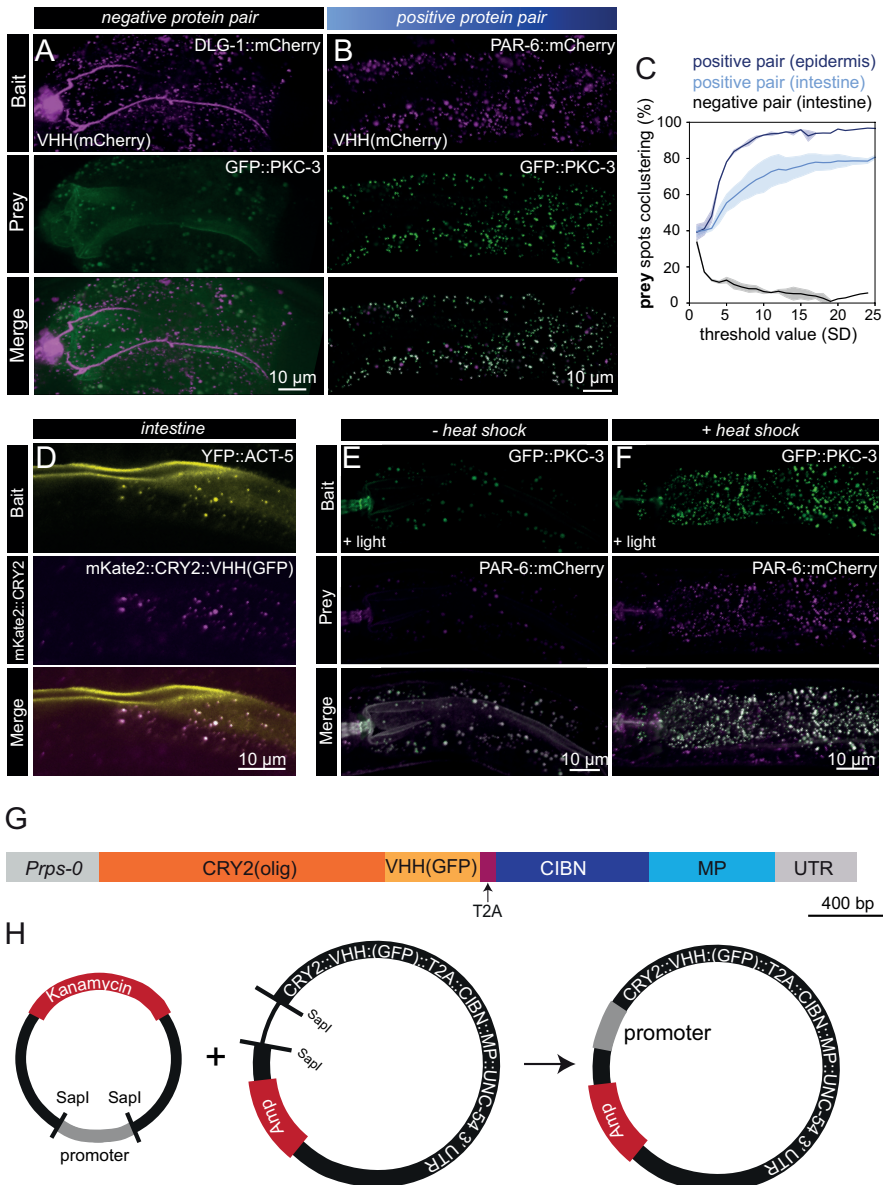


Figure 6. Expansion of CeLINC with additional modules and constructs.

(A,B) Fluorescent maximum z-stack projections of a negative (A) and positive (B) protein pair assayed with CeLINC using an mCherry nanobody to enable mCherry tagged proteins to be used as the bait protein. In both protein pairs, the mCherry-tagged protein was recruited to clusters, but only in the positive protein pair (B) did the prey protein cocluster. All proteins are tagged endogenously. (C) Detected prey spots that cocluster with bait spots were quantified in the positive and negative protein pairs seen in (A,B). $n = 2$ animals per condition. (D) YFP can be captured into clusters by the GFP nanobody. Image of the intestine of an animal with an integrated YFP::ACT-5 transgene expressing mKate2::CRY2(olig)::VHH(GFP) and CIBN-MP from an extrachromosomal array using a general promoter (*rps-0*). Image is representative of multiple animals. (E,F) Interaction between PKC-3 and PAR-6 assessed

using CRY2(olig) expressed from a heat shock promoter and the CIBN-MP protein from the *rps-0* promoter. Images are maximum z-stack projections of intestinal cells in animals kept at 20°C (E) or treated with a 2-h heat shock at 30°C (F). Larger round spheres in both the bait and prey channels in the non heat-shocked animals correspond to autofluorescence from gut granules. Images are representative of 7 control animals and 5 heat-shocked animals. (G) Diagram of the coding region of the Prps-0::CRY2(olig)-T2A-CIBN-MP plasmid (pJRK260), which simplifies the system and allows for both CeLINC proteins to be translated from the same mRNA molecule. (H) Schematic of the CRY2-T2A-CIBN-MP destination plasmid (pJRK261) which contains an empty promoter module. The desired promoter donor plasmid can be combined and assembled with the SapTrap method in one-step to generate a functional and complete CeLINC plasmid.

Next, since GFP and YFP share structural similarities, we tested the GFP nanobody against a YFP tagged protein, YFP::ACT-5. After injection with the CeLINC plasmids, we identified intestinal clusters in the YFP::ACT-5 strain that co-localized with mKate2::CRY2::VHH(GFP) clusters, indicating YFP tagged proteins interact with the VHH(GFP) nanobody and can also be used as bait proteins in the assay (Figure 6D).

In order to be able to easily adapt or change the components of CeLINC, we have made the plasmid cloning system modular with the use of the SapTrap plasmid assembly method (Schwartz and Jorgensen, 2016). In this way, different promoters, nanobodies, CRY2 variants, or 3' UTRs can be combined with previously generated donor plasmids and assembled into the final destination vector (File S2, S4). We have already generated a series of CRY2(olig) plasmids with more specific promoters, such as tissue specific promoters for the intestine (*elt-2*), the hypodermis (*wrt-2*) (Figure 4A, B), and a heat-shock promoter (*hsp-16.48*) (Figure 6E, F). The heat-shock promoter might be useful for some tagged-protein combinations, since even in the dark, nanobodies will still be targeted to GFP or mCherry proteins, which could cause unintended effects for certain types of proteins (though no problems have been identified with the proteins tested thus far). We kept CIBN-MP with the *rps-0* promoter since it is the more “passive” element of the CeLINC system. We have also used the T2A system that allows two peptides to be produced from the same mRNA (Ahier and Jarriault, 2014), and have created a single plasmid encoding both the CRY2(olig)::VHH(GFP) nanobody element and the CIBN-MP element from the *rps-0* promoter (Figure 6G). Finally, we generated a version of this T2A based plasmid with an empty promoter module with flanking *SapI* sites so that any promoter can be swapped in with a single donor plasmid and reaction (Figure 6H). This toolkit of plasmids will allow any particular tissue type or cell type to be targeted with the CeLINC system and increases the types of proteins that can be used as bait proteins in the assay.

Discussion

We have adapted and tested the light-induced co-clustering assay (LINC), for use in *C. elegans*. We have shown that in *C. elegans*, expressed CRY2(olig) is activated by blue light, and efficiently clusters in multiple tissues, cell types, and cellular compartments. When we compared the interaction of PKC-3 with a wild-type PAR-

6 protein and an interaction-defective mutant, we saw a clear difference in the co-clustering of PAR-6. We tested additional negative reference protein pairs and no false positives were detected among them. Testing for physical interactions among apical and basolateral cell polarity regulators using the system also did not identify false-positive interactions, and successfully recapitulated the known interaction between PAR-3 and PAR-6. Finally, we developed a toolkit of plasmids to enable flexibility and adaptability of the system for future uses.

The siphoning of proteins from their endogenous location to clusters or to ectopic locations within the cell could cause gain or loss-of-function phenotypes, as the original purpose of the LARIAT system was to disrupt protein function (Lee et al., 2014). We saw no apparent lethality or toxicity associated with CRY2/CIBN-MP expression in any of the strains generated. Therefore, the CeLINC system appears to have little detrimental effect on the fitness of animals, even when clustering cell polarity proteins that are essential for animal development. However, throughout our experiments, we limited the amount of light exposed to the animals. Longer exposure of the animals to blue or bright light conditions could cause developmental or cellular phenotypes. Moreover, since every protein may behave differently or have different thresholds for a “knock sideways”-like inhibition, other protein combinations or bait proteins may still show unexpected phenotypes or effects. Finally, while we observed regularly sized and spaced cluster formation, it is possible that CRY2 clusters may form in different shapes or sizes with the use of different bait proteins, depending on what interactions the bait protein normally engages in. For example, filamentous proteins or proteins strongly associated with a membrane may produce clusters that are larger or more amorphous in shape.

One consideration for the proper interpretation of the assay is protein mobility or accessibility. Some proteins could be resistant to clustering or less likely to form ectopic clusters than other proteins. Proteins unable to mis-localize from their endogenous localization would produce a false-negative result if used as a prey protein in the assay. For example, fewer clusters formed in the LET-413 (Scribble) strains when used as a bait, suggesting that LET-413 protein is either tightly bound or highly integrated to its endogenous location in the cell. However, since each extrachromosomal array in our experiments resulted from a distinct injection, differences in clustering ability could also be attributed to differing levels of CeLINC construct expression. Similar to other PPI assays, a negative result needs to be taken with caution. However, positive results from the assay are likely to be highly significant, since no false-positives were identified in any negative protein pair that was tested, even among basolateral proteins that co-localize. Additionally, the assay is limited by the intensity of the particular fluorophore and expression level of the target proteins. While one advantage is that the clusters concentrate the signal in a small area, giving a bright focused spot (Figure 3E), some lowly expressed proteins could still be barely visible. For example, red fluorescent proteins tend to have a reduced signal compared to GFP, so weakly expressing proteins might be prioritized to be tagged with GFP. Another way to overcome low expression of target proteins

is to use overexpression constructs. The use of transgenes can also circumvent detrimental phenotypes and is necessary to test proteins carrying non-viable mutations, as was the case with *par-6(ΔPB1)*. Finally, like many protein-protein interaction assays, CeLINC cannot distinguish between indirect and direct protein-protein interactions.

One potential concern of the CeLINC assay is that overexpression of a prey protein may “force” a particular physical interaction. In the PKC-3/PAR-6 protein pair, the strain with the *par-6(ΔPB1)* binding mutant prey protein had higher expression levels than the strain with wild-type prey protein, yet no interactions were detected (Figure S1). Additionally, we injected 4-fold more prey plasmid than bait plasmid for the expression of the DLG-1/AJM-1 protein combinations (Figure 3I, J), yet failed to detect any interactions with the mutant protein pair. Thus, CeLINC can be specific even when overexpressing the proteins tested.

While light activation of CRY2 formation is useful for temporal control of cluster formation, for the purposes of the CeLINC assay, blue light activation and cluster formation during the microscopy session is not necessarily needed. Pre-activation of the clusters during mounting the animals on slides increased the throughput of the assay, as more animals could be imaged per slide, and animals exhibiting clusters could be more rapidly identified. In our experiments, we easily identified animals and cells expressing the CeLINC constructs because GFP or mCherry clusters were distributed in the cytoplasm of the cells, a completely different location than the normal localization of the tagged proteins. Additionally, due to mosaicism of the extrachromosomal array, surrounding cells where no clusters were observed could often be used as negative controls within the same animal. This ensured we were not analyzing cluster-like aggregates, gut granules that are auto fluorescent, or endogenous localization of the proteins. Nevertheless, light activation of CRY2 on the microscope might be useful for certain tagged proteins that are already prone to aggregation or exhibit an endogenous localization pattern that might easily be confused with CRY2 mediated clusters. The CeLINC assay is mainly a binary assay, answering whether two particular proteins do or do not interact. However, with the use of particle analysis software or tools, more quantitative measurements could be made, such as the degree of clusters that contain a fluorescent signal of the prey protein. However, caution should be given when comparing different combinations of proteins, since their degree of co-clustering may be influenced by other factors than purely their physical association.

Compared to other PPI assays available for use in *C. elegans*, CeLINC uses relatively few special reagents, is rapid, and is straight-forward to interpret. Many proteins under study already have fluorescently tagged alleles available, and no further modifications need to be made for use in the CeLINC system. While we mainly use proteins tagged with mCherry, proteins tagged with YFP, mScarlet, mKate2, or BFP could be used with the system. With the recent development of CRISPR/Cas9 editing techniques and split protein fluorescent based systems, such as sfGFP₁₁ and Split-mScarlet₁₁ (Goudeau et al., 2021), where only a small fragment of the fluorescent protein needs to be integrated in a genetic background

expressing the complementary fragment, fluorescent protein tags can be made with relative ease. Overall, the CeLINC system is a powerful technique to study protein-protein interactions that can utilize many existing strains and produces a clear result with commonly available equipment in any *C. elegans* laboratory.

Acknowledgments

Thanks to Vincent Portegijs and Ruben Schmidt for plasmids, and Alison Woollard, Amalia Riga, Victoria Castiglioni, Jorian Sepers, and Helena Pires for strains. The authors thank members of the S. van den Heuvel, S. Ruijtenberg, and M.B. groups for helpful discussions. Some strains were provided by the Caenorhabditis Genetics Center (CGC), which is funded by NIH Office of Research Infrastructure Programs (P40 OD010440).

Funding

This work was supported by a Dutch Research Council (NWO) OCENW.XS3.087 grant to J.R.K. and a Dutch Research Council (NWO) VICI 016.VICI.170.165 grant to M.B.

Supplementary figures

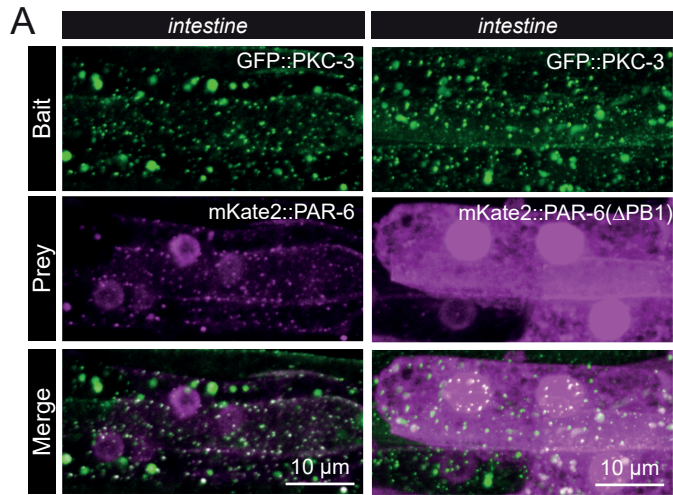


Figure S1. Intestinal interaction of PKC-3 with PAR-6 and a highly overexpressed interaction defective PAR-6 variant. Intestinal images from CeLINC interaction experiment of Figure 3C- D taken with same microscopy settings and displayed with same image processing settings.

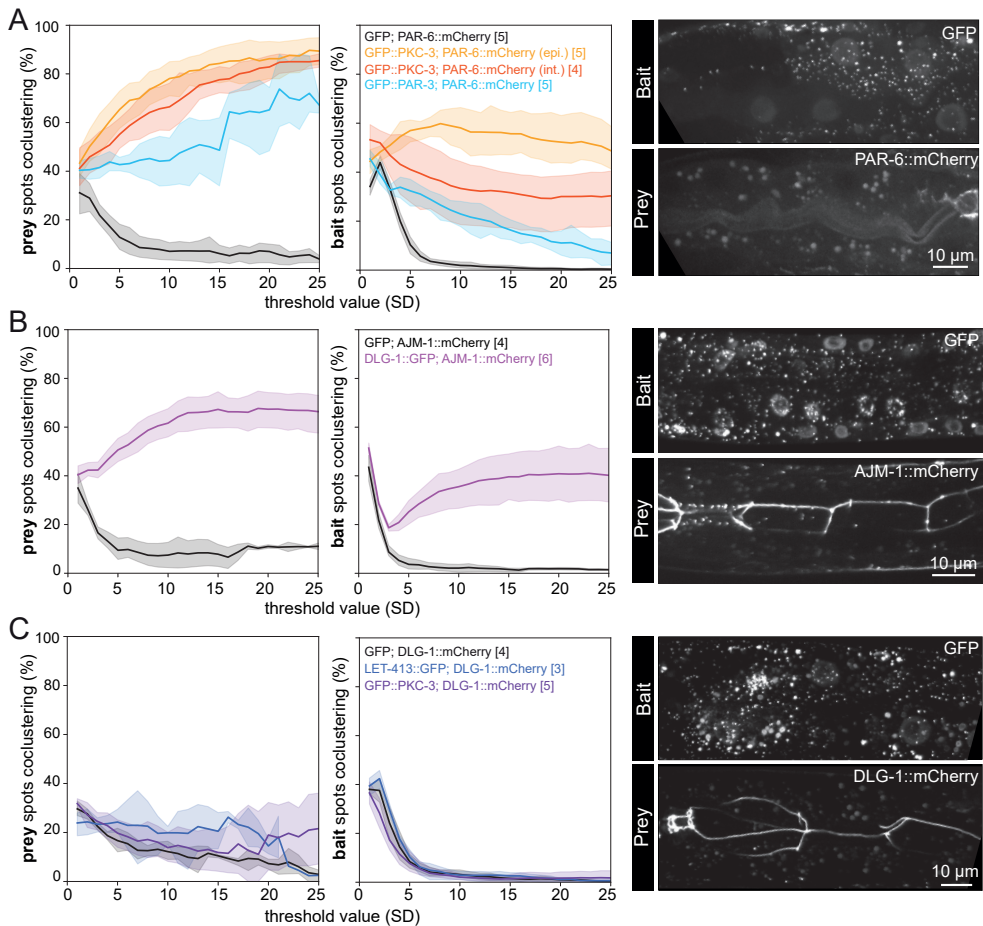


Figure S2 (part 1 of 2). Image quantifications and negative controls for various CeLINC experiments. (A–F) The percentage of prey and bait spots colocalizing are graphed for indicated protein combinations. Dark line indicates the mean value, while shaded areas indicate the 95% confidence interval. Threshold value is the ComDet intensity threshold value used to detect an interaction. Negative controls use GFP protein alone expressed as bait. All CeLINC plasmids are expressed from the *rps-0* promoter. Representative images of the clustered GFP bait and prey are also shown. Intestinal cells were used for quantifications. The number of animals quantified in each genotype are shown in brackets on the graphs.

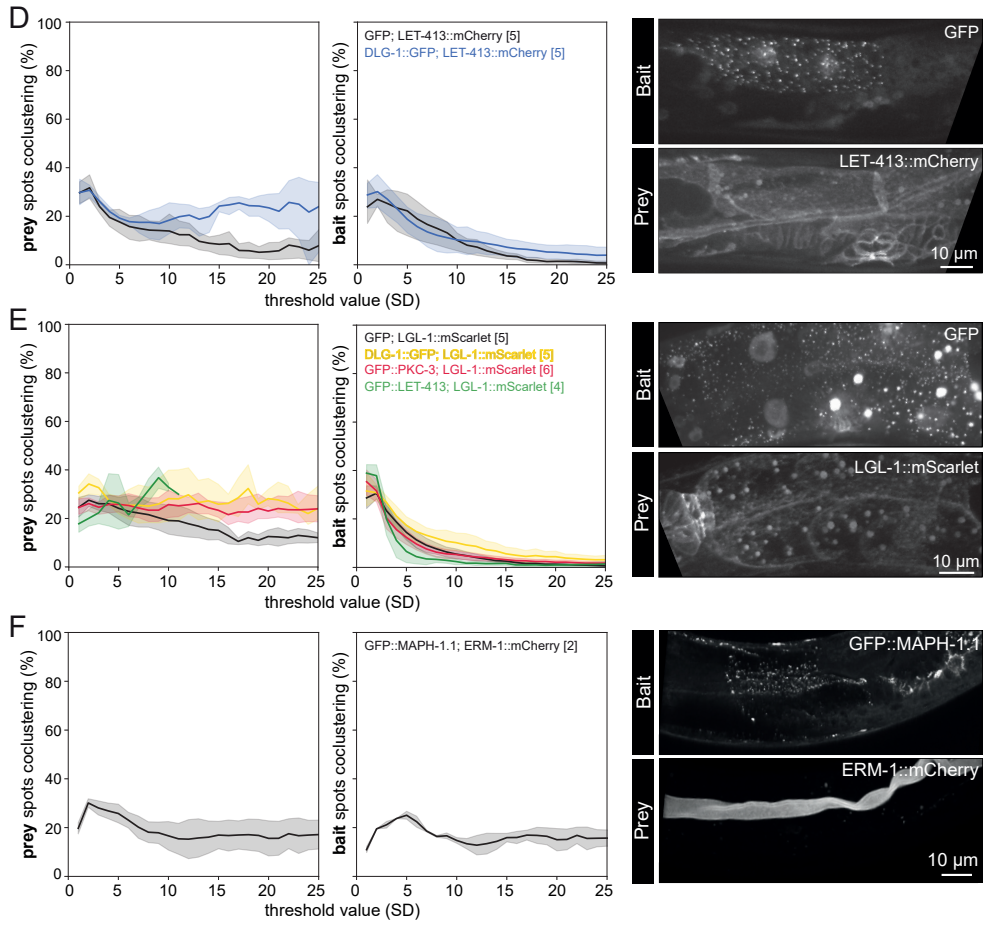


Figure S2 (part 2 of 2).

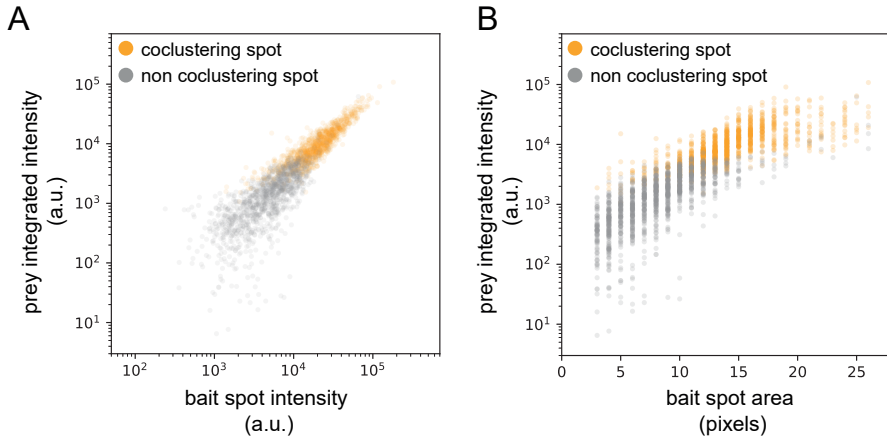


Figure S3. Correlation between bait cluster size and intensity with prey cluster intensity. (A) Correlation between the sum of pixel intensity in the bait and prey spots in endogenously tagged GFP::PKC-3; PAR-6::mCherry CeLINC protein expressing animals. For every bait spot detected, the sum of the pixel intensity in the bait spot and the corresponding area in the prey image is plotted. Images were analyzed at intensity threshold level of 25 and the sum of pixel intensities within each identified cluster were corrected for spot-specific background intensity by subtracting the average intensity of the surrounding pixels using the ComDet plugin. (B) The correlation between the size of the bait cluster in pixels and the sum of pixel intensity in the prey spot, as calculated in (A). (A–B) $n = 1093$ bait spots coclustering spots and 1352 bait spots that were found to be non coclustering, from the analysis of 5 animals.

Supplementary files

File S1. *C. elegans* strains

Name	Genotype	Reference
BOX249	<i>let-413(mib29[let-413::mCherry-LoxP]) V; dlg-1(mib22[dlg-1::eGFP-LoxP]) X</i>	This study
BOX451	<i>let-413(mib32[let-413::AID::eGFP-LoxP]) V; dlg-1(mib23[dlg-1::mCherry-LoxP]) X</i>	This study
BOX484	<i>par-6(mib25[par-6::mCherry-LoxP]) I; pkc-3(mib78[eGFP-LoxP::AID::pkc-3]) II; mibls49[Pwrt-2::TIR-1::tagBFP2-Lox511::tbb-2-3'UTR, IV:5014740-5014802 (cxTi10816 site))] IV</i>	(Castiglioni <i>et al.</i> 2020)
BOX486	<i>par-6(mib25[par-6::mCherry-LoxP]) I; par-3(mib68[eGFP-Lox2272::AID::par-3b+eGFP(nolntrons)-LoxP::AID::par-3g]) III; mibls49[Pwrt-2::TIR-1::tagBFP2-Lox511::tbb-2-3'UTR, IV:5014740-5014802 (cxTi10816 site))] IV</i>	(Castiglioni <i>et al.</i> 2020)
BOX493	<i>pkc-3(mib78[eGFP-LoxP::AID::pkc-3]) II; mibls49[Pwrt-2::TIR-1::tagBFP2-Lox511::tbb-2-3'UTR, IV:5014740-5014802 (cxTi10816 site))] IV; dlg-1(mib23[dlg-1::mCherry-LoxP]) X</i>	(Castiglioni <i>et al.</i> 2020)
FT1991	<i>dpy-10(cn64) pkc-3(it309[GFP::pkc-3]) II; lgl-1(xn103[lgl-1::zf1::mScarlet]) X</i>	(Montoyo-Rosario <i>et al.</i> 2020)
BOX740	<i>lgl-1(xn103[lgl-1::zf1::mScarlet]) X</i>	This study
BOX756	<i>lgl-1(xn103[lgl-1::zf1::mScarlet]) dlg-1(mib22[dlg-1::eGFP-LoxP]) X</i>	This study
BOX757	<i>pkc-3(it309[GFP::pkc-3]) II; lgl-1(xn103[lgl-1::zf1::mScarlet]) X</i>	This study
BOX758	<i>let-413(mib81[GFP::LoxP::AID::let-413]) V; lgl-1(xn103[lgl-1::zf1::mScarlet]) X</i>	This study
KK1228	<i>pkc-3(it309[GFP::pkc-3]) II</i>	CGC
BOX235	<i>dlg-1(mib23[dlg-1::mCherry-LoxP]) X</i>	This study
JM125	<i>cals[Pges-1::YFP::ACT-5]</i>	(Bossinger <i>et al.</i> 2004)
BOX742	<i>mibEx255[Prps-0::mKate2-CRY2olig-VHH(GFP)::unc-54 3'UTR; Prps-0::CIBN-3xFLAG-MP::unc-54 3'UTR; pJRK248, λ DNA]</i>	This study
BOX743	<i>mibEx254[Prps-0::mKate2-CRY2olig-VHH(GFP)::unc-54 3'UTR; pJRK248, λ DNA]</i>	This study
BOX759	<i>par-6(mib25[par-6::mCherry-LoxP]) I; pkc-3(mib78[eGFP-LoxP::AID::pkc-3]) II; mibls49[Pwrt-2::TIR-1::tagBFP2-Lox511::tbb-2-3'UTR, IV:5014740-5014802 (cxTi10816 site))] IV; mibEx259[Pwrt-2::CRY2olig-VHH(GFP)::unc-54 3'UTR; Prps-0::CIBN-3xFLAG-MP::unc-54 3'UTR; pJRK248, λ DNA]</i>	This study
BOX760	<i>par-6(mib25[par-6::mCherry-LoxP]) I; pkc-3(mib78[eGFP-LoxP::AID::pkc-3]) II; mibls49[Pwrt-2::TIR-1::tagBFP2-Lox511::tbb-2-3'UTR, IV:5014740-5014802 (cxTi10816 site))] IV; mibEx260[Pelt-2::CRY2olig-VHH(GFP)::unc-54 3'UTR; Prps-0::CIBN-3xFLAG-MP::unc-54 3'UTR; pJRK248, λ DNA]</i>	This study
BOX761	<i>par-6(mib25[par-6::mCherry-LoxP]) I; par-3(mib68[eGFP-Lox2272::AID::par-3b+eGFP(nolntrons)-LoxP::AID::par-3g])</i>	This study

File S2. Plasmid information

Name	Description	Function	Res. Cassette	Addgene #	Reference
pJRK136	<i>Prps-0::CIBN-3xFLAG::MP::unc-54 3' UTR</i>	CeLINC assay	Ampicillin	173744	This study
pJRK137	<i>Prps-0::mKate2::CRY2(olig)::VHH(GFP)::unc-54 3' UTR</i>	CeLINC assay test	Ampicillin	173745	This study
pJRK138	<i>Prps-0::CRY2(olig)::VHH(GFP)::unc-54 3' UTR</i>	CeLINC assay	Ampicillin	173746	This study
pJRK248	<i>Prps-0::HygR::unc-54 3'UTR; Psqt-1::sqt-1::sqt-1 3' UTR</i>	coinjection marker	Kanamycin	173755	This study
pJRK249	<i>Prps-0::CRY2(olig)::VHH(mCherry)::unc-54 3' UTR</i>	CeLINC assay	Ampicillin	173747	This study
pJRK251	<i>Pwrt-2::CRY2(olig)::VHH(GFP)::unc-54 3' UTR</i>	CeLINC assay	Ampicillin	173748	This study
pJRK252	<i>Pelt-2::CRY2(olig)::VHH(GFP)::unc-54 3' UTR</i>	CeLINC assay	Ampicillin	173749	This study
pJRK253	<i>Phsp-16.48::CRY2(olig)::VHH(GFP)::unc-54 3' UTR</i>	CeLINC assay	Ampicillin	173750	This study
pJRK258	<i>Prps-0::mKate2::par-6::unc-54 3' UTR</i>	CeLINC assay test	Ampicillin	173751	This study
pJRK259	<i>Prps-0::mKate2:: par-6(ΔPB1)::unc-54 3' UTR</i>	CeLINC assay test	Ampicillin	173752	This study
pJRK260	<i>Prps-0::CRY2(olig)::VHH(GFP)::T2A::CIBN-3xFLAG::MP::unc-54 3' UTR</i>	CeLINC assay	Ampicillin	173753	This study
pJRK261	(empty promoter module with flanking SapI sites)::CRY2(olig)::VHH(GFP)::T2A::CIBN-3xFLAG::MP::unc-54 3' UTR	destination plasmid	Ampicillin	173754	This study
pJRK262	<i>Pelt-2::ajm-1::mCherry::unc-54 3' UTR</i>	CeLINC assay test	Ampicillin	N/A	This study
pJRK263	<i>Pelt-2::dlg-1::GFP::unc-54 3' UTR</i>	CeLINC assay test	Ampicillin	N/A	This study
pJRK264	<i>Pelt-2::dlg-1(ΔL27)::GFP::unc-54 3' UTR</i>	CeLINC assay test	Ampicillin	N/A	This study
pMLS257	backbone destination plasmid	destination plasmid	Ampicillin	73716	(Schwartz and Jorgensen 2016)
pJRK1	<i>Prps-0 (TGG/ATG overhangs)</i>	donor plasmid	Kanamycin	173730	(Yao <i>et al.</i> 2020)
pJRK151	<i>Prps-0 (TGG/AAG overhangs)</i>	donor plasmid	Kanamycin	173739	(Yao <i>et al.</i> 2020)
pJRK142	<i>Phsp-16.48</i>	donor plasmid	Kanamycin	173736	This study

File S3. Primers and sequences used for cloning

Name	Sequence 5' to 3'	Use
112 F	GAGCTCTTCGACGATGGACCAAGTCCAACCTCGT	pJRK112 GFP nanobody amplification
112 R	CCGCTCTTCGGCAGGAGGAGACGGTGACTTGGG	pJRK112 GFP nanobody amplification
120 F	CTGCTCTTCGAAGATGTCCTACAACGGCTCCTA	pJRK120 par-6 cDNA amplification
120 R	CTGCTCTTCGCGTGTCTCTCCACTGTCCGAA	pJRK120 par-6 cDNA amplification
248a F	GCATGGATGTTTTCCAGTCACGACGTTGTAAAAC	pJRK248 Gibson assembly fragment A
248a R	GAAAGCAAAAATCTGAATCTCAAATATTTTATTAGAAAA CACCAAC	pJRK248 Gibson assembly fragment A
248b F	ATTTGAGATTGAGATTTTTGCTTTCGTCGTAATC	pJRK248 Gibson assembly fragment B
248b R	GTCGTGACTGGGAAAACATCCATGCTAGCGTTAAC	pJRK248 Gibson assembly fragment B
259a F	CATCATTCAACATCAATACCAATGCATTCTGCGTCTG	pJRK259 Gibson assembly fragment A
259a R	AAAAGTGCTCATCATTGGAAAACGTTCTTCGGGGCGA	pJRK259 Gibson assembly fragment A
259b F	ACGTTTTCCAATGATGAGCACTTTTAAAGTTCTGCTATG	pJRK259 Gibson assembly fragment B
259b R	GCATTGGTATTGATGTTGAATGATGATTTTGATGGTAG	pJRK259 Gibson assembly fragment B
142 F	CTGCTCTTCGTGGGGTTCGGTTTTGCTACTGTA	pJRK142 Phsp-16.48 amplification
142 R	AGGCTCTTCGCTTTTCTGAAGTTTAGAGAATG	pJRK142 Phsp-16.48 amplification
143 F	CTGCTCTTCGTGGTAATTTCGAAAT	pJRK143 Pelt-2 amplification
143 R	GTGCTCTTCGCTTTCTATAATCTATTTTCTAGT	pJRK143 Pelt-2 amplification
246 F	AGCTGCTCTTCGTGGCAGGTCGACTCCACGTAATT	pJRK246 Pwrt-2 amplification
246 R	GTGCTCTTCGCTTCCGAGAAACAATTGGCAGGT	pJRK246 Pwrt-2 amplification
260a F	ACCGCAATTTTAAATCAAGCTTATCGATACCGTCG	pJRK260 Gibson assembly fragment A
260a R	CGAAAGCAAAAATCCAATCGAATTCCTGCAGCC	pJRK260 Gibson assembly fragment A
260b F	GAATTCGATTGGATTTTTGCTTTCGTGCTGATAACTACAC AC	pJRK260 Gibson assembly fragment B
260b R	GGAGGAGACGGTGACTTGGG	pJRK260 Gibson assembly fragment B

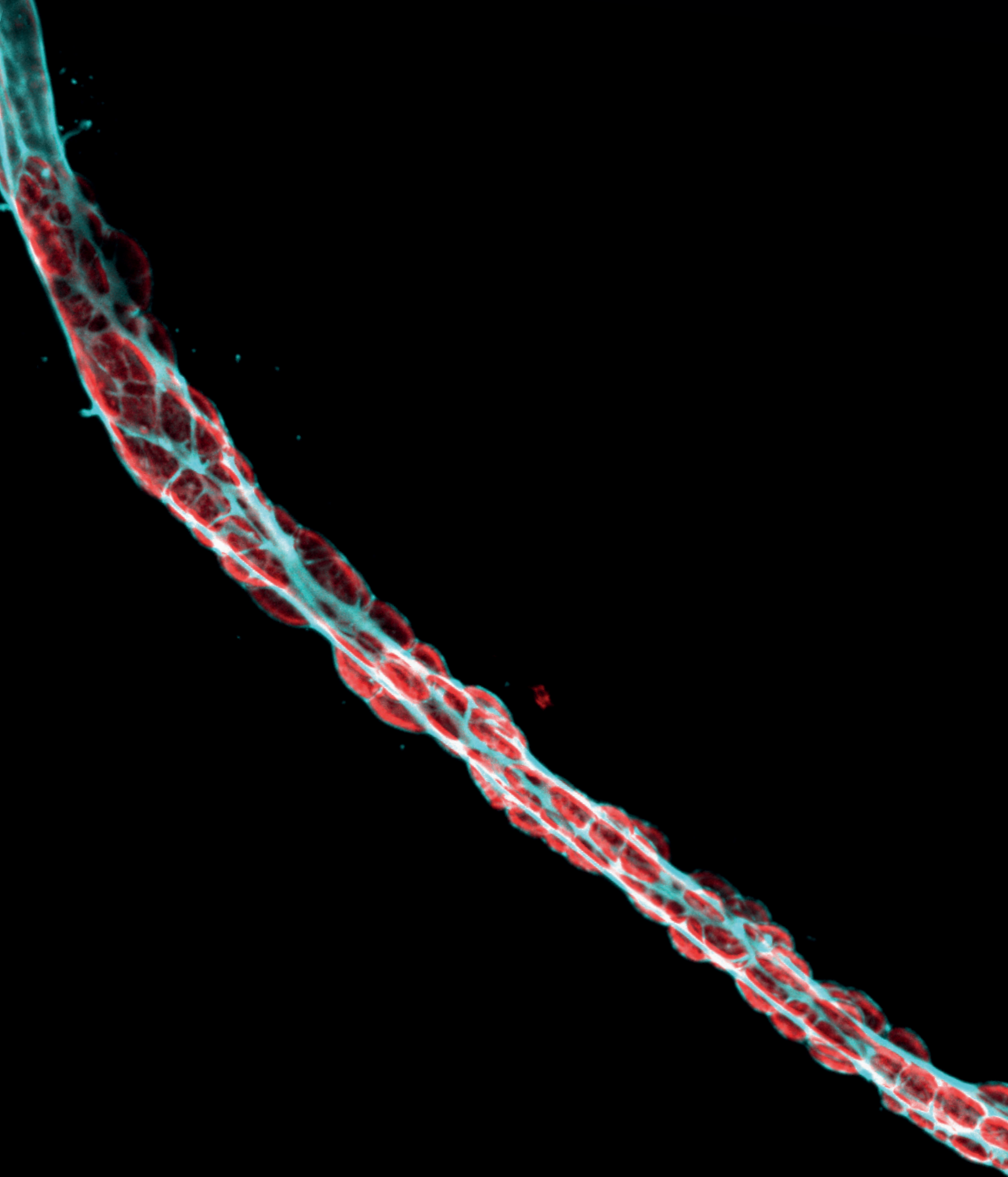
File S4. SapTrap assembly information

Four Module CeLINC Donor Plasmid Assembly (pMLS257 as destination vector)			
Slot 1 – promoter	Slot 2	Slot 3	Slot 4 – 3' UTR
5' TGG / AAG 3' overhangs	5' AAG / ACG 3' overhangs	5' ACG / TGC 3' overhangs	5' TGC / GTA 3' overhangs
pJRK151 (<i>Prps-0</i>) pJRK142 (<i>Phsp-16.48</i>) pJRK143 (<i>Pelt-2</i>) pJRK246 (<i>Pwrt-2</i>)	pJRK107 (CIBN-3xFLAG) pJRK109 (CRY2(olig))	pJRK108 (MP) pJRK112 (VHH(GFP)) pJRK254 (VHH(mCherry))	pJRK153 (<i>unc-54 3'UTR</i>)

Five Module CeLINC Donor Plasmid Assembly (fluorescent CRY2 or CIBN N-terminal tag) pMLS257 as destination vector				
Slot 1 - promoter	Slot 2 - FP	Slot 3	Slot 4	Slot 5- 3' UTR
5' TGG / ATG 3' overhangs	5' ATG / AAG 3' overhangs	5' AAG / ACG 3' overhangs	5' ACG / TGC 3' overhangs	5' TGC / GTA 3' overhangs
pJRK1 (<i>Prps-0</i>)	pDD375 (mKate2)	pJRK107 (CIBN-3xFLAG) pJRK109 (CRY2(olig))	pJRK108 (MP) pJRK112(VHH(GFP)) pJRK254(VHH(mCherry))	pJRK153 (<i>unc-54 3' UTR</i>)

Four Module Fluorescent Bait or Prey Protein Tag Assemblies (fluorescent N-terminal tag) pMLS257 as destination vector			
Slot 1 - promoter	Slot 2 - FP	Slot 3 - cDNA	Slot 4 - 3' UTR
5' TGG / ATG 3' overhangs	5' ATG / AAG 3' overhangs	5' AAG / ACG 3' overhangs	5' ACG / GTA 3' overhangs
pJRK1 (<i>Prps-0</i>)	pDD375 (mKate2)	pJRK120 (<i>par-6</i> cDNA)	pJRK150 (<i>unc-54 3'UTR</i>)

One-step promoter insertion into CRY2(olig)::VHH(GFP)::T2A::CIBN-3xFLAG::MP::unc-54 3' UTR
pJRK261 as destination vector
Slot 1 - promoter
5' TGG / ATG 3' overhangs
pJRK1 (<i>Prps-0</i>)



Chapter 4

BBLN-1 is essential for intermediate filament organization and apical membrane morphology

Sanne Remmelzwaal¹, Florian Geisler², Riccardo Stucchi^{3,4,5}, Suzanne van der Horst^{6,7}, Milena Pasolli³, Jason R. Kroll¹, Olga D. Jarosinska¹, Anna Akhmanova³, Christine A. Richardson⁸, Maarten Altelaar⁴, Rudolf E. Leube², João J. Ramalho^{1,9}, and Mike Boxem¹

¹ Developmental Biology, Institute of Biodynamics and Biocomplexity, Department of Biology, Faculty of Science, Utrecht University, Padualaan 8, 3584 CH, Utrecht, The Netherlands

² Institute of Molecular and Cellular Anatomy, RWTH Aachen University, 52074 Aachen, Germany

³ Cell Biology, Neurobiology and Biophysics, Institute of Biodynamics and Biocomplexity, Department of Biology, Faculty of Science, Utrecht University, Padualaan 8, 3584 CH, Utrecht, The Netherlands

⁴ Biomolecular Mass Spectrometry and Proteomics, Bijvoet Center for Biomolecular Research and Utrecht Institute for Pharmaceutical Sciences, Utrecht University, Padualaan 8, 3584 CH, Utrecht, The Netherlands

⁵ Present address: Philochem AG, Libernstrasse 3, CH-8112 Otelfingen, Switzerland

⁶ Molecular Cancer Research, Center for Molecular Medicine, University Medical Center Utrecht, Utrecht University, The Netherlands

⁷ Onco Institute, The Netherlands

⁸ Department of Biosciences, Durham University, United Kingdom.

⁹ Present address: Laboratory of Biochemistry, Wageningen University & Research, Stippeneng 4, 6708 WE, Wageningen, The Netherlands

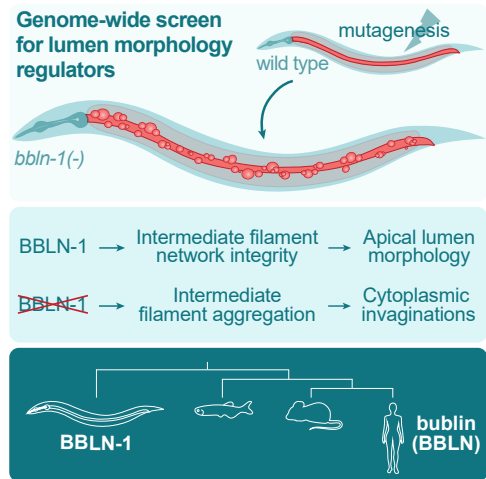
An adapted version of this chapter is published:

Remmelzwaal, S., Geisler, F., Stucchi, R., van der Horst, S., Pasolli, M., Kroll, J. R., ... & Boxem, M. (2021). BBLN-1 is essential for intermediate filament organization and apical membrane morphology. *Current Biology*, 31(11), 2334-2346.

Abstract

Epithelial tubes are essential components of metazoan organ systems that control the flow of fluids and the exchange of materials between body compartments and the outside environment. The size and shape of the central lumen confer important characteristics to tubular organs and need to be carefully controlled. Here, we identify the small coiled-coil protein BBLN-1 as a regulator of lumen morphology in the *C. elegans* intestine. Loss of BBLN-1 causes the formation of bubble-shaped invaginations of the apical membrane into the cytoplasm of intestinal cells, and abnormal aggregation of the

subapical intermediate filament (IF) network. BBLN-1 interacts with IF proteins and localizes to the IF network in an IF-dependent manner. The appearance of invaginations is a result of the abnormal IF aggregation, indicating a direct role for the IF network in maintaining lumen homeostasis. Finally, we identify bublin (BBLN) as the mammalian ortholog of BBLN-1. When expressed in the *C. elegans* intestine, bublin recapitulates the localization pattern of BBLN-1 and can compensate for the loss of BBLN-1. In mouse intestinal organoids, bublin localizes subapically, together with the IF protein keratin 8. Our results therefore may have implications for understanding the role of IFs in regulating epithelial tube morphology in mammals.



Graphical abstract.

Introduction

Epithelial and endothelial tubes are fundamental building units of many organs, including the digestive tract, vascular system, kidney, and lung. Tubular organs are essential for the transport of nutrients, waste products, gases, and ions across large distances. Furthermore, epithelial tubes function as a protective barrier to the outside environment. Tubes consist of a central lumen bounded by the apical domains of one or more epithelial or endothelial cells, and are remarkably varied in size, complexity and mechanism of development (Iruela-Arispe and Beitel, 2013; Iruela-Arispe and Davis, 2009; Lubarsky and Krasnow, 2003). The size and shape of the central lumen are precisely controlled, as they confer important biophysical and biochemical properties to biological tubes. Lumen morphology can be very stable, but can also be highly plastic during tissue growth or when subjected to mechanical stimuli or stress (Iruela-Arispe and Davis, 2009; Stutz et al., 2015; Sundaram and Buechner, 2016). The importance of mechanisms that control lumen morphology is highlighted by common pathologies that are characterized by altered lumen architecture, including polycystic kidney disease, cystic fibrosis, and inflammatory bowel disease (Bergmann et al., 2018; Cutting, 2015; Ramos and Papadakis, 2019; Schelling, 2016).

The *Caenorhabditis elegans* intestine provides a simple model to study the regulation of lumen morphology. The *C. elegans* intestine is a tube composed of 20 cells arranged in nine segments surrounding a central lumen (Figure 1A) (Sulston et al., 1983b; Leung et al., 1999). Specialized cell-cell junctions at the lateral membrane, known as *C. elegans* apical junctions (CeAJ), keep neighboring cells tightly adherent, ensuring integrity of the epithelium and impermeability of the lumen (Pasti and Labouesse, 2014). The intestinal cells are born during embryogenesis and do not divide or renew during larval development or in adulthood. They are polarized along an apicobasal axis and resemble mammalian enterocytes at the ultrastructural level (Coch and Leube, 2016). The lumen forming apical surface of both cell types is covered by microvilli that contain bundled actin filaments, and are supported by the subapical actin-rich terminal web (Leung et al., 1999; Bossinger et al., 2004). The luminal surface is further supported by an intermediate-filament (IF) rich fibrous sheet that directly underlies—and is likely connected to—the terminal web. The *C. elegans* IF network forms a particularly electron-dense structure anchored at the lateral cell junctions that is known as the ‘endotube’ (Bossinger et al., 2004; Coch and Leube, 2016; Munn and Greenwood, 1984).

Cytoplasmic IF proteins form resilient and flexible networks that mediate the mechanical properties of cells and tissues and contribute to a diverse range of processes including organelle positioning, intracellular trafficking, and cell motility (Coulombe and Wong, 2004; Etienne-Manneville, 2018). In tubular epithelia, subapical IF networks are ideally positioned to contribute to the regulation of lumen morphology and functioning. Indeed, intestinal IF networks have essential roles in epithelial polarization, maintenance of lumen morphology, and protection from environmental stresses (Etienne-Manneville, 2018; Geisler and Leube, 2016; Salas et al., 2016; Sanghvi-Shah and Weber, 2017; Toivola et

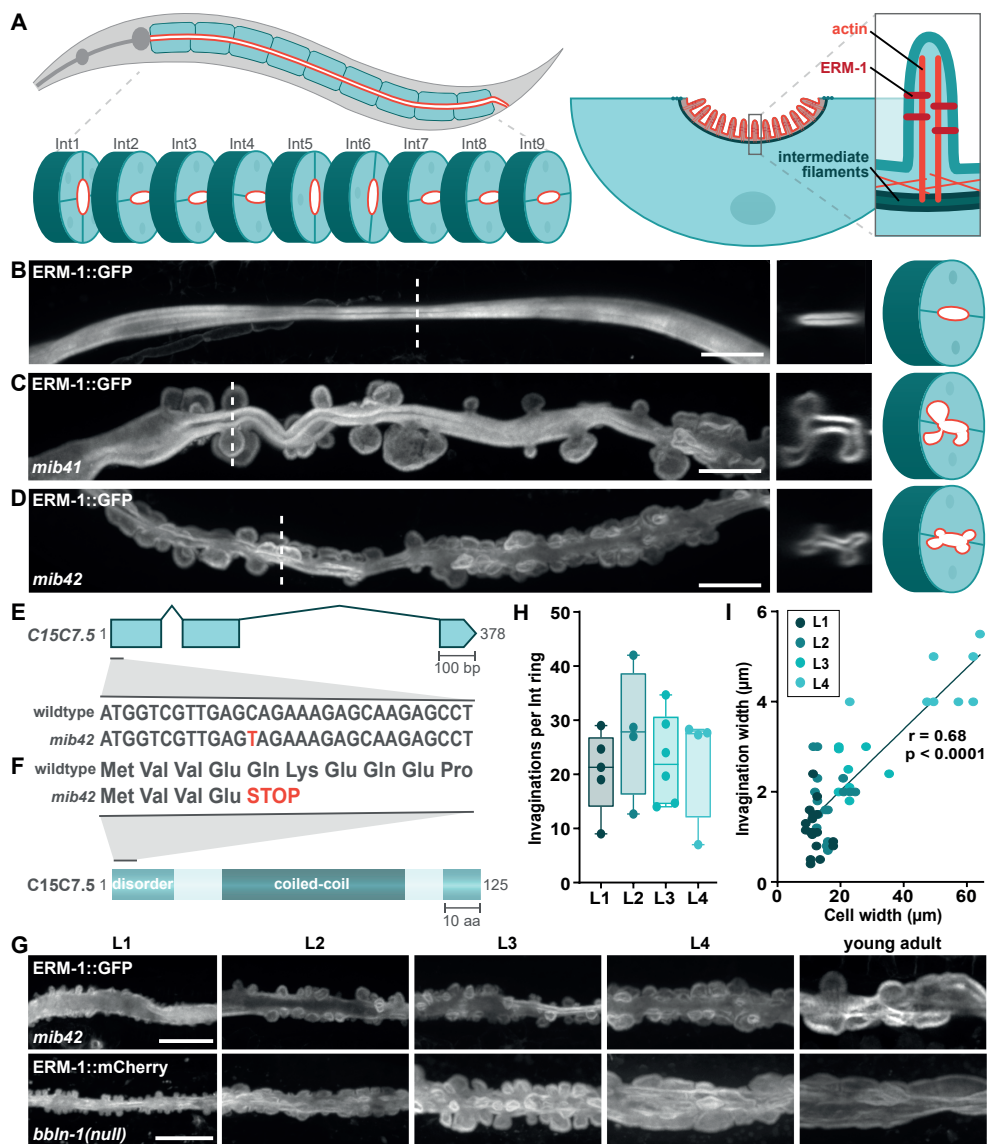


Figure 1. The intestines of *mib41* and *mib42* mutants show cytoplasmic invaginations.

(A) Schematic representation of the *C. elegans* intestine (left) and the subcellular intestinal localization of proteins and cytoskeletal elements relevant for this study (right). (B–D) Intestinal apical membrane morphology in L4 animals visualized with an endogenous ERM-1::GFP reporter. Dotted lines in left panels indicate position of cross-section views. Schematics depict cross-section with apical membrane in red. Unless otherwise indicated, in this and all other figures, images were acquired using spinning-disk confocal microscopy, lateral views are maximum intensity projections, anterior is to the left, and scale bars indicate 10 μm . (E, F) Genomic structure of the *C15C7.5* gene (E) and representation of the *C15C7.5* protein with predicted domains (F). Boxes in the genomic structure correspond to exons while lines represent introns. Part of the DNA and amino acid sequence is shown for both the wild-type and *mib42* mutant allele. (G) Progression of *mib42* and *bbln-1(null)* invagination phenotype

throughout development visualized by endogenous ERM-1::GFP and ERM-1::mCherry reporters, respectively. (H) Quantification of number of invaginations per intestinal ring, per larval stage in *bbln-1(null)* animals. Each data point represents the average number of invaginations per intestinal ring in one animal. Data are presented as median \pm interquartile range. Differences are not significant (Kruskal-Wallis followed by Dunn's multiple comparisons test; $P > 0.99$). (I) Correlation between cell and invagination width in *bbln-1(null)* animals, color coded per larval stage. Linear regression is shown for all data points combined. Data are analyzed with nonparametric Spearman correlation; $r = 0.6824$, $P < 0.0001$.

al., 2010). In the *C. elegans* intestine, loss of IF subunits, or of the IF organizers IFO-1 and SMA-5, can result in morphological abnormalities of the lumen and increased susceptibility to microbial, osmotic, and oxidative stresses (Carberry et al., 2012; Geisler et al., 2016, 2019, 2020).

Here, we report the identification of an evolutionary conserved regulator of intestinal tube morphology and IF organization we term *bbln-1*, for bulges budding from the lumen. *bbln-1* mutants are characterized by the presence of large invaginations of the apical lumen into the cytoplasm of intestinal cells. The BBLN-1 protein physically interacts with IF proteins and localizes to the endotube in an IF-dependent manner. Loss of BBLN-1 causes defects in the organization of the intestinal IF network, which aggregates into thick bundles at the neck of cytoplasmic invaginations. Surprisingly, the invagination phenotype of *bbln-1* mutants is rescued by removal of the IF network. This indicates that the cytoplasmic invaginations are the result of the aggregated IF network state caused by loss of *bbln-1*. Based on sequence similarity, we identified a mammalian ortholog of BBLN-1, which we termed bublin (BBLN). Bublin shares multiple protein interaction partners with BBLN-1 and can partially substitute for BBLN-1 functioning in the *C. elegans* intestine. Our findings provide further evidence that the subapical IF network plays an active role in regulating the morphology of tubular epithelia, while the structural and functional conservation from *C. elegans* to humans provides a model for studying IF modulation *in vivo*.

Results

Loss of *bbln-1* causes cytoplasmic invaginations of the intestinal apical membrane

To investigate the mechanisms that regulate intestinal lumen morphology, we performed a genetic screen in *C. elegans* for mutants with lumen morphology defects. We mutagenized a strain expressing the apical membrane protein ERM-1 endogenously fused to GFP, and screened for viable F2 progeny with aberrations in lumen morphology (Figure 1A–D). We identified two viable mutants (*mib41* and *mib42*) with dramatic bubble-shaped protrusions of the apical plasma membrane into the cytoplasm of the intestinal cells (Figure 1C, D). Complementation analysis indicated that *mib41* and *mib42* affect two independent loci. We determined the genomic regions of interest by single nucleotide polymorphism (SNP) mapping (Davis et al., 2005), and identified candidate causative mutations using the sibling subtraction method for mapping by whole-genome sequencing (Joseph et al., 2018). We obtained a

single cluster of candidate mutations for each mutant allele on opposite arms of the X chromosome, consistent with the SNP mapping data.

Only one among the candidate *mib41* mutations was predicted to exert a detrimental effect on protein function, by inducing a missense mutation within the *sma-5* open reading frame (ORF) (C370T in *sma-5a*). At the protein level, this mutation results in an arginine to tryptophan substitution in the kinase domain of all predicted isoforms (Arg124Trp in SMA-5a) (Figure S1A). SMA-5 is a member of the conserved mitogen-activated protein kinase (MAPK) family that is required for intestinal lumen morphogenesis (Geisler et al., 2016). *sma-5* mutations induce a lumen invagination phenotype similar to *mib41* mutants (Geisler et al., 2016) and the strong loss of function *sma-5(n678)* allele (Watanabe et al., 2005) failed to complement *mib41*. Together, these data show that *mib41* is a novel *sma-5* allele.

The *mib42* sequencing data also yielded a single potentially deleterious mutation within a predicted ORF: a C to T transition resulting in an early stop at the fifth codon of the uncharacterized gene *C15C7.5* (Figure 1E, F). We used several strategies to confirm that loss of *C15C7.5* function was responsible for the intestinal lumen morphology defects in *mib42* animals. First, *C15C7.5* RNA interference (RNAi) feeding experiments in ERM-1::GFP animals revealed apical membrane invaginations similar to those observed in the mutant (Figure S1B). Second, transgenic expression of *GFP::C15C7.5* from the intestinal specific *vha-6* promoter fully rescued the invagination phenotype of *mib42* animals (Figure S1C). Lastly, we generated a *C15C7.5* null allele, *mib70*, by removing the entire *C15C7.5* coding sequence using CRISPR/Cas9 engineering. The *mib70* deletion, from here on referred to as *C15C7.5(null)*, caused cytoplasmic invaginations (Figure S1D) and was unable to complement *mib42*. The invagination phenotype in *C15C7.5(null)* animals was more severe than in *mib42* mutants (Figure 1G). This data indicates that *mib42* is a partial loss-of-function mutation in the *C15C7.5* gene, and that *C15C7.5* controls intestinal lumen morphology. We have named the *C15C7.5* gene *bbln-1* for bulges budding from the intestinal lumen.

bbln-1(null) animals are homozygous viable. However, in addition to the intestinal lumen defects, we noticed that *bbln-1(null)* animals are developmentally delayed (Figure S1E, F). This delay is likely a consequence of the intestinal abnormalities, as expression of GFP::BBLN-1 from the *vha-6* promoter nearly fully rescued the developmental delay (Figure S1E, F). We next examined the intestinal cytoplasmic invaginations in more detail. In *bbln-1(null)* animals, invaginations were visible from hatching, and the number of invaginations per intestinal ring remained constant throughout development (Figure 1G, H). Time-lapse imaging showed that the invaginations were stable, at least over a period of several hours (Video S1). Invagination width correlated with intestinal cell width, and in late larval and adult stages invaginations had an elongated appearance (Figure 1I). The *bbln-1* invaginations were spread uniformly along the length of the intestine (Figure 1D, G). However, in cross section, invaginations seemed to preferentially localize at the vertices of the ellipse-shaped lumen, in proximity to cell junctions. This was particularly noticeable in *mib42* animals, which have fewer invaginations than

the *bbln-1(null)* mutant (Figure 1D). To confirm this, we visualized invaginations in a *bbln-1(mib42)* strain expressing the junctional protein DLG-1 endogenously tagged with mCherry. Indeed, invaginations occurred in proximity to cell junctions (Figure S2A–D).

To assess intestine morphology and integrity we fed animals with three sizes of Texas Red-dextran conjugates (3kDa, 10kDa, and 40kDa). In wild-type animals, Texas Red signals filled the lumen and were enclosed by the ERM-1::GFP-labelled apical membrane (Figure S2E–G). Similarly, in *bbln-1(mib42)* animals, all invaginations contained Texas Red signal, indicating that they are contiguous with the lumen. Moreover, we never observed internalized invaginations or presence of Texas Red signal in the cytoplasm of intestinal cells, indicating that the invaginations are stable and do not internalize. We also did not observe paracellular passage of conjugates in the intestine (Figure S2F, G). This contrasted with the pharynx, where we observed paracellular passage of the 3kDa conjugate in both wild-type and *bbln-1* animals (Figure S2H, I). These data indicate that paracellular permeability of the intestine is not significantly affected by loss of BBLN-1.

BBLN-1 is a small coiled-coil protein that localizes dynamically to intermediate filament-rich structures

bbln-1 is predicted to encode a single protein isoform of just 125 amino acids. A central coiled-coil domain (aa 39–102) is the only recognizable feature, with the remainder of the protein predicted to be intrinsically disordered (Figure 1F). To investigate the function of BBLN-1 in intestinal lumen morphogenesis, we first analyzed its expression pattern and subcellular localization. We used CRISPR/Cas9 engineering to introduce the GFP coding sequence immediately upstream of the *bbln-1* start codon. Homozygous *gfp::bbln-1* animals show no intestinal lumen defects or developmental delay (Figure S1E, F), demonstrating that the GFP::BBLN-1 fusion protein is functional. We also generated a C-terminally mKate2 tagged variant. However, homozygous *bbln-1::mKate2* animals displayed the intestinal cytoplasmic invagination phenotype, indicating a non-functional protein fusion. We therefore used the N-terminal GFP fusion for our experiments.

BBLN-1 was first apparent at the comma stage of embryonic development, at the apical domain of intestinal cells (Figure 2A). In subsequent embryonic stages, BBLN-1 became visible in the hypodermis and pharynx as well. During larval and adult stages, we detected BBLN-1 in many epithelial tissues including the pharynx, intestine, excretory canal, and hypodermis (Figure 2B). In each of these tissues the distribution of BBLN-1 was similar to previously reported distribution of intermediate filament proteins. In the marginal cells of the pharynx, we observed a pattern of short radial filaments, reminiscent of the IF containing tonofilaments (Karabinos et al., 2003). In the excretory canal, BBLN-1 localization was similar to that of the intermediate filament proteins IFA-4, IFB-1, and EXC-2/IFC-2 (Al-Hashimi et al., 2018a; Khan et al., 2019). In the hypodermis, we observed a pattern strongly resembling that of intermediate filaments in the *C. elegans* hemidesmosomes (Pasti and Labouesse, 2014; Woo

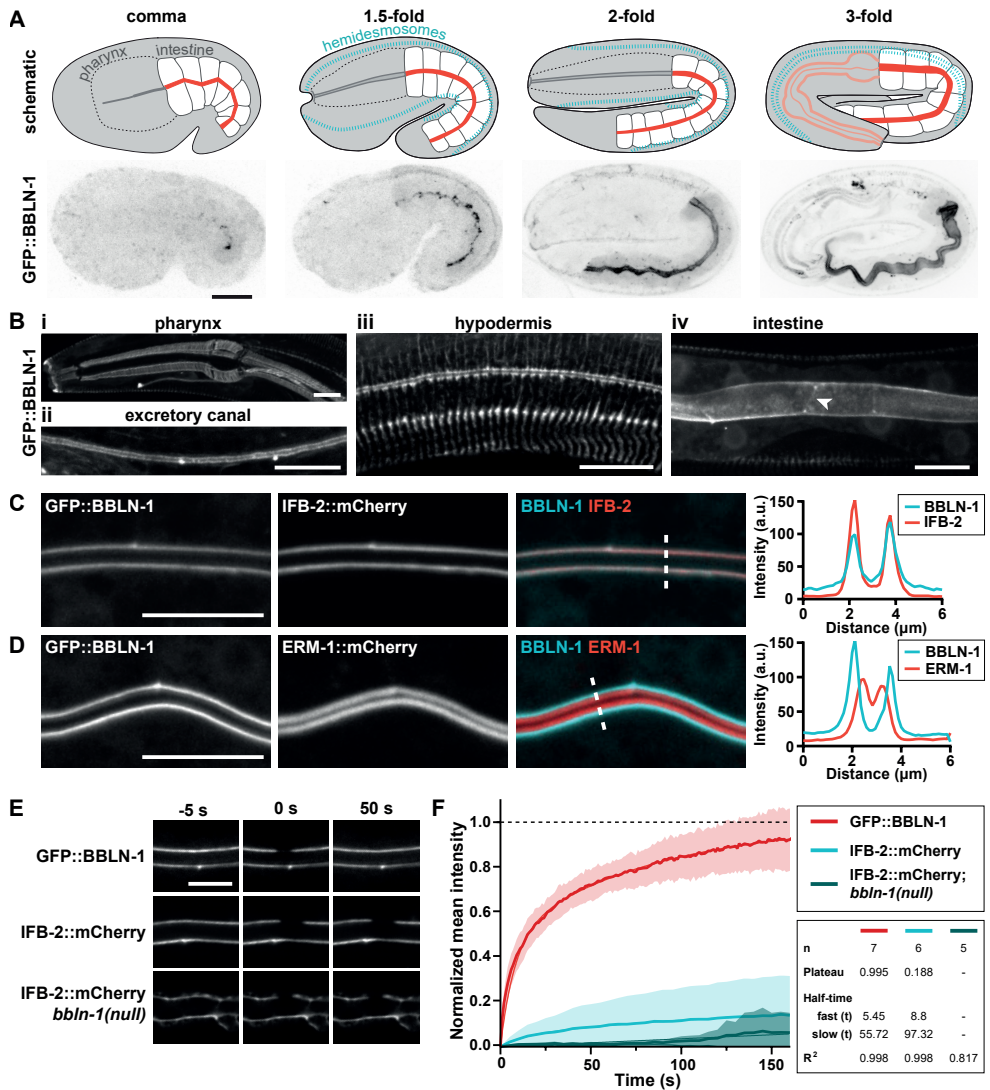


Figure 2. BBLN-1 localizes dynamically to intermediate filament-rich structures. (A, B) Distribution of the endogenous GFP::BBLN-1 reporter during late embryonic development (A) and in different tissues in late L3-young adult animals (B). Arrowhead indicates apical junction. All scale bars indicate 10 μm . (C, D) Distribution of GFP::BBLN-1 compared with ERM-1::mCherry (C) and IFB-2::mCherry (D) at the apical domain of intestinal cells of L3 larvae. Dashed lines indicate sites of intensity profiles shown in the graphs to the right. (E, F) Stills from time-lapse movies (E) and FRAP curves (F) corresponding to bleached portions of the apical domain in larval intestines. Time-lapse data was acquired at 1 s intervals for GFP::BBLN-1 ($n = 7$) and 5 s intervals for IFB-2::mCherry (WT: $n = 6$, *bbln-1(null)*: $n = 5$). Thin lines and shading represent the mean \pm SD. No plateau or half-times could be accurately determined for IFB-2::mCherry; *bbln-1(null)*.

et al., 2004). We also observed expression of BBLN-1 in the uterine seam and vulva, as previously reported for IFA-1, MUA-6/IFA-2, IFB-1 and EXC-2/IFC-2 (Al-Hashimi et al., 2018; Hapiak et al., 2003; Karabinos et al., 2003; Williams et al., 2015; Woo et al., 2004). To investigate the localization of BBLN-1 relative to IFs, we engineered an endogenous IFB-1::mCherry fusion. Close overlap between GFP::BBLN-1 and IFB-1::mCherry in each tissue indicates that BBLN-1 indeed localizes to IFs (Figure S3A–C).

In the intestine, BBLN-1 localized subapically with apparent accumulation around cell junctions (Figure 2Biv). This localization pattern corresponds to the distribution of the endotube (Bossinger et al., 2004). To confirm that BBLN-1 resides at the endotube, we generated an endogenous mCherry fusion of the intestinal intermediate filament protein IFB-2. We then analyzed the localization of BBLN-1 relative to IFB-2 and to ERM-1, which localizes apically at microvilli (Bidaud-Meynard et al., 2019; Ramalho et al., 2020). Consistent with localization to the endotube, we found that BBLN-1 colocalizes with IFB-2, basal to ERM-1 (Figure 2C, D). To determine if BBLN-1 stably associates with the IF network, we performed fluorescence after photobleaching (FRAP) experiments. IFB-2 fluorescence recovered only ~15% in 150 seconds (Figure 2E, F). Similar slow recovery was previously reported for IFA-1 and IFB-1 in the pharynx (Karabinos et al., 2003). In contrast, BBLN-1 recovered roughly 90% within the same period, indicating that BBLN-1 localizes to the IF network in a dynamic fashion. Taken together, these results indicate that BBLN-1 is a dynamic component of the endotube in intestinal cells.

The subcellular localization of BBLN-1 depends on IFs

As BBLN-1 localizes together with IF proteins, we next determined whether the apical localization of BBLN-1 depends on IFs. The *C. elegans* intestine expresses six cytoplasmic IF proteins, all of which localize almost exclusively to the endotube (Bossinger et al., 2004; Geisler et al., 2020; Karabinos et al., 2002, 2004). We used RNAi feeding to knock down the individual intestinal IF proteins in a strain that endogenously expresses GFP::BBLN-1 and ERM-1::mCherry. We observed significant reduction in apical BBLN-1 upon knockdown of IFB-2, IFD-1, IFD-2, or IFP-1 (Figure 3A, B). In *ifb-2(RNAi)* animals, the loss of BBLN-1 from the apical cortex was most striking. IFB-2 is an essential component of the apical intestinal IF network, and loss of IFB-2 results in a complete absence of the endotube (Geisler et al., 2019, 2020). Therefore, the strong reduction in apical BBLN-1 likely reflects the loss of all IFs from the apical domain. We also examined the localization of BBLN-1 in the excretory canal of *ifc-2(RNAi)* animals, as IFC-2 has been shown to be important for the structure of this tissue (Al-Hashimi et al., 2018). We observed a marked relocalization of BBLN-1 from the apical cortex to the cytoplasm and basal membrane, which suggests that dependency on IFs is a general aspect of BBLN-1 localization (Figure 3C).

The reliance on an intact IF network for BBLN-1 to properly localize indicates a potential association with IF proteins. To identify candidate interacting proteins, we performed affinity purification of GFP::BBLN-1 from mixed-stage

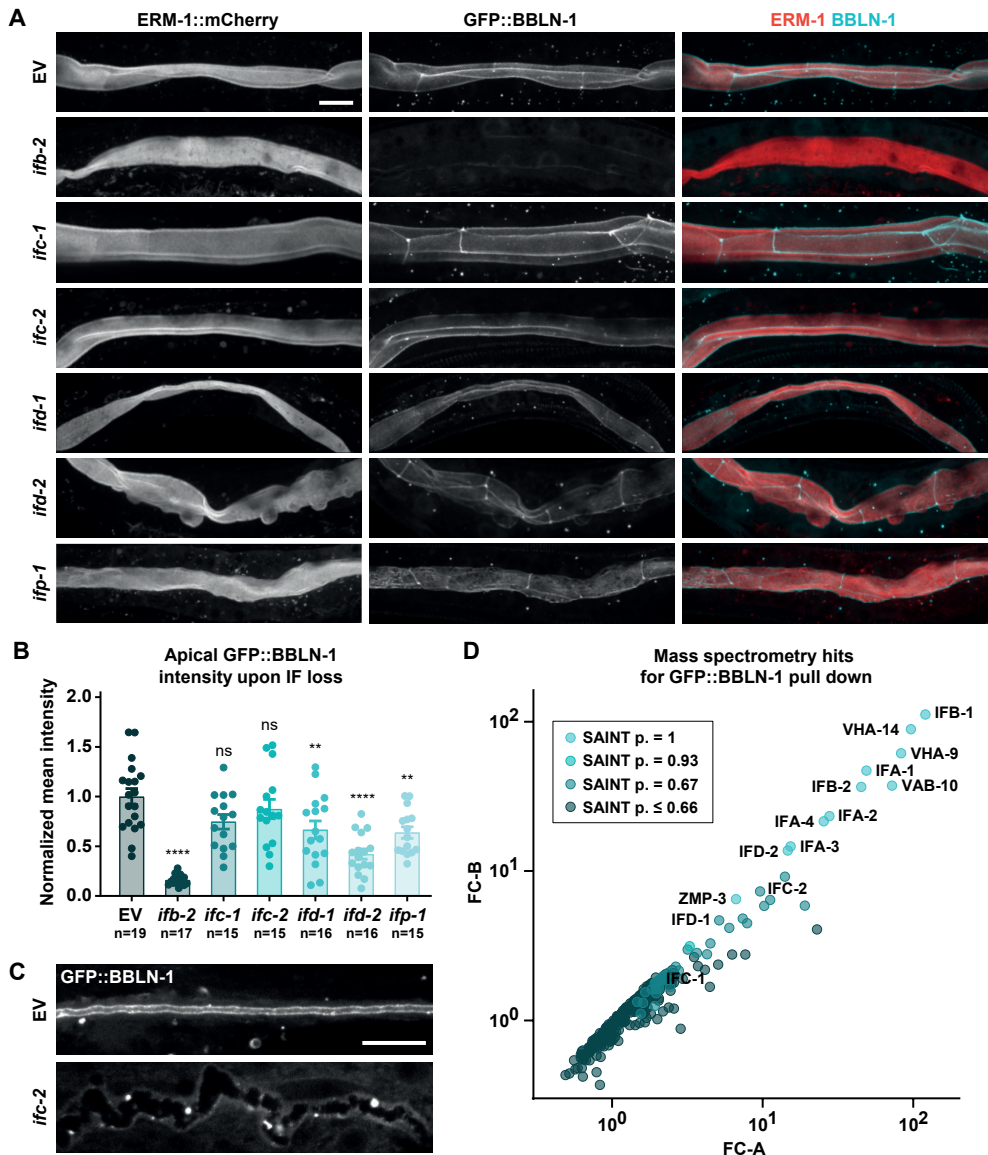


Figure 3. BBLN-1 requires intermediate filaments for its apical localization in the intestine. (A) Intestinal GFP::BBLN-1 distribution and apical membrane morphology, visualized by ERM-1::mCherry, upon RNAi knockdown of targets indicated to the left. EV = empty vector. All scale bars indicate 10 μ m. (B) Quantification of GFP::BBLN-1 levels at the intestinal apical domain of larvae subjected to RNAi knockdown of targets indicated at the left. Each data point represents the average of six or eight measurements in a single animal ($n = 19, 17, 15, 15, 16, 16,$ and 15 animals, respectively). Larvae were L2–L4 stage. Data are presented as mean \pm SEM and analyzed with ordinary one-way ANOVA followed by Dunnett's multiple comparisons test; ns = $P > 0.05$, ** = $P < 0.005$, **** = $P < 0.0001$. (C) GFP::BBLN-1 distribution in the excretory canal upon RNAi knockdown of *ifc-2* or EV control. (D) Mass spectrometry hits for GFP::BBLN-1 pull down plotted as correlation between fold-change (FC) score A and more stringent FC score B. Data points are color coded for different SAINT probability scores.

C. elegans cultures, followed by mass spectrometry analysis. Consistent with the localization and dependency on intermediate filaments, the highest-ranking proteins we identified included all intestinal IF proteins except IFP-1, as well as all proteins of the IFA/IFB system (IFA-1, 2, 3, 4 and IFB-1) (Figure 3D). After IFB-1, the two most highly ranked candidate interactors were VHA-9 and VHA-14, the *C. elegans* orthologs of subunits F and D of the stalk region of the highly conserved vacuolar ATPase (V-ATPase) V1 domain, which localizes to the luminal domain of the intestine (Ji et al., 2006). Other high-confidence hits included various hemidesmosome components (i.e. VAB-10, LET-805, PAT-12 and MUP-4) and actin-interacting proteins like the crosslinker FLN-2, and the myosins UNC-15 and MYO-2. Altogether, our mass spectrometry data suggests a physical interaction between BBLN-1 and IFs and provides cues for future investigations into the activities of BBLN-1.

To further confirm the dependency of BBLN-1 localization on IFs, we examined the effects of inactivation of known regulators of intermediate filament organization on BBLN-1. In addition to *sma-5*, loss of *ifo-1*, *act-5*, and *let-413* have all been reported to disrupt IFB-2 distribution in the *C. elegans* intestine (Bossinger et al., 2004b; Carberry et al., 2012b; Estes et al., 2011b; Stutz et al., 2015). IFO-1 localizes to the adluminal domain, together with but independently from IFB-2, and its depletion causes aggregation of IFs at cell junctions as well as in the cytoplasm (Carberry et al., 2012). Reducing the levels of the intestinal actin ACT-5 causes gaps in the normally uninterrupted IFB-2 network, and has been reported to result in the appearance of cytoplasmic invaginations (Estes et al., 2011; Stutz et al., 2015). Finally, depletion of LET-413 causes aberrant localization of IFB-2 to the lateral and basal domains of intestinal cells in the embryo (Bossinger et al., 2004). We depleted each protein by RNAi in a strain expressing either ERM-1::mCherry (to visualize lumen morphology) or IFB-2::mCherry, together with GFP::BBLN-1. The phenotypes we observed matched published reports, though RNAi for *act-5* caused more severe IFB-2 defects, with invaginations only visible in a small subset of animals (Figure 4A-C). In each case, the localization of BBLN-1 mimicked the localization pattern of IFB-2, including basolateral mislocalization in *let-413(RNAi)* embryos (Figures 4A-4C). This confirms that BBLN-1 associates with IFs.

Interestingly, in *sma-5(RNAi)* intestines, we observed a significant reduction in cortical enrichment of BBLN-1 (Figure 4D). This suggests that *sma-5* acts upstream of *bbln-1*. To determine if *sma-5* and *bbln-1* act in a linear pathway, we performed *sma-5* RNAi in a *bbln-1(null)* background. The resulting animals displayed more severe intestinal abnormalities than either *sma-5(RNAi)* or *bbln-1(null)* alone (Figure 4E). Thus, while *sma-5* may act in part through *bbln-1*, both genes act at least partially independent.

Collectively, the dependence on IFs, the colocalization of BBLN-1 with aberrantly localized IFB-2, and the co-purification of BBLN-1 with IF proteins suggests that BBLN-1 associates with the IF network.

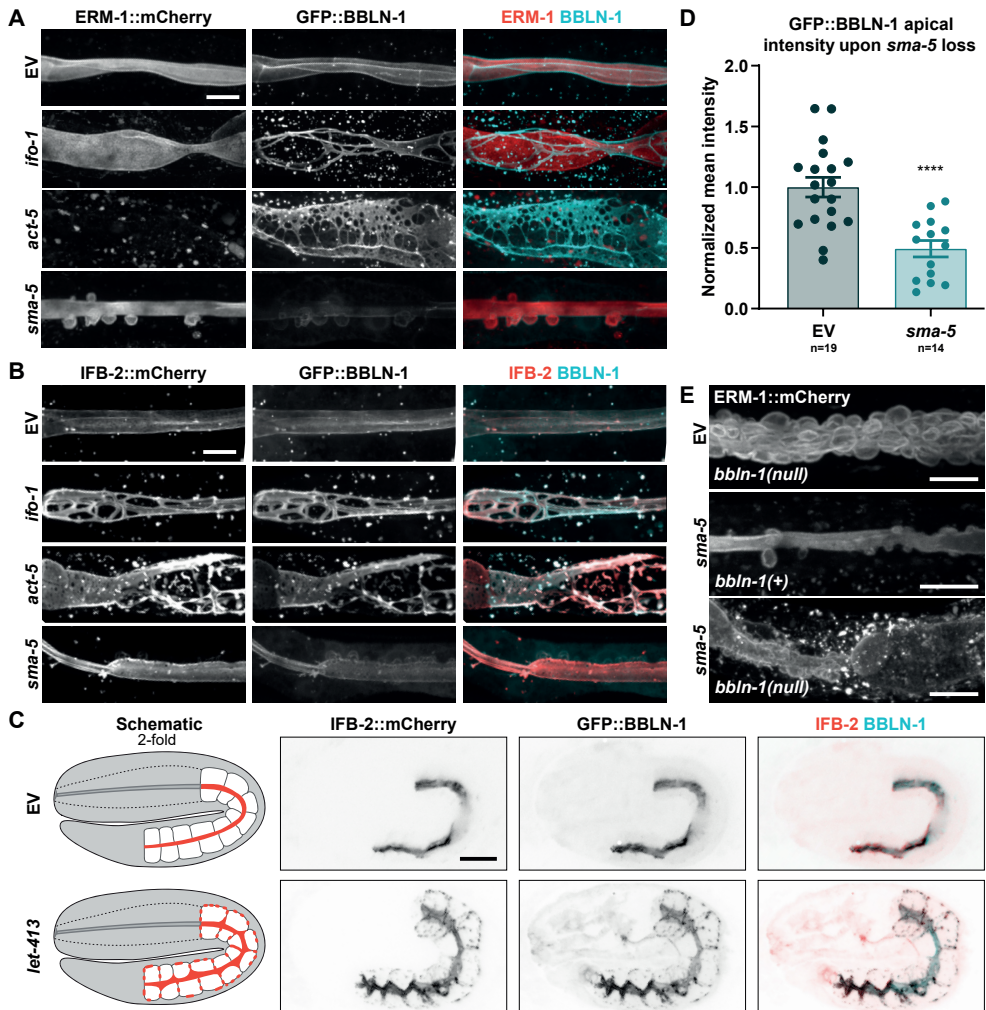


Figure 4. BBLN-1 co-localizes with mislocalized IFs. (A) Intestinal GFP::BBLN-1 distribution and apical membrane morphology, visualized by ERM-1::mCherry, after RNAi knockdown of targets indicated on the left. EV = empty vector control. Same EV control is shown as in Figure 3A since data are from a single experiment. All scale bars indicate 10 μ m. (B, C) GFP::BBLN-1 and IFB-2::mCherry distribution in L2-L4 larvae (B) and 2-fold embryos (C) after RNAi knockdown of targets indicated on the left. (D) Quantification of GFP::BBLN-1 levels at the intestinal apical domain of L3/L4 larvae subjected to RNAi knockdown of *sma-5*. Each data point represents the average of six or eight measurements in a single animal ($n = 19$ and 14 animals, respectively). Data are presented as mean \pm SEM and analyzed with ordinary one-way ANOVA followed by Dunnett's multiple comparisons test; **** = $P < 0.0001$. EV control data are same as in Figure 3B. (E) Apical membrane morphology, visualized by ERM-1::mCherry, after RNAi knockdown of targets indicated on the left in *bbln-1*(+) or *bbln-1*(null) background.

Loss of *bbln-1* compromises the integrity of the IF network

Apical domain invaginations in *sma-5* mutants were previously linked to defects in IF organization by fluorescence and electron microscopy (Geisler et al., 2016). Unlike the uniform electron-dense endotube surrounding the lumen in wild-type animals, endotube thickness in *sma-5* mutant animals is highly variable (Geisler et al., 2016). The phenotypic similarities between *sma-5* and *bbln-1* mutants, as well as the localization of BBLN-1 to IF-rich structures, led us to hypothesize that apical domain invaginations in *bbln-1* mutant animals were similarly associated with defects in intestinal IF organization. To address this, we analyzed the distribution of three different intestinal IF proteins in *bbln-1(null)* animals: IFB-2, IFC-2, and IFD-2. For IFC-2, we used an existing CRISPR knock-in line expressing IFC-2a/e fused to the yellow fluorescent protein (IFC-2a/e::YFP) (Geisler et al., 2019, 2020). For IFD-2 we generated an endogenous *gfp::ifd-2* locus using CRISPR/Cas9.

In control animals, IFB-2 and IFC-2 were distributed evenly along the adluminal domain (Figure 5A, C). Both proteins were also enriched at cell junctions, with IFC-2 showing stronger junctional enrichment than IFB-2. These localization patterns match prior observations (Hüsken et al., 2008; Carberry et al., 2012; Geisler et al., 2016, 2020). In contrast to IFB-2 and IFC-2, IFD-2 showed a clearly punctate localization pattern and was excluded from cell junctions (Figure 5E, S5A). The distinct localization of IFD-2 indicates functional specialization within the IF network.

Upon loss of *bbln-1*, all three IF proteins retained their subapical localization, but formed a network of cables or bundles of increased fluorescence intensity, surrounding protrusions into the cytoplasm with reduced fluorescence signal (Figure 5B, D, F). IFD-2 lost its punctate localization pattern, instead localizing to cable-like structures (Figure 5F). To investigate the stability of IFs within the aggregated bundles, we performed FRAP on IFB-2::mCherry in *bbln-1(null)* animals. IFB-2 showed very little fluorescence recovery, appearing if anything even more stable than in control animals (Figure 2E, F). Together these data indicate that BBLN-1 is required for the integrity of the IF network but not for IF recruitment to the subapical cortex.

Interestingly, loss of BBLN-1 did not cause defects in the organization of the intermediate filament network in the pharynx or hypodermis, as marked by IFB-1::mCherry (Figure S4A–C). The only minor effect we noticed was in the excretory canal. In this tissue, GFP::BBLN-1 and IFB-1::mCherry are enriched apically, but are also present in small puncta of unknown nature. These IFB-1::mCherry puncta were absent in *bbln-1* mutants (Figure S4D). The lack of severe defects in other tissues indicates that the intestinal intermediate filament network is uniquely sensitive to BBLN-1 loss.

To investigate whether BBLN-1 is required for IF network integrity throughout development or only during a critical time in intestinal development, we used the auxin-inducible degradation (AID) system. The AID system enables targeted degradation of AID-degron tagged proteins through expression of the plant-

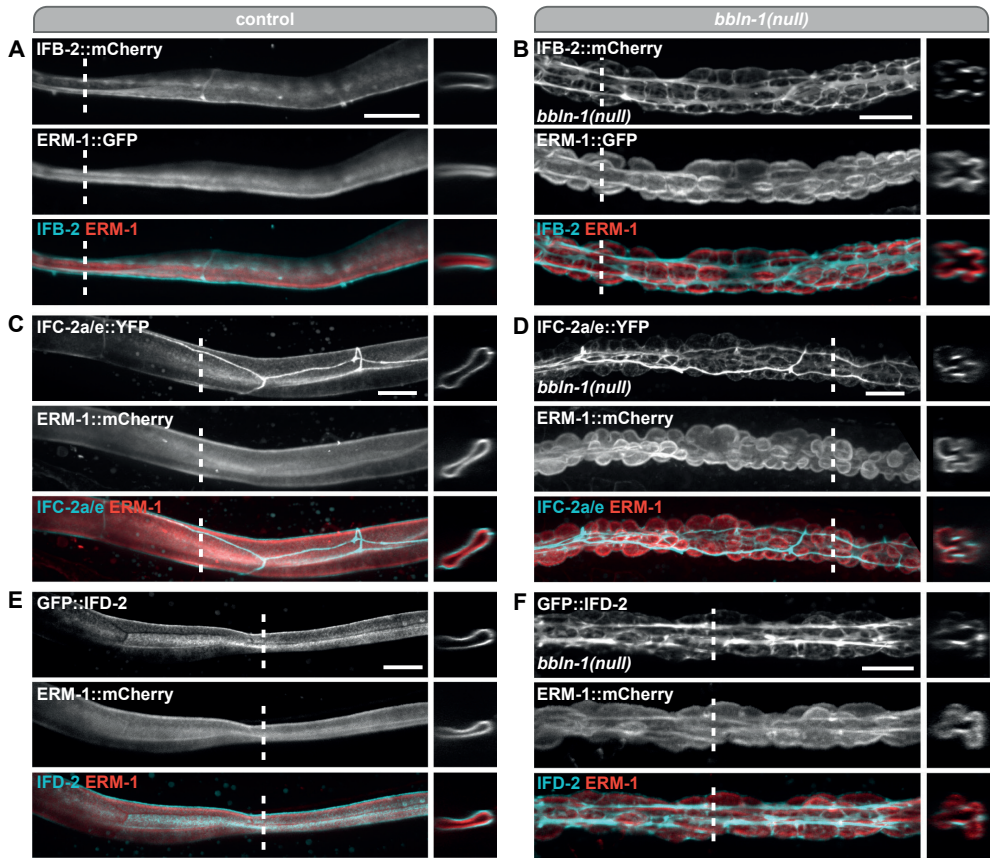


Figure 5. Loss of *bbln-1* compromises the integrity of the intermediate filament network. (A–F) Organization of the intestinal IF network visualized with IFB-2::mCherry (A, B), IFC-2a/e::YFP (C, D) or GFP::IFD-2 (E, F) in control (A, C, E) or *bbln-1*(null) (B, D, F) animals. Large panels are lateral views and small panels are cross-sections at the site indicated by the dashed lines. All scale bars indicate 10 μ m.

derived auxin-dependent E3 ubiquitin ligase specificity factor TIR1 (Nishimura et al., 2009; Zhang et al., 2015). We used CRISPR/Cas9 genome engineering to tag BBLN-1 N-terminally with GFP and the AID-degron and expressed TIR1 from the intestine-specific *elt-2* promoter. Within 1 hour of addition of auxin to L1-stage animals, GFP::AID::BBLN-1 was no longer detectable at the luminal domain of the intestine (Figure S5B). We next added auxin to late L1 stage or early L4 stage animals and imaged the intestinal lumen after 24 and 48 hours, using IFB-2::mCherry and ERM-1::GFP as markers (Figure S5C). Irrespective of the starting time point, approximately half of the animals had developed invaginations after 24 hours of auxin treatment (Figure S5D, 48-hour developmental timepoint). The remainder showed small “holes” in the normally contiguous IFB-2::mCherry fluorescent pattern (Figure S5E). Eventually, all animals treated with auxin from L1 developed cytoplasmic invaginations (Figure S5D, 72-hour developmental timepoint). These data show that *bbln-1* is required to maintain the integrity of the IF network throughout development.

We also used the AID system to determine if re-expression of BBLN-1 could revert already formed invaginations. We hatched GFP::AID::BBLN-1 animals in the presence of auxin, and transferred L1 animals to plates lacking auxin. BBLN-1 levels recovered within 24 hours (Figure S5F). However, we still observed invaginations in L4 and adult animals (Figure S5G, H), demonstrating that the presence of BBLN-1 is not sufficient to restore an already malformed luminal domain.

In addition to the IF network, the apical domain of the intestine is highly enriched in actin, which is present both in microvilli and the supporting terminal web. To investigate if the actin cytoskeleton is disrupted, we examined the localization of the intestinal actin ACT-5 in *bbln-1(null)* animals, using a YFP::ACT-5 transgene (Bossinger et al., 2004). In *bbln-1* animals, ACT-5 smoothly decorated the surface of the cytoplasmic invaginations and was not enriched in bundles or cables (Figure S5I, J). Thus, loss of BBLN-1 function appears to specifically affect the IF network and not the terminal web or microvillar actin. We also investigated whether the loss of *bbln-1* disrupted the overall polarization of the intestinal cells. Inactivation of *bbln-1* by RNAi did not affect the basolateral localization of an endogenous LET-413/Scribble::mCherry marker, nor the apical localization of an endogenous PAR-6::GFP marker (Figure S5K, L). Thus, the effects of *bbln-1* on the IF network are not due to a loss of intestinal polarity. Moreover, as invaginations are coated with PAR-6, ERM-1, and ACT-5, the formation of invaginations is not accompanied by a loss of apical identity.

To confirm loss of IF network integrity in *bbln-1* mutants and analyze intestinal morphology at the ultrastructural level, we performed electron microscopy on *bbln-1(null)* mutants. Previously, it was shown that in *sma-5* mutant intestines, the endotube is lost or diminished at sites of invagination and thickened around invagination necks (Geisler et al., 2016). In *bbln-1(null)* animals, the endotube appears to be similarly affected as in *sma-5* mutants. Endotube remnants appeared as aggregated electron-dense material, and no longer displayed the characteristic two lines of electron-dense material defining the endotube in wild-type intestines (Figure 6, compare A versus B or C versus D). Nevertheless, as in wild-type animals, aggregated endotube material in *bbln-1(null)* intestines still maintained a characteristic distance from the apical membrane, consistent with the continued presence of the subapical terminal web (Figure 6A and 6B, inlays). Finally, similar to *ifb-2* mutants (Geisler et al., 2019), the electron microscopy images revealed that microvilli are still abundant in invaginations. These data suggests that the presence of BBLN-1 and a fully assembled endotube are not required for microvilli formation, which is consistent with previous data on *ifb-2* null mutants (Geisler et al., 2019).

Taken together, the EM and light microscopy observations demonstrate that the intestinal IF network collapses and aggregates into stable bundles upon loss of BBLN-1, without affecting other aspects of intestinal epithelial polarity or the actin cytoskeleton.

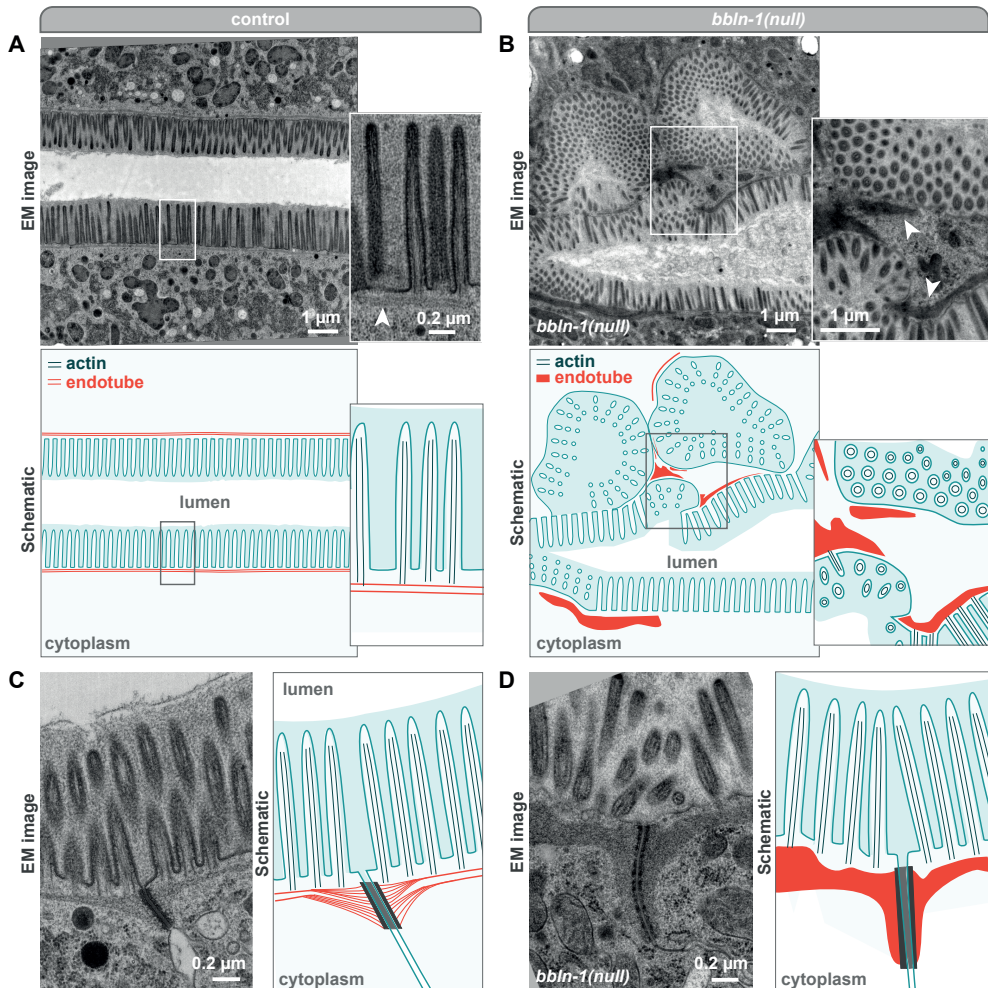


Figure 6. Loss of *bbln-1* compromises the integrity of the endotube. (A, B) Ultrastructure of the apical domain in intestinal cells of *bbln-1*(+) and *bbln-1*(null) adult animals visualized by transmission electron microscopy. Boxed region is shown enlarged and arrowheads point to the endotube. Schematics indicate actin bundles in blue and endotube in red. (C, D) Electron microscopy images showing the endotube at apical junctions. Schematics indicate actin bundles in blue, endotube in red, and junction in grey.

Apical IF aggregation drives cytoplasmic invaginations

We next sought to better understand the relationship between the cytoplasmic invaginations and collapsed IF network observed in *bbln-1* mutants. If invaginations are a consequence of the IF network collapse, direct disruption of the IF network might be expected to similarly cause invaginations. A recent study showed that *ifd-2* knockout causes cytoplasmic invaginations, while retaining apical IFB-2 and IFC-2 localization (Geisler et al., 2020). Indeed, *ifd-2*(*RNAi*) induced cytoplasmic invaginations, though with much lower penetrance and severity than *bbln-1* mutants (Figure 3A). We also observed that knockdown

of *ifp-1* causes an irregular apical surface and mildly fragmented BBLN-1 distribution (Figure 3A). To determine if invaginations in *ifd-2(RNAi)* animals are due to the partial loss of BBLN-1, we performed *ifd-2(RNAi)* in a *bbln-1(null)* mutant background. The combined loss of *ifd-2* and *bbln-1* resulted in more severe lumen abnormalities than loss of *bbln-1* alone (Figure S6A). While we cannot exclude that loss of BBLN-1 localization contributes to the *ifd-2(RNAi)* defects, the increased severity indicates that both genes have at least partially independent functions. These data are consistent with a model in which the cytoplasmic invaginations observed in *bbln-1* mutants are caused by defects in the IF network.

Surprisingly, despite the loss of the complete intestinal IF network, *ifb-2* knockout animals have been reported to be overall healthy in appearance, with only mild intestinal lumen morphology defects and an increased susceptibility to stresses (Geisler et al., 2020). We also observed an irregular lumen morphology in only a subset of *ifb-2(RNAi)* animals (Figure 3A, S6B). Importantly, loss of *ifb-2* does not result in cytoplasmic invaginations (Figure 3A, S6B). This indicates that the invaginations observed in *bbln-1* mutants are due to an altered IF network state. If this is the case, loss of the IF network should suppress the invaginations in *bbln-1* animals. To test this, we generated a double mutant carrying the *bbln-1(null)* allele and the *ifb-2(kc14)* deletion allele (Geisler et al., 2019), expressing ERM-1::mCherry to mark the membrane. Lumen morphology in the double knockout indeed appeared identical to that seen for IFB-2 depletion alone in *ifb-2(RNAi)* animals (Figs. 3A and S6C) as well as previously published for *ifb-2(kc14)* (Geisler et al., 2020). Thus, *ifb-2(kc14)* suppresses the intestinal defects of *bbln-1(null)* (Figure S6C).

In agreement with the fluorescence microscopy data, we did not observe cytoplasmic invaginations by electron microscopy in *ifb-2(kc14); bbln-1(null)* double mutants (Figure S6D). No endotube was visible, confirming the requirement for IFB-2 in endotube formation. Surprisingly, we did observe occasional small membrane protrusions directed towards the lumen (Figure S6E), which were also visible by light microscopy in both *ifb-2(kc14); bbln-1(null)* (Figure S6F) and *ifb-2(RNAi)* animals (Figure S6Biii). These are therefore likely to be the result of IFB-2 depletion alone. Microvillar actin bundles appeared to cluster together at the neck of these small protrusions, forming fan-like structures. One possibility is that, in the absence of the supporting role of the endotube, microvillar actin bundles become linked together, causing the formation of these small extrusions.

Taken together, our data are consistent with a model in which loss of *bbln-1* leads to an altered, pathogenic IF network state that results in cytoplasmic invaginations.

Bublin is the mammalian ortholog of BBLN-1

In both *C. elegans* and mammals, intestinal IFs function in mechanical support and protection against stresses. While the IF protein families have diverged

between *C. elegans* and mammals (Erber et al., 1998; Weber et al., 1989), it is likely that essential aspects of the regulation of IF networks are conserved. We therefore investigated if BBLN-1 is conserved in mammals. An iterative search using Jackhmmer (Potter et al., 2018) revealed the uncharacterized protein C9orf16 as the only candidate mammalian homolog (E-value 3.8e-16). The 83 aa human C9orf16 protein is predicted to consist of a coiled-coil domain, flanked by intrinsically disordered regions—similar to the predicted structure of BBLN-1 (Figure 7A). The region between amino acids 27 to 102 in BBLN-1 is most similar to C9orf16, with 26% shared amino acid identity and 48% similarity. A reciprocal Jackhmmer search starting with C9orf16 also identified BBLN-1 as the only *C. elegans* homolog (E-value 8.4e-07). We used the DRSC Integrative Ortholog Prediction Tool v7.1 (Hu et al., 2011) to query multiple orthology prediction databases, but only OrthoDB v9 (Zdobnov et al., 2017) identified C9orf16 and BBLN-1 as candidate orthologs. Nevertheless, given the bi-directional best hit in Jackhmmer and the absence of other candidate orthologs, we consider it likely that BBLN-1 and C9orf16 are evolutionary orthologs and we have therefore named the human gene product bublin coiled-coil protein (BBLN).

To investigate if bublin and BBLN-1 are functionally conserved, we generated transgenic animals expressing GFP::bublin in the intestine of *C. elegans* from an extrachromosomal array. Bublin showed apical and perinuclear enrichment, resembling the localization pattern of BBLN-1 when similarly expressed from an extrachromosomal array (Figure 7B). Moreover, as we observed for BBLN-1, the sub-apical localization of bublin was dependent on the presence of an intact IF network (Figure S7A). To determine if bublin can functionally replace BBLN-1, we examined the effects of mosaic GFP::bublin expression in a *bbln-1(null)* background. As expected, *bbln-1(null)* animals not inheriting the transgenic array all showed invaginations from hatching (Figure 7D). In contrast, in mutant animals that did inherit the transgene, cells expressing GFP::bublin did not show invaginations at hatching (Figure 7C, D). As animals developed, invaginations began to form in all cells, and animals became phenotypically indistinguishable from non-transgenic animals by mid-L1 stage. Thus, expression of bublin delays the invagination phenotype in young larvae. Together, these findings indicate that bublin is a functional homolog of BBLN-1.

We next investigated if the association with intermediate filaments is conserved. Keratin 8 (KRT8) is the most common type II keratin IF in simple epithelia, and in enterocytes keratin 8 is part of an apical IF network (Schwarz et al., 2015). As keratin 8 forms functional heterodimers with keratin 18 (KRT18) (Asghar et al., 2015), we investigated if bublin interacts with keratin 8/18 by affinity purification from HEK293T cells. Pull-down analysis from HEK293T cell lysates showed that keratin 8/18 co-purify with bublin (Figure 7E). Additionally, multiple high-throughput studies found bublin as an interactor of the type I intestinal keratin 20 (Luck et al., 2020; Rolland et al., 2014; Rual et al., 2005). Thus, the association with intermediate filaments is conserved between BBLN-1 and bublin.

We also performed mass spectrometry analysis on bublin purified from HEK293T cells. The top scoring hit was V-ATPase subunit D (ATP6V1D), the ortholog of *C.*

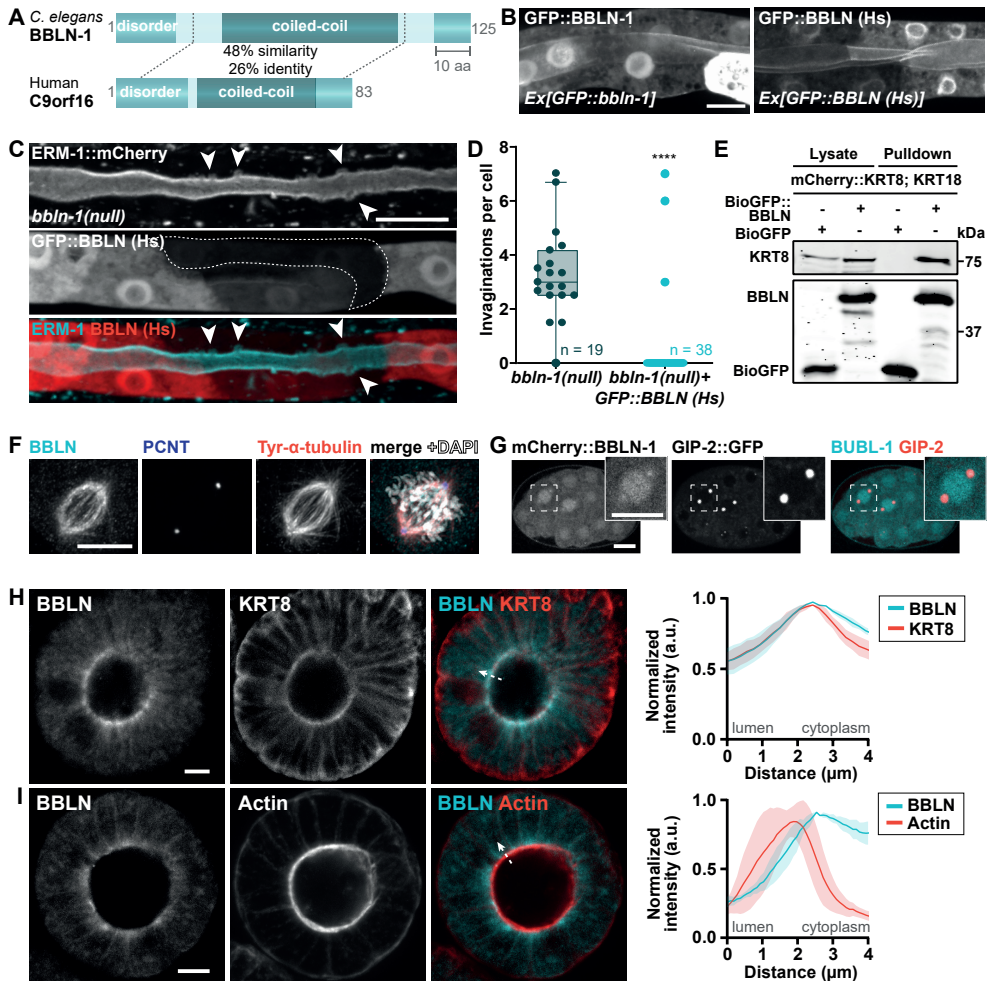


Figure 7. Bublin is the mammalian homologue of BBLN-1. (A) Schematic representation of *C. elegans* BBLN-1 and human C9orf16 proteins with predicted domains. EMBOSS Water analysis calculates 26% identity and 48% similarity over a length of 77 aa. (B) Overexpression of GFP-tagged BBLN-1 and bublin (BBLN (Hs)) in *C. elegans* L3-stage larvae under control of the intestine-specific *vha-6* promoter. All scale bars indicate 10 μ m. (C) Apical membrane morphology visualized by ERM-1::mCherry in a *bbln-1*(null) L1 larva with mosaic expression of GFP tagged bublin (BBLN (Hs)) from an extrachromosomal array. A cell without GFP::BBLN (Hs) expression (dotted outline) displays cytoplasmic invaginations (arrowheads). (D) Quantification of invagination number in *bbln-1*(null) early L1 intestinal cells with or without GFP::BBLN (Hs) expression. Analysis was performed within 4 h of hatching. Each dot corresponds to a single cell (19 cells over 8 animals for control, 38 cells over 16 animals for the rescue). Data are presented as median \pm interquartile range with Tukey whiskers, and data are analyzed with Mann-Whitney test; **** = $P < 0.0001$. (E) Western blots of Biotin pull-down from extracts of HEK293T cells transfected with BirA, mCherry::KRT8, KRT18 and either BioGFP::BBLN or BioGFP alone as control. Blots were probed for keratin 8 (KRT8, top) and GFP (bottom). The input is 10% of the biotin pull-down. (F) Point-scanning confocal microscopy images of HeLa cell stained with antibodies for bublin (BBLN), pericentrin (PCNT) and tyrosinated α -tubulin. (G) Endogenous mCherry::BBLN-1 and GIP-2::GFP distribution

during cell division in the early *C. elegans* embryo. (H, I) Section of mouse small intestinal organoid stained with antibodies against bublin and keratin 8 (KRT8, top) or with phalloidin to visualize actin (bottom). Images were acquired using point-scanning confocal microscopy. Graphs to the right show the fluorescence intensity from lumen to cytoplasm (dotted arrow indicates example). Fluorescent intensity was measured across all cells that are in focus, and displayed as mean \pm SD.

elegans VHA-14 and second highest scoring hit in our BBLN-1 interaction screen (Figure S7B, 4D). We additionally found subunit F of this complex (ATP6V1F), the ortholog of the high-confidence BBLN-1 interactor VHA-9. Thus, the similarity in candidate interactions between BBLN-1 and bublin extends to V-ATPase subunits, further strengthening that bublin is the ortholog of BBLN-1.

Finally, we investigated the subcellular localization of bublin in mammalian cells using a GFP::bublin expression construct and a polyclonal antibody directed against human bublin. We first confirmed specificity of the antibody by immunostaining HeLa cells transfected with a GFP::bublin expression construct. The staining and GFP fluorescence patterns overlapped, demonstrating that the antibody recognizes bublin (Figure S7C). We next stained HeLa cells with antibodies recognizing bublin and keratin 8. However, we did not detect overlap between the bublin and keratin 8 localization patterns (Figure S7D). Thus, whereas *C. elegans* BBLN-1 appears to exclusively co-localize with intermediate filaments, this is not the case for bublin. Interestingly, in dividing HeLa cells, bublin localized to interpolar and kinetochore microtubules, a localization we had not observed for BBLN-1 (Figure 7F). We therefore re-examined the localization of BBLN-1 in *C. elegans* embryonic mitotic cells also expressing the γ -tubulin interacting protein GIP-2::GFP to mark the centrosomes. BBLN-1 was enriched at the interpolar region (Figure 7G), indicating that both BBLN-1 and bublin operate at the mitotic spindle.

HeLa cells do not contain the subapical IF web present in *C. elegans* intestinal cells or in differentiated enterocytes. We reasoned that the lack of co-localization between bublin and Keratin 8 might reflect the absence of this particular IF structure. We therefore examined the localization of bublin in mouse small intestinal organoids, which mimic the normal structure and composition of the intestinal epithelium much more closely than traditional cell cultures. In organoids, bublin showed clear enrichment at the apical domain of intestinal epithelial cells. Bublin localized just below the apical actin network, at the same level as Keratin 8 (Figure 7H, I). Thus, the localization of bublin in mouse intestinal organoids mimics that of BBLN-1 in *C. elegans* intestinal cells. Collectively, the overlap in localization, rescue of phenotype, and similarity in putative interaction partners, suggest that bublin and BBLN-1 have at least partially overlapping functionality.

Discussion

Formation and maintenance of tubular architecture is a complex and dynamic morphogenetic process that relies on apically localized structural components

conserved across animal species. Using an unbiased approach in the animal model *C. elegans* we identified the small protein BBLN-1 as a regulator of tubular architecture of the intestinal epithelium. Loss of BBLN-1 causes bubble-shaped invaginations of the apical plasma membrane into the cytoplasm, characterized by aggregation of IFs into a network of fibers that outline these protrusions. Ultrastructurally, loss of BBLN-1 results in endotube thickening between invaginations and endotube loss at invaginating membrane regions. In contrast to the severe defects in IF organization, actin, cell polarity markers, and cell junctions are largely unaffected. When we were preparing this work for publication, it came to our attention that some similar observations were made in a dissertation that describes the identification of a mutant carrying the same point mutation present in *bbln-1(mib42)* (Paulson, 2009).

We identified C9orf16 as the mammalian ortholog of BBLN-1 based on sequence homology and named it bublin coiled-coil protein (BBLN). When expressed in the intestine of *C. elegans*, the localization pattern of bublin mimicked that of BBLN-1, including the IF-dependent apical localization. Moreover, expression of bublin was able to partially suppress the *bbln-1* phenotype, delaying the appearance of invaginations. Affinity purification and mass spectrometry experiments also showed a strong overlap in candidate interaction partners between BBLN-1 and bublin. Finally, in mouse intestinal organoids we observed localization of bublin to the apical IF network, just below the actin-rich terminal web. All of these observations are consistent with bublin being the ortholog of BBLN-1. Nevertheless, while BBLN-1 seems to strictly co-localize with IFs in *C. elegans*, this is not the case for bublin, as we did not observe co-localization with keratin 8 in HeLa cells. Thus, while bublin may regulate IF organization, its functioning may have diverged between *C. elegans* and mammals.

Multiple observations support that BBLN-1 is a direct regulator of IFs, and that the cytoplasmic invaginations in *bbln-1* mutants are a consequence of a disorganized IF network organization. First, BBLN-1 colocalizes with IFs, in a manner dependent on the presence of an IF network. Multiple IF proteins copurified with BBLN-1 from *C. elegans* lysates, indicating that the localization of BBLN-1 is mediated through physical interactions. Second, phenotypes similar to *bbln-1(null)* have been described for mutants of the IF member *ifd-2*, and for *sma-5*, a regulator of the IF network whose loss causes cytoplasmic invaginations that are strikingly similar to those present in *bbln-1* mutants (Carberry et al., 2012; Geisler et al., 2016, 2020). Finally, and most strikingly, loss of the apical IF network through knockout of *ifb-2* suppressed the *bbln-1* phenotype, demonstrating that the presence of apical IFs is a prerequisite for invagination formation. The most likely explanation is that *bbln-1* causes an altered, pathogenic IF network state that leads to the formation of invaginations into the cytoplasm.

Why a compromised IF network leads to cytoplasmic invaginations is not clear. One explanation is that pressure from the lumen physically forces invaginations through weak spots in the IF network. However, *ifb-2* mutants which lack an apical IF network entirely, have a largely normal intestinal morphology and do not show lumen widening until the L4 stage (Geisler et al., 2020). Possibly

the actin network compensates for the loss of the IF network and delimits luminal widening. The presence of compensatory mechanisms involving actin is supported by the observation that loss of *ifb-2* leads to an increase in apical levels of the actin-bundling protein plastin 1 (PLST-1) (Geisler et al., 2020). Another explanation for the formation of invaginations is that the IF network plays a more direct instructive role in determining the width of the lumen or the surface area of the apical membrane. Such a role has recently been proposed for the excretory canal, where IFs work in conjunction with actin and tubulin to control intracellular lumenogenesis (Khan et al., 2019). Here, IFs are hypothesized to regulate access of membrane formation promoting vesicles to the lumen, to restrain lateral lumen expansion. Defects in apical membrane trafficking in the intestine have been shown to cause ectopic lateral lumen formation (Shafaq-Zadah et al., 2012). Hence, it is possible that the IF network plays a role in apical trafficking in the intestine.

The molecular nature of the change to the IF network in *bbln-1* and the phenotypically very similar *sma-5* mutants also remains to be determined. SMA-5 is a stress-activated MAPK homolog, and its loss results in increased phosphorylation of IFs. Hence it likely exerts an indirect effect on IFs, but relevant downstream targets have not been identified. We therefore considered the possibility that BBLN-1 acts downstream of SMA-5. However, the increased phenotype severity we observed when *sma-5* was depleted in the *bbln-1(null)* background suggests that these genes do not act in a simple linear pathway. The protein sequence of BBLN-1 does not clearly hint at its function, as it lacks functionally distinct domains. Possible roles for BBLN-1 include cross-linking or stabilizing IF filaments, and anchoring of IFs to components of the overlying terminal web. The tendency of invaginations to occur at cell junctions may also indicate a role in linking IFs to cell junctions. However, our FRAP data indicates that BBLN-1 associates dynamically with the IF layer. Hence, the activities of BBLN-1 may be more indirect, for example localizing unidentified regulators to the IF network or promoting post-translational modifications of IF proteins. Our interaction studies identified subunits of V-ATPases as prominent candidate interactors of BBLN-1 and bublin. Whether these interactions are physiologically relevant and if they are involved in IF regulation or other aspects of BBLN-1 function remains to be determined. A final intriguing hypothesis is that BBLN-1 is involved in protein aggregation. Bublin was found in a search for highly heat-resistant proteins that remain soluble upon boiling (Tsuboyama et al., 2020). The identified proteins, termed 'Hero' for heat-resistant obscure proteins, were shown to protect different subsets of proteins from aggregation or denaturation under stress conditions (Tsuboyama et al., 2020). Indeed, bublin is differentially expressed in diseases characterized by protein aggregation, including amyotrophic lateral sclerosis (ALS) (Nijssen et al., 2018), Alzheimer's (Kong et al., 2009), and Parkinson's disease (Kim et al., 2020b). As the loss of BBLN-1 leads to IF aggregation, a potential future avenue of investigation is to examine if BBLN-1 plays a direct role in protecting against protein aggregation.

In summary, we identified a conserved regulator of IF organization, whose

functioning highlights the importance of IF network integrity in maintaining regular lumen shape. While our study has focused on the role of BBLN-1 in organization of the apical IF network of intestinal cells, it is likely that BBLN-1 plays additional roles in different tissues and processes. The BBLN-1 localization pattern in other tissues strongly resembled that of IFs, and the sub-apical localization of BBLN-1 in the excretory canals depended on IFC-2. Thus, BBLN-1 may be a broad regulator of IF organization in *C. elegans*.

Methods

Data and code availability

The mass spectrometry proteomics data have been deposited to the ProteomeXchange Consortium via the PRIDE partner repository⁶⁰ with the dataset identifier PXD024387.

Caenorhabditis elegans strains and culture conditions

Caenorhabditis elegans strains were cultured on standard nematode growth medium (NGM) agar plates at 15 or 20 °C and fed with *Escherichia coli* OP50 (Brenner, 1974). Table S1 contains a list of all the strains used. Transgenic lines were generated by injecting 15 ng/μl of either plasmid pSMR10 or pSMR30 together with 65 ng/μl lambda DNA (Thermo Scientific) into the gonads of young adults.

Cell line culture

HeLa and HEK293T cell lines were cultured in DMEM/Ham's F10 (50:50) supplemented with 10% FCS and 1% penicillin/streptomycin at 37 °C and 5% CO₂. All cell lines routinely tested negative for mycoplasma.

Organoid culture

Mouse small intestinal organoids derived from the duodenum of C57BL/6 mice were cultured in ENR medium: Advanced DMEM/F12 (Invitrogen) with 1% Penicillin/Streptomycin (P/S, Lonza), 1% Hepes buffer (Invitrogen) and 1% Glutamax (Invitrogen), supplemented with 5% R-spondin conditioned medium, 10% Noggin conditioned medium, 50 ng/ml EGF (Invitrogen), 1x B27 (Invitrogen), 1.25 mM n-Acetyl Cysteine (Sigma-Aldrich).

Isolation and initial mapping of *mib41* and *mib42*

L4 stage *erm-1::GFP* animals were incubated for 6 hours at room temperature (RT) in M9 buffer (0.22 M KH₂PO₄, 0.42 M Na₂HPO₄, 0.85 M NaCl, 0.001 M MgSO₄) supplemented with 50 mM ethyl methanesulfonate (EMS), in a 15 ml tube with gentle rotation. Mutagenized L4 animals were placed on 9 cm NGM agar plates seeded with *E. coli* (35 plates, 10 animals per plate) and allowed to lay eggs. Parents were removed after ~1000 F1 progeny had been produced. Three days after F1 progeny started egg-laying, all F1 adults and L2 larvae were washed off the plate, leaving behind a semi-synchronous population of F2 embryos. F2 animals were allowed to develop for 2–4 days at 20 °C and scored for intestinal

morphology defects using a Leica MZ16 fluorescence stereoscope. Two mutants, *mib41* and *mib42*, were isolated and backcrossed with N2 males 3 times before further analysis. To identify an approximate genetic location for both mutations, single-nucleotide polymorphism (SNP) mapping using the polymorphic strain CB4856 was performed as described previously (Davis et al., 2005).

Genomic DNA purification

C. elegans lysis and genomic DNA purification were performed using the DNeasy Blood and Tissue kit (Qiagen). Animals from two recently starved populations were collected, pooled, washed twice using M9, and resuspended in 400 μ l of lysis (ATL) buffer. Samples were then flash-frozen in liquid nitrogen and stored overnight at -80 °C. After three rounds of liquid nitrogen freeze-thawing, proteinase K was added to a final concentration of 2 mg/ml and samples were incubated for 3 hours at 56 °C while shaking at 600 rpm. Samples were further incubated with 2 mg/ml RNase A for 30 min at RT and for 10 min at 56 °C after addition of 400 μ l of AL buffer. Finally, samples were mixed with 400 μ l of 100% ethanol and loaded into purification columns. Wash and elution steps were performed according to the manufacturer's instructions. Concentration of genomic DNA samples was measured using Qubit Fluorometric Quantification (Invitrogen).

Identification of *mib41* and *mib42* mutations

We used the sibling subtraction method to identify the causative *mib41* and *mib42* mutations by whole-genome sequencing (WGS) (Joseph et al., 2018). From heterozygous *erm-1::GFP/+; mib41/+* or *erm-1::GFP/+; mib42/+* hermaphrodites we isolated homozygous *mib41* or *mib42* mutant, homozygous nonmutant, or heterozygous F2 progeny. Genomic DNA was then purified from pooled F3 progeny derived from 12–16 F2 animals and sequenced on an Illumina HiSeq X Ten platform. Candidate causative variants were defined as present at a frequency >0.8 in the homozygous mutant sample, <0.8 in the heterozygous sample, and <0.1 in the homozygous wild-type sample. For both mutant alleles, only a single variant from the resulting selection was predicted to affect a protein coding sequence, which was selected for further analysis. See Supplemental methods for a complete description of the bioinformatics pipeline to identify variants.

Protein structure and domain predictions

General protein domain searches were done using the SMART service at <http://smart.embl-heidelberg.de/>. Coiled-coils predictions were done using DeepCoil at <https://toolkit.tuebingen.mpg.de/#/tools/deepcoil>. Disorder predictions were done using DisEMBL at <http://dis.embl.de/>. Default settings were used.

Phylogenetic analysis

To identify proteins related to C15C7.5/BBLN-1, we performed a three-iteration HMMER search against the Reference Proteomes dataset at <http://www.ebi.ac.uk/Tools/hmmer/>.

Molecular cloning

SapTrap assembly was done as described (Schwartz and Jorgensen, 2016) using existing SEC donor modules (Dickinson et al., 2018) or new donor modules generated by cloning PCR fragments or custom gBlocks (IDT) into Eco53kI-digested vector pHSG298 (Takara Biosciences). For the *Pvha-6::GFP::bbln-1::tbb-2 3'UTR* and *Pvha-6::GFP::bublin (Hs)::tbb-2 3'UTR* rescue constructs, *Pvha-6* was amplified from genomic N2 DNA, *GFP* and the *tbb-2 3'UTR* were amplified from prior plasmids, and the *bbln-1* and *bublin* sequences were synthesized as gBlocks (IDT). *GFP* sequence is codon-optimized and contains 3 artificial introns. A list of all used plasmids are listed in Table S1 and used oligonucleotides (IDT) and gBlocks (IDT) is included in Table S2. PCR fragments were generated using Q5 Hot Start High-Fidelity DNA Polymerase (New England Biolabs) and gel purified using the Nucleospin kit (Machery-Nagel). DNA concentrations were measured using a BioPhotometer D30 (Eppendorf). All DNA vectors used for genome editing were purified from DH5 α *E. coli* using a Qiagen midiprep kit. Annotated DNA files of all plasmids used are available for download online (Remmelzwaal et al., 2021).

CRISPR/Cas9 genome engineering

Endogenous gene fusions were generated in an N2 background by homology-directed repair of CRISPR/Cas9-induced DNA double-strand breaks (DSBs). Microinjection of young adult hermaphrodite germlines was done using an inverted microinjection setup (Eppendorf FemtoJet 4x mounted on a Zeiss Axio Observer A.1 equipped with an Eppendorf Transferman 4r). In cases where the sgRNA target site was not disrupted by sequence integration, silent mutations were incorporated to prevent repeated DNA cleavage. In all cases correct integration was confirmed by Sanger sequencing (Macrogen). A list of all DNA- and RNA-based reagents is included as Table S2.

erm-1::mCherry was generated using the SEC method, using a plasmid-based repair template. sgRNA expression plasmids were generated by ligating annealed oligo pairs into BbsI-digested pJJR50 as previously described (Waijers et al., 2016). The repair template was assembled into pMLS257 (Addgene #73716) using SapTrap with custom and SEC modules as follows (from 5' to 3'): left homology arm, a C-terminal linker (pMLS287), mCherry, SEC (pDD363), auxin-inducible degron (AID; pDD398), and right homology arm. Homology arms of ~600 bp upstream and downstream of the DSB were amplified from N2 genomic DNA. The injection mix contained: 60 ng/ μ l *Peft-3::Cas9* (Addgene #46168), 15 ng/ μ l repair template, 100 ng/ μ l for each sgRNA, and 2.5 ng/ μ l *Pmyo-2::mCherry* (Addgene #19327). Three injected animals were pooled and incubated for 3 days at 20 °C before adding 250 ng/ μ l of hygromycin per plate. Rol animals lacking visible mCherry expression were selected after 4–5 days. To eliminate the selection cassette through Cre-Lox recombination, L1 progeny of selected homozygous Rol animals were heat-shocked in a water bath at 34 °C for 1 hour. Correct excision was confirmed by selection of non-Rol animals and subsequent Sanger sequencing. Sequence files of the final gene fusions are included in Document S2: DNA_files.zip (Remmelzwaal et al., 2021).

The *bbln-1(mib70)*, *GFP::bbln-1*, and *ifb-2::mCherry* alleles were generated using the plasmid-free nested-CRISPR approach (Vicencio et al., 2019). Injection mixes contained the following reagents (IDT): 250 ng/μl Alt-R S.p. Cas9 Nuclease V3 (IDT), 2 μM step 1 ssODN repair template, 400 ng/μl step 2 PCR repair template, 4.5-5 μM step 1 and step 2 crRNAs, 10 μM tracrRNA, as well as 1 μM *dpy-10* crRNA and ssODN repair for co-CRISPR selection (Arribere et al., 2014). Reagents for *dpy-10* co-CRISPR selection were omitted in *ifb-2::mCherry* injection mixes, and for *bbln-1(mib70)* only step 1 editing events were selected. To select for integration events, injected animals were transferred to individual plates and allowed to recover at 20 °C overnight before incubation at 25 °C for 2–3 days. F1 animals were either visually screened for presence of fluorescence using a Leica MZ16 fluorescence stereomicroscope, or singled from plates with high numbers of Dpy and Rol animals followed by PCR screening.

All other strains were produced using a plasmid-free protocol incorporating melting of double stranded DNA (dsDNA) repair templates (Ghanta and Mello, 2020). Selection of positive editing events was done by visually screening for expression of fluorescent protein, or by PCR analysis of single animals from plates with high numbers of Rol animals.

Light microscopy

Imaging of *C. elegans* was done by mounting embryos or larvae on a 5% agarose pad in a 10 mM Tetramisole solution in M9 buffer to induce paralysis. Spinning disk confocal imaging was performed using a Nikon Ti-U microscope equipped with a Yokogawa CSU-X1-M1 confocal head and an Andor iXon DU-885 camera, using a 60x 1.4 NA objective. Time-lapse imaging for FRAP experiments was performed on a Nikon Eclipse-Ti microscope equipped with a Yokogawa CSU-X1-A1 spinning disk and a Photometrics Evolve 512 EMCCD camera, using a 100x 1.4 NA objective. Targeted photobleaching was done using an ILas system (Roper Scientific France/ PICT-IBiSA, Institut Curie). Point-scanning confocal microscopy was done on a Zeiss AiryScan LSM 880 setup using a Plan-Apochromat 63x 1.2 NA objective. *bublin* antibody test was imaged on an upright fluorescence Nikon Eclipse Ni-U microscope using a Plan Apo Lambda 100x N.A. 1.45 oil objective. Confocal imaging for keratin 8 and *bublin* in HeLa cells was performed with Leica TCS SP8 STED 3X microscope using HC PL APO 100x/1.4 oil STED WHITE objective driven by LAS X controlling software. Microscopy data was acquired using MetaMorph Microscopy Automation & Image Analysis Software (Spinning Disk), and Zen Black software (AiryScan). All stacks along the z-axis were obtained at 0.25 μm intervals. For quantifications, the same laser power and exposure times were used within experiments.

Texas Red-dextran assay

Mixed-stage populations were collected in egg buffer (118 mM NaCl, 48 mM KCl, 2 mM MgCl₂, 2 mM CaCl₂, 25 mM HEPES pH 7.3) and washed three times. The worm pellet was concentrated and resuspended in a solution containing 1 mg/ml Texas Red-dextran (40,000 MW, D1829, Molecular Probes). The samples were incubated for 90 min while shaking at 300 rpm in the dark. The dye in

solution was removed by washing the samples with egg buffer until the solution was clear, and animals were either imaged directly or transferred to standard culture plates for 1 hour prior to imaging. Animals were paralyzed in 10 mM Tetramisole, transferred to a 5 % agarose pad on a glass slide, and imaged by spinning disk confocal microscopy.

FRAP experiments and analysis

For FRAP assays, laser power was adjusted in each experiment to avoid complete photobleaching of the selected area. Photobleaching was performed on a circular region with a diameter of 30 or 40 px (respectively 3.33 or 4.44 μm) at the cortex, and recovery was followed at 5 second intervals for 15 minutes. Time-lapse movies were analyzed in ImageJ. The size of the area for FRAP analysis was defined by the full width at half-maximum of an intensity plot across the bleached region in the first post-bleach frame. For each time-lapse frame, the mean intensity value within the bleached region was determined, and the background, defined as the mean intensity of a non-bleached region outside the animal, was subtracted. The mean intensities within the bleached region were corrected for acquisition photobleaching per frame using the background-subtracted mean intensity of a similar non-bleached region at the cortex, which was normalized to the corresponding pre-bleach mean intensity. FRAP recovery was calculated as the change in corrected intensity values within the bleached region. The first frame after bleach was defined as 0, and the mean intensity of the 10 frames before bleach as 1.

Curve fitting was done using GraphPad Prism 8, on averaged recovery data per sample using non-linear regression analysis (least squares regression). One and two-phase association were tested and, in all cases, data were best fitted with a two-phase curve.

Feeding RNAi

RNAi clones for *bbln-1*, *ifb-2*, *ifc-2*, *ifd-2* and *let-413* were obtained from the genome wide Vidal full-length HT115 RNAi feeding library derived from the ORFeome 3.1 collection (Rual et al., 2004). The RNAi clone for *ifc-1* was obtained from the genome wide Ahringer fragment HT115 RNAi feeding library (Kamath et al., 2003), supplied through Source BioScience. All clones were verified using Sanger sequencing. RNAi clones for *ifo-1*, *ifd-1*, *ifp-1* and *sma-5* were generated by subcloning the corresponding cDNA into a modified L4440 RNAi feeding vector, containing a linker with *Ascl* and *NotI* restriction sites. To specifically target *act-5*, and no other actin isoforms that share extensive sequence homology, we followed a previously described strategy and designed an RNAi clone against the unique 3'UTR (MacQueen et al., 2005). For all custom RNAi clones, fragments were amplified from a cDNA library, digested with *Ascl*/*NotI*, ligated into *Ascl*/*NotI*-digested L4440, and transformed into *E. coli* DH5a. Single colonies were isolated, plasmid DNA was purified, and presence of an insert was confirmed by Sanger sequencing. Correct clones were re-transformed into *E. coli* HT115, again confirmed by sequencing and stored at -80 °C in 50% glycerol (1:1). All primer pairs are listed in Table S2.

For feeding RNAi experiments, bacterial clones were pre-cultured in 2 ml Lysogeny Broth (LB) supplemented with 100 µg/ml ampicillin and 2.5 µg/ml tetracycline at 37 °C while rotating at 200 rpm for 6–8 hours, and then transferred to new tubes with a total volume of 10 mL and cultured overnight. An HT115 bacterial clone expressing the L4440 vector lacking an insert was used as a control in feeding experiments. To induce production of dsRNA, cultures were incubated for 90 min in the presence of 1 mM Isopropyl β-D-1-thiogalactopyranoside (IPTG). Bacterial cultures were pelleted by centrifugation at 3220 g for 15 min and concentrated 5x. NGM agar plates supplemented with 100 µg/ml ampicillin and 1 mM IPTG were seeded with 250 µl of bacterial suspension, and kept at room temperature for 48 hour in the dark. L1 or L4 hermaphrodites were placed on the seeded RNAi plates and incubated at 20 °C (Timmons and Fire, 1998).

Electron microscopy

Young adult animals were transferred into a 100 µm deep membrane carrier containing 20% bovine serum albumin in M9 worm buffer (22 mM KH₂PO₄, 42 mM Na₂HPO₄, 86 mM NaCl, 1 mM MgSO₄) and then high-pressure frozen in a Leica EM Pact high-pressure freezer. A minimum of five samples with 10-20 animals were frozen per experiment. Quick freeze substitution with agitation using 1% OsO₄, 0.2% uranyl acetate in acetone followed by rapid epoxy resin embedding was performed as previously described (McDonald, 2014; Reipert et al., 2018). Subsequently, 50 nm thick sections of the embedded samples were prepared using a Leica UC7. These were contrasted for 10 min in 1% uranyl acetate in ethanol and Reynolds lead citrate and recorded at 100 kV on a Hitachi H-7600 transmission electron microscope (Tokyo, Japan).

Auxin Inducible Degradation

Auxin treatment was performed by transferring worms to NGM plates seeded with *E. coli* OP50 and containing 1 mM auxin. To prepare plates, auxin (Alfa Aesar A10556) was added to the autoclaved NGM agar medium after cooling to 60 °C prior to plate pouring. Plates were kept for a maximum of 2 weeks in the dark at 4 °C. 40 adults were placed on NGM plates seeded with *E. coli* OP50 and allowed to lay eggs. After 1 hour of egg laying, plates were washed with M9 (0.22 M KH₂PO₄, 0.42 M Na₂HPO₄, 0.85 M NaCl, 0.001 M MgSO₄) buffer to remove larvae and adults. For the auxin withdrawal experiments, additional synchronization was performed by washing the plates with M9 again after 1 h, to collect larvae hatched within that time span.

Affinity-purification and mass spectrometry analysis

GFP pull-down from C. elegans - Animals endogenously expressing GFP-tagged BBLN-1 or control animals expressing an integrated GFP transgene (Waaaijers et al., 2016) were grown on 6–8 9 cm NGM plates until starvation, to enrich for L1 animals. Animals were then transferred into 250 ml of S-Medium supplemented with 1% Penn/Strep (Life Technologies), 0.1% nystatin (Sigma) and OP50 bacteria obtained from the growth of a 400 ml culture. Animals were grown at 20 °C at low shaking for 96 hours and were harvested and cleaned using a sucrose gradient, as previously described (Waaaijers et al., 2016) with one exception being

the inclusion of MgSO_4 in the M9 medium. Worms were distributed into 15 ml TPX tubes (Diagenode) to reach 200–400 μl worm pellet per tube and were washed with lysis buffer (25mM Tris-HCl pH 7.5, 150mM NaCl, 1mM EDTA, 0.5% IGEPAL CA-630, 1X cOmplete Protease Inhibitor Cocktail (Roche)). The liquid was removed, and the sample was flash frozen in liquid nitrogen for storage at -80°C .

To lyse the worms, tubes were thawed on ice and ice-cold lysis buffer was added to reach a total volume of 2 ml. Tubes were sonicated for 10 mins (sonication cycle: 30 sec ON, 30 sec OFF) at 4°C in a Bioruptor ultrasonication bath (Diagenode) at high energy setting. After lysis, lysates were cleared by centrifugation and protein levels were measured using the Bradford BCA assay (Thermo Scientific).

Immunoprecipitation was performed using GFP-Trap Magnetic Agarose beads (Chromotek) according to manufacturer's protocol, using 25 μl of beads per sample. To prep the beads, they were first equilibrated in wash buffer (10 mM Tris/Cl pH 7.5, 150 mM NaCl, 0.5 mM EDTA, 0.1% IGEPAL CA-630), blocked with 1% BSA for 1 hour, then washed 4 times with wash buffer. Next, lysate was added to the beads and they were incubated for 1 hour tumbling end-over-end. Lysate was then removed, and the beads were washed 4 times in wash buffer. After the final wash step, all liquid was removed, and the beads were flash frozen with liquid nitrogen. The experiment was performed in triplicate (biological replicates) and processed on independent days.

Biotin-streptavidin pull-down from cells - Confluent HEK293T cells were split in a 1:3 dilution 24 hours before transfection. Cells were transfected with overexpression constructs indicated in figure legend together with BirA. 1 $\mu\text{g}/\mu\text{L}$ PEI (Polyethylenimine HCl MAX Linear MW 40000 (PolySciences, 24765-2)) and 1 $\mu\text{g}/\mu\text{L}$ DNA (3:1) were mixed in Ham's F10 and incubated for 5 minutes at room temperature. The mixture was added to cells and incubated for 24 hours to allow expression. The cells were harvested in ice-cold PBS and lysed with lysis buffer (150 mM Tris-HCl pH 7.5, 150 mM NaCl, 1% Triton X-100 and cOmplete protease inhibitor cocktail (Roche)). 90% of each cell lysate was centrifuged at 13,000 rpm for 5 minutes and the supernatants were transferred and incubated with streptavidin beads (Dynabeads M-280, Invitrogen), which were already blocked by 0.2% Chicken Egg Albumine (Sigma). The remaining cell lysates were denatured with SDS/DTT sample buffer and used as input sample. Beads were incubated for 40 minutes at 4°C , before washing 5 times with washing buffer (100mM Tris pH7.5, 150 mM NaCl, 0.5% Triton X-100 and 0.5x protease inhibitor cocktail).

Western blot analysis for bublin/keratin pull-down - For western blot assays, pull-down samples were eluted with SDS/DTT sample buffer and boiled for 5 min at 95°C . Both pull-down and input were loaded into 10% SDS-PAGE gels and transferred to nitrocellulose membrane. Membranes were blocked with 2% BSA (bovine serum albumin) in PBS/0.05% Tween-20. Primary antibodies were diluted in blocking buffer and incubated with the membranes overnight at 4°C , washed 3 times with PBS/0.05% Tween-20 and incubated with IRDye 680LT

and IRDye 800CW antibodies (LI-COR Biosciences) for 45 min at RT. Membranes were washed 3 times with PBS/0.05% Tween-20 before imaging on an Odyssey Infrared Imaging system (LI-COR Biosciences).

Mass spectrometry analysis for BBLN-1/bublin - Streptavidin and anti-GFP beads after affinity purification were resuspended in 15 μ l of 4 \times Laemmli sample buffer (Biorad), boiled at 99 $^{\circ}$ C for 10 min and supernatants were loaded on 4–12% Criterion XT Bis-Tris precast gel (Biorad). The gel was fixed with 40% methanol and 10% acetic acid and then stained for 1 hour using colloidal coomassie dye G-250 (Gel Code Blue Stain, Thermo Scientific). Each lane from the gel was cut and placed in 1.5 ml tubes. Samples were then washed with 250 μ l of water, followed by 15 min dehydration in acetonitrile. Proteins were reduced (10mM DTT, 1 hour at 56 $^{\circ}$ C), dehydrated and alkylated (55mM iodoacetamide, 1 hour in the dark). After two rounds of dehydration, trypsin was added to the samples and incubated overnight at 37 $^{\circ}$ C. Peptides were extracted with acetonitrile, dried down and reconstituted in 10% formic acid prior to MS analysis.

Samples were analyzed on an Orbitrap Q-Exactive mass spectrometer (Thermo Fisher Scientific) coupled to an Agilent 1290 Infinity LC (Agilent Technologies). Peptides were loaded onto a trap column (Reprosil pur C18, Dr. Maisch, 100 μ m \times 2 cm, 3 μ m; constructed in-house) with solvent A (0.1% formic acid in water) at a maximum pressure of 800 bar and chromatographically separated over the analytical column (Poroshell 120 EC C18, Agilent Technologies, 100 μ m \times 50 cm, 2.7 μ m) using 90 min linear gradient from 7% to 30% solvent B (0.1% formic acid in acetonitrile) at a flow rate of 150 nl min⁻¹. The mass spectrometers were used in a data-dependent mode, which automatically switched between MS and MS/MS. After a survey scan from 375 to 1600m/z the 10 most abundant peptides were subjected to HCD fragmentation. MS spectra were acquired with a resolution > 30,000, whereas MS2 with a resolution > 17,500.

Raw data files were converted to mgf files using Proteome Discoverer 1.4 software (Thermo Fisher Scientific). Database search was performed using the *C. elegans* or the human database and Mascot (version 2.5.1, Matrix Science, UK) as the search engine. Carbamidomethylation of cysteines was set as a fixed modification and oxidation of methionine was set as a variable modification. Trypsin was set as cleavage specificity, allowing a maximum of two missed cleavages. Data filtering was performed using a percolator, resulting in 1% false discovery rate (FDR). Additional filters were search engine rank 1 and mascot ion score > 20.

Crapome (Mellacheruvu et al., 2013) was used to analyze BBLN-1 interacting proteins in three biological replicas and bublin binding proteins in a single experiment, using proteins identified in the GFP pull downs as control. Significance analysis of interactome (SAINT) score (Choi et al., 2011) and simpler fold-change (FC) calculations FC-A and FC-B were derived from the Crapome analysis by averaging the spectral counts across the controls. FC-A averages the counts across all controls while the more stringent FC-B takes the average of the top 3 highest spectral counts for the abundance estimate.

Antibodies and Immunofluorescence Cell Staining

We used rabbit polyclonal antibodies against bublin (Sigma-Aldrich Cat# HPA020725, RRID:AB_1845816), mouse monoclonal antibodies against PCNT (Abcam Cat# ab28144, RRID:AB_2160664), and rat monoclonal antibodies against tyrosinated α -tubulin (YL1/2; Thermo Fisher Scientific Cat# MA1-80017, RRID:AB_2210201) and KRT8 (DSHB Cat# TROMA-I, RRID:AB_531826). We used Alexa Fluor 568-conjugated Phalloidin to stain actin (Life Technologies). We used Alexa Fluor 488-, 594- and 647-conjugated goat antibodies against respectively mouse, rabbit and rat (Life Technologies) as secondary antibodies.

HeLa cells were fixed with -20°C methanol or 4% PFA for 10 min and permeabilized with 0.1% Triton X-100 in phosphate-buffered saline (PBS) for 10 min. Subsequent washing and labeling steps were carried out in PBS supplemented with 2% bovine serum albumin and 0.05% Tween-20. Slides were rinsed in 70 and 100% ethanol and mounted in Vectashield mounting medium supplemented with DAPI (Vector Laboratories).

Mouse small intestinal organoids were fixed in suspension using ice-cold 4% PFA (Aurion) and immunolabeled as described previously (van Ineveld et al., 2020).

Image analysis

Invagination numbers in *bbln-1(null)* animals were counted manually from intestinal rings int2 to int4, using Z-stacks that span the entire intestinal lumen. Invagination widths were measured by determining the full width at half-maximum of an intensity plot drawn across the center of the invagination in an orthogonal view. Corresponding cell lengths were quantified by drawing a spline through the lumen from lateral membrane to lateral membrane. Intensity distribution profiles of fluorescent proteins at the apical domains of the intestine or organoids were obtained by performing a 40-pixel (4.7 μm) wide line-scan perpendicular to the apical membrane. GFP::BBLN-1 intensity at the apical domain was determined by taking the maximum intensity value of a 40-pixel wide line-scan perpendicular to the apical membrane, and subtracting the mean background intensity (measured in a 40-pixel diameter circle outside of the worm). Each data point shown represents the average of 6–8 measurements per animal. All images were analyzed and processed using ImageJ alone (spinning disk) or in combination with Zen Black software (Airyscan).

Quantification of brood size and lethality

Starting at the L4 stage, individual P0 animals were cultured at 20°C and transferred to a fresh plate every 24 hours for 6 days. Hatched and unhatched progeny were scored 24 hours after removal of the P0, and larval lethality was scored 48 hours after removal of the P0.

Statistical analysis

All statistical analyses were performed using GraphPad Prism 8. For population comparisons, a D'Agostino & Pearson test of normality was first performed to determine if the data was sampled from a Gaussian distribution. For data drawn

from a Gaussian distribution, comparisons between two populations were done using an unpaired t-test, with Welch's correction if the SDs of the populations differ significantly, and comparisons between >2 populations were done using a one-way ANOVA if the SDs of the populations differ significantly. For data not drawn from a Gaussian distribution, a non-parametric test was used (Mann-Whitney for 2 populations and Kruskal-Wallis for >2 populations). ANOVA and non-parametric tests were followed up with multiple comparison tests of significance (Dunnett's, Tukey's, Dunnett's T3 or Dunn's). Tests of significance used and sample sizes are indicated in the figure legends. No statistical method was used to pre-determine sample sizes. No samples or animals were excluded from analysis. The experiments were not randomized, and the investigators were not blinded to allocation during experiments and outcome assessment.

Acknowledgments

We thank R. Schmidt for sharing strain BOX459, V. Garcia Castiglioni for strains BOX251 and BOX260, K. Oegema for strain OD2509, J. Sepers for the NRFL-1::mCherry fusion, and B. van der Vaart for the keratin plasmids. We thank M. Kersten, J.-P. ten Klooster, W. Nijenhuis, and N. Schwarz for technical assistance. We thank S. van den Heuvel, S. Ruijtenberg, M. Harterink, B. Mulder, B. Snel and members of the Van den Heuvel and Boxem groups for helpful discussions. We also thank WormBase, the HUGO Gene Nomenclature Committee (HGNC), and the Biology Imaging Center, Faculty of Sciences, Department of Biology, Utrecht University. Some strains were provided by the Caenorhabditis Genetics Center, which is funded by NIH Office of Research Infrastructure Programs (P40 OD010440). This work was supported by the Netherlands Organization for Scientific Research (NWO)-CW ECHO 711.014.005 and NWO-VICI 016.VICI.170.165 grants to M. Boxem, the German Research Council (LE566/14-1, 3; R. Leube), the START Program of the Medical Faculty of RWTH Aachen University (131/20). This research was part of the Netherlands X-omics Initiative and partially funded by NWO, project 184.034.019.

Supplemental Information

Figures S1–S7, Table S1, Table S2, Supplemental methods.

DNA files: Methods_S1.zip (Remmelzwaal et al., 2021)

Video S1 (Remmelzwaal et al., 2021)

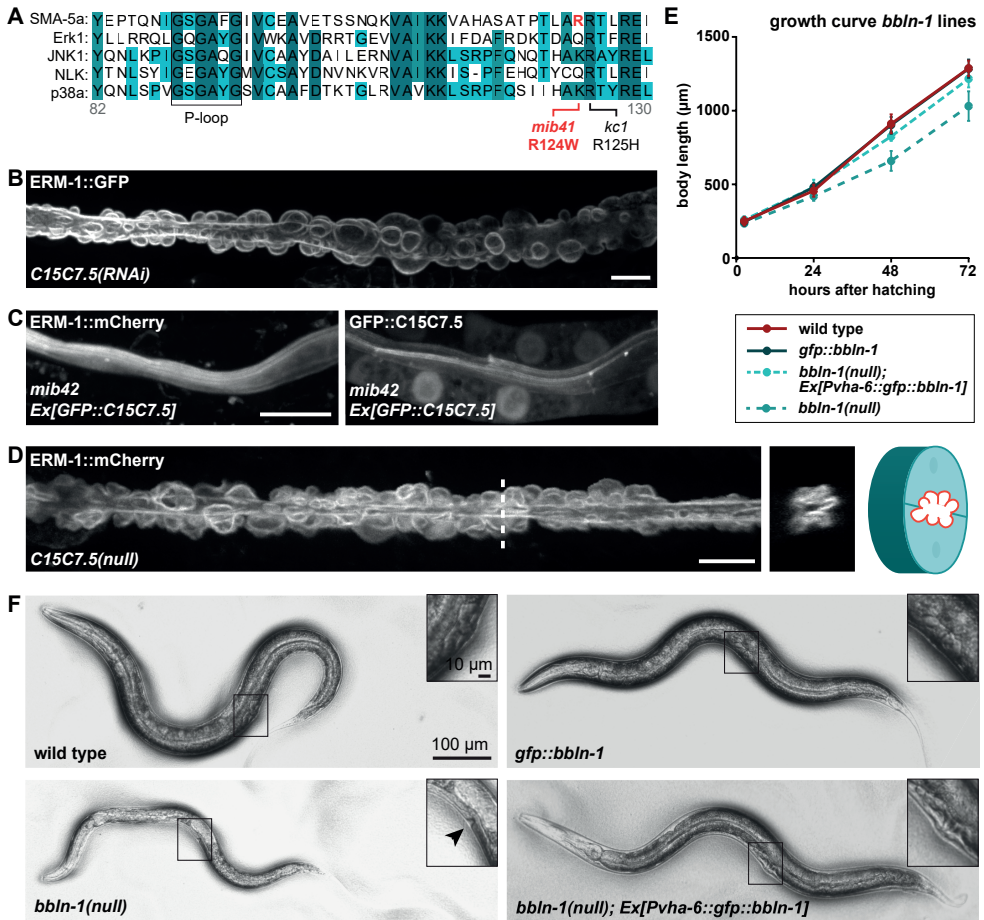


Figure S1. Loss of *bbln-1* causes intestinal cytoplasmic invaginations and developmental delay. (A) Partial sequence alignment of the kinase domain of SMA-5 and human MAPK family kinases. The boxed region corresponds to the conserved phosphate-binding loop (P-loop). The positions of *mib41* (red) and *kc1* (black) mutations are indicated below. (B) L3 *C15C7.5(RNAi)* larva expressing an *erm-1::GFP* knock-in. (C) *mib42* L3 larva expressing an *erm-1::mCherry* knock-in and a *GFP::C15C7.5* transgene driven by the intestine-specific *vha-6* promoter. (D) Intestinal apical membrane morphology in a *C15C7.5(null)* L4 animal visualized with an endogenous *ERM-1::mCherry* reporter. Dotted line in left panel indicates position of cross-section view. Schematic depicts cross-section with apical membrane in red. (E) Growth curves of lines of indicated genotypes. Data are presented as mean \pm SD. $n = 9$ for *bbln-1(null)* and 10 for the other strains. Data at 72 hour timepoint are analyzed with Welch's ANOVA followed by Dunnett's multiple comparisons test for each condition compared to wild type: *gfp::bbln-1* $P = 0.9995$, *bbln-1(null)* $P < 0.0001$, *bbln-1(null)*+*EX[Pvha-6::gfp::bbln-1]* $P = 0.0310$. (F) Example brightfield microscopy images of animals analyzed in (E) at the 48-hour timepoint. Inset depicts boxed region of the vulva area. Arrowhead indicates early L4 vulval invagination in *bbln-1(null)*, indicative of developmental delay (compare with adult vulva structure in other genotypes).

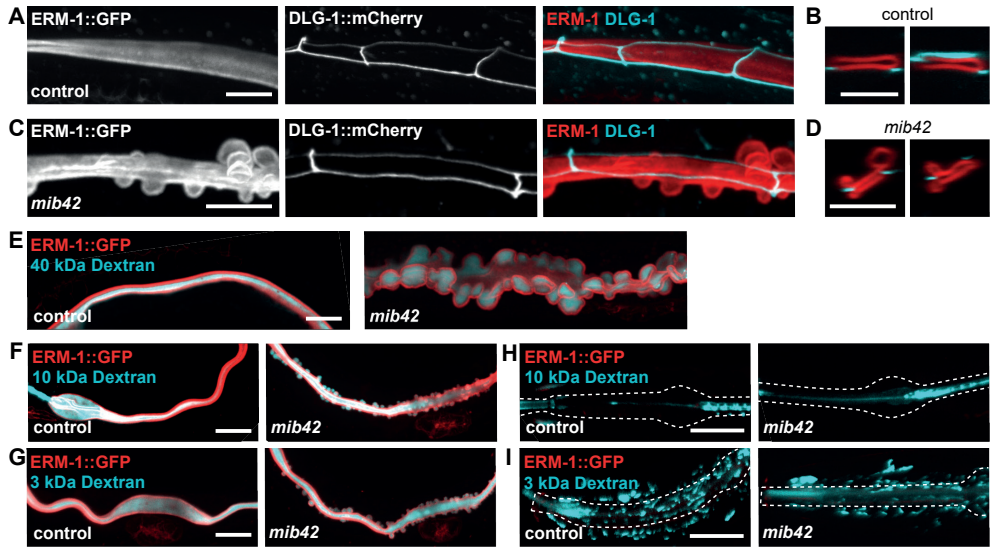


Figure S2. *bln-1(mib42)* induced invaginations preferentially occur at cell junctions and are contiguous with the lumen. (A–D) Organization of the *C. elegans* apical junctions (CeAJs) in intestinal cells of control (A, B) and *mib42* mutant animals (C, D), visualized by an endogenous DLG-1::mCherry reporter in larvae in which the apical membrane is labelled by ERM-1::GFP. (E) Feeding of 40 kDa Dextran-Texas Red to L3 animals expressing ERM-1::GFP indicates invaginations are contiguous with the lumen. (F–I) Feeding of 10 kDa and 3 kDa Dextran-Texas Red to L2 animals expressing ERM-1::GFP to assess intestinal (F, G) and pharyngeal (H, I) epithelium integrity.

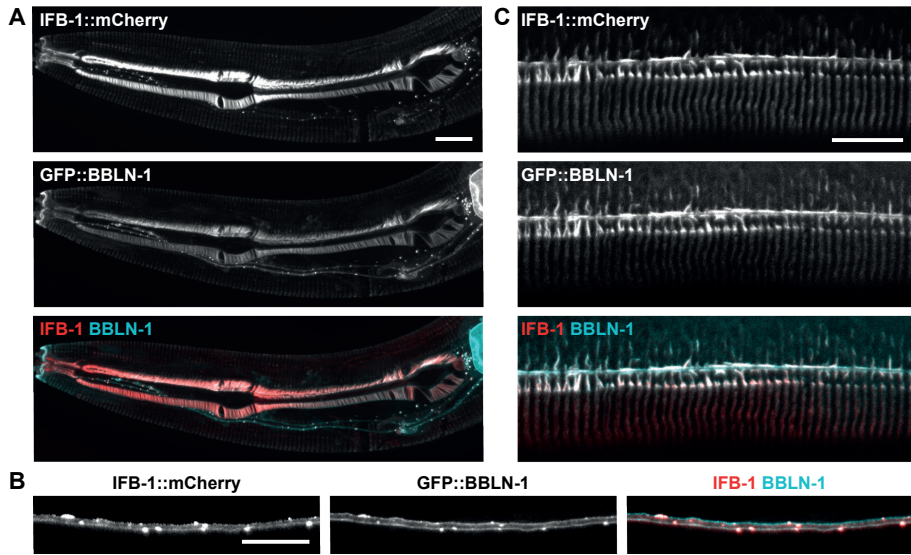


Figure S3. BBLN-1 colocalizes with non-intestinal intermediate filaments.
 (A-C) Dual color imaging of L3/L4-stage animals expressing IFB-1::mCherry and GFP::BBLN-1.
 A: pharynx, B: excretory canal, C: hypodermis.

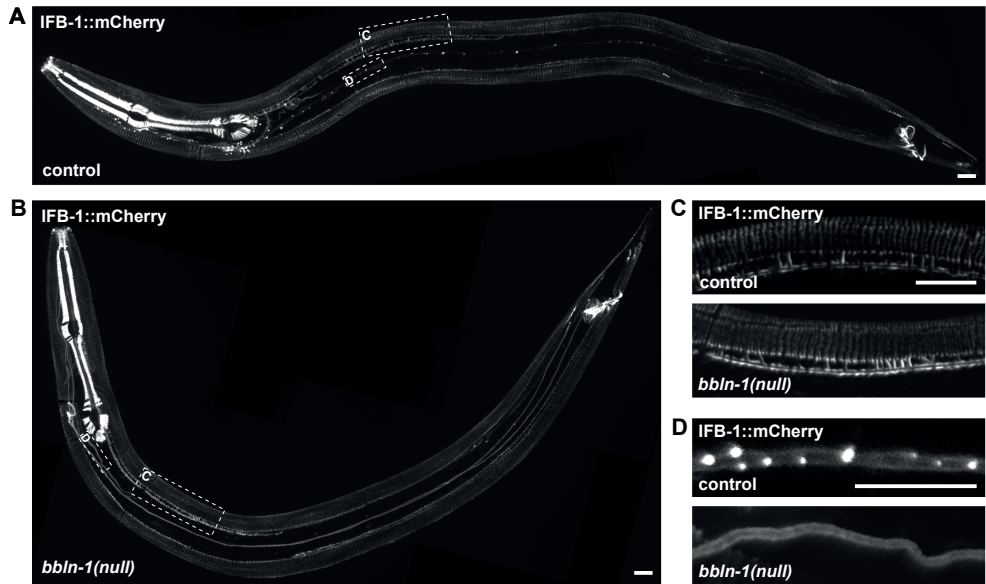


Figure S4. Loss of BBLN-1 does not affect intermediate filaments in the pharynx and hypodermis. Distribution of IFB-1::mCherry in L3-stage control and *bbln-1(null)* animals. Boxed regions in A and B are shown enlarged in C and D.

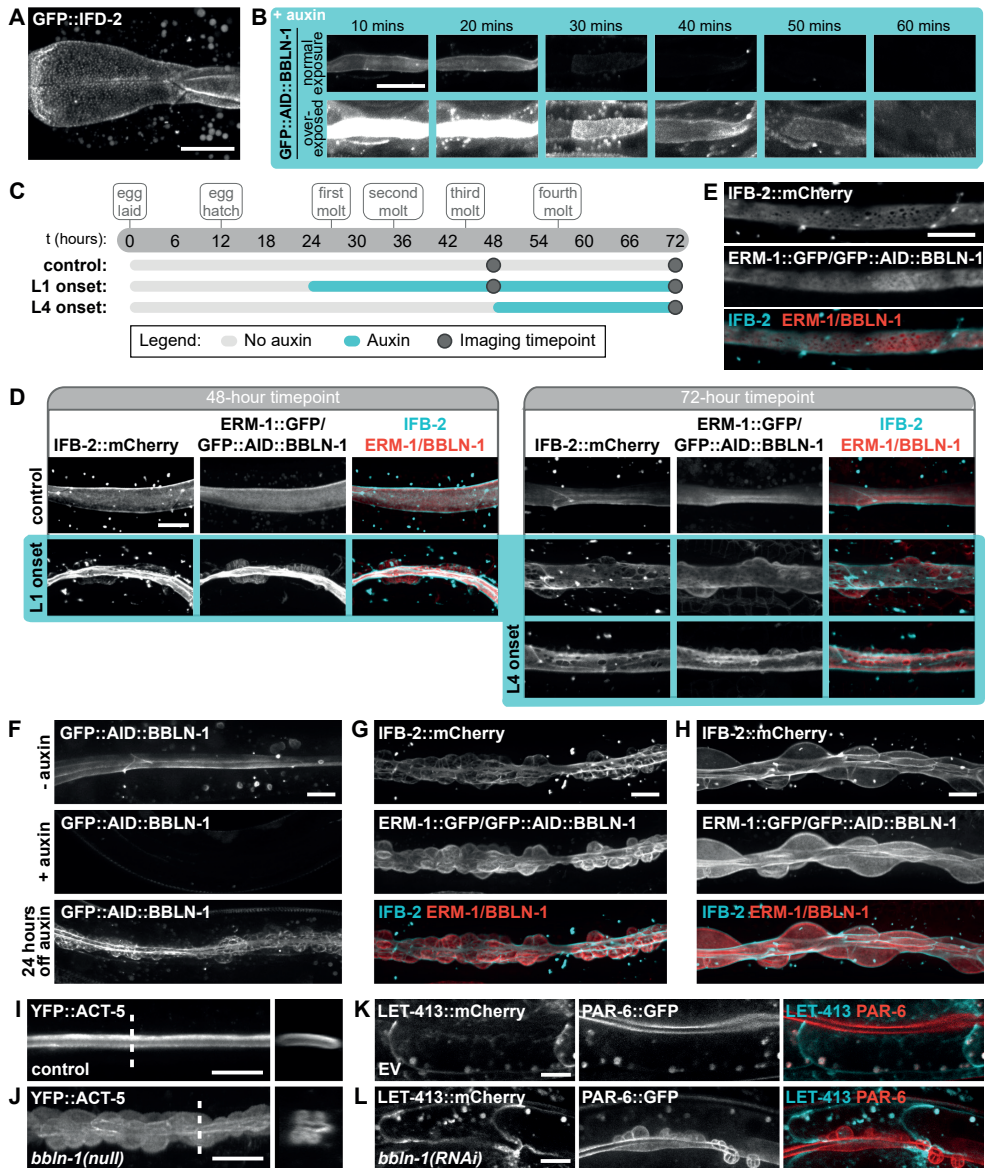


Figure S5. BBLN-1 is required for apical membrane morphology throughout development. (A) Localization of GFP::IFD-2 in the anterior most section of the intestine, highlighting the punctate localization pattern of IFD-2. (B) Distribution of GFP::AID::BBLN-1 in L1 larvae in the presence of 1 mM auxin for 10 to 60 mins. Degradation was induced in the intestine. Bottom row depicts the same images as top row, but computationally overexposed in ImageJ (Fiji) to visualize low levels of fluorescence. (C) Schematic overview of experiment design for the data in D. Eggs were laid on $t = 0$ and allowed to develop on NGM plates for 24 (L1 onset) or 48 (L4 onset) hours before being transferred to plates containing 1 mM auxin. Larvae were imaged after 24 (L1 and L4 onset, 48-hour timepoint) and 48 (L1 onset, 72-hour timepoint) hours of degradation. (D) Distribution of IFB-2::mCherry, ERM-1::GFP and GFP::AID::BBLN-1 upon intestine specific degradation of GFP::AID::BBLN-1 in L4 larvae (left, 48-hour timepoint) and young adults (right, 72-hour timepoint). (E) L4 larva displaying “holes”

in IFB-2::mCherry expression pattern upon 24 hours of degradation from the L1 stage. (F) Expression of GFP::AID::BBLN-1 in L3/L4-stage animals not treated with auxin (- auxin), treated with auxin from hatching (+ auxin), or treated with auxin from hatching but recovered on plates without auxin for 24 h (24 hours off auxin). (G, H) IFB-2::mCherry, ERM-1::GFP, and GFP::AID::BBLN-1 distribution in L4 (G) and adult (H) animals after 48 and 72 hours recovery without auxin, respectively. (I, J) Organization of the YFP::ACT-5 transgene in intestinal cells as seen in lateral and cross-section views as indicated by the dashed lines. (K, L) Apicobasal polarity of the intestine visualized by endogenous LET-413::mCherry (basolateral) and PAR-6::GFP (apical) reporters.

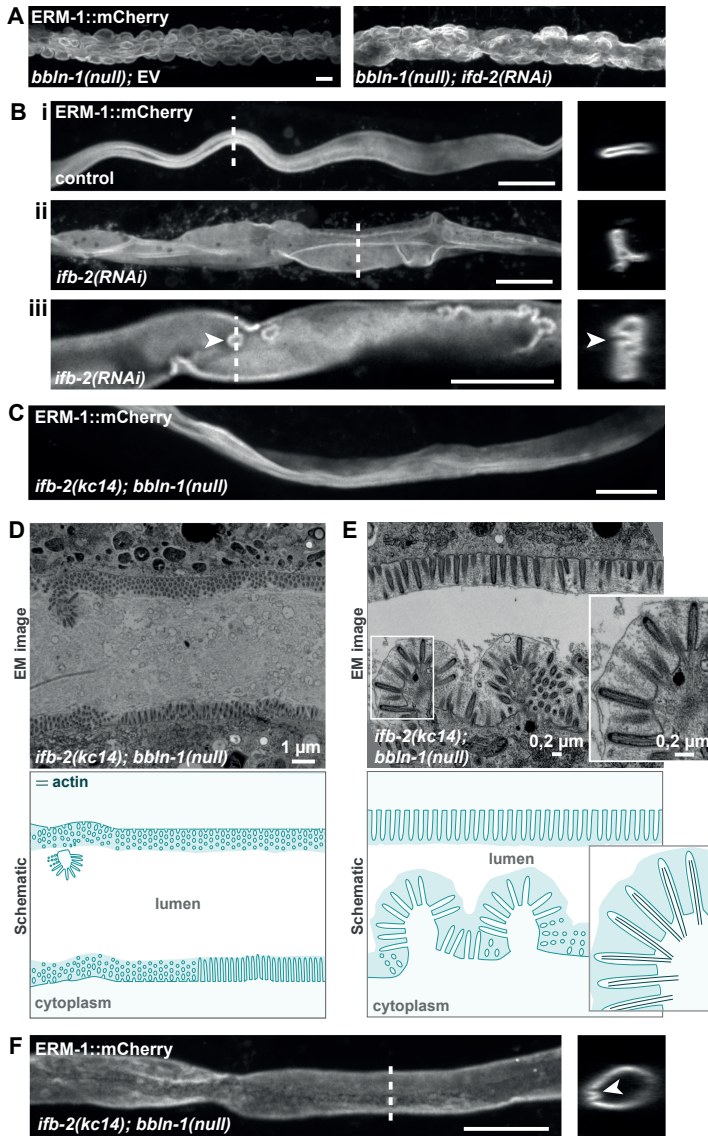


Figure S6. Intermediate filament aggregation drives cytoplasmic invaginations.

(A, B) Apical membrane morphology visualized by ERM-1::mCherry in *bbln-1(null)* L3/L4-stage animals subjected to RNAi knockdown of *ifd-2* (A) and *ifb-2* (B). Dashed lines in B indicate the position of the cross-sections. Arrowheads in (Biii) point to apical membrane protrusion towards the lumen (same protrusion is indicated in lateral and cross-section views). (C) Apical membrane morphology visualized by ERM-1::mCherry in *ifb-2; bbln-1* double knockout L4 animal. (D, E) Ultrastructure of the apical domain in intestinal cells visualized by transmission electron microscopy. Boxed region in (E) is shown in zoom-in. Schematics indicate actin bundles in dark blue in the zoom inset. (F) Apical membrane morphology visualized by ERM-1::mCherry in *ifb-2; bbln-1* double knockout L3 animal. Arrowhead indicates apical membrane protrusion towards the lumen.

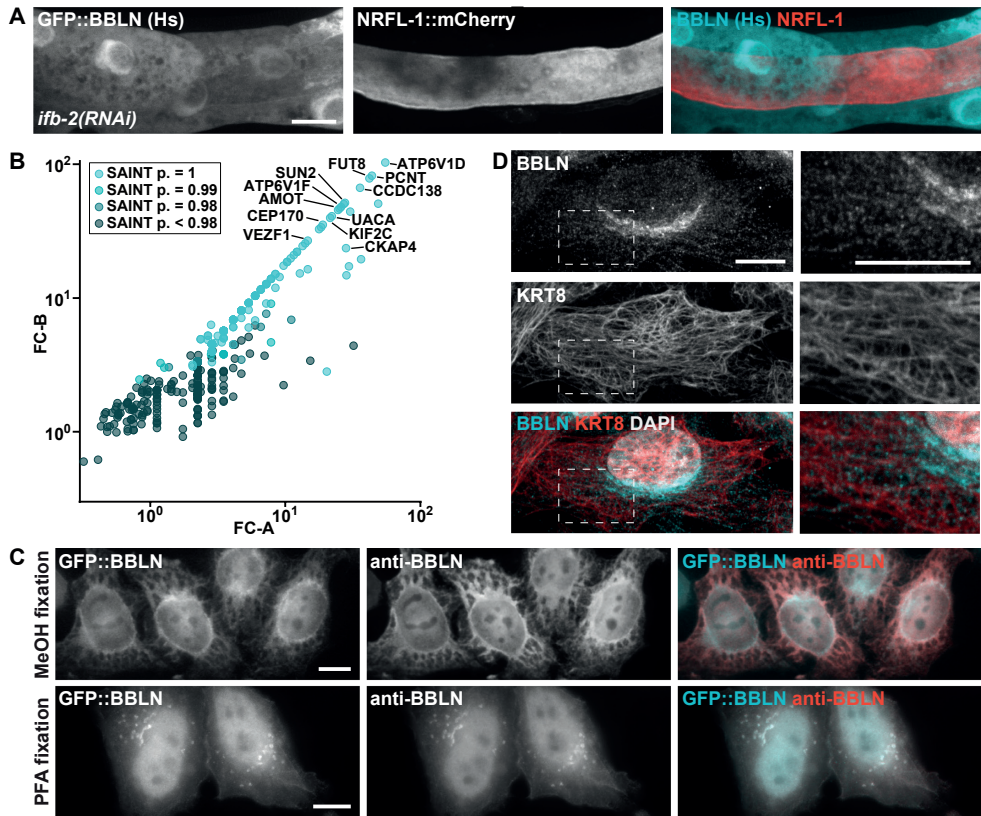


Figure S7. Expression of bublin in *C. elegans* intestine and mammalian cell culture, and AP-MS/MS of bublin. (A) Larva expressing intestinal GFP-tagged bublin (BBLN (Hs)) fed with a bacterial RNAi clone against *ifb-2*. An endogenous NRFL-1::mCherry fusion was used as an apical membrane marker. (B) Mass spectrometry hits for biotin::GFP::bublin streptavidin purified from HEK 293T cells plotted as correlation between fold-change (FC) score A and more stringent FC score B. Data points are color coded for different SAINT probability scores. (C) Upright fluorescence microscopy images of HeLa cells transfected with GFP-tagged bublin (BBLN (Hs)) and stained with bublin (BBLN) antibody fixed with either -20 °C methanol (top) or 4% PFA (bottom). (D) Confocal images of HeLa cells stained with bublin (BBLN) antibody, keratin 8 (KRT8) antibody and DAPI and fixed by 4% PFA. Boxed region indicates location of zoom-in on the right.

Table S1. Key Resources Table.

REAGENT or RESOURCE	SOURCE	IDENTIFIER
Antibodies		
Rabbit anti-BBLN	Sigma-Aldrich	Cat# HPA020725; RRID: AB_1845816
Mouse anti-PCNT	Abcam	Cat# ab28144; RRID: AB_2160664
Rat anti-Tyrosinated α -tubulin (YL1/2)	Thermo Fisher Scientific	Cat# MA1-80017; RRID: AB_2210201
Rat anti-KRT8	DSHB	Cat# TROMA-I; RRID: AB_531826
Alexa Fluor 568-conjugated Phalloidin	Life Technologies	Cat# A12380
Goat anti-mouse Alexa Fluor 488	Life Technologies	Cat# A11029; RRID: AB_2534088
Goat anti-rabbit Alexa Fluor 594	Thermo Fisher Scientific	Cat# A-11012; RRID AB_2534079
Goat anti-rat Alexa Fluor 647	Thermo Fisher Scientific	Cat# A-21247; RRID AB_141778
Rabbit anti-GFP	Abcam	Cat# AB290; RRID: AB_2313768
Goat anti-rabbit IgG Antibody, IRDye 680LT Conjugated	LI-COR Biosciences	Cat# 827-11081; RRID: AB_107950 15
Goat anti-rat IgG Antibody, IRDye 800CW Conjugated	LI-COR Biosciences	Cat# 926-32219; RRID: AB_1850025
Bacterial and Virus Strains		
<i>E. coli</i> OP50	CGC	N/A
<i>E. coli</i> DH5a	Thermo Fisher Scientific	Cat# 18265017
<i>E. coli</i> HT115	CGC	N/A

Vidal full-length HT115 RNAi feeding library	SourceBioScience	3320_Cel_ORF_RNAi
Ahringer fragment HT115 RNAi feeding library	SourceBioScience	3318_Cel_RNAi_complete
Chemicals, Peptides, and Recombinant Proteins		
Vectashield mounting medium with DAPI	Vector Laboratories	Cat# H-1200
PEI	PolySciences	Cat# 24765-2
cComplete, EDTA-free Protease Inhibitor Cocktail	Roche	Cat# 4693116001
Dextran, Texas Red™, 3000 MW	Thermo Fisher Scientific	Cat# D3329
Dextran, Texas Red™, 10,000 MW	Thermo Fisher Scientific	Cat# D1828
Dextran, Texas Red™, 40,000 MW	Thermo Fisher Scientific	Cat# D1829
Alt-R S.p. Cas9 Nuclease V3	IDT	Cat# 1081058
Auxin	Alfa Aesar	Cat# A10556
Critical Commercial Assays		
MinElute PCR purification kit	QIAGEN	28004
Dynabeads M-280 streptavidin beads	Thermo Fisher	Cat# 11206D
Deposited Data		
Mass Spectrometry data	PRIDE	PXD024387
Experimental Models: Cell Lines		
Human embryonic kidney 239T (HEK293T)	ATCC	Cat# CRL-3216
HeLa (Kyoto)	Serra-Marques <i>et al.</i> , 2020.	N/A
Mouse C57BL/6 small intestine organoids; isolated from duodenum.	This study	N/A
Experimental Models: Organisms/Strains		
wild type (Bristol)	CGC	N2
<i>mibIs39[Prps-27::GFP-2xTEV-Avi 10 ng/ul + Prab-3::mCherry 5 ng/ul + lambda DNA 65 ng/ul]</i> I	This study	BOX64

<i>erm-1(mib15[erm-1::eGFP]) I</i>	Ramalho <i>et al.</i> , 2020.	BOX213
<i>erm-1(mib15[erm-1::eGFP]) I; sma-5a(mib41[C370T]) X</i>	This study	BOX320
<i>erm-1(mib15[erm-1::eGFP]) I; bbln-1(mib42[C13T]) X</i>	This study	BOX321
<i>bbln-1(mib71[eGFP::bbln-1]) X</i>	This study	BOX414
<i>bbln-1(mib79[bbln-1::mkate2(co)]) X</i>	This study	BOX459
<i>erm-1(mib40[erm-1::AID::mCherry]) I; bbln-1(mib70[Pbbln-1::eGFP1-3, X:3151104..3153328]) X</i>	This study	BOX415
<i>erm-1(mib40[erm-1::AID::mCherry]) I; bbln-1(mib71[eGFP::bbln-1]) X</i>	This study	BOX427
<i>ifb-2(mib74[ifb-2::mCherry]) II; bbln-1(mib70[Pbbln-1::eGFP1-3, X:3151104..3153328]) X</i>	This study	BOX435
<i>ifb-2(mib74[ifb-2::mCherry]) II; bbln-1(mib71[eGFP::bbln-1]) X</i>	This study	BOX436
<i>erm-1(mib15[erm-1::eGFP]) I; ifb-2(mib74[ifb-2::mCherry]) II</i>	This study	BOX514
<i>erm-1(mib15[erm-1::eGFP]) I; ifb-2(mib74[ifb-2::mCherry]) II; bbln-1(mib70[Pbbln-1::eGFP1-3, X:3151104..3153328]) X</i>	This study	BOX515
<i>erm-1(mib40[erm-1::AID::mCherry]) I</i>	This study	BOX303
<i>erm-1(mib40[erm-1::AID::mCherry]) I; bbln-1(mib42[C13T]) X</i>	This study	BOX330
<i>erm-1(mib15[erm-1::eGFP]) I; bbln-1(mib42[Q5STOP]) X; dlg-1(mib23[dlg-1::mCherry-LoxP]) X</i>	This study	BOX307
<i>erm-1(mib15[erm-1::eGFP]) I; dlg-1(mib23[dlg-1::mCherry-LoxP]) X</i>	This study	BOX368
<i>nrf1-1(mib72[nrf1-1::mCherry]) IV</i>	Boxem lab	BOX416
<i>ifb-2(mib74[ifb-2::mCherry]) II; bbln-1(mib70[Pbbln-1::eGFP1-3, X:3151104..3153328]) X; dlg-1(mib35[dlg-1::AID::eGFP-LoxP]) X</i>	This study	BOX454
<i>ifb-2(mib74[ifb-2::mCherry]) II; dlg-1(mib35[dlg-1::AID::eGFP-LoxP]) X</i>	This study	BOX455
<i>erm-1(mib40[erm-1::AID::mCherry]) I; ifc-2a::yfp(kc16)X</i>	This study	BOX456

<i>erm-1(mib40[erm-1::AID::mCherry]) I; ifc-2a::yfp(kc16) X; bbln-1(mib70[Pbbln-1::eGFP1-3, X:3151104..3153328]) X</i>	This study	BOX457
<i>erm-1(mib40[erm-1::AID::mCherry]) I; ifd-2(mib94[eGFP::ifd-2]) X</i>	This study	BOX614
<i>erm-1(mib40[erm-1::AID::mCherry]) I; ifd-2(mib94[eGFP::ifd-2]) X; bbln-1(mib70[Pbbln-1::eGFP1-3, X:3151104..3153328]) X</i>	This study	BOX615
<i>Is[Pges-1::YFP::ACT-5]</i>	Bossinger <i>et al.</i> , 2004.	JM125
<i>bbln-1(mib70[Pbbln-1::eGFP1-3, X:3151104..3153328]) X; Is[Pges-1::YFP::ACT-5]</i>	This study	BOX438
<i>par-6(mib24[par-6::eGFP-LoxP]) I; let-413(mib29[let-413::mCherry-LoxP]) V</i>	Boxem lab	BOX251
<i>gip-2(lt19[gip-2::GFP::loxP::cb-unc-119(+):loxP]) I; bbln-1(mib93[mCherry::bbln-1]) X</i>	This study	BOX544
<i>mibIs48[Pelt-2::TIR-1::tagBFP2-Lox511::tbb-2-3'UTR, IV:5014740-5014802 (cxTi10882 site))] IV; bbln-1(mib111[eGFP::AID::bbln-1]) X</i>	This study	BOX632
<i>erm-1(mib15); IFB-2(mib74[IFB-2::mCherry]) II; mibIs48[Pelt-2::TIR-1::tagBFP2-Lox511::tbb-2-3'UTR, IV:5014740-5014802 (cxTi10882 site))] IV; bbln-1(mib111[GFP::AID::BBLN-1]) X</i>	This study	BOX637
<i>erm-1(mib40[erm-1::AID::mCherry]) I; ifb-2(kc14) II; bbln-1(mib70[Pbbln-1::eGFP1-3, X:3151104..3153328]) X</i>	This study	BJ364
<i>gip-2(lt19[gip-2::GFP::loxP::cb-unc-119(+):loxP]); unc-119(ed3)III</i>	Wang <i>et al.</i> , 2015.	OD2509
<i>ifb-1(mib134[ifb-1::mCherry]) II</i>	This study	BOX717
<i>ifb-1(mib134[ifb-1::mCherry]) II; bbln-1(mib70[Pbbln-1::eGFP1-3, X:3151104..3153328])X</i>	This study	BOX724
<i>ifb-1(mib134[ifb-1::mCherry]) II; bbln-1(mib71[GFP::bbln-1])X</i>	This study	BOX725

Recombinant DNA		
<i>Pvha-6::gfp::bbln-1::N-taglinker::tbb-2_3'UTR</i>	This study	pSMR10
<i>vha-6</i> promoter	This study	pSMR13
<i>tbb-2</i> 3'UTR	This study	pSMR18
<i>Pvha-6::gfp::BBLN (Hs)::N-taglinker::tbb-2_3'UTR</i>	This study	pSMR30
<i>act-5</i> 3'UTR (L4440)	This study	pSMR33
<i>ifp-1</i> (L4440)	This study	pSMR34
<i>ifd-1</i> (L4440)	This study	pSMR35
<i>ifo-1</i> (L4440)	This study	pSMR36
L4440	Addgene	Cat# 1654
pHSG298	Takara Biosciences	Cat# 3298
pMLS257	Addgene	Cat# 73716
pMLS288	Addgene	Cat# 73735
pMLS287	Addgene	Cat# 73730
pDD363	Addgene	Cat# 91829
pDD398	Addgene	Cat# 91832
<i>Peft-3::Cas9</i>	Addgene	Cat# 46168
<i>Pmyo-2::mCherry</i>	Addgene	Cat# 19327
pJJR82	Addgene	Cat# 75027
pJJR83	Addgene	Cat# 75028
Software and Algorithms		
ImageJ	Rasband,W.S (NIH)	RRID: SCR_003070
Graphpad Prism	GraphPad	RRID: SCR_002798
Zen Black	Zeiss	RRID: SCR_018163
SnapGene	Insightful Science	RRID: SCR_015052
Proteome Discoverer 1.4	Thermo Scientific	RRID: SCR_014477

Table S2. DNA reagents used.

Primers used to generate RNAi clones		Sequence source*
<i>sma-5</i>		
Forward	aggcgcgccACATTGTCCTCTCCGTGAC	Wormbase
Reverse	agcgccgcTTCGTCGTCATGCTTCTTG	Wormbase
<i>jfp-1</i>		
Forward	aggcgcgccTGACCACCATAGCCGAACTT	Wormbase
Reverse	agcgccgcTTTGAAGCCACCAACGTCTG	Wormbase
<i>jfd-1</i>		
Forward	aggcgcgccTCAAACCGGGTTCTCGAGA	Wormbase
Reverse	agcgccgcTTCCTGCGGAGGTTGATCT	Wormbase
<i>jfo-1</i>		
Forward	aggcgcgccCCTACAAGTCGACTTGAATGCAGC	Wormbase
Reverse	agcgccgcAGTGAAGTGGGCGAGTGATG	Wormbase
<i>act-5</i>		
Forward	aggcgcgccaacatgtgccttccattttaggcg	Wormbase
Reverse	agcgccgcAGAAAATGAAGTATCTCATGGAATTTG	Wormbase
Reagents to generate <i>Pvha-6::gfp::bbln-1::tbb-2 3'UTR</i> construct		Sequence source*
<i>vha-6</i> promoter		
Forward	ctGCTCTTCgTGGTTGCCAGTGATGAATCCAAGCAC	Wormbase
Reverse	ctGCTCTTCgCATttttatgggttttgtaggttttagtcg	Wormbase
<i>tbb-2 3'UTR</i>		
Forward	ctGCTCTTCgACGTAAgataaatgcaaaatcctttcaag	Wormbase
Reverse	ctGCTCTTCgTACtgagactttttcttggcggc	Wormbase
<i>bbln-1</i>	gcatggctGCTCTTCgAAGATGGTCGTTGAGCAGAAAGAGCAAGAGC	Wormbase
gBlock	CTATTGTCAAGATGCGCGACCGCAATGTCAACGCTGCTGCACATTC TGCGTTGGCTCGTGGAAATTGAGGCACTCAACGAAGGAGAAGTGAC CGAGGAGACGGAAGgtgaaaactcttctcagattcagattacttatagcattggtt ttttcagAAATTCGCAAGCTGGACACCCAGCTTGATCATCTTAATGACT ACATGTCTAAGATGGATGAGCGTCTGAAGGCACACAACGACAGAA TGATGGAGACGTTGAAGCAGCAGAAGGATGAGCGCGAAAAGAGA CGTCGAGCTTCCACGAGCGTATGTCCAAAATCAATCTGAAGATG AGGAGTTCAAAAAGCAAATGAGCAGCATCCTGAAGAGAGTTCAATC TGTCAAACGCACCGAAAAAGGTcGAAGAGCagccgga	

Reagents to generate <i>Pvha-6::gfp::BBLN (Hs)::tbb-2 3'UTR</i> construct		Sequence source*
<i>vha-6</i> promoter		
Forward	ctGCTCTTCgTGGTTGCCAGTGATGAATCCAAGCAC	Wormbase
Reverse	ctGCTCTTCgCATtttttagggttttagtagtttttagtgc	Wormbase
<i>tbb-2 3'UTR</i>		
Forward	ctGCTCTTCgACGTAAgataaatgcaaaatcctttcaag	Wormbase
Reverse	ctGCTCTTCgTACtgagactttttcttggcggc	Wormbase
BBLN (Hs)	gcatggctGCTCTTCgAAGATGTCCGGACCAACGGAGACCTCGGAAT	NCBI Reference
gBlock	GCCAGTCCGAGCCGGAGCCGAGGGAGAGGAGGACGGATTCGGA GAGGCCGAGTACGCCCATCAACTCCATGCTCGACCAATCAACT CCTGCCTCGACCACCTCGAGGAGAAGtaagtttaacatatataact aacctgatttttaaattttcagAACGACCACCTCCACGCCCTCCCAAGA GCTCTCGAGTCCAACCGTCAAACCGTCTCGAGTCCAACAACAA CTCGGAGAGGCCCATCCGACGCTCCCAGGTcGAAGAGCagccg gat	Sequence: NM_024112.4 (Sayers et al., 2021)

Reagents to generate <i>erm-1::mCherry::AID</i>		Sequence source*
sgRNA 1		
Forward	tcttAAGACTCTCCGTCAAATCCG	Wormbase
Reverse	aaacCGGATTTGACGGAGAGTCTT	Wormbase
sgRNA 2		
Forward	tcttACTCTCCGTCAAATCCGTGG	Wormbase
Reverse	aaacCCACGGATTTGACGGAGAGT	Wormbase
Repair template primers		
arm forward	GGCTGCTCTTCgTGGGGAGgttcgtatttttaaaaaactcg	Wormbase and
LH arm	TGATCGATTCTTCGTTTTGTGTTTCTCCcCtaATcTGcCGGAGAGTC	Addgene plasmid
reverse 1	TTGTACTGTCCG	#75028
LH arm	GGGTGCTCTTCgCGCCATATTTTCGATTGATCGATTCTTCGTTTTGT	
reverse 2	GTTTCC	
arm forward	GGCTGCTCTTCgACGTAAAttattgttctatcgtatttcctt	
arm reverse	GGGTGCTCTTCgTACgctccatcgaaaccttggg	
Genotyping primers		
Forward	CTGCACTGACTACGACGTTCTG	Wormbase
Reverse	CCCGAGGAGAAGCACATG	Wormbase

Reagents to generate <i>bbln-1(mib70)</i>		Sequence source*
crRNA		
N-terminal	ctcatttcagttgaacacaa	Wormbase
C-terminal	gaagagagttcaatctgtca	Wormbase
Repair template		
ssODN	cgctcttttctccatttcctcatttcagttgaacacaatgTCCAAGGGAGAGGAGCT CTTCACCGGAGTCGTCCCAATCCTCGTCGAGCTCGACGGAGTCAAG GAGTTCGTACCCGCTGCCGGAATCACCCACGGAATGGACGAGCTC TACAAGtaagagagttcaatctgtcaaacgcaccgaaaaataaa	Wormbase and Addgene plasmid #75027
Genotyping primers		
Forward	atcatcaccatctccaacc	Wormbase
Reverse	CGCGCATCTTGACAATAGGC	Wormbase

Reagents to generate <i>gfp::bbln-1</i>		Sequence source*
crRNA		
Step 1	ctcatttcagttgaacacaa	Wormbase
Step 2	cgtcgagctcgacggagtca	Wormbase
Repair template ssODN		
Step 1	cgctcttttctccatttcctcatttcagttgaacacaatgTCCAAGGGAGAGGAGCT CTTCACCGGAGTCGTCCCAATCCTCGTCGAGCTCGACGGAGTCAAG GAGTTCGTACCCGCTGCCGGAATCACCCACGGAATGGACGAGCTC TACAAGgtcgttgagcagaaagagcaagagcctattgtcaa	Wormbase and Addgene plasmid #75027
Repair template primers		
Step 2		Addgene plasmid
forward	CCAAGGGAGAGGAGCTCTTCA	#75027
Step 2		Addgene plasmid
reverse	CTGTAGAGCTCGTCCATTC	#75027
Repair template		
PCR	CCAAGGGAGAGGAGCTCTTCACCGGAGTCGTCCCAATCCTCGTCG AGCTCGACGGAGACGTCAACGGACACAAGTTCTCCGTCTCAGGAG AGGGAGAGGGAGACGCCACCTACGAAAGCTCACCTCAAGTTCA TCTGCACCACCGAAAGCTCCCAGTCCCATGGCCAACCCTCGTCAC CACCTTCACTTACGGAGTCCAATGCTTCTCCGTTACCCAGACCACA TGAAGCGTCACGACTTCTTCAAGTCCGCCATGCCAGAGGGATACGT CCAAGAGCGTACCATCTTCTTCAAGtaagtttaaacattaataactaact aacctgattatttaatttcagGACGACGGAACTACAAGACCCGTGCCG AGGTCAAGTTCGAGGGAGACACCCTCGTCAACCGTATCGAGTCA AGtaagtttaaacagttcgggtactaactaaccatacatatttaatttcagGGAATC GACTTCAAGGAGGACGGAAACATCCTCGGACACAAGCTCGAATAC AACTACAACCTCCACAACGTCTACATCATGGCCGACAAGCAAAAAGA ACGGAATCAAGGTCAACTTCAAGtaagtttaaacatgattttactaactaact aatctgattaaatttcagATCCGTCAACATCGAGGACGGATCTGTCCA ACTCGCCGACCACTACCAACAAAACACCCCAATCGGAGACGGACCA GTCCTCTCCAGACAACCACTACCTCTCCACCAATCCGCCCTCTC CAAGGACCCAAACGAGAAGCGTGACCACATGGTCTCAAGGAGTT CGTACCCGCTGCCGGAATCACCCACGGAATGGACGAGCTCTACAA G	Addgene plasmid #75027

Genotyping primers

Forward	atcatcaccctctccaacc	Wormbase
Reverse	CGCGCATCTTGACAATAGGC	Wormbase

Reagents to generate *bbln-1::mKate2***Sequence source***

crRNA	gtaccaattgaaaagcattc	Wormbase
--------------	----------------------	----------

Repair template 5'SP9 modified primers

Forward	TGAAGAGAGTTCAATCTGTCAAACGCACCGAAAAATGTCCGAGCT CATCAAGGAG	Wormbase and Addgene plasmid
Reverse	gtgtacatgtaccaattgaaaagcattctggtTTAACGGTGTCCGAGCTTGGAT	Wormbase and Addgene plasmid

Repair template	ATGTCCGAGCTCATCAAGGAGAACATGCACATGAAGCTCTACATGG AGGGAACCGTCAACAACCACCACTTCAAGTGCACCTCCGAGGGAG	Wormbase and Addgene plasmid
PCR	AGGGAAAGCCATACGAGGGAAACCAACCATGCGTATCAAGgtaagt ttaaacaatataataactaactaaccctgattatttaaattttcagGCCGTCGAGGGAG GACCACTCCCATTGCGCTTCGACATCCTCGCCACCTCCTTCATGTAC GGATCCAAGACCTTCATCAACCACCCAAAGGAATCCCAGACTTCT TCAAGCAATCCTTCCCAGAGGGATTACCTGGGAGCGTGTACCAC CTACGAGGACGGAGGAGTCCTCACCGCCACCCAAGACACCTCCCT CCAAGACGGATGCCTCATCTACAACGTCAAGgtaagttaaacagttcggg actaactaaccatacatatttaaattttcagATCCGTGGAGTCAACTTCCCATCC AACGGACCAGTCATGCAAAAGAAGACCCTCGGATGGGAGGCCTCC ACCGAGACCCTTACCCAGCCGACGGAGGACTCGAGGGACGTGCC GACATGGCCCTCAAGCTCGTCGGAGGAGGACCTCATCTGCAAC CTCAAGgtaagttaaacaatgattttactaactaactaatctgatttaaattttcagACC ACCTACCGTTCCAAGAAGCCAGCCAAGAACCTCAAGATGCCAGGA GTCTACTACGTCGACCGTCGTCGAGCGTATCAAGGAGGCCGACA AGGAGACCTACGTCGAGCAACACGAGGTCGCCGTCGCCCGTTACT GCGACCTCCCATCCAAGCTCGGACACCGT	#91825

Genotyping primers

Forward	GCAAATGAGCAGCATCCTG	Wormbase
Reverse	cgaggaaccaaatcattttcc	Wormbase

Reagents to generate <i>ifb-2::mCherry</i>	Sequence source*
--	------------------

crRNA

Step 1 gatgatggagattcTTAAC	Wormbase
Step 2 GTTCATGCGTTTCAAGGCCG	Wormbase

Repair template ssODN

Step 1	
tcatcgaaaaagaatcgattagatgatggagattcTTACTTGTAGAGCTCGTC	
CATTCTCCGGTGGAGTGACGTCCCTCGGCCTGAAACGCATGAAC	Wormbase and
TCCTTGATGATGGCCATGTTGTCTCTCTCCCTTGGAACGGGAAG	Addgene plasmid
AAGCGACCGTCGCTGGATGTGCGAAGCCTTC	#75028

Repair template primers

Step 2 TCCAAGGGAGAGGAGGACAA	Addgene plasmid
forward	#75028
Step 2 CTTGTAGAGCTCGTCCATTC	Addgene plasmid
reverse	#75028

Repair template	TCCAAGGGAGAGGAGGACAA	Addgene plasmid
	CGTTTCAAGGTCCACATGGAGGGATCAGTCAACGGACACGAGTTC	#75028

PCR

GAGATCGAGGGAGAGGGAGAGGGACGTCCATACGAGGGAAACCA
AACCGCCAAGCTCAAGgtaagttaaacaatatataactaactaacctgattatt
aaatcttcagGTCACCAAGGGAGGACCACTCCCATTCGCCTGGGACAT
CCTCTCCCCACAATTCATGTACGGATCAAAGGCCTACGTCAAGCAC
CCAGCCGACATCCCAGACTACCTCAAGCTCTCCTTCCCAGAGGGAT
TCAAGTGGGAGCGTGTATGAATTCGAGGACGGAGGAGTGTCA
CCGTACCCCAAGACTCCTCCCTCCAAGACGGAGAGTTCATCTACAA
GgtaagttaaacaagttcggtactaactaaccatacatattaaatcttcagGTCAGC
TCCGTGGAACCAACTTCCCATCCGACGGACCAGTCATGCAAAAGAA
GACCATGGGATGGGAGGCCTCCTCCGAGCGTATGTACCCAGAGGA
CGGAGCCCTCAAGGGAGAGATCAAGCAACGTCTCAAGCTCAAGGA
CGGAGGACACTACGACGCCGAGGTCAAGACCACCTACAAGGCCAA
GAAGCCAGTCCAACCTCCAGgtaagttaaacaatgattttactaactaactatct
gatttaaatttcagGAGCCTACAACGTCAACATCAAGCTCGACATCACCT
CCCACAACGAGGACTACCATCGTCGAGCAATACGAGCGTGCCG
AGGGACGTCACTCCACCGGAGGAATGGACGAGCTCTACAAG

Genotyping primers

Forward tcgtagctataaccgcttca	Wormbase
Reverse caaggaaaggattcaatgggc	Wormbase

Reagents to generate <i>gfp::ifd-2</i>		Sequence source*
crRNA (5')	TGGGTTGAGAGGGTCAGTCA	Wormbase
Repair template primers		
Forward	tattcaaaactaatttctagaataaaaacgccATGTCCAAGGGAGAGGAGCTC TT	Addgene plasmid #75027
Reverse	ATGATTTTGCAGACGCGTTGGGTTGAGAGGGTCAGTCTTGAGAG CTCGTCCATTC	Addgene plasmid #75027
Genotyping primers		
Forward	ggaacggctcagttttctc	Wormbase
Reverse	CTACATATCGTCCAATCGG	Wormbase
Reagents to generate <i>mCherry::bbln-1</i>		Sequence source*
crRNA	ctcatttcagttgaacacaA	Wormbase
Repair template primers		
Forward	cgcttttttctcatttctcatttcagttgaacacaATGTCCAAGGGAGAGGAGG ACAA	Wormbase and Addgene plasmid
Reverse	TTGACAATAGGCTCTTGCTCTTTCTGCTCAACGACCTTGAGAGCTC GTCCATTC	Wormbase and Addgene plasmid
Repair template PCR	TCCAAGGGAGAGGAGGACAACATGGCCATCATCAAGGAGTTCATG CGTTTCAAGGTCCACATGGAGGGATCAGTCAACGGACACGAGTTC GAGATCGAGGGAGAGGGAGAGGGACGTCATACGAGGGAAACCCA AACCGCCAAGCTCAAGGtaagtttaaacatatataactaactaacctgattatt aaattttcagGTCACCAAGGGAGGACCACTCCCATTGCGCTGGGACAT CCTCTCCCCACAATTCATGTACGGATCAAAGGCCTACGTCAAGCAC CCAGCCGACATCCCAGACTACCTCAAGCTCTCCTTCCAGAGGGAT TCAAGTGGGAGCGTGTATGAACTTCGAGGACGGAGGAGTCGTCA CCGTACCCCAAGACTCCTCCCTCCAAGACGGAGAGTTCATCTACAA GgtaagtttaaacagttcggtaactaaccatacatatttaaattttcagGTCAGC TCCGTGGAACCAACTTCCCATCCGACGGACCAAGTCATGCAAAAGAA GACCATGGGATGGGAGGCCTCCTCCGAGCGTATGTACCCAGAGGA CGGAGCCCTCAAGGGAGAGATCAAGCAACGTCTCAAGCTCAAGGA CGGAGGACACTACGACGCCGAGGTCAAGACCACCTACAAGGCCAA GAAGCCAGTCCAACCTCCCAGgtaagtttaaacatgattttactaactaactaatc gatttaaattttcagGAGCCTACAACGTCAACATCAAGCTCGACATCACCT CCCACAACGAGGACTACACCATCGTCGAGCAATACGAGCGTGCCG AGGGACGTCACTCCACCGGAGGAATGGACGAGCTCTACAAAG	Wormbase and Addgene plasmid #75028
Genotyping primers		
Forward	atcatcaccatctccaacc	Wormbase
Reverse	CGCGCATCTTGACAATAGGC	Wormbase

Reagents to generate <i>gfp::aid::bbln-1</i>		Sequence source*
crRNA	ctcatttcagttgaacacaA	Wormbase
Repair template 5'SP9 modified primers		
Forward	cgtctttttctccatttctcatttcagttgaacacaATGTCCAAGGGAGAGGAGC TCTT	Wormbase, Addgene plasmid #75027 and Zhang et al., 2015.
Reverse	TTGACAATAGGCTCTTGCTCTTTCTGCTCAACGACCTTCACGAACGC CGCCGCCT	Wormbase, Addgene plasmid #75027 and Zhang et al., 2015.
Repair template PCR		Wormbase, Addgene plasmid #75027 and Zhang et al., 2015.

cgtctttttctccatttctcatttcagttgaacacaATGGTCTCCAAGGGAGAGG
AACTCTTCACCGGAGTCGTCCCAATCCTCGTCGAGCTCGACGGAGA
CGTCAACGGACACAAGTTCTCCGTCTCAGGAGAGGGAGAGGGAGA
CGCCACCTACGGAAAGCTCACCTCAAGTTCATCTGCACCACCGGA
AAGCTCCAGTCCCATGGCCAACCCTCGTACCACCTTCACTTACG
GAGTCCAATGCTTCTCCGTTACCCAGACCACATGAAGCGTCACGA
CTTCTTCAAGTCCGCCATGCCAGAGGGATACGTCCAAGAGCGTACC
ATCTTCTTCAAGGtaagtttaaacattaattaactaactaacctgattattaaatt
ttcagGACGACGGAAACTACAAGACCCGTGCCGAGGTCAAGTTCGA
GGGAGACACCTCGTCAACCGTATCGAGCTCAAGtaagtttaaacagtt
cggtaactaactaacatacatatttaaattttcagGGAATCGACTTCAAGGAGGA
CGAAACATCCTCGGACACAAGCTCGAATACAACATACTCCAC
AACGTCTACATCATGGCCGACAAGCAAAAGAACGGAATCAAGGTC
AACTTCAAGGtaagtttaaacatgattttactaactaactaatctgattaaatttcag
ATCCGTACAACATCGAGGACGGATCTGTCCAACCTCGCCGACCACT
ACCAACAAAACACCCCAATCGGAGACGGACCAGTCTCCTCCCAGA
CAACCACTACCTTCCACCCAATCCGCCCTCTCAAGGACCCAAAC
GAGAAGCGTGACCACATGGTCTCAAGGAGTTCGTACCCGCTGCC
GGAATCACCCACGGAATGGACGAGCTTACATGCCTAAAGATCCA
GCCAAACCTCCGGCCAAGGCACAAGTTGTGGGATGGCCACCGGTG
AGATCATACCGGAAGAACGTGATGGTTTCTGCCAAAAATCAAGCG
GTGGCCCGGAGGCGGGCGGCTTCTGTGAAGGTTGAGCAGAAAAGAG
CAAGAGCCTATTGTCAA

Genotyping primers

Forward	atcatcaccatctccaacc	Wormbase
Reverse	CGCGCATCTTGACAATAGGC	Wormbase

Reagents to generate <i>ifb-1::mCherry</i>		Sequence source*
crRNA	aataatgagagcTTATTGTC	Wormbase
Repair template 5'SP9 modified primers		
Forward	TGCAACACACACCCAGAAGACCATCCAATCCGGACAATCCAAGGGA GAGGAGGACAA	Wormbase and Addgene plasmid
Reverse	aagagaaaaagtgtttaaataatgagagcTACTTGTAGAGCTCGTCCAT TC	Wormbase and Addgene plasmid
Repair template	TGCAACACACACCCAGAAGACCATCCAATCCGGACAATCCAAGGGA GAGGAGGACAACATGGCCATCATCAAGGAGTTCATGCGTTTCAAG	Wormbase and Addgene plasmid
PCR	GTCCACATGGAGGGATCAGTCAACGGACACGAGTTCGAGATCGAG GGAGAGGGAGAGGGACGTCCATACGAGGGAACCCAAACCGCCAA GCTCAAGgtaagttaaacaatatataactaactaacctgattatttaaatttcagGT CACCAAGGGAGGACCACTCCATTTCGCTGGGACATCCTCTCCCCA CAATTCATGTACGGATCAAAGGCCTACGTCAAGCACCCAGCCGACA TCCCAGACTACCTCAAGCTCTCCTTCCCAGAGGGATTCAAGTGGGA GCGTGTACGAACTTCGAGGACGGAGGAGTCGTACCCTCACCCA AGACTCTCCCTCAAAGACGGAGAGTTCATCTACAAGgtaagttaaac agttcggtaactaaccatacatatttaaatttcagGTCAAGCTCCGTGGAAC CAACTTCCCATCCGACGGACCAGTCATGCAAAAGAAGACCATGGGA TGGGAGGCCTCCTCCGAGCGTATGTACCCAGAGGACGGAGCCCTC AAGGGAGAGATCAAGCAACGTCTCAAGCTCAAGGACGGAGGACAC TACGACGCCGAGGTCAAGACCACCTACAAGGCCAAGAAGCCAGTC CAACTCCAGgtaagttaaacaatgattttactaactaactaatctgatttaaatttca gGAGCCTACAACGTCAACATCAAGCTCGACATCACCTCCCACAACG AGGACTACACCATCGTCGAGCAATACGAGCGTGCCGAGGGACGTC ACTCCACCGAGGAATGGACGAGCTCTACAAGTAAgctctcattattttta aacaactttttctctt	#75028
Genotyping primers		
Forward	ATCAACAACCCACCAGAGTC	Wormbase
Reverse	cttgagtgtttggggag	Wormbase

*Sequences from indicated sources may have been modified by addition of restriction sites, mutation of sites to prevent CRISPR/Cas9 recutting, by codon optimization and addition of artificial introns (gBlocks).

All final genomic sequences are available in Methods S1.zip



Chapter 5

A possible link between BBLN-1
and vacuolar H⁺-ATPases in
regulating lumen morphology

Sanne Remmelzwaal, Olga D. Jarosinska, and Mike Boxem.

Developmental Biology, Institute of Biodynamics and Biocomplexity, Department of Biology,
Faculty of Science, Utrecht University, Padualaan 8, 3584 CH, Utrecht, The Netherlands.

Abstract

Maintenance of tubular tissue structure and function is vital for the homeostasis of an animal's body. BBLN-1 was previously identified as a regulator of intestinal lumen morphology in *C. elegans* and loss of *bbln-1* leads to the formation of bubble-shaped apical membrane invaginations into the cytoplasm of the intestinal cells. Interaction analyses identified V₁ subunits of vacuolar H⁺-ATPase proteins as putative interactors of BBLN-1. V-ATPases are proton pumps that are required for membrane trafficking and lumen formation. Here, we aim to understand the functional significance of the interaction of BBLN-1 with V-ATPase proteins in the maintenance of lumen morphology. We found that endogenous fluorescent protein fusions of V-ATPases and BBLN-1 co-express in various tissues, but clear colocalization is lacking. Nevertheless, *in vivo* interaction analysis using CeLINC suggests that V-ATPases interact with BBLN-1 in intestinal cells and the epidermis. Knockdown experiments reveal a mutual dependency for V-ATPase V₁ subunits and BBLN-1 for their localization to the apical domain of the intestinal cells. Additionally, loss of various V-ATPase subunits leads to intestinal protrusion phenotypes reminiscent to those of early loss of *bbln-1* function. Thus, we provide a new phenotypical and molecular link between V-ATPases and the small coiled-coil protein BBLN-1. These results may have future implications in understanding the role of the V-ATPase complex in maintaining lumen morphology.

Introduction

Biological tubes are of key importance in multicellular organisms: they regulate the transport and exchange of molecules and ions, nutrient uptake, and the removal of waste. Tubular tissues are formed by epithelial cells and the surfaces of these cells form a protective layer between the internal and external environment, while hosting an important site for intercellular communication. Epithelia are thus vital in maintaining proper homeostasis of an animal's body and exist in various shapes and sizes. Their structure is imposed on their tissue's morphology and needs to be precisely controlled to maintain proper function. Any

abnormalities in tube morphology or biochemical properties can result in diseases (Coskun, 2014; Hiemstra et al., 2015). However, many of the mechanisms responsible for maintaining the integrity and shape of the tubular lumen remain elusive.

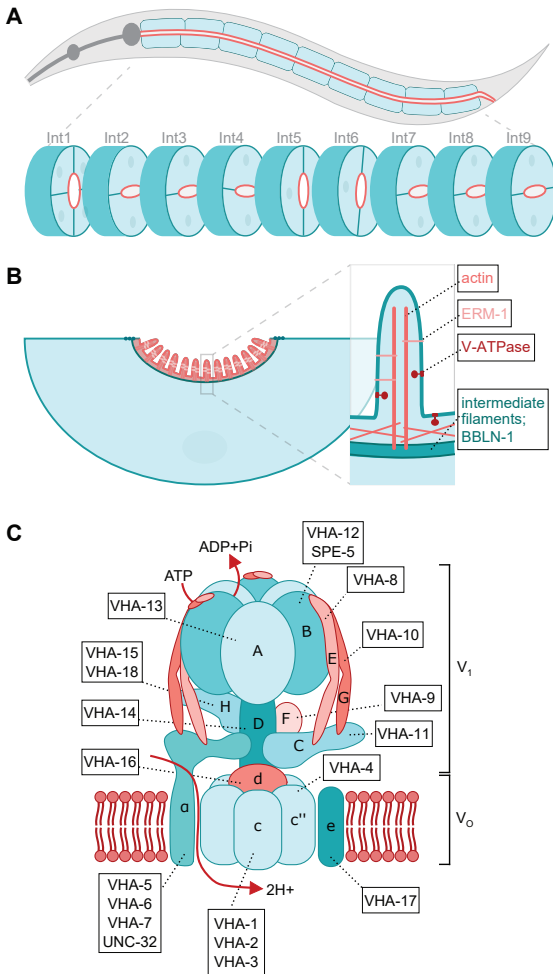


Figure 1. *C. elegans* as a model for intestine morphology and vacuolar H⁺-ATPase function.

Schematic representation of the *C. elegans* intestine (A), the enterocyte with structures relevant for the study (B), and the V-ATPase complex (C). Labels in C indicate the *C. elegans* proteins corresponding to each subunit. Image based on Lee et al., 2010.

The intestinal epithelium of the nematode *Caenorhabditis elegans* is a powerful system to study lumen integrity regulation, due to its simple structure and well understood developmental pathway. The intestine is made of a single-layered intestinal epithelium, which allows for in-depth single-cell level analysis. This multicellular tube is composed of polarized epithelial cells with an apical and basolateral membrane, representative of many tubular tissues in other organisms. The intestinal cells are born during development and do not renew over the animal's lifetime. This feature is beneficial for genetic screens and manipulations, where subtle effects can be discovered and analyzed as they persist over time. The intestine forms an epithelial tube made of 20 cells, organized into nine segments (Int1–9; Figure 1A) (Leung et al., 1999a; Sulston et al., 1983). The first segment is

made of four cells, followed by eight segments made of pairs of semi-circular cells. The intestinal cells are polarized along the apicobasal axis, with the apical domain defining the intestinal lumen (Figure 1B). The lumen is lined with a brush border made of microvilli, which contain bundles of actin filaments anchored at their base to the sub-apical actin-rich terminal web. Under the terminal web lays the endotube, an electron-dense structure comprised of intermediate filament cytoskeletal networks (Munn and Greenwood, 1984). The intermediate filaments are anchored in the apical junction complexes, which are responsible for sealing the plasma membranes of adjacent cells and making the lumen impermeable.

The ease of handling and maintaining large numbers of *C. elegans* allows for genetic screens which can aid in investigating the mechanisms underpinning lumen integrity. Previously, a forward genetic screen identified *bbln-1* as a regulator of intestinal lumen morphology (Chapter 4; Remmelzwaal et al., 2021). Loss of the small coiled-coil protein BBLN-1 leads to luminal herniations into the cytoplasm of *C. elegans* intestinal cells. Abnormal intermediate filament aggregation induces these cytoplasmic invaginations, but it remains unclear what drives luminal expansion. Whole-animal affinity purification of GFP::BBLN-1 followed by mass spectrometry analysis identified the cytoplasmic subunits of the vacuolar H⁺-ATPase (V-ATPase) VHA-9, VHA-13 and VHA-14 as potential BBLN-1 interactors (Chapter 4; Remmelzwaal et al., 2021). These proteins are the *C. elegans* orthologues of respectively subunits F, A and D of the V₁ domain of the highly conserved V-ATPase. Subunits F and D were identified in a similar experiment to uncover interactors of the mammalian homologue of BBLN-1 (bublin/BBLN) using HEK293T cells (Chapter 4; Remmelzwaal et al., 2021).

V-ATPases are rotary pump protein complexes responsible for proton (H⁺) transport across the membrane, driven by ATP hydrolysis. They comprise of two sections, the peripheral V₁ sector which is a catalytic hexamer and the site of ATP hydrolysis, and the integral membrane V₀ sector which is responsible for the movement of the protons across the membrane (Figure 1C). The *C. elegans* genome harbors 21 orthologs of 13 V-ATPase subunits which are expressed in a tissue-specific manner (Futai et al., 2019). They are phylogenetically highly conserved from yeast, plants to mammals and are essential for the development, growth, and survival of the organism (Lee et al., 2010). Their primary site of action is in intracellular membranes including lysosomes, endosomes, and secretory vesicles. However, they are also found in the plasma membrane of some specialized and polarized cells, such as mammalian osteoclasts and kidney intercalated cells (Li et al., 1999; Sun-Wada et al., 2003). Their canonical function is the acidification of lumens by transmembrane proton pumping which is crucial for protein sorting and vesicle trafficking by endo- and exocytosis (Lee et al., 2010). Their function is mainly regulated by their targeted localization to the membrane and their assembly. The free floating V₁ sector gets phosphorylated in response to extracellular and intracellular cues, which drives its assembly with the membrane bound V₀ sector (Voss et al., 2007). They perform non-canonical roles in many other cellular processes, such as the maintenance of cell polarity, cytoskeletal assembly, and the facilitation of membrane fusion (Bidaud-Meynard

et al., 2019; Kontani et al., 2005; Zhang et al., 1998). Additionally, V-ATPases were found to be important in tubulogenesis by modulating the activity of matrix metalloproteinases to drive lumen formation (Chung et al., 2011; Maxson and Grinstein, 2014; Sacharidou et al., 2012).

In this chapter, we have described preliminary experiments aimed at assessing the function of BBLN-1 in the maintenance of lumen morphology by uncovering a molecular and phenotypic link to the archetype of conserved proteins, the V-ATPases. We confirm the recently found interaction between BBLN-1 and subunits of the V-ATPase V_1 domain and uncover tissue-specific expression of the V_1 -ATPase. Lastly, we show that loss of various V_1 -subunits leads to the formation of bubble-shaped protrusions, reminiscent of early loss of *bbln-1*. We therefore provide an interesting avenue in unravelling V-ATPase function as regulators of lumen morphology.

Results

V_1 -ATPases localize to the intestinal apical membrane, hypodermis, amphid glia and excretory canal

To examine the subcellular localization of V_1 -ATPases and to shine light on the location of their potential interaction with BBLN-1, we tagged three V-ATPase subunits N-terminally with a tag for auxin-inducible degradation (AID) and GFP (GFP::AID) using CRISPR/Cas9. The AID-degron allows for tissue-specific and temporally-controlled protein degradation, additionally it has previously been suggested to serve as a functional linker, increasing the functionality of the tagged protein or complex (Boxem lab, unpublished). The homozygous knock-in animals for VHA-9 and VHA-14 were embryonic lethal, indicating that the tagging impaired the protein function. To test whether VHA-9 was not functional due to N-terminal tagging, we generated an endogenous C-terminally tagged VHA-9::AID::GFP variant. However, we obtained similar results and only heterozygous animals survived. Homozygous GFP::AID::VHA-13 animals were viable and no defects in animal development, brood size or morphology were observed by regular maintenance, demonstrating that the fusion protein is functional. All experiments were therefore performed using animals with heterozygous expression of GFP::AID::VHA-9 or GFP::AID::VHA-14 fusion proteins or homozygous GFP::AID::VHA-13 expression.

Fluorescent microscopy analysis of animals expressing GFP::AID fusion proteins of VHA-9, VHA-13 or VHA-14 revealed indistinguishable expression patterns for each subunit, therefore only VHA-9 images are shown. The proteins were highly expressed at the amphid glia in the head of the animal, the apical membrane of the intestinal cells, the hypodermis, and the apical membrane of the excretory canal (Figure 2A). We additionally observed that the fluorescent intensity at the apical membrane of int1 was distinctively lower than in the other intestinal rings (Figure 2A, intestine).

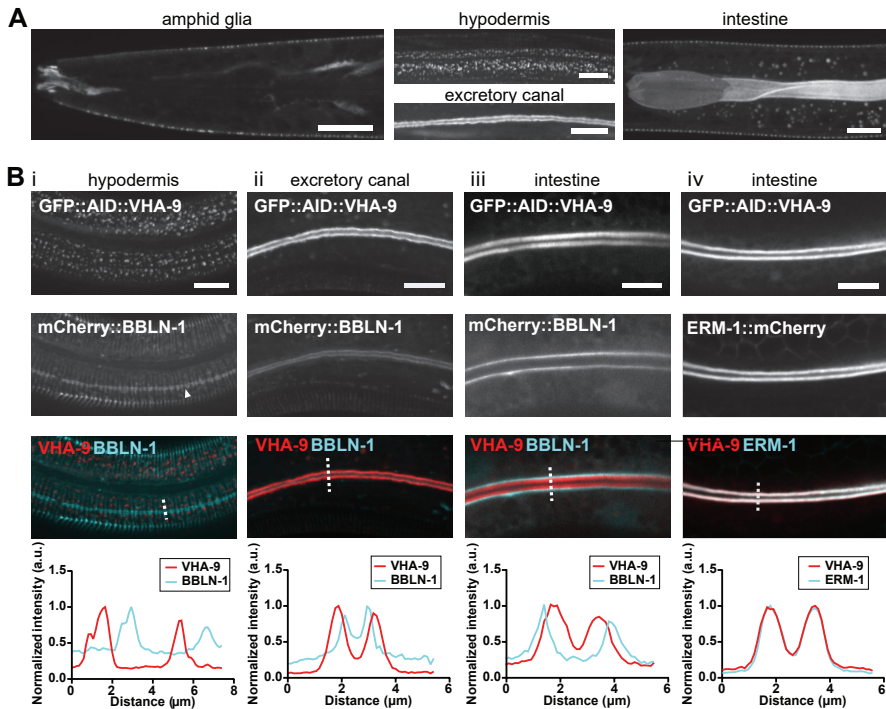


Figure 2. Subcellular localization of V_1 -ATPases in *C. elegans*. (A) GFP::AID::VHA-9 localizes to the amphid glia, hypodermis, excretory canal and apical domain of the intestine. (B) Fluorescent microscopy images showing the subcellular localization of GFP::AID::VHA-9 in respect to mCherry::BBLN-1 (i–iii) or ERM-1::mCherry (iv). Graphs show fluorescent intensity by line scans over the regions represented by the dotted lines in the microscopy images.

No expression pattern has previously been reported for VHA-9 and VHA-14, and previous studies placed VHA-13 exclusively in the intestine and the excretory canal (Lee et al., 2010). However, here we show that the localization patterns of VHA-9, VHA-13 and VHA-14 can be extended to the amphid glia, excretory canal, intestine, and hypodermis. These findings were recently confirmed by fluorescent microscopy images of VHA-13, in a study developing split fluorescent proteins to facilitate endogenous insertion (Goudeau et al., 2021). Apart from *vha-13*, *vha-14*, and *vha-9*, no other genes are known to encode the V-ATPase subunits A, D and F in *C. elegans* (Lee et al., 2010). These localization patterns therefore resemble overall V_1 -ATPase distribution and surprisingly reveal that major tissues like the pharynx or vulva lack the proton-pumping entity of the V-ATPase. We therefore conclude that the cytoplasmic V_1 -entity of the V-ATPase complex specifically localizes to the amphid glia, excretory canal, intestine and hypodermis of *C. elegans*.

BBLN-1 and V_1 -ATPases do not clearly colocalize in any tissue

VHA-9, VHA-13 and VHA-14 localize to similar tissues as BBLN-1. To investigate the potential subcellular locations where the BBLN-1/V-ATPase interaction takes place, we developed double fluorescent reporter strains encoding endogenous

mCherry::BBLN-1 and GFP::AID fusion variants of VHA-9, VHA-13 or VHA-14. In the hypodermis, BBLN-1 localizes to the hemidesmosomes and nerve cords (Figure 2Bi, arrowhead). The three V-ATPase subunits are expressed in speckles flanking these structures (Figure 2Bi) and do not clearly overlap with BBLN-1. In the excretory canal, both BBLN-1 and VHA-9/13/14 were apically localized (Figure 2Bii). In intensity profile analysis, parts of the curves overlapped, but both maxima did not. The imaging resolution is limiting in resolving finer structures, so we were not able to determine with certainty whether BBLN-1 and V_1 -ATPases co-localize in this tissue. BBLN-1::mCherry and GFP::AID::VHA-9/13/14 both localize to the apical domain of the intestine (Figure 2Biii). However, BBLN-1 localizes to the underlying endotube (Chapter 4), whereas V-ATPases localize to the microvilli (Bidaud-Meynard et al., 2019). This is demonstrated further by the perfect colocalization between GFP::AID::VHA-9 and the microvillar protein ERM-1::mCherry (Figure 2Biv). These results suggests that V-ATPases do not colocalize with BBLN-1 at their most prominent expression sites of main *C. elegans* epithelia, but additional high-resolution imaging is needed to exclude colocalization at the apical domain of the excretory canal.

BBLN-1 and VHA-9 interact in the intestinal cells and the epidermis

As we were unable to identify a potential interaction site of BBLN-1 and V-ATPases by colocalization, we next validated their interaction using the recently

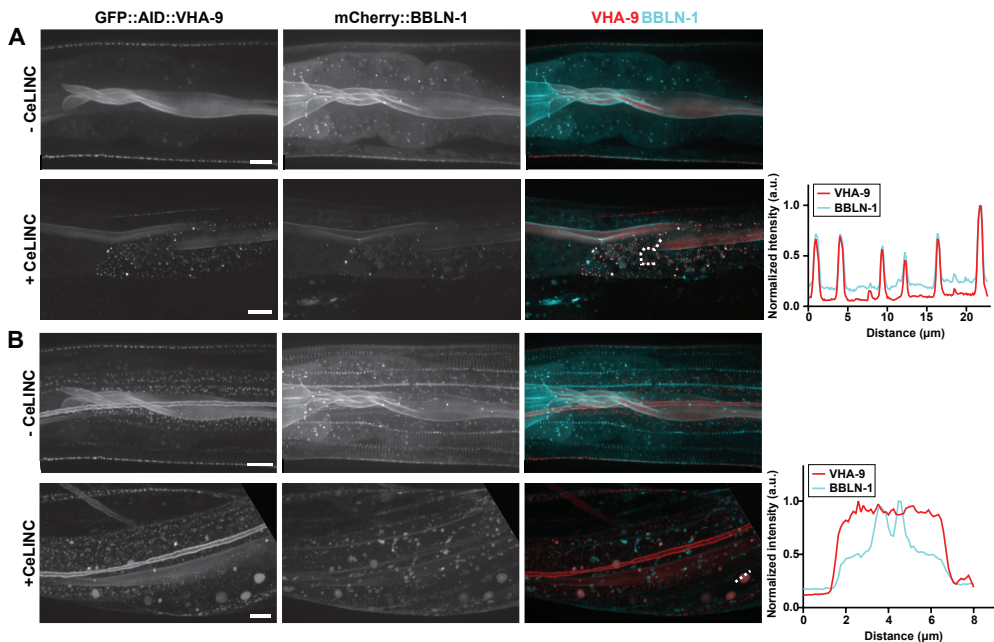


Figure 3. BBLN-1 interacts with VHA-9. Fluorescent images of intestine (A) and hypodermis (B) in animals with (+CeLINC) or without (-CeLINC) transgenic expression of CeLINC plasmids. +CeLINC images show cluster formation of GFP::AID tagged VHA-9 proteins and colocalization of mCherry::BBLN-1 clusters in the intestine (A) and hypodermis (B). Graphs show fluorescent intensity from line scans performed over regions represented by the dotted lines in the microscopy images.

developed CeLINC interaction assay (Chapter 3; Kroll et al., 2021). CeLINC uses a nanobody directed against a fluorescent protein to trap the fluorescently-tagged bait protein in artificial clusters within the cell (Chapter 3; Kroll et al., 2021). Colocalization of a fluorescently-tagged prey protein in the clusters indicates a protein interaction. As BBLN-1 and V-ATPases show no clear colocalization, their interaction might occur where their concentration is not high enough to give a strong intensity readout. Trapping the respective proteins into clusters with CeLINC was anticipated to overcome that problem. To identify and visualize the interaction between BBLN-1 and V-ATPases, we injected animals endogenously expressing GFP::AID::VHA-9/+ and BBLN-1::mCherry with the CeLINC plasmids. Control animals did not express the CeLINC plasmids, and displayed BBLN-1 and VHA-9 expression at the apical domain of the intestine, in the canal and the hypodermis (Figure 3A, B). Upon exposure to light, CeLINC positive animals showed clustering of GFP::AID::VHA-9 in the intestinal cells (Figure 3A). Dual-color imaging and intensity analysis using line scans indicated that mCherry::BBLN-1 colocalizes with the GFP::AID::VHA-9 positive clusters (Figure 3A). We did not obtain animals with sufficient clustering in the excretory canal, nor at the hemidesmosome level in the hypodermis. However, upon expression of the CeLINC proteins, we did observe GFP::AID::VHA-9 and mCherry::BBLN-1 colocalization in large cytoplasmic inclusions reminiscent of the intermediate-filament rich ectopic inclusions of the lateral epidermis of unknown function (Kaminsky et al., 2009) (Figure 3B).

These data suggest that BBLN-1 and VHA-9 interact in the intestinal cells and the lateral epidermis. However, additional protein-protein interaction analysis is needed to exclude the possibility that the interaction takes place in additional cell types.

Loss of *bbln-1* affects apical V_1 -ATPase levels in the *C. elegans* intestine

Given the recognized role of V-ATPases in trafficking and membrane fusion events (Bidaud-Meynard et al., 2019; Cotter et al., 2015), it is tempting to consider that the interaction between BBLN-1 and V-ATPases might be relevant for the apical membrane expansion phenotype. We therefore wondered if *bbln-1* expression might have a direct effect on V-ATPase localization or activity at the apical membrane. We therefore knocked down *bbln-1* expression and analyzed its effect on the three V-ATPase V_1 subunits. We fed animals expressing GFP::AID fusion proteins of VHA-9, VHA-13 and VHA-14 with *bbln-1* dsRNA-encoding bacteria. Loss of *bbln-1* produced membrane protrusions into the intestinal cytoplasm, but we observed no obvious change in subcellular localization of the V_1 -ATPase. However, fluorescent intensity analysis of the different V-ATPase subunits revealed a significant reduction in apical expression levels of VHA-9, but no significant increase in VHA-9 cytoplasmic intensity. For VHA-13 and VHA-14, the variance of apical intensities was high and non-significant compared to control (Figure S1). This difference might be assigned to varying levels of RNAi efficiency.

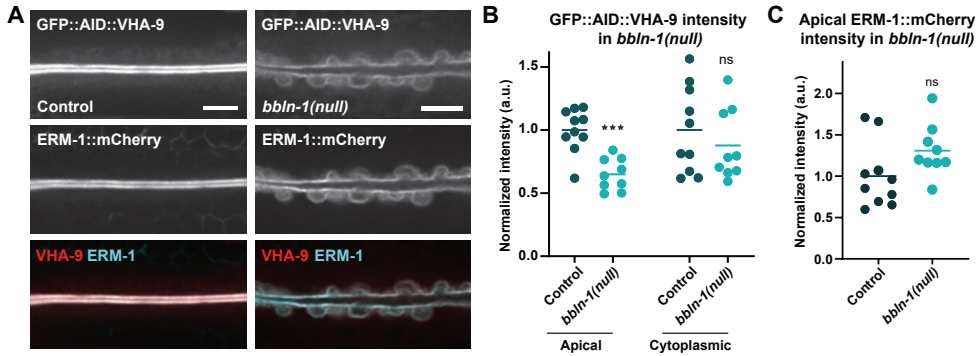


Figure 4. *bbln-1* loss reduces V₁-ATPase levels at the apical domain of the intestine.

(A) Fluorescent microscopy images of GFP::AID::VHA-9 and the apical membrane labelled by ERM-1::mCherry in intestines of *bbln-1*(+) (Control) and *bbln-1*(null) animals. (B) Quantification of apical and cytoplasmic intensity of GFP::AID::VHA-9 in intestinal cells of *bbln-1*(+) (Control) and *bbln-1*(null) animals. Each data point represents the average of four to eight measurements in a single animal (n = 10, each). Larvae were at L3 and L4 stages. Data is represented as mean and analyzed with unpaired t-test, two-tailed P value; ns = P = 0.4131, *** = P = 0.0001. (C) Quantification of apical intensity of ERM-1::mCherry in intestinal cells, in *bbln-1*(+) (Control) and *bbln-1*(null) animals. Each data point represents the average of eight measurements in a single animal (n = 10). Larvae were at L3 larval to young adult stage. Data is represented as mean and analyzed with unpaired t-test, two-tailed P value; ns = P = 0.0775.

To overcome possible complications due to varying levels of *bbln-1* RNAi efficiency, we crossed GFP::AID::VHA-9/+ expressing animals with *bbln-1*(null)-knockout animals. Both the control and *bbln-1*(null) strains endogenously expressed ERM-1::mCherry as an apical membrane marker. To assess whether diminished levels of apical VHA-9 localization were a direct effect of *bbln-1* loss or indirect by the consequential increase of apical membrane surface area, we investigated relative fluorescent intensity levels of GFP::AID::VHA-9 and ERM-1::mCherry at the apical membrane. VHA-9 apical localization levels were significantly reduced in *bbln-1*(null) animals (Figure 4A, B), while cytoplasmic VHA-9 levels were not. Fluorescent intensity analysis of ERM-1::mCherry levels at the apical membrane revealed a non-significant change upon loss of *bbln-1* (Figure 4C). This suggests that the increase in membrane area by invagination formation does not lead to an overall decrease in apical membrane components.

Together these data show that loss of *bbln-1* results in diminished V-ATPase levels at the apical domain of the *C. elegans* intestine.

Loss of *bbln-1* affects apical V-ATPase V₁ domain expression levels in the excretory canal

To investigate whether the effect of *bbln-1* expression on apical V-ATPase V₁ domain levels in the intestine was a tissue specific effect, we expanded our expression analysis from the intestine to the excretory canal. Again, both control and *bbln-1*(null) strains express ERM-1::mCherry fusion proteins endogenously, to serve as an apical membrane marker. As has previously been observed, tagging ERM-1 with a fluorescent protein caused a partial loss of ERM-1 function

(Ramalho et al, 2020), leading to gross deformations of the excretory canal, making it cystic and short (Figure S2A). Surprisingly, in *GFP::AID::vha-9/+* animals expressing ERM-1::mCherry, the canal appeared wild-type, extending to the end of the animal as narrow tubes (Figure S2B). This observation suggests that the phenotype induced by partial loss of ERM-1 function is restored by the partial loss of VHA-9 function. This may be a consequence of opposing roles of ERM-1 and VHA-9, as previous studies proved ERM-1 to be essential for excretory canal lumen extension by expanding the apical membrane (Khan et al., 2013), while V-ATPases prevent unregulated growth (Hahn-Windgassen and Gilst, 2009; Kolotuev et al., 2013; Liégeois et al., 2006). In *erm-1::mCherry; GFP::AID::vha-9/+* animals, both ERM-1 and VHA-9 localized to the apical membrane of the excretory canal (Figure S2B), but VHA-9 expression extended subapically, most likely representing canaliculi (Buechner et al., 2020).

In *bbln-1(null)* animals, the lumen of the canal greatly increased in width and seemed divided into circular confinements with little or no luminal continuation between them (Figure S2C). These canal deformations were visibly distinct from the phenotypes caused by ERM-1 tagging, but are unlikely the result of the lack of BBLN-1 alone, since loss of *bbln-1* does not induce excretory canal deformation as shown by expression of IFC-2 (Figure S2D), one of the main intermediate filaments in the excretory canal (Al-Hashimi et al., 2018). In *bbln-1(null)* animals, ERM-1 retained its apical localization, but VHA-9 appeared to additionally localize to the cytoplasm.

Together, these results hint towards a role for BBLN-1 in controlling V_1 -subunit localization. However, future experiments will be needed to elucidate the relationship between BBLN-1 and V_1 . Specifically, fluorescent marker proteins are needed that do not affect the morphology of the canal, and higher-resolution microscopy will be needed to compensate for the small diameter of the excretory canal.

Loss of V_1 -ATPase subunits affects apical BBLN-1 levels and causes apical membrane protrusions in the intestine

To investigate the role of the interaction between BBLN-1 and the V-ATPase V_1 domains further, we next explored the effect of V_1 -ATPases on BBLN-1 localization. We performed RNAi feeding experiments targeting the three V-ATPase subunits individually in animals expressing endogenous GFP::BBLN-1 fusion proteins to follow BBLN-1 localization, combined with either ERM-1::mCherry to visualize apical membrane morphology or IFB-2::mCherry to observe the underlying intermediate filament network. Both mCherry-fusion proteins were chosen to visually control for RNAi activity, as knockdown of BBLN-1 results in the formation of apical membrane protrusions and holes in the intermediate filament network. As knockdown of V-ATPases is lethal (Lee et al., 2010), we started RNAi feeding in both the first (L1) or last (L4) larval stage to disrupt V-ATPase functions during late or early development, respectively. Compared to empty vector control, RNAi directed at the V_1 -ATPases from L4 stage yielded very few first-generation animals that did not grow in length. The animals fed from L1 developed to

adults but had low progeny numbers. By analyzing fluorescent intensities, we observed a significant reduction of apical BBLN-1 levels upon the knockdown of genes encoding each of the three V-ATPase subunits (Figure 5A, B). There was no significant change in cytoplasmic BBLN-1 levels upon the knockdown of *vha-13*, but we did observe a significant reduction upon RNAi of *vha-9* and *vha-14* (Figure 5B).

Since we started RNAi feeding at different developmental stages, the experiment generated animals with varying phenotypes (Figure 5A). Nevertheless, the occurrence of the diverging phenotypes was homogenous among all three knockdowns. Interestingly, one of the most prominent phenotypes occurring

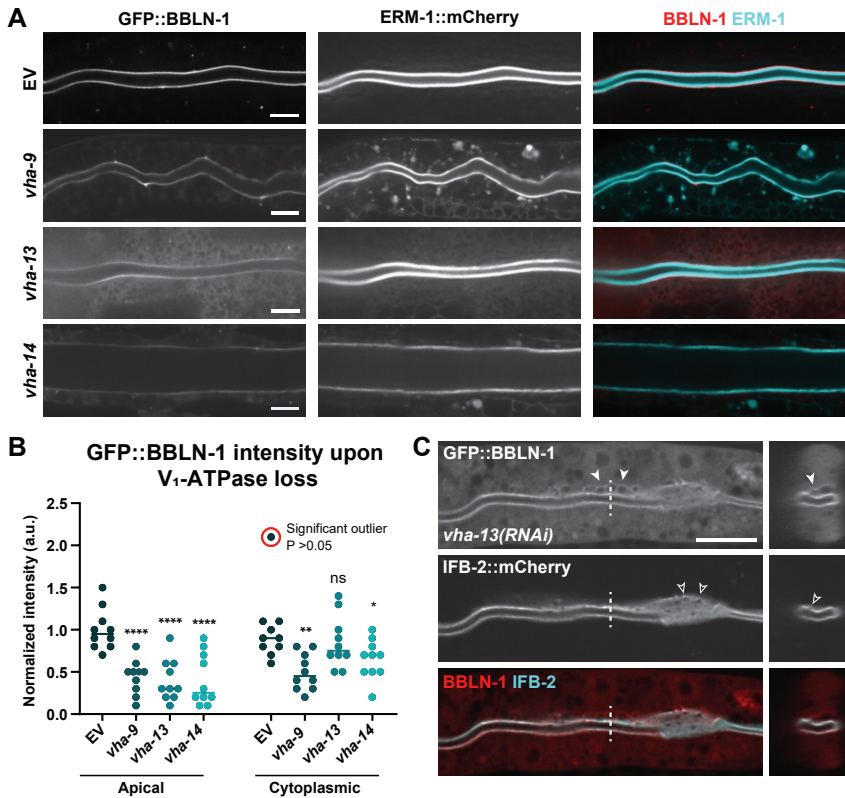


Figure 5. Loss of V₁-ATPases reduces apical BBLN-1 levels and causes apical bubble-shaped structures in the intestine. (A) GFP::BBLN-1 localization at the apical membrane of the intestine visualized using ERM-1::mCherry apical marker, upon the knockdown of targets (indicated on the left). EV: Empty vector. (B) Quantification of apical and cytoplasmic intensity of GFP::BBLN-1 in intestinal cells upon the knockdown of targets indicated on the X-axis. Each data point represents the average of eight measurements in a single animal (n = 10, each). Larvae were at L1 to L4 stage. Data is represented as mean and analyzed with ordinary one-way ANOVA followed by Dunnett's multiple comparisons test; ns = P = 0.5589, * = P = 0.0379, ** = P = 0.0022, **** = P < 0.0001. There was one significant outlier in the data (encircled in red), P > 0.05, which was excluded from statistical analysis. (C) Distribution of GFP::BBLN-1 and IFB-2::mCherry at the apical membrane of intestinal cells in *vha-13(RNAi)* animals. Dotted line indicates site of cross section.

in knockdown animals for each of the individual subunits was the formation of small, bubble-shaped membrane protrusions into the cytoplasm (Figure 5C, filled arrowheads). Equally prominent was the occurrence of 'holes' in the normally sheet-like intermediate filament network (Figure 5C, empty arrowheads). These phenotypes are both reminiscent of early *bbln-1* loss phenotypes, as demonstrated by temporally-controlled degradation of BBLN-1 protein (Remmelzwaal et al., 2021). This suggests that BBLN-1 and V_1 -ATPases perform similar rather than opposing functions in controlling lumen morphology.

In conclusion, these data indicate that BBLN-1 depends on V_1 -ATPases for its localization at the apical domain. These results combined with the data showing decreased V_1 -ATPase expression upon loss of *bbln-1*, suggest that BBLN-1 and V_1 -ATPases are mutually dependent for their localization at the apical domain. Furthermore, loss of each of them is responsible for the induction of apical membrane protrusions in the *C. elegans* intestine, although these invaginations occur with much lower penetrance and severity upon loss of the V-ATPase subunits than upon loss of BBLN-1. These findings suggest that BBLN-1 and V-ATPases act in parallel to control apical membrane morphology.

BBLN-1 localization upon loss of V-ATPase proton pumping activity

To investigate whether the reduction of apical BBLN-1 localization was due to loss of the V-ATPase proton pumping activity or non-canonical V-ATPase function, we subjected GFP::BBLN-1 expressing animals to Bafilomycin A_1 treatment. Bafilomycin A_1 is a drug that targets the V_o domain of V-ATPases, inhibiting the rotation and hence the passage of protons through the membrane (Yoshimori et al., 1991). We used two different strains to additionally investigate the phenotypic effect of Bafilomycin A_1 treatment on *C. elegans* intestinal morphology. The animals either endogenously expressed ERM-1::mCherry to visualize the apical membrane or IFB-2::mCherry to visualize the effect on the intermediate filament network structure, and GFP::BBLN-1.

Upon Bafilomycin A_1 treatment, around half of the animals were dead after 24 hours. This is in line with previous reports showing high lethality upon blocking V-ATPase function (Lee et al., 2010), suggesting successful inhibition of proton pumping activity. We observed a large variety of phenotypes among surviving animals, including divergent intestinal morphologies. For example, many intestines displayed the aggregation of apical material in the cytoplasm (Figure S3A, B); less frequent was the appearance of small holes in the IFB-2 network (Figure S3A), the formation of bubbles at the apical domain (Figure S3B), and widened lumens (Figure S3A, B).

Under normal conditions, BBLN-1 localizes subapically in the intestine at the intermediate-filament rich endotube structure (Figure S3A, B). Animals treated with Bafilomycin A_1 exhibited remarkably diverse patterns and levels of GFP::BBLN-1 expression. The phenotypes did not only vary between animals, but also within intestinal cells within a single animal (Figure S3A, B). This variance might likely be a secondary effect of the equally diverging intestinal

morphologies in Bafilomycin A₁-treated animals. We therefore refrain from drawing any conclusions regarding the effect of V-ATPase proton pumping activity on BBLN-1 localization.

Discussion

Initially found as components of endosomes, research on V-ATPase function has primarily been focused on intracellular organelles. Embedded in these organelles, the multi-subunit complex performs canonical functions that rely on its proton pumping ability to regulate endocytosis, synaptic vesicle loading, protein processing and degradation, etcetera. V-ATPase implications in pH sensing, scaffolding protein-protein interactions and membrane fusion reveal a collection of molecular roles besides its proton pumping activity, and expands V-ATPase function beyond the acidification of organelles. This plethora of functions makes unravelling V-ATPase function everything but straightforward, wherefore many open questions remain. Previously, the small coiled-coil protein BBLN-1 was identified as a potential interactor of V₁-ATPase subunits. BBLN-1 is a regulator of apical domain morphology and intermediate filament network integrity, and causes bubble-shaped membrane protrusions in the *C. elegans* intestine when lost. In this study we investigated V-ATPase function in relation to BBLN-1 using *C. elegans* as a model. Our characterization reveals a mutual dependency and phenotypic link between V₁-ATPases and BBLN-1 and provides new implications of V-ATPase function in apical membrane morphology. This study brings us forward in unravelling the functions of the multifaceted V-ATPase multi-subunit complex.

Subcellular VHA-9, VHA-13 and VHA-14 localization in the intestine resembled the localization of the intestine-specific α -subunit of the V_o domain VHA-6 (Oka et al., 2001). VHA-6 is responsible for the localization of the V-ATPase complex to the apical membrane and the acidification of the intestinal lumen (Allman et al., 2009). Localization of the V₁ subunits at the apical membrane therefore indicates incorporation of the proteins in VHA-6 containing complexes, where they at least ensure acidification of the intestinal lumen. The induced lethality of animals homozygously expressing endogenous VHA-9 or VHA-14 fluorescent reporter proteins revealed that these proteins lost essential functionality upon tagging. Nevertheless, heterozygous animals for said fusion proteins displayed similar expression patterns as functional VHA-13 fusions. Both VHA-9 and VHA-14 are part of the rotary stalk unit needed for the coupling the V₁ and V_o domains, so these data would indicate that at least the rotary stalk of the V₁ domain is able to assemble with the membrane-bound V_o domain without being fully functional.

BBLN-1 and V-ATPases most prominently localize to the apical domain of intestinal cells. Here, V-ATPases are embedded in the cell membrane while BBLN-1 is enriched at the intermediate-filament rich endotube, both structures separated by the actin-rich terminal web. The physical separation suggests that these proteins do not interact at the apical domain, but in a location with less prominent expression levels. We hypothesize two potential sites of BBLN-

1 and V_1 -ATPase interaction. One interesting candidate interaction site is the cytoplasm. Studies have shown that the V_1 domain of V-ATPases can assemble independently of the membrane bound V_0 domain. Yeast analysis showed that the assembly takes place in the cytoplasm over a series of smaller complex formations that come together to form the full V_1 domain (Tomashek et al., 1997). The full mechanism of assembly still remains largely elusive, but it is known that the F and D subunits initially interact to assemble one of the smaller sub-complexes (Graham et al., 2000; Tomashek et al., 1997; Wang et al., 2020). The *C. elegans* orthologues of the F and D subunits, respectively VHA-9 and VHA-14, establish a highly conserved interaction with BBLN-1. The interaction has repeatedly been identified between the human orthologue of BBLN-1 (Bublin/BBLN) and the human D (ATP6V1D) and F (ATP6V1F) subunit (Luck et al., 2020; Rolland et al., 2014). In an across species study, human Bublin was additionally found to interact with the yeast orthologue of the D subunit, VMA8 (Zhong et al., 2016). The strong interaction of BBLN-1 with specifically the stalk region could indicate that BBLN-1 interacts with the F and D subunits particularly at this point of V_1 domain assembly. BBLN-1 might perform a chaperone-like function in facilitating rotary stalk complex formation. This hypothesis fits well with our results in which loss of *bbln-1* lead to lower levels of the full V-ATPase at the apical domain. However, since loss of *bbln-1* is not lethal whereas the loss of V-ATPase subunits is, BBLN-1 cannot be an essential component in complex formation.

A second potential interaction site for BBLN-1 and V_1 -ATPase is at transporting vesicles. The localization of BBLN-1 at the apical region depends on the V_1 -ATPase, and vice versa. It can be hypothesized that they are transported to the apical domain together, and then are assigned to their designated locations. With its 125 amino acids, BBLN-1 is a small protein that could possibly associate with the V-ATPase core without hindering rotary properties. V_1 -ATPase and BBLN-1 could therefore together bind a V_0 domain found in exocytotic vesicles, destined to go to the apical membrane. Rab proteins, from the small GTPase superfamily, are found on vesicles and act as tags to target and transport vacuoles to their destined subcellular location. RAB-11 is enriched in exocytotic vesicles and is, amongst many, required for exocytosis (Sato et al., 2008; Szumowski et al., 2014). RNAi experiments showed that the knockdown of *rab-11* causes the formation of holes in the intermediate filament network (S.R., O.D.J., unpublished data), which is known to precede protrusion formation. Additionally, *rab-11* knockdown animals occasionally formed bubble-shaped membrane protrusions on the apical membrane (S.R., unpublished data). Phenotypes reminiscent of *rab-11* loss were seen in Bafilomycin A₁ treated animals, in which V_0 proton pumping activity was blocked. This RAB-11 dependence on V_0 activity is in agreement with prior observations (Bidaud-Meynard et al., 2019). Interestingly, RAB-11 was identified, with low confidence, in the BBLN-1 pull down and mass spectrometry analysis (PRIDE (Perez-Riverol et al., 2019) dataset PXD024387). These findings fit with a model in which the V_1 -domain and BBLN-1 assemble with the V_0 -moiety in RAB-11-positive vacuoles for transport to the apical domain.

The potential of these suggested interaction sites is further supported by observations from our knockdown experiments. Reduction of either of the three investigated V_1 -ATPases resulted in diminished apical BBLN-1 levels, while we observed no significant change in cytoplasmic BBLN-1 levels upon the knockdown of *vha-13*, but we did for RNAi of *vha-9* and *vha-14*. Interestingly, this is in accordance with the confidence with which either subunits are identified as interactors of BBLN-1: VHA-13 was identified as a low-confidence interactor, and both VHA-9 and VHA-14 as high-confidence interactors (Rommelzwaal et al., 2021). If BBLN-1 is indeed involved in V_1 -ATPase stalk assembly in the cytoplasm, knockdown of either stalk subunit—but not VHA-13—would make BBLN-1 redundant. If the entire V-ATPase complex is involved in BBLN-1 delivery at the apical domain, depletion of any V-ATPase subunit would result in lowered apical BBLN-1 levels. Imaging with increased resolution should elucidate whether BBLN-1 colocalizes with V-ATPase coated vesicles. Furthermore, pulldown experiments could identify relative V-ATPase subcomplex levels in the presence and absence of BBLN-1, revealing whether loss of BBLN-1 results in a decrease of the rotary stalk subcomplex or general V-ATPase levels.

The V_o domain has been shown to perform non-canonical solitary functions (Bidaud-Meynard et al., 2019), but the V_1 domain cannot perform any function without the V_o domain, due to its auto-inhibition by the H-subunit (Oot et al., 2016). We aimed to uncover if BBLN-1 collaborates with V-ATPases through its canonical (V_o+V_1) or non-canonical (V_o) function using Bafilomycin- A_1 induced inhibition of V-ATPase protein pumping activity, but failed to draw any conclusions on the matter. However, since BBLN-1 interacts specifically with V_1 subunits of the V-ATPase complex, BBLN-1 likely collaborates on its canonical function. We therefore initially discarded any V_o -specific functions in our hypotheses leading to this investigation. Intriguingly, yeast cells lacking the V-ATPase F-subunit show decreased levels of the V_o -complex (Graham et al., 1994). This is not observed for the deletion of any other V_1 -subunits and suggests that the V_o -moiety forms a more direct link with the rotary stalk than with the entire V_1 -domain. This implies that the rotary stalk has a more direct effect on V_o function, complicating the segregation of the BBLN-1/V-ATPase collaboration into non-canonical or canonical V-ATPase function. Nevertheless, it would be interesting to investigate whether V_o levels are comparatively higher than V_1 levels at the apical domain upon *bbln-1* loss, to understand if V_o expression compensates for V_1 loss and if BBLN-1 affects overall V-ATPase assembly.

The bubble-shaped membrane protrusions induced by loss of *bbln-1* and loss of V-ATPase function showed several structural dissimilarities. Loss of *bbln-1* induces cytoplasmic invaginations of the apical membrane that are covered with microvilli and marked by ERM-1 expression. The intermediate filament network collapses into bundles or cables around these luminal protrusions. V_1 -ATPase loss induced small invaginations that were sparsely decorated by BBLN-1. Functional V-ATPase loss by Bafilomycin A_1 -induced inhibition lead to bubbles that were not marked by apical membrane proteins and might therefore not be directly connected to the intestinal lumen. Breaches in the IF network were

sparse and small, and the network did not fall into cable-like structures in either situation. The V-ATPase phenotypes were reminiscent of early *bbln-1* loss. Future endeavors should reveal if BBLN-1 and V-ATPases collaborate on maintaining lumen morphogenesis and elucidate the mechanistic cause underlying both phenotypes.

We solely investigated the relation between BBLN-1 and V-ATPases under controlled culture conditions, in the absence of environmental or microbiological stresses. However, V-ATPases are known to be manipulated for viral entry (Santos-Pereira et al., 2021) and are found on membrane-repairing endosomes induced upon infection in *C. elegans* (Julien et al., 2018). Furthermore, the intermediate filament network is known to function as a barrier against pathogens (Geisler and Leube, 2016), and phenotypes reminiscent of *bbln-1* mutants have repeatedly been observed upon microbial infection (Geisler et al., 2019; Stutz et al., 2015). We did not find any structural sites of BBLN-1 and V₁-ATPase interaction, but this might well change under pathological conditions. It would therefore be an interesting avenue to explore a potential interplay between BBLN-1 and V-ATPase in the context of microbiological stresses.

Mammalian Bublin (BBLN) has recently been identified as a negative regulator of osteoclast longevity (Yamakawa et al., 2020). Osteoclasts are cells that destroy old bone and regulation of their cell number is deeply involved in the pathogenesis of bone diseases (Teitelbaum, 2007). Mice lacking Bublin exhibited low bone mass due to increased osteoclast and bone resorption (Yamakawa et al., 2020). The authors of the study refer to the gene as Merlot and find that it induces apoptosis of osteoclasts. Osteoclasts rely on V-ATPases at their ruffled membranes to acidify extracellular space to facilitate degradation of the bone during bone resorption (Chu et al., 2021; Toyomura et al., 2003). Interestingly, defects in V-ATPase function can both lead to bone excess, a condition called osteopetrosis, or low bone mass, called osteoporosis. The implication of both Bublin and V-ATPases in bone resorption presents an interesting avenue for future research on both Bublin/V-ATPase interplay as well as therapeutic approaches to target bone diseases.

Irrespective of the precise role of the V₁-sector in respect to BBLN-1 function and lumen morphogenesis, our findings bear potentially important implications. First, we uncovered the cellular organization of three V₁-ATPase subunits, VHA-9, VHA-13, and VHA-14. The expression patterns of these essential components limited V₁-sector function to four tissues: amphid glia, excretory canal, intestine, and hypodermis. A major objective will be to unravel what acidifies cellular compartments in other cells of the animal's body. In particular, how and if lysosomal degradation is regulated in these tissues. Second, we identified a mutual dependency of BBLN-1 and V₁-ATPases for their subcellular localization. Lastly, we describe analogous phenotypes between loss of *bbln-1* and the V₁-ATPase. Both findings have to be explored further to broaden our understanding of the mechanisms employed to control V-ATPase activity and to comprehend its mode of action. This will contribute to both our basic understanding of cell physiology and to the efforts to therapeutically target the

V-ATPase in treating diseases in which it participates, including viral infection and osteoporosis.

Materials and methods

Laboratory strains and culture conditions

All nematodes used, wild-type strain and transgenic animals, were derived from Bristol N2 *C. elegans* strain, and were maintained on nematode growth medium (NGM) seeded with *Escherichia coli* OP50 and kept at 15°C, unless stated otherwise. A complete list of strains and associated genotypes used in the study are included in Table 1.

Generation of genetically modified strains

Knock-in and knockout animal strains were generated with CRISPR/Cas9 genome editing using a plasmid-free approach (Ghanta & Mello, 2020). In order to generate the repair template, the desired insert was PCR amplified using specifically designed primers. The amplification of the GFP, mCherry, and AID::GFP sequence was done from pre-existing donor vectors pHRP020, pHRP019, and pJK86 respectively and GFP::AID from the newly generated plasmid pSMR37. crRNA and primer sequences are found in Supplemental Table 1 and all generated lines were sequence verified.

Generation of GFP::AID donor vector - The GFP::AID donor vector, pSMR37, was generated using the SapTrap approach (Dickinson, 2016). The final concentration of each of the reagents in the SapTrap reaction mix was dependent on its fragment size (bp) and concentration. The pMLS257 plasmid was pre-digested, 1 ng of plasmid, 1 µl of SapI (NEB R0569), 1X CutSmart Buffer (NEB) and water up to 50 µl, at 37°C for at least 20 min. Prior to preparing the reaction mix, 6x SAP enzyme mix was prepared using 28 µl of SapI, 6 µl of T4 polynucleotide kinase (NEB M0201) and 6 µl of 400 U/µl T4 DNA ligase (NEB M0202S), and stored at -20°C until use. The 6x reaction buffer contained 24 µl of 10X NEB T4 DNA ligase buffer (NEB), 1 µl of 1M Potassium Acetate and 15 µl of water, and was stored at -20°C until use. GFP was amplified from pHRP020 and AID was ordered as a gBlock. The SapTrap reaction mix was set up using the pre-digested plasmid, GFP and AID sequences, 1X SAP trap reaction buffer mix, 1X SAP trap enzyme mix and water. The tube was incubated in a thermocycler for 2 to 4 h (37 °C for 1 min, 16 °C for 1 min, 99 cycles), to enhance enzyme-mix function. The vector was transformed into DH5α competent cells. All generated plasmids were sequence verified (Macrogen) and a list of all used oligonucleotides (IDT) and gBlocks (IDT) is included in Table S1.

RNAi feeding

RNA interference (RNAi) was done by feeding *C. elegans* dsRNA producing *E. coli* grown on NGM plates with final concentration of ampicillin at 50 µg/ml and isopropyl-β-D-1-thiogalactopyranoside (IPTG) at 1mM concentration. The *bbln-1*, *ifb-2*, *ifd-2*, and *let-413* RNAi clones were obtained from the genome wide full-length HT115 RNAi library ORFeome 3.1 collection (Rual et al., 2004). The

RNAi clone for *ifc-2* was obtained from the genome wide Ahringer fragment HT115 RNAi feeding library (Kamath et al., 2003). *ifd-1*, *ifp-1*, *sma-5*, *act-5*, and *ifo-1* were generated at the Boxem lab (Remmelzwaal et al., 2021; Chapter 4). All constructs were made in the L4440 vector and served as a RNAi control. Prior to use, all colonies were cleaned up using NucleoSpin® Plasmid Easy Pure Kit (Macherey-Nagel) and were verified using Sanger sequencing (Macrogen). For RNAi feeding experiments, the bacterial clones were pre-cultured in 2 ml lysogeny broth (LB), with 100 µg/ml ampicillin and 2.5 µg/ml tetracycline, for 6 to 8 hours. The culture was replenished with LB to 10 ml and cultured overnight, at 37°C shaking at 200 rpm. To induce the expression of dsRNA, IPTG was added to the bacteria to final concentration 1mM and shaken at 37°C for 60 min. The bacteria was then spun down, 15 min at 4°C and 3220 g and 8 ml supernatant was removed, concentrating the colony five times. The bacterial pellet was re-suspended in the remaining 2 ml, and 200 µl of bacteria was plated onto the NGM RNAi plates. The plates were kept at room temperature for 48 h. Animals of L1 and L4 developmental stage were placed on the seeded plates and incubated at 20°C until analyzed.

Auxin-inducible degradation

Auxin treatment was done by transferring *C. elegans* to seeded NGM plates with indole-3-acetic acid (auxin) (Alfa Aestar A10556). The plates were stored at 4 °C until used and stored in the dark. The auxin was added to the NGM after initial cooling to 60 °C and before pouring the plates at the final 1mM concentration. The plates were seeded with standard OP50 and kept at room temperature for 1-2 days before transferring the animals. The animal strains with AID-tagged endogenous BBLN-1 protein and TIR expression driven by the intestine specific *elt-2* promoter, were transferred to the plates minimum an hour before imaging. The animals were semi-synchronized by putting 40 adults on a plate for 1 hour, allowing them to lay eggs. The plates were washed with M9 buffer (0.22 M KH₂ PO₄, 0.42 M Na₂ HPO₄, 0.85 M NaCl, 0.001 M MgSO₄) to remove the larvae and adults, leaving only eggs behind for future analysis.

CeLINC optogenetic protein interaction analysis

CeLINC was carried out by injecting animals with an cluster-forming mix, allowing for protein clustering and imaging them (Chapter 3). The injection mix included a plasmid encoding a cryptochrome (CRY2) fused to an anti-GFP nanobody (pJRK138) at 15ng/µl, a cryptochrome- interacting bHLH1 (CIB1) fused to multimerization domain (MP) of Ca²⁺/calmodulin-dependent protein kinase II α (pJRK136) at 15 ng/µl, carrier DNA Lambda DNA (ThermoFisher Scientific™) at 55 ng/µl and roller phenotype co-injection marker (pDD382) at 20 ng/µl. The mix was injected into the gonads of animals of double fluorescent reporter strain, expressing proteins of interest tagged with GFP and mCherry. After injection, the singled animals were put on seeded NGM plates, kept at 20 °C in the dark until imaged. The reversible clustering of the proteins occurs seconds after exposure to blue light, therefore the animals were handled in the dark when preparing the slides. The slides were only illuminated with blue/white light when imaged. Only animals expressing the roller phenotype were used for analysis.

Bafilomycin A₁ treatment

Animals of varying ages were grown on OP50 seeded NGM plates. Bafilomycin A₁ (BioViotica) was diluted using 100% methanol to a stock concentration of 1mM, and kept in the dark and at -20 °C until use. The final concentration of Bafilomycin A₁ used in the experiment was 6 μM diluted in water. The Bafilomycin A₁ solution was placed on plate to fully cover the NGM with a layer of liquid so all animals were suspended in the liquid. The animals were kept at 20 °C for 24 hours before imaging. Control animals were suspended in 0.6 % methanol in water. Animals were picked directly from the liquid onto the imaging slides.

Microscopy

C. elegans imaging was done by mounting larvae or embryos in a 10 mM Tetraimazole solution in M9 (0.22 M KH₂ PO₄, 0.42 M Na₂ HPO₄, 0.85 M NaCl, 0.001 M MgSO₄) to paralyze the animals, on a 5% agarose pad. Spinning disk confocal imaging was carried out using a Nikon Ti-U microscope equipped with a Yokogawa CSU-X1 spinning disk using a 60X DIC N.A. 1.40 oil-immersion objective, with the exception of imaging RNAi feeding of *vha-9*, *vha-13*, *vha-14* on *bbln-1(null)* animals, where the imaging was done using a 20x DIC N.A. 0.50 dry objective. The temperature of the microscopy room was maintained at 20°C. Laser power, exposure time and gain were kept constant throughout the experiments for individual strains and their control genotypes. The data and images were acquired using MetaMorph Microscopy Automation & Image Analysis software. All stacks along the z-axis were done with 0.25 μm intervals. Fluorophores in this study included GFP, mCherry, and YFP.

Image analysis

All images obtained were analyzed and processed using ImageJ (Fiji). Intensity distribution profiles of fluorescent proteins were obtained from a Z-stack spanning the tissue of interest: the intestinal lumen, the excretory canal or the dorsal hypodermis. For obtaining the intestinal apical intensity measurements, the values were measured from the intestinal rings int2 to int4, where a 40-pixel (4.7 μm) wide line was drawn perpendicular to the lumen of the intestine, crossing the two walls of the intestine when possible. For *bbln-1(null)* animals, values were acquired from the fragments of straight lumen and not at the protrusions. For cytoplasmic intensity analysis, the average value from a 40-pixel diameter circle was used. For intensity distribution profiles of relative localization of BBLN-1 and VHA-9 in different tissue, or the presence of fluorescence protein in clusters in LARIAT experiments, a 1 pixel wide line was drawn through the structure. The background, also measured using 40-pixel diameter circle, was subtracted from the values.

Images used for the analysis of relative GFP::AID::VHA-9/ERM-1::mCherry levels were obtained with different image acquisition settings. In order to make the results as comparable as possible, the background values were normalized to the control background, and from this we calculated relative apical intensity levels.

Statistical analysis

Statistical analysis was done using GraphPad Prism 8.4.3. For population comparisons, a Kolmogorov-Smirnov test for normality was performed to ensure data followed Gaussian distribution. For data following Gaussian distribution, comparison between two populations was done using the unpaired t-test for data with comparable variances, and Welch's test for data with significantly different variances. Ordinary one-way ANOVA followed by Dunnett's multiple comparison test was used for comparisons between more than two data sets. An outlier test was performed using the ROUT (Q = 1%) method. The number of samples and the significance of data was included in the figure legends.

Supplemental Information

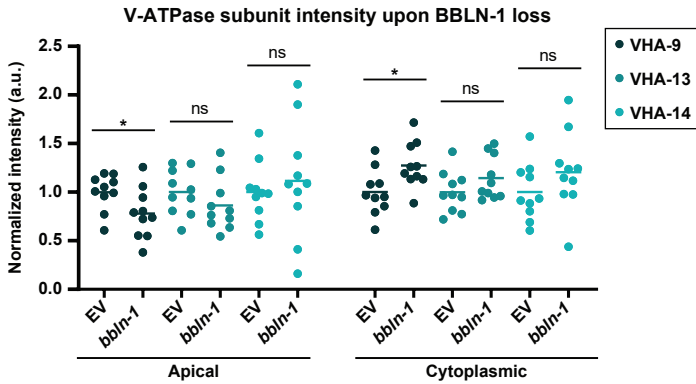


Figure S1. Quantification of apical and cytoplasmic intensity of GFP::AID::VHA-9, GFP::AID::VHA-13 and GFP::AID::VHA-14 in intestinal cells, in control (EV = empty vector) and *bbln-1(RNAi)* animals. Each data point represents the average of eight measurements in a single animal ($n = 10$, each). Larvae were at L3 larval to young adult stage. Data points are color coded for the different VHA proteins analyzed. Data represented as mean and analyzed with unpaired t-test, two tailed P value; ns = $P > 0.05$, * = $P < 0.05$.

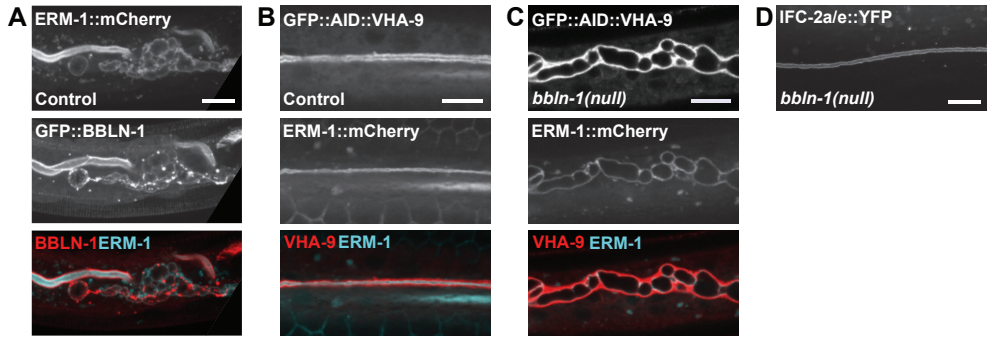


Figure S2. Structure of the excretory canal in animals expressing (A) ERM-1::mCherry and GFP::BBLN-1 (L3 larva), (B) GFP::AID::VHA-9 and ERM-1::mCherry (L4 larva), (C) GFP::AID::VHA-9 and ERM-1::mCherry in *bbln-1(null)* background (L3 larva), and (D) IFC-2a/e::YFP in *bbln-1(null)* background (L2 larva).

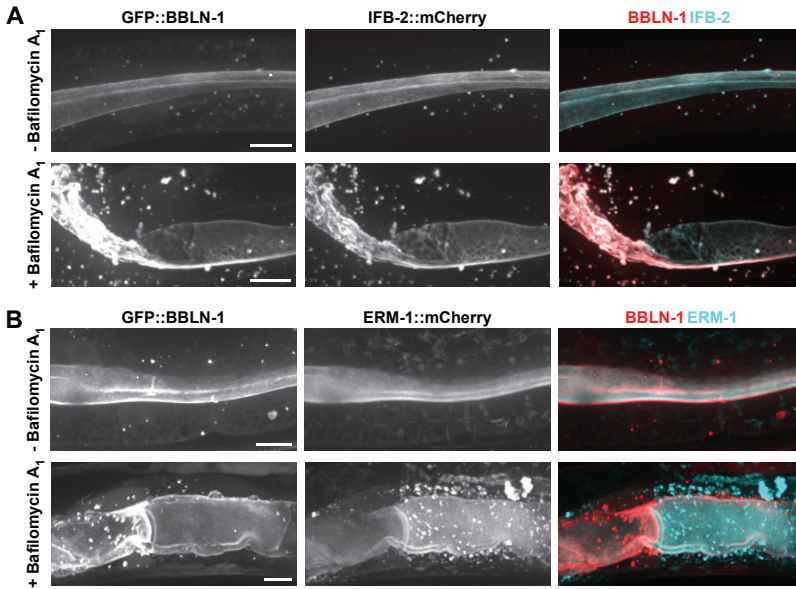


Figure S3. (A) Distribution of GFP::BBLN-1 and IFB-2::mCherry at the apical membrane of intestinal cells with (+) and without (-) Bafilomycin A₁ treatment. The animals were young adults. (B) Distribution of GFP::BBLN-1 and ERM-1::mCherry apical membrane of intestinal cells with (+) and without (-) Bafilomycin A₁ treatment. The animals were at L4 larval stage.

Table S1. List of strain used.

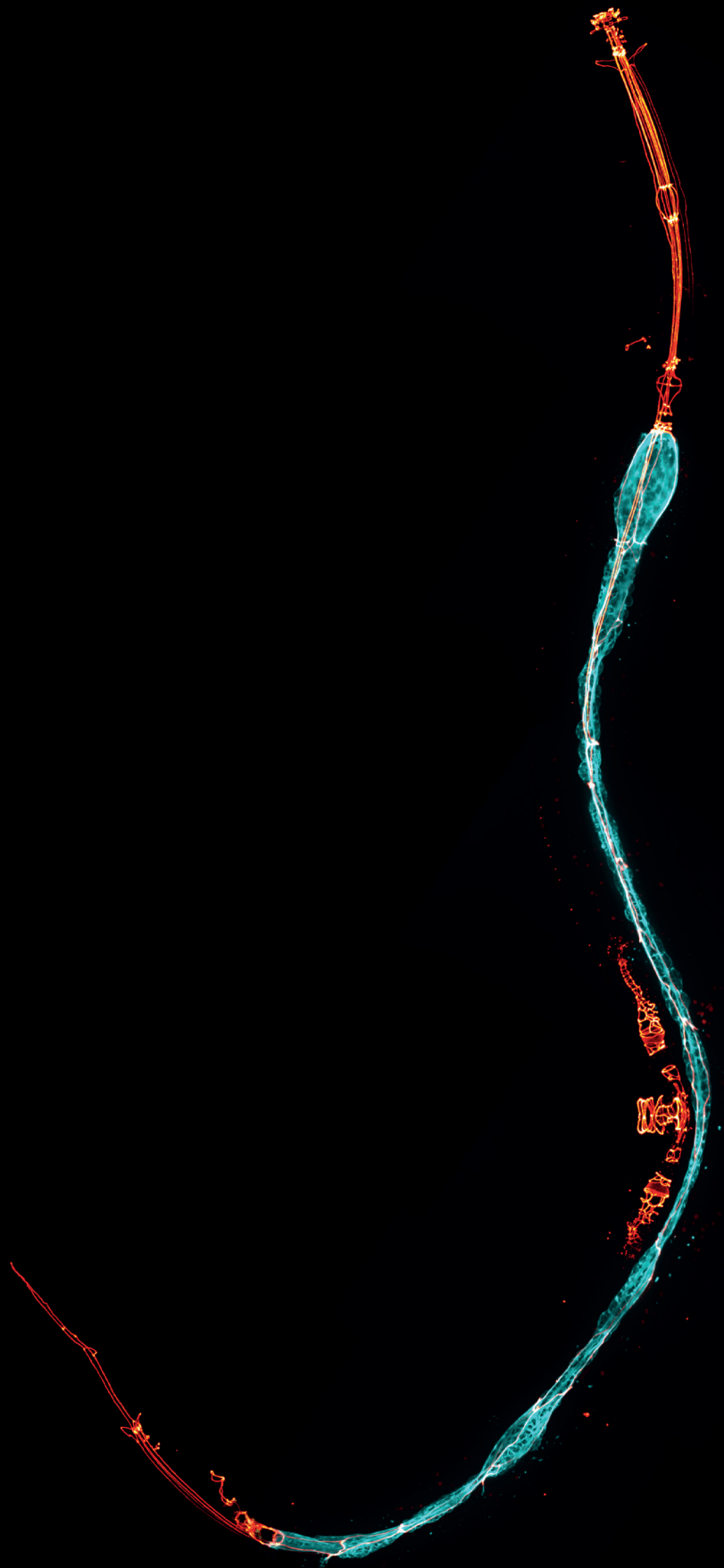
Name	Genotype	Source
N2	Wild type	CGC
BOX427	<i>erm-1(mib40[erm-1::AID::mCherry])l;</i> <i>bbln-1(mib71[GFP::bbln-1]) X</i>	Rommelzwaal et al. 2021
BOX436	<i>ifb-2(mib74[IFB-2::mCherry]) ll;</i> <i>bbln-1(mib71[GFP::C15C7.5]) X</i>	Rommelzwaal et al. 2021
BOX481	<i>ifc-2a::yfp(kc16) X;</i> <i>bbln-1(mib70[Pbbln-1::GFP1-3, Δ0-914bp]) X</i>	Rommelzwaal et al. 2021
BOX612	<i>vha-9(mib109[GFP::AID::VHA-9]) ll/+</i>	This study
BOX613	<i>vha-9(mib109[GFP::AID::VHA-9]) ll/+;</i> <i>bbln-1(mib93[mCherry::bbln-1])X</i>	This study
BOX618	<i>erm-1(mib40[erm-1::AID::mCherry]) l;</i> <i>vha-9(mib109[GFP::AID::VHA-9]) ll/+;</i> <i>bbln-1(mib70[Pbbln-1::GFP1-3, Δ0-914bp])X</i>	This study
BOX619	<i>erm-1(mib40[erm-1::AID::mCherry]) l;</i> <i>vha-9(mib109[GFP::AID::VHA-9]) ll/+</i>	This study
BOX639	<i>vha-9(mib118[vha-9::aid::GFP]) ll allele #1</i>	This study
BOX640	<i>vha-9(mib119[vha-9::aid::GFP]) ll allele #2</i>	This study
BOX641	<i>vha-13(mib120[GFP::AID::vha-13]) V allele #1</i>	This study
BOX642	<i>vha-13(mib120[GFP::AID::vha-13]) V allele #2</i>	This study
BOX643	<i>vha-14(mib122[GFP::AID::vha-14]) III allele #1</i>	This study
BOX644	<i>vha-14(mib123[GFP::AID::vha-14]) III allele #2</i>	This study
BOX666	<i>vha-13(mib121[GFP::AID::vha-13]) V;</i> <i>bbln-1(mib93[mCherry::bbln-1])X</i>	This study
BOX680	<i>vha-14(mib122[GFP::AID::vha-14]) III;</i> <i>bbln-1(mib93[mCherry::bbln-1])X</i>	This study

Table S2. DNA reagents used for the generation of the pSMR37 GFP::AID donor plasmid.

		Sequence (5'-3')
GFP	Forward primer	CTGCTCTTCGTGGTCCAAGGGAGAGGAACTC
	Reverse primer	CTGCTCTTCGCATGTAGAGCTCGTCCATTCCGTG GG
AID	gBlock	CTGCTCTTCGATGCCTAAAGATCCAGCCAAACCTC CGGCCAAGGCACAAGTTGTGGGATGGCCACCGG TGAGATCATACCGGAAGAACGTGATGGTTTCCTG CCAAAATCAAGCGGTGGCCCGAGGCGGCGGC GTTCGTGAAGGTACGAAGAGCAG

Table S3. DNA reagents used to generate strains.

Genotype	Oligonucleotide	Sequence (5'-3')
<i>gfp::aid::vha-9</i>		
	crRNA (5')	TTATGAATAACTTTTCCAGA
	Repair template primers	
	Forward	ATGACAGCCAAAATCTTACCCTTCGCAG CAGATGCCTTCACGAACGCCGCCGCCT
	Reverse	CGATTA ACTTCAAGTTTTTTATGAATAAC TTTTCCCAGATGTCCAAGGGAGAGGAAC TCTT
<i>vha-9::aid::gfp</i>		
	crRNA (3')	TGTGAAGTTTTATAATTTAT
	Repair template primers	
	Forward	GAGCCCGTGGATTGTTCAACCCAGAGG ATTTCCGAATGCCTAAAGATCCAGCCAA
	Reverse	TGTCGAAGAGAAGCGTGATGTGAAGTTT TATAATTTAGTAGAGCTCGTCCATTCCGT
<i>gfp::aid::vha-13</i>		
	crRNA (5')	TCATTCATTCCAGGAAAAGA
	Repair template primers	
	Forward	CCATATAGCTTTCTAAATTCATTCATTCC AGGAAAAGATGTCCAAGGGAGAGGAAC TCTT
	Reverse	ACTCCGTAAACGAATCCGTACGAAGATT CTGCGGCCTTCACGAACGCCGCCGCCT
<i>gfp::aid::vha-14</i>		
	crRNA (5')	TTCCAGGTCTGAACCATGTCC
	Repair template primers	
	Forward	AGAAATAACAACTTTTTTTTCCAGGTCTGA ACCATGTCCAAGGGAGAGGAACTCTT
	Reverse	GGGAAAACCGCGATTCTGTCTTTTCCTC CCCCGACTTCACGAACGCCGCCGCCT



Chapter 6

Perturbed intermediate filament regulation
causes aggregate toxicity

Florian Geisler¹, Sanne Rimmelzwaal², Christine Richardson³, Mike Boxem², and Rudolf E. Leube¹.

¹ Institute of Molecular and Cellular Anatomy, RWTH Aachen University, 52074 Aachen, Germany

² Developmental Biology, Institute of Biodynamics and Biocomplexity, Department of Biology, Faculty of Science, Utrecht University, Padualaan 8, 3584 CH, Utrecht, The Netherlands.

³ School of Biological and Biomedical Sciences, Durham University, Durham DH1 3LE, United Kingdom

Abstract

Intermediate filaments are major components of the metazoan cytoskeleton. A long-standing debate concerns the question whether intermediate filament network organization only reflects or also determines cell and tissue function and dysfunction. This is particularly relevant for aggregate-forming diseases involving intermediate filaments. Using *Caenorhabditis elegans* as a genetic model organism, we have recently described mutants of signaling and stress response pathways with perturbed intermediate filament network organization. In a mutagenesis screen, we now identify the intermediate filament polypeptide IFB-2 as a highly efficient suppressor of these phenotypes restoring not only intestinal morphology but also rescuing compromised development, growth, reproduction and stress resilience. Ultrastructural analyses show that downregulation of IFB-2 leads to depletion of the aggregated intermediate filaments. The findings provide compelling evidence for the toxic function of deranged intermediate filaments and reveal novel insights into the cross talk between signaling and structural functions of the intermediate filament cytoskeleton.

Introduction

Intermediate filaments (IFs) together with actin filaments and microtubules are important components of the cytoskeleton. They mediate mechanical tissue stability and have been implicated in multiple cellular processes such as vesicle transport, organelle positioning, cell cycle regulation, differentiation, metabolism, motility and stress response (Coch et al., 2020; Etienne-Manneville, 2018; Geisler and Leube, 2016; Jacob et al., 2018; Margiotta and Bucci, 2016; Schwarz and Leube, 2016; Toivola et al., 2010; Yoon and Leube, 2019). An ongoing debate is whether IFs are simply bystanders of these cellular processes or contribute actively to cell function and dysfunction. This is particularly relevant for the multiple aggregate forming diseases that involve IF polypeptides (e.g. Chamcheu et al., 2011; Clemen et al., 2013; Coulombe et al., 2009; Didonna and Opal, 2019; Gentil et al., 2015; Yoshida and Nakagawa, 2012). Whether and how the different cell type-specific aggregates are responsible for the respective pathogenesis remains to be elucidated.

To study the morphogenesis and function of the IF system, we use the nematode *Caenorhabditis elegans* (Carberry et al., 2009). A striking example of unique IF network organization is its intestine, where six IF polypeptides, i.e. IFB-2, IFC-1, IFC-2, IFD-1, IFD-2 and IFP-1, co-localize in the apical cytoplasm forming the electron dense endotube, which surrounds the lumen as a compact fibrous sheath (Carberry et al., 2009; Jahnel et al., 2016) and is attached to the composite *C. elegans* apical junction (CeAJ). It is assumed that this evolutionary conserved localization of the intestinal IF network (cf. Coch and Leube, 2016) mediates protection against mechanical stress (Geisler and Leube, 2016; Geisler et al., 2019; Toivola et al., 2010). Accordingly, the endotube is positioned at the interface between the cortical actin cytoskeleton with the stiff microvillar brush border and the soft cytoplasm (Bossinger et al., 2004; Geisler et al., 2020; McGhee, 2007). Because of its high degree of elasticity it likely dampens mechanical stresses occurring during food intake, defecation and body movement (Geisler et al., 2020). Elimination of the intestinal IFs IFB-2, IFC-2 and IFD-2 therefore leads to luminal widening although loss of IFC-1, IFD-1 and IFP-1 does not (Geisler et al., 2020). Ultrastructural analyses further showed that IFC-2 mutants have a rarefied endotube, whereas IFB-2 mutants lack it completely (Geisler et al., 2019, 2020; Chapter 4). The intestinal IF mutants present very mild organismal phenotypes with only minor or no detectable effects on development, progeny production, survival and stress sensitivity with the exception of mutants of IFC-2 that is also expressed in the excretory canal and induces more pronounced deficiencies (Geisler et al., 2020).

Modulators of IF distribution have been identified and characterized in *C. elegans* (Carberry et al., 2012; Estes et al., 2011; Geisler et al., 2016, 2019; Stutz et al., 2015; Rimmelzwaal et al., 2021 (Chapter 4)). One of them is SMA-5, a stress-activated kinase orthologue of the mitogen-activated protein kinase (MAPK) type. Abundant cytoplasmic invaginations of the adluminal, apical plasma membrane develop over time in *sma-5* mutant intestines (Geisler et al., 2016). These changes correlate with the development of a locally thickened endotube

consisting of amorphous material next to areas with complete endotube loss. The cytoplasmic invaginations form at the transition between both areas. The structural changes go along with biochemical changes, i.e. altered IFB-2 phosphorylation. Furthermore, in comparison to the wild type and to intestinal IF mutants loss-of-function *sma-5* mutants are smaller, produce less offspring, develop more slowly, live shorter and are more sensitive to microbial pathogens and osmotic as well as oxidative stress (Geisler et al., 2016, 2019). It is not known, whether these pathologies are attributable to the altered IF cytoskeleton or other *sma-5(n678)*-dependent cellular perturbations. Another modulator of the intestinal IF cytoskeleton is the intestinal intermediate filament organizer gene *ifo-1* (Carberry et al., 2012), which was originally identified as a cellular defense gene against pore-forming toxins and as part of the MAPK/JNK defense network (referred to as *ttm-4* in (Kao et al., 2011)). The IF network collapses in loss-of-function *ifo-1* mutants into large aggregates, which accumulate primarily at the CeA and occasionally in the cytoplasm. *ifo-1* mutants are small, have reduced progeny and are hypersensitive to different types of stress. The phenotypes are not only much more pronounced than those observed in the wild type and in IF mutants but are also more pronounced than in *sma-5* mutants (Carberry et al., 2012; Geisler et al., 2019, 2020). Again, the contribution of the deranged IF network to the *ifo-1* mutant phenotype has not been determined to date.

To identify components of the IF-regulatory pathways in the *C. elegans* intestine, we performed an exhaustive genome-wide suppressor screen of *sma-5(n678)* mutants, which identified *ifb2* mutation as the most efficient suppressor. Loss-of-function *ifb-2* mutation also partially rescued the *ifo-1* phenotype. Remarkably, the intestinal IF network including the pathological aggregates was completely depleted in both double mutants. These findings demonstrate that the deranged and aggregated IF network is the major toxic effector in both backgrounds highlighting the detrimental effects of pathologically assembled IF polypeptides for the wellbeing of an entire organism.

Results

A genetic suppressor of *sma-5(n678)* rescues prolonged time of development, intestinal lumen pathology and small body size

To identify downstream effectors of the MAPK SMA-5, we performed an exhaustive genomewide suppressor screen in OLB18 carrying the loss-of-function *sma-5(n678)* allele together with a cyan fluorescent protein-labelled IFB-2a reporter. Since *sma-5* mutation leads to delayed development and small body size, we selected for fast developing lines with normalized adults. Two isolates were chosen and outcrossed. Later analyses showed that they were identical. Careful analyses of time of development confirmed the rescue, though time of development was still significantly increased in comparison to the wild type (Figure 1A). Light microscopy also revealed a rescue of the luminal widening and cytoplasmic invagination phenotypes (Figure 1B-D"). Together, the findings demonstrate that SMA-5-dependent structural and pathophysiological

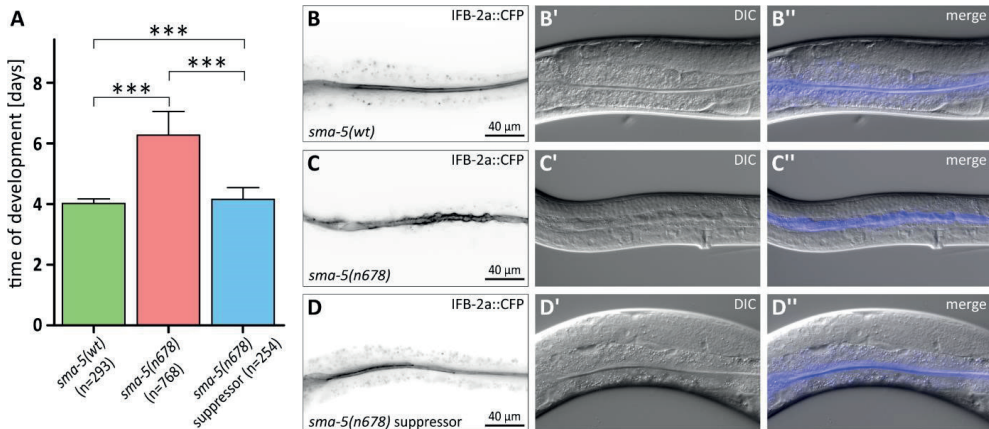


Figure 1. *sma-5(n678)* suppressor *kc20* rescues prolonged time of development, luminal widening and cytoplasmic invagination. (A) The histogram shows the time of development determined for control strain BJ49 (*sma-5(wt)*) containing only the integrated reporter *ifb2a::cfp* (4.0 ± 0.2 days), strain OLB18 containing the reporter together with the *sma-5(n678)* allele (6.3 ± 0.8 days) and strain BJ355, which contains, in addition, the suppressor allele *kc20* (4.2 ± 0.4 days) (***) $p < 0.0001$). (B-D'') The microscopic images show the localization of integrated *ifb-2a::cfp* reporter (inverse fluorescence presentation) at left) together with the corresponding differential interference contrast (DIC, middle; merged images at right) in *sma5(wt)* (B-B''), *sma-5(n678)* (C-C'') and *sma-5(n678)* suppressor animals (D-D'').

downstream changes are efficiently, though not completely repaired by the suppressor mutation.

The *sma-5* suppressor presents a rarefied intermediate filament network, lacks expression of endogenous IFB-2 and maps to the endogenous *ifb-2* gene

The endotube of *sma-5(n678)* animals was massively enlarged in some regions and thinned or missing in others (Geisler et al., 2016). To find out how the rescue affected the endotube, we performed electron microscopy. A drastically reduced endotube was noticed in the suppressor animals (compare Figure 2A and 2B). In some regions, the endotube was completely absent. This was reminiscent of the previously described effect of IFB-2 deletion, which completely abrogated the endotube (Geisler et al., 2019). We therefore tested for the expression of endogenous IFB-2 and the IFB-2a::CFP reporter by immunoblotting of total cell lysates. As expected, the reporter could be detected in the control, *sma-5(n678)* and the *sma5(n678)* suppressor but not in wild-type N2 (Figure 2C). The expression of the endogenous IFB2 isoforms a and c, however, was not detectable in the *sma-5(n678)* suppressor although it was well detected in the control reporter strain and N2.

Based on these observations we decided to sequence the *ifb-2* gene to find out whether the loss of IFB-2 is caused by upstream modulators of IFB-2 expression or by mutation of the *ifb2* gene itself. Using primers that do not react with the *ifb-2* reporter, an 83 base pair deletion was detected in both *sma-5(n678)*

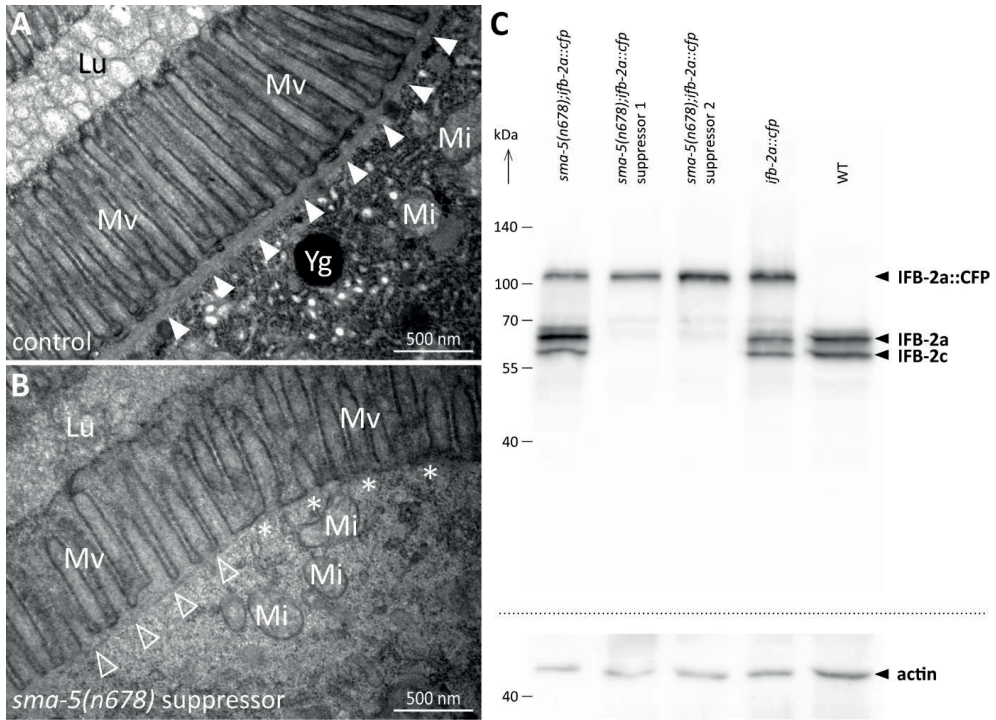


Figure 2. *sma-5(n678)* suppressor animals have a rarefied endotube and lack endogenous IFB-2 expression. (A, B) Electron microscopic images of chemically-fixed control carrying the *ifb-2a::cfp* reporter alone (A) or together with the *sma-5(n678)* mutant allele and the suppressor allele *kc20* (B). Note, that the perilluminal endotube (filled arrowheads in A) is considerably rarefied or even completely absent in some regions in the suppressor (nonfilled arrowheads and asterisks in B). Lu, lumen; Mv, microvilli; Mi, mitochondrium; Yg, yolk granule. (C) The immunoblots show the reaction of anti-IFB-2 (top) and anti-actin antibodies (bottom) in total lysates of *sma-5(n678);ifb-2a::cfp* (lane 1), *sma-5(n678);ifb-2a::cfp* suppressor (lanes 2 and 3), *ifb-2a::cfp* reporter control (lane 4) and wild type (lane 5). Position and size of co-electrophoresed molecular weight markers at left in kDa.

suppressors (position 5.751.812 - 5.751.893; Figure S1). The mutant *ifb-2* gene encodes 120 amino acids, 116 of which correspond to the aminoterminal amino acids of IFB-2. The fragment corresponds to the head domain together with 73 amino acids of the coiled-coil rod domains 1a and 1b (Karabinos et al., 2004). The allele will be referred to as *ifb-2(kc20)*.

***ifb-2* knockout allele *kc14* abolishes the *sma-5(n678)*-dependent cytoplasmic invaginations and completely removes the mutant intermediate filament network**

To demonstrate that loss-of-function of *ifb-2* is by itself sufficient and necessary to rescue the *sma-5(n678)* phenotype and to exclude that the residual aminoterminal fragment that is still produced from *kc20* is responsible for the rescue, we crossed *sma-5(n678)* mutants with the previously described *ifb-2* knockout allele *kc14* in an *ifb-2a::cfp*-free background. The *kc14* allele encodes a 29

amino acid-long oligopeptide encompassing only 13 of the most aminoterminal amino acids of IFB-2a (Geisler et al., 2019). The resulting homozygous double mutants showed a full rescue of the apical invagination/luminal widening phenotype (Figure 3A-D). Ultrastructural analyses further revealed a reversion of the phenotype to a near normal wild-type situation in the double mutants with only minor luminal undulations and slight perturbation of microvillar order (Figure 3E-H). Most notably, the endotube was completely absent (Figure 3 H). We therefore concluded that the residual endotube that was still detectable in the reporter-containing suppressor (Figure 2B) was due to the remaining IFB2a::CFP fusion protein in that situation. The reporter, however, was obviously not able to fully compensate for the complete loss of endogenous IFB-2c and hence did not prevent rescue of the *sma-5(n678)* phenotype. The observation that the head domain of IFB-2 alone did not prevent the suppressor function further suggested that loss of filamentous IFB-2 is needed for the suppressor activity.

***ifb-2(kc14)* knockout rescues *sma-5(n678)*-dependent developmental retardation, larval arrest, body length, reduced survival, reduced progeny and increased sensitivity to oxidative stress**

Similar to the *sma-5(n678)* suppressor allele *ifb-2(kc20)*, the *ifb-2(kc14)* knockout allele restored the prolonged time development of *sma-5(n678)* to near wild-type level (Figure 4A). Developmental time was, however, still considerably elevated in comparison to the wild type but was only slightly different from the single *ifb-2(kc14)* mutant. To define minor alterations in development more precisely, analysis of the different developmental stages was carried out next. The results shown in Figure 4B illustrate the high degree of similarity in the developmental time course of the single *ifb-2(kc14)* and double *sma-5(n678);ifb-2(kc14)* mutants. Both develop more slowly than the wild type and much faster than the *sma-5(n678)* animals, some of which never reached adulthood. The latter could be ascribed to larval arrest at the L4 stage (Figure 4C).

Assessment of body length revealed a near normal body size of the double *sma-5(n678);ifb2(kc14)* mutants with only slight reduction at day 4 as was the case for *ifb-2(kc14)* single mutants (Figure S2). Normal body length was reached by day 5 in *sma-5(n678);ifb-2(kc14)* and *ifb-2(kc14)* but not in *sma-5(n678)* (not shown).

Life span determinations further showed that the shortened median life span of *sma-5(n678)* animals could be rescued in the *sma-5(n678);ifb-2(kc14)* double mutants to the level observed in *ifb-2(kc14)* single mutants. Yet, the life span of the latter mutants was still reduced in comparison to the wild type by one day (Figure 4D). Similarly, the drastic reduction in progeny of *sma-5(n678)* was rescued in the double mutant to the level observed in *ifb-2(kc14)*, which, again, was significantly less than in the wild type (Figure 4E).

In a next set of experiments, we investigated whether loss of IFB-2 would also rescue the increased stress sensitivity of *sma-5(n678)* (Geisler et al., 2019). We therefore determined how oxidative stress affected the survival (Fig. 4 F). The

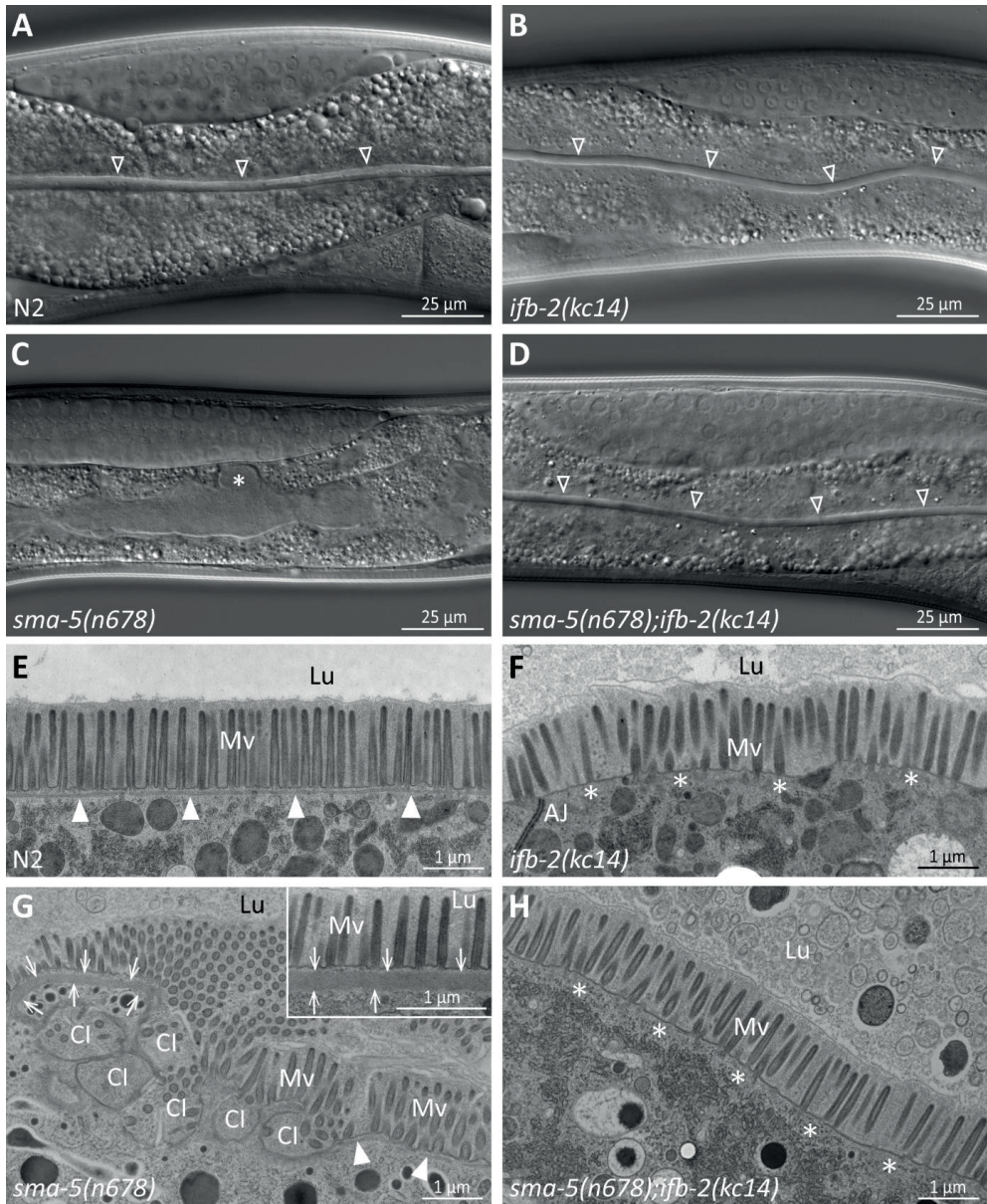


Figure 3. The *ifb-2(kc14)* knockout allele rescues the *sma-5(n678)* luminal widening and cytoplasmic invagination phenotypes. (A-D) Differential interference contrast pictures of viable wild-type N2 (A), *ifb-2(kc14)* (B), *sma-5(n678)* (C) and *sma-5(n678);ifb-2(kc14)* animals (D). *ifb-2* knockout causes only minor intestinal defects. In contrast, *sma-5(n678)* animals display luminal widening and large cytoplasmic invaginations of the apical plasma membrane in intestinal cells (asterisk in C). This phenotype is effectively reversed by the *ifb-2(kc14)* knockout allele. (E-H) Electron microscopy images of high-pressure frozen samples show wild-type N2 (E), *ifb-2(kc14)* (F), *sma-5(n678)* (G) and *sma-5(n678);ifb-2(kc14)* intestinal apices (H). *sma-5(n678)* animals contain regions with an enlarged endotube consisting of densely aggregated IFs (arrows)

and differently-sized cytoplasmic invaginations (CI) with no endotube or a reduced endotube (arrowheads). Additional knockout of *ifb-2* almost restores the wild-type morphology with only residual luminal widening and mildly perturbed microvillar arrangement. But the endotube, which is easily detected in the wild type (filled arrowheads), is completely absent in *ifb-2(kc14)* (expected position marked by asterisks). Lu, lumen; Mv, microvilli; AJ, *C. elegans* apical junction.

survival of *sma-5(n678)* was reduced by 3.5 h in comparison to wild-type N2 but was only reduced by 0.5 h and 1.5 h in *ifb-2(kc14)* and *sma-5(n678);ifb-2(kc14)*, respectively. All mutants appeared to be similarly affected in osmotic stress assays and a statistically significant rescue phenotype could not be observed (Figure 4G).

Taken together, we can conclude that loss of IFB-2 rescues all major SMA-5 phenotypes to levels observed in *ifb-2(kc14)*. This demonstrates that the altered distribution and phosphorylation of IFB-2 observed in *sma-5(n678)* exert a negative effect on intestinal and organismal physiology. The findings together with previous reports (Geisler et al., 2019, 2020) assign a major role of IFB-2 in regulation of endotube function and intestinal physiology.

Depletion of different intestinal intermediate filament polypeptides reveals isotype-specific rescue efficiency of the *sma-5* phenotype

To test whether the observed rescue is specific for IFB-2 or applies also to the other five IFs that are expressed in the intestine, each IF was downregulated by RNAi in the *sma-5(n678)* background. As a simple readout, F1 progeny from RNAi-treated worms was imaged on agar plates four days after hatching (Figure 5A-G) and the body length was measured (Figure 5H). The assay confirmed the expected efficient rescue of the developmental growth defect in *sma5(n678)* by *ifb-2(RNAi)*. An easily detectable, though reduced rescuing efficiency was observed for *ifc-2(RNAi)*. An even less pronounced but statistically still significant rescue could be identified in *ifd-1*, *ifd-2* and *ifp-1* RNAi-treated animals and none for *ifc-1(RNAi)*.

We next examined whether the cytoplasmic invagination phenotype could be rescued in a similar fashion. To this end, the different IF-encoding RNAs were downregulated in the IFB2a::CFP reporter strain (Figure 5I-O'). As predicted, *ifb-2(RNAi)* abolished the reporter fluorescence as well as the cytoplasmic invaginations of *sma-5(n678)*. *ifc-2(RNAi)* also led to a reduction of the cytoplasmic invagination phenotype but was much less efficient than *ifb2(RNAi)*. All other interfering RNAs, however, did not visibly affect the invagination phenotype.

We cannot exclude, however, that the presence of the reporter obscured the effect of RNA downregulation of these IF polypeptides.

Taken together, the isotype-specific phenotypes may be explained by the abundance and polymerization of the different IF polypeptides. Thus, IFB-2 has been shown to pair with multiple intestinal IFs (Karabinos et al., 2017) and has been identified as the master regulator of the endotube (Geisler et al.,

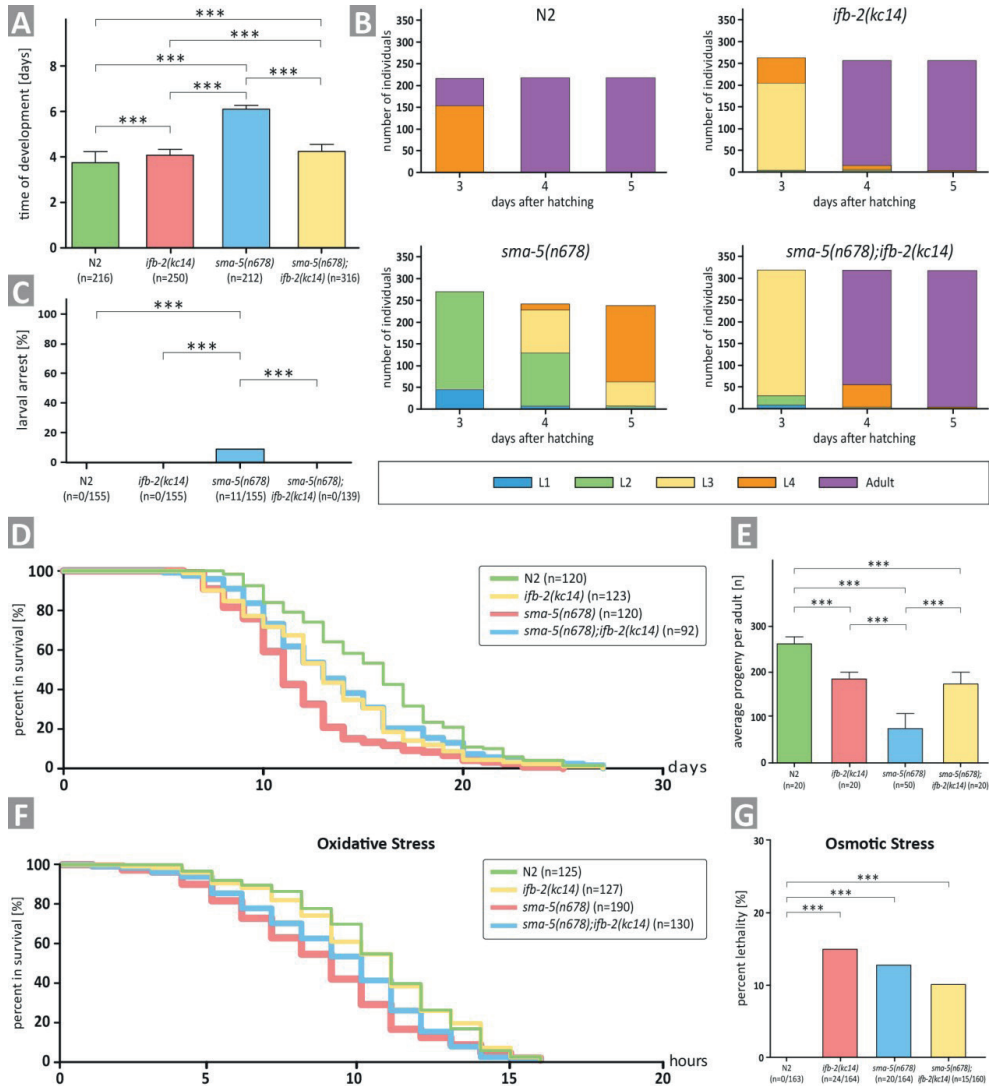


Figure 4. *ifb-2(kc14)* knockout rescues the *sma-5(n678)* developmental retardation, larval arrest, reduced median survival and brood size and increased sensitivity to oxidative stress to *ifb-2(kc14)* single mutant levels. (A) The histogram shows a comparison of the time of development in N2, *ifb-2(kc14)*, *sma-5(n678)* and *sma-5(n678);ifb-2(kc14)* (N2: 3.7±0.5 days; *ifb-2(kc14)*: 4.1±0.2 days; *sma-5(n678)*: 6.0±0.2 days; *sma-5(n678);ifb-2(kc14)*: 4.2±0.4 days; *** p<0.0001). (B) The color-coded histogram depicts the number of larval and adult stages detected 3, 4 and 5 days after hatching. (C) The histogram illustrates a complete rescue of the larval arrest phenotype observed in *sma-5(n678)* by *ifb-2(kc14)* (N2: 0%; *ifb-2(kc14)*: 0%; *sma-5(n678)*: 7.1%; *sma-5(n678);ifb-2(kc14)*: 0%). (D) The survival plot shows that the reduced survival of *sma-5(n678)* is rescued by addition of *ifb-2(kc14)* to *ifb-2(kc14)* but not wild-type level (median survival for N2: 16 days; *ifb-2(kc14)*: 13 days; *sma-5(n678)*: 11 days; *sma-5(n678);ifb-2(kc14)*: 13 days; p=0.0004 *ifb-2(kc14)* versus N2; p<0.0001 *sma-5(n678)* versus N2; p=0.0003 *sma-5(n678)* versus *ifb-2(kc14)*; p<0.0001 *sma-5(n678);ifb-2(kc14)* versus N2; p<0.0046 *sma-5(n678);ifb-2(kc14)* versus *sma-5(n678)*). (E) The histogram reveals that the average progeny per adult is reduced in *ifb-2(kc14)* in comparison to wild-type N2 (183±15

versus 263 ± 13 ; $p < 0.001$). Note that the even higher reduction in progeny observed in *sma-5(n678)* mutants versus N2 (76 ± 31 versus 263 ± 13 ; $p < 0.0001$) and *ifb-2(kc14)* (76 ± 31 versus 183 ± 15 ; $p < 0.0001$) is rescued in *sma-5(n678);ifb-2(kc14)* double mutants (175 ± 21 ; $p < 0.001$ versus *sma-5(n678)*) but does not reach wild-type level (175 ± 21 versus 263 ± 13 ; $p < 0.001$). (F) The survival plot shows the effect of acute oxidative stress in the wild-type (N2), *ifb-2(kc14)*, *sma-5(n678)* and *sma-5(n678);ifb2(kc14)* backgrounds (median survival for N2: 11 h; *ifb-2(kc14)*: 11 h; *sma-5(n678)*: 9 h; *sma5(n678);ifb-2(kc14)*: 10 h; $p < 0.0001$ for N2 or *ifb-2(kc14)* versus *sma-5(n678)*; $p < 0.05$ *sma5(n678);ifb-2(kc14)* versus *sma-5(n678)*; $p < 0.01$ for N2 or *ifb-2(kc14)* versus *sma-5(n678);ifb2(kc14)*). (G) The histogram scores the percentage of dead worms in response to acute osmotic stress for N2 (0%), *ifb-2(kc14)* (14.6%), *sma-5(n678)* (12.2%) and *sma-5(n678);ifb2(kc14)* (9.4%). *** $p < 0.0001$.

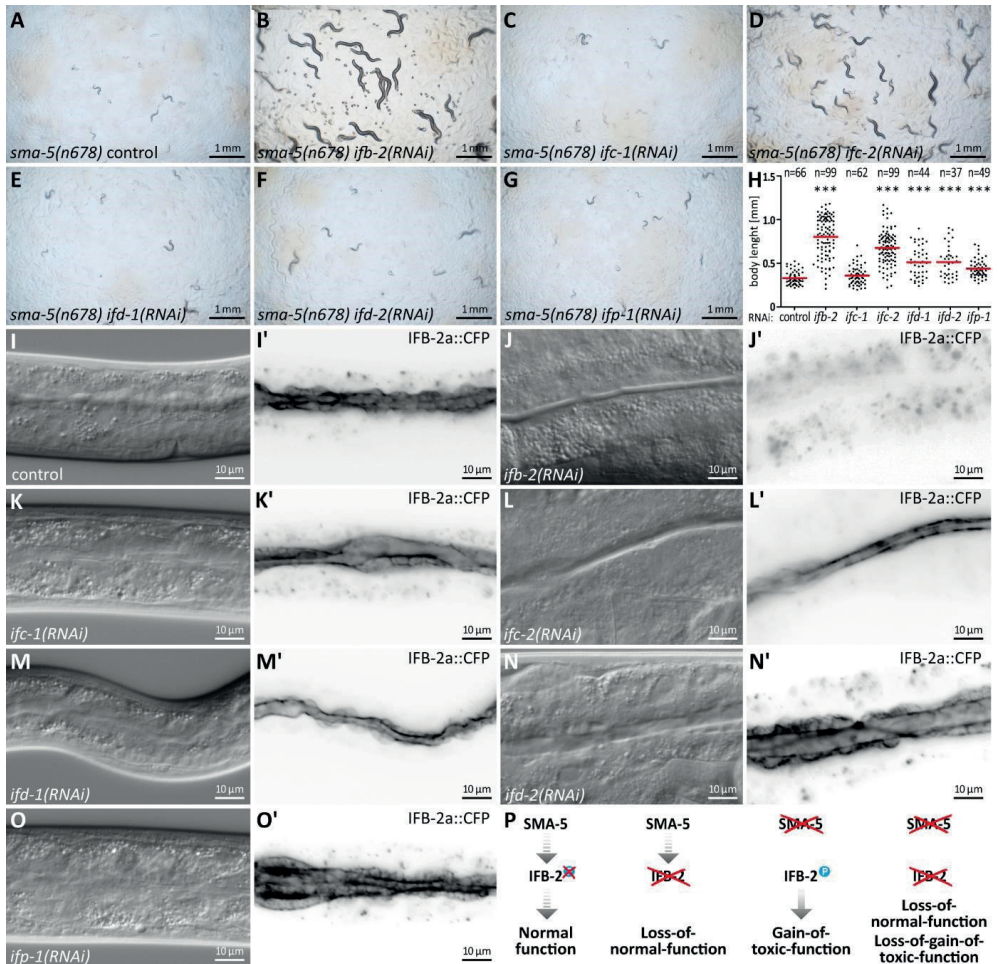
2020). It is therefore not surprising that IFB-2 depletion elicits the strongest rescuing activity of the *sma-5(n678)* mutant phenotype. It is also in line with IFC2 depletion being second in line as also evidenced in previously reported effects on endotube structure and stress sensitivity (Geisler et al., 2020). Overall, our findings demonstrate that the altered IF network and not a single IF is responsible for the observed rescue of the *sma5(n678)* phenotype.

***ifb-2(kc14)* partially rescues the *ifo-1(kc2)* phenotype**

The above findings suggested that the rescue function of IFB-2 deletion in *sma-5(n678)* was caused by removal of the densely aggregated IFs (Figure 5P). To test the hypothesis that aggregated IFs exert a toxic effect, we studied another paradigm, namely the *ifo-1(kc2)* phenotype, which is characterized by prominent IF polypeptide-containing junctional aggregates (Carberry et al., 2012). To this end, we crossed *ifo-1(kc2)* with *ifb-2(kc14)*. As predicted, the double mutant lacked the junctional IF aggregates altogether (Figure 6A-D). Occasionally, a faint, but largely reduced remnant endotube structure was detectable, often in the vicinity of the CeAJ. Furthermore, double mutants had an almost normal intestinal lumen and inconspicuous microvilli (Figure 6D). Additional analyses showed a significantly reduced time of development of *ifo-1(kc2);ifb-2(kc14)* in comparison to *ifo-1(kc2)*, which was, however, significantly retarded in comparison to *ifb-2(kc14)* or wild-type N2 (Figure 6E-I). Taken together, these observations provide compelling evidence for the gain-of-toxic function hypothesis of IF polypeptide-containing aggregates.

Discussion

Exploiting rapid *C. elegans* genetic screening, we made the observation that the complex phenotype induced by mutation of the MAPK orthologue SMA-5 can be rescued by deletion of the cytoskeletal IF protein IFB-2. It included rescue of structural defects (cytoplasmic invagination and lumen dilatation), developmental and growth defects as well as oxidative stress resilience. The obtained rescue levels coincided precisely with the mild phenotype of single *ifb-2(kc14)* mutants. These findings therefore provide conclusive *in vivo* evidence that the rescued *sma-5* mutant phenotype is caused by the presence of IFB-2-containing pathological assemblies. This conclusion was confirmed in *ifo-1* mutants. Removal of the pathological IFB-2 aggregates, which are positioned at



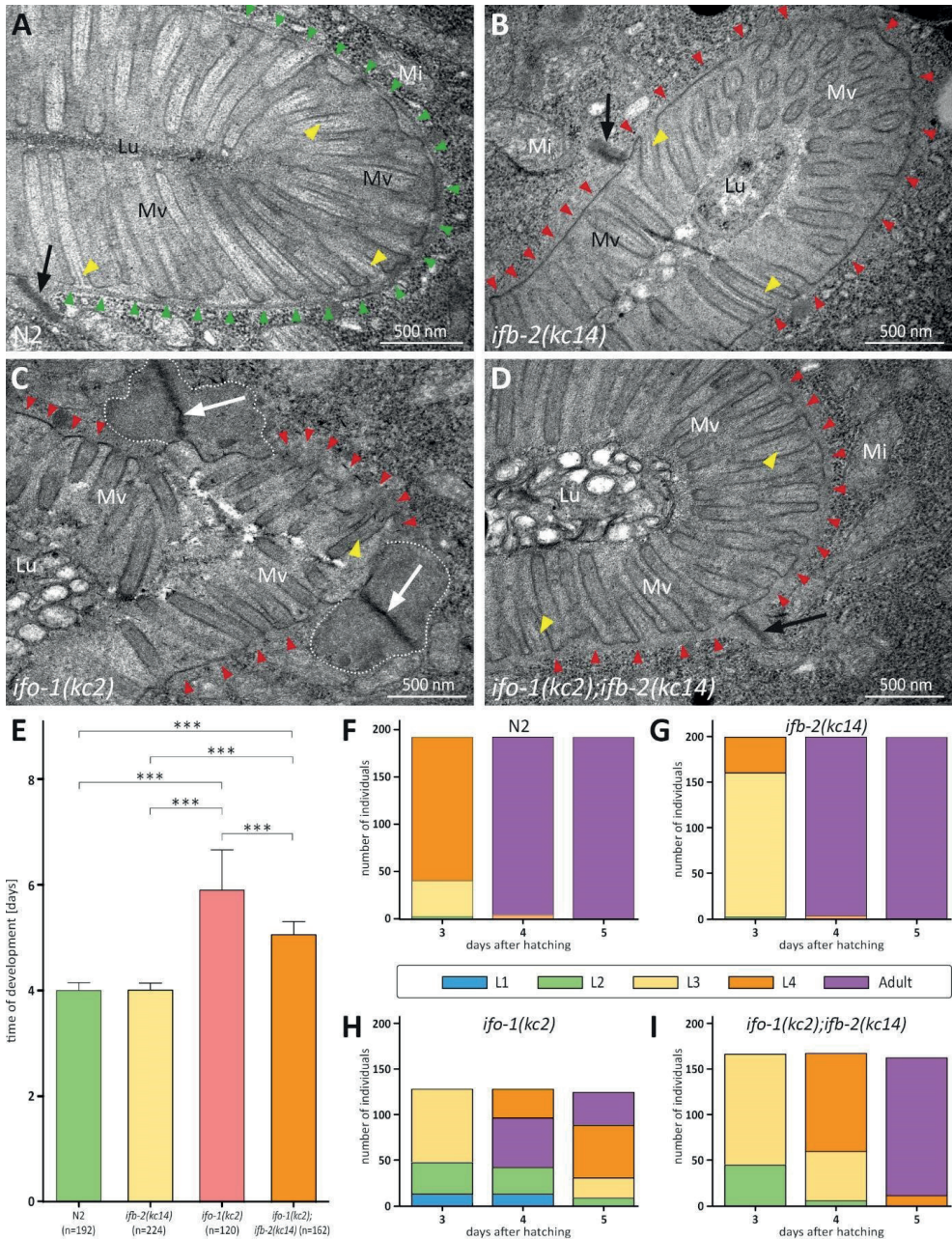


Figure 6. Depletion of IFB-2 partially rescues the *ifo-2(kc2)* phenotype. (A-D) The electron micrographs show a comparison of the cell apices surrounding the intestinal lumen (Lu) of wild-type N2 (A), *ifb-2(kc14)* (B), *ifo-1(kc2)* (C) and *ifo-1(kc2); ifb-2(kc14)* (D). Note the distinct endotube in N2 (green arrowheads) and its absence in *ifb-2(kc14)*, *ifo-1(kc2)* and *ifo-1(kc2); ifb-2(kc14)* (red arrowheads). The pathognomonic large junctional aggregates of *ifo-1(kc2)* are delineated by broken white lines. Note the improved brush border morphology in D compared to C (Mv, microvilli). Arrows, CeA; yellow arrowheads, microvillar actin bundles; Mi, mitochondrion. (E-I) The histograms depict the time of development in E and the number

of staged worms at different times after hatching in N2 (F), *ifb-2(kc14)* (G), *ifo-1(kc2)* (H) and *ifo1(kc2);ifb-2(kc14)* (I). Note the partial rescue in the double mutants. (N2: 4.0 ± 0.1 days; *ifb2(kc14)*: 4.0 ± 0.1 days; *ifo-1(kc2)*: 5.9 ± 0.8 days; *ifo-1(kc2);ifb-2(kc14)*: 5.1 ± 0.3 days; *** $p < 0.0001$).

the *C. elegans* junction in this instance, also rescued complex biological functions. We can therefore state that the deranged intestinal IF cytoskeleton has toxic effects, which have detrimental consequences for cell and tissue function with adverse results on the growth and reproduction of the entire organism.

Based on our findings, we propose the following scenario (Figure 5P). In the wild-type background SMA-5 keeps network formation and phosphorylation of IFB-2 and possibly other IFs at bay supporting the normal function of the IF-based endotube network. This is either accomplished through a SMA-5 signaling cascade supporting IF dephosphorylation or an inhibitory mechanism, e.g. by SMA-5-dependent binding of an IF-associated factor preventing IF phosphorylation. Be it as it may, deletion of SMA-5 induces a gain-of-toxic-function on the IF cytoskeleton. This gain-of-toxic-function at the tissue level is reflected in (i) structural alterations, i.e. the extreme local thickening of densely aggregated IFs, (ii) biochemical alterations, i.e. increased phosphorylation of IFB-2 and likely other IF polypeptides, and (iii) functional deficiencies, i.e. reduced stress resilience of the intestine (Geisler et al., 2016, 2019). We postulate that a comparable gain-of-toxic function also applies to *ifo1(kc2)*. The partial rescue, however, argues in this instance for additional pathways that are affected by *ifo-1* mutation and are independent of IFs.

The fact that removal of the very differently deranged IFs, i.e. the thick subapical slabs in *sma5(n678)* and the large granular junctional aggregates in *ifo-1(kc2)*, rescued the phenotypes in both instances is quite remarkable since the mechanical dysfunction appears to be fundamentally different in both mutant backgrounds. Mechanical dysfunction manifests in *sma5* mutants as prominent cytoplasmic invaginations and primarily as luminal widening in *ifo-1* mutants (see also (Carberry et al., 2012; Geisler et al., 2016)). Furthermore, the absence of an endotube in *ifo-1* mutants predicts that the force equilibrium is affected differently from that in *sma-5* mutants with the locally thickened endotube. One would therefore expect that changes in force equilibrium are similar in *ifo-1* and *ifb-2* mutants, both of which lack an intact endotube. All these arguments indicate that restored mechanics alone unlikely explain the phenotypic restoration in the double *sma-5/ifb-2* and *ifo-1/ifb-2* mutants. Thus, other nonmechanical functions must be attributable to the abnormal IF aggregates. It is interesting in this context that IFs may serve as signaling platforms by providing a large scaffold capable of sequestering and positioning signaling molecules that can be recruited by weak interactions and can be released, e.g., by protein modification or structural changes of the IF cytoskeleton (review in (Bott and Winckler, 2020; Coulombe and Omary, 2002; Magin et al., 2007)). Future experiments will show, whether such a scaffolding function is compromised in *sma-5* and *ifo1* mutants by either sequestering or setting free regulatory factors that modulate pathways needed for normal growth, development and stress responses.

Material and methods

C. *elegans* strains and bacteria

Wild-type strain N2, strain FK312 *sma-5(n678)X* and OP50 bacteria were obtained from the Caenorhabditis Genetics Center (CGC; University of Minnesota, MN, USA). Strains BJ49 *kcls6[ifb-2p::ifb-2a::cfp]IV* (Hüsken et al., 2008), BJ142 *ifo-1(kc2)IV* (Carberry et al., 2012), OLB18 *sma-5(n678)X;kcls6[ifb-2p::ifb-2a::cfp]IV* (Geisler et al., 2016) and BJ309 *ifb-2(kc14)II* (Geisler et al., 2019) have been described. Strain FK312 was crossed with strain BJ309 to obtain strain BJ346 *sma-5(n678)X;ifb-2(kc14)II*. Strain BJ328 *ifo-1(kc2)IV;ifb-2(kc14)II* was generated by crossing strain BJ142 with strain BJ309. The generation of the *sma-5(n678)* suppressor allele *ifb-2(kc20)* is described in the following section.

Suppressor screen

10 cm diameter agar plates containing normal nematode growth medium (NGM) were prepared by autoclaving a solution containing 3 g NaCl (Carl Roth, Karlsruhe, Germany), 2.5 g Bacto peptone (BD BioSciences, Heidelberg, Germany) and 18.75 g Bacto agar (BD BioSciences) per 1 l and pouring the solution after addition of 1 mL cholesterol (5 mg/mL in ethanol), 0.5 mL 1 M CaCl₂, 1 mL 1 M MgSO₄ and 25 mL 1 M KH₂PO₄ (pH 6.0). After solidification, OP50 were placed on top of the agar and plates were incubated overnight at 37°C. They were then used for growing OLB18. Adult animals were bleached with a solution containing 170 µl 12% NaOCl, 100 µl 4M NaOH per 1 mL PBS (Biochrom, Berlin, Germany) and the resulting embryos were grown on new plates. The resulting synchronized L4 larvae were washed off with PBS and were then centrifuged in 15 ml Falcon tubes at 340xg for 2 min. 5 ml of the pelleted worms were mixed with 50 µl of 50 mM N-ethyl-N-nitrosourea (ENU; SigmaAldrich, Munich, Germany) and the suspension was incubated for 4 h at room temperature on a rotating shaker. Two washing steps with PBS followed before the mutagenized worms were resuspended in PBS and transferred onto 100 mutagenized L4 animals were placed per agar plate containing enriched NGM containing additionally 5 g Difco yeast extract (ThermoFisher Scientific, Massachusetts, USA) (total of 200 plates). The plates were then incubated at 20°C. It was ensured that the F2 generation was completely laid on these plates before food was used up. Then 1.5x1.5 cm pieces were cut out and placed on new plates, which were again incubated at 20°C until food was completely used up. After repeating these steps three times, the development of the mutant lines compared to OLB18 was monitored using a stereomicroscope. Criteria for suppressor activity were body size and developmental stage. If both were rescued, lines were subjected to further selection rounds. Only stable lines were subsequently examined by light microscopy for rescue of invaginations of the apical intestinal membrane. The mutant line, which met all three criteria best, was named strain BJ334 (*sma5(n678)X;ifb-2(kc20)II*) and was backcrossed twice with OLB18 resulting in strain BJ355 (*sma5(n678)X;ifb-2(kc20)II*). To determine the mutation of allele *kc20 ifb-2* DNA was amplified in three parts using three primer pairs outside the protein coding regions (oSMR66 (gggtgtggtttttaactgctg) and oSMR68 (acacaccatttctccaga), oSMR67 (tctggaggaaatgggtgtg), and

oSMR70 (tccttgccgatacactctga), oSMR69 (tcggtagctataaccgcttca), and oSMR71 (caaggaaaggattcaatgggc). The DNA was purified and analyzed by Sanger sequencing using the same primers as for amplification. A parallel isolate turned out to be identical and was therefore not separately annotated. BJ355 was used for the analyses described in this study.

Microscopy

Light microscopy was performed with a Zeiss (Jena, Germany) apotome in combination with a ZeissAxioCamMRm camera.

For electron microscopy worms were either chemically fixed (Figure 2 and 6) or cryofixed at high pressure (Figure 3):

- *Chemical fixation:* Young adult animals (40 for each strain) were submerged in freshly prepared fixation solution containing 2.5% glutaraldehyde (using 25% (w/v) glutardialdehyde from Carl Roth), 1% (w/v) paraformaldehyde (using a stock solution with 0.4 g paraformaldehyde dissolved in 10 ml 0.1 M sucrose with 0.6 μ l 10 N sodium hydroxide [all from Sigma-Aldrich]), 0.05 M cacodylate buffer (using dimethylarsinic acid sodium salt trihydrate from Merck and HCl for pH adjustment to 6.4-7.4) at room temperature in a glass staining block. Each worm was cut through at the anterior and posterior end with a scalpel. The fixation solution was exchanged two times with 1.5-2 h incubation at room temperature in between. After the third replacement of the fixation solution an overnight incubation followed at 4°C in a moist chamber. The samples were then transferred to 0.2 M cacodylate buffer and incubated for 3x10 min in this buffer with buffer changes in between. Samples were then incubated for 4 h in 0.1 M cacodylate buffer containing 1% (w/v) OsO₄ (Paesel-Lorei, Frankfurt/Main, Germany) and 0.5% (w/v) K₃[Fe(CN)₆] (Carl Roth), followed by 3x10 min in 0.1 M cacodylate buffer. Sometimes samples were incubated overnight at 4°C in a moist chamber in 0.1 M cacodylate buffer. The following incubations ensued at room temperature: 3x10 min in 0.1 M maleic acid buffer (Sigma-Aldrich; pH 6), 2 h in the dark in 0.5% (w/v) uranyl acetate (EMS, Hatfield, PA, USA) dissolved in 0.05 N maleic acid buffer (pH 5.2), 3x5 min in 0.1 M maleic acid buffer, 3x5 min in double distilled water, 5 min in 20% ethanol, 5 min in 30% ethanol, 3x10 min in 50% ethanol, 2x15 min in 75% ethanol, 2x15 min in 95% ethanol, 3x10 min in 100% ethanol, 10 min in a 1:1 ethanol/acetone mixture and 2x10 min in acetone. Finally, samples were embedded in araldite (Agar scientific, Stansted, UK). To this end samples were first placed overnight at 4°C in a 3:1 mixture of acetone/araldite with 1.5% (v/v) DMP30 [Agar scientific] followed by incubation steps at room temperature: 1 h in a 1:1 mixture of acetone/araldite with 1.5% DMP30, 2 h in a 1:3 mixture of acetone/araldite with 1.5% DMP30, and two days in araldite with 2% DMP30. The final polymerization was done at 60°C for two days in silicone molds with pre-polymerized araldite at the bottom. 75 nm sections were prepared using a Leica (Wetzlar, Germany) Reichert Ultracut S microtome. They were contrasted for 4 min in uranyl acetate and 3 min in lead citrate and finally imaged at 60 kV in a Zeiss EM 10.

- *High-pressure freezing:* Young adult animals were transferred into a 100 μm deep membrane carrier containing 20% bovine serum albumin in M9 worm buffer (22 mM KH_2PO_4 , 42 mM Na_2HPO_4 , 86 mM NaCl, 1 mM MgSO_4) and then high-pressure frozen in a Leica EM Pact highpressure freeze. A minimum of five samples with 10-20 animals were frozen per experiment. Quick freeze substitution using 1% OsO_4 , 0.2% uranyl acetate in acetone followed by epoxy resin embedding was performed as previously described (McDonald and Webb, 2011). Subsequently, 50 nm thick sections of the embedded samples were prepared using a Leica UC6/FC6 ultramicrotome. These were contrasted for 10 min in 1% uranyl acetate in ethanol and Reynolds lead citrate and recorded at 100 kV on a Hitachi H-7600 transmission electron microscope (Tokyo, Japan).

Immunoblotting

60 young adults of strains OLB18, BJ355, BJ49 and N2 were picked in 30 μl dH_2O each and frozen at -80°C . To disrupt the cuticle, the samples were then rapidly thawed on a heating block and three times sucked up and down through a 30G hypodermal syringe (BD Medical, Heidelberg, Germany). After addition of 7.5 μl 5x Laemmli loading buffer (15 ml stacking gel buffer [0.15 M Tris-Cl, 0.1% SDS, pH: 6,8], 12.5 ml glycerine, 2.5 ml β -mercaptoethanol, 2.5 g SDS, some bromophenol blue), the samples were incubated for 5 min at 90°C . Polypeptides were separated by electrophoresis in an 8% sodium dodecyl sulfate (SDS) polyacrylamide gel. Separated proteins were then transferred by wet tank-blotting (100 V for 60 min) onto a polyvinylidene difluoride (PVDF) membrane (Merck, Darmstadt, Germany). The membrane was blocked with Roti®-Block (2 h at room temperature; Carl Roth) and incubated overnight at 4°C with the primary antibody (mouse monoclonal anti-IFB-2 antibody MH33, 1:1000 dilution in Roti®-Block, Developmental Studies Hybridoma Bank, (Francis and Waterston, 1991); rabbit polyclonal anti-actin antibody, 1:1000 dilution in Roti®-Block, Sigma-Aldrich, #A2066). The membrane was washed three times with TBST (20 mM tris(hydroxymethyl)-aminomethane, 0.15 M NaCl, 0.1% Tween 20 (v/v), pH 7.6) and then incubated with the secondary antibody (goat anti-mouse IgG antibodies and goat anti-rabbit IgG antibodies coupled to horseradish peroxidase from DAKO at 1:5000 in Roti®-Block) for 1 h at room temperature. Chemiluminescence substrate AceGlow (VWR, Darmstadt, Germany, #730-1510) was detected by Fusion Solo (Vilber Lourmat, Eberhardzell, Germany).

Analysis of larval development and progeny production

For the analysis of larval development, a defined number of isolated embryos were placed on a NGM plate with an OP50 bacterial lawn and incubated at 18°C . The number of adult stages was then determined daily, and the remaining larval stages were transferred to a new plate. For further in-depth analysis of the different stages of development, the individual age of each larvae was also determined. The larval arrest rate was calculated from the following quotient: number of animals that died as larvae divided by the total number of animals at the beginning of the experiment. Significance was calculated using the Chi square function of Excel (Microsoft, Redmont, WA). Time of development was

calculated based on the time it took to complete development from the embryo (up to 24 cell stage) to the adult stage. The offspring of these animals was determined and is presented as average progeny per individual. The generated data are presented as mean value \pm SD. Significance was calculated using the unpaired, two-tailed t-test function of GraphPad Prism 5.01 (GraphPad Software Inc., LaJolla, CA).

Life span analysis

Embryos were isolated, transferred to NGM plates with OP50 bacterial lawns and then incubated at 18°C. The hatched animals were checked daily for vitality. Animals without reaction to mechanical stimulus, triggered by a platinum wire, were considered dead. Animals that could not be found were censored. In order to avoid mix up with the following generation, the animals were transferred to new plates at least every three days. Statistical analysis was performed using the survival function and the Gehan-Breslow-Wilcoxon test of GraphPad Prism 5.01.

Stress assays

For the oxidative stress assay, NGM agar plates containing 200 mM methyl viologen dichloride hydrate (paraquat; Sigma-Aldrich) were prepared, stored at room temperature overnight and then inoculated with 50 μ l of a 10 x concentrated OP50 overnight culture. After another day at room temperature plates were stored at 4°C and were used for a maximum of three days. L4 larvae were placed on the bacterial lawn and incubated at 18°C. Every hour the viability of the animals was checked by mechanically provoking them with a platinum wire. Vital animals showed an active response to this stimulus. Animals that did not respond were considered dead. In parallel, plates without paraquat were used as a control. For statistical analysis, the Gehan-Breslow-Wilcoxon test of GraphPad Prism 5.01 was used.

To perform the osmotic stress assay, plates containing 300 mM NaCl were prepared, stored overnight at room temperature, then inoculated with 300 μ l of an OP50 overnight culture and incubated for another day at room temperature. Afterwards, L4 stages were placed on the bacterial lawn and plates were incubated overnight at 18°C. The animals were then washed in recovery buffer (M9 buffer with 150 mM NaCl) and transferred to normal NGM plates. After a further overnight incubation at 18°C, single worms were tested for viability as described above. Data shown correspond to mean value \pm SD. Statistical calculations were performed using the Chi square function of Excel.

RNAi and body length determination

RNAi by feeding was performed as described previously (Geisler et al., 2016) without supplement of tetracycline. In brief, RNAi plates were inoculated with 300 μ l of overnight grown HT115 bacteria producing dsRNA targeted against *ifb-2*, *ifc-1/-2*, *ifd-1/-2* and *ifp-1* mRNA followed by overnight incubation at room temperature. L4 larvae were placed onto plates and incubated for 48 hours at 18°C. Subsequently, adult grown animals were transferred to new plates

and incubated for 4 days at 18°C. Laid progeny was used for imaging and body length measurements. Animals were either imaged on the plate using a Nikon AZ100M stereoscope (Düsseldorf, Germany) equipped with a SONY Alpha 7R (Berlin, Germany) camera or mounted on agar slides using 10% levamisole as anaesthetic. Body length was determined using the segmented line tool in combination with the measurement function of Fiji

(<https://imagej.net/Fiji>). Results are shown as mean value \pm SD. Significance was calculated using the unpaired, two-tailed t-test function of GraphPad Prism 5.01.

RNAi-inducing bacteria were commercially available through the Vidal library (clone *ifb-2*, *ifc2*, *ifd-2*, Source BioScience, Nottingham, UK), the Ahringer feeding library (clone *ifc-1*, Source BioScience, Nottingham, UK). RNAi clones for *ifd-1* and *ifp-1* were generated by subcloning 1 kb of the corresponding cDNA into a modified L4440 RNAi feeding vector, containing a linker with *AscI* and *NotI* restriction sites, analogous to the site of insertion (Rommelzwaal et al., 2021). The following primers were used: oSMR57 (aggcgcgccTGACCACCATAGCCGAAGTT), oSMR58 (agcggccgcTTTGAAGCCACCAACGTCTG), oSMR59 (aggcgcgccTCAAAACCGGGTTCTCGAGA), oSMR60 (agcggccgcTTCAGTGCAGGAGTTGATCT). Vector identity was verified by DNA sequencing in each instance.

Acknowledgments

We thank Barbara Bonn, Janis Moeller and Sabine Eisner for their commitment and excellent technical support and Adam Breitscheidel for thoughtful figure arrangement. We are particularly thankful to Christine Richardson and Martin Goldberg (Durham University, UK) for high-pressure freeze electron microscopy. We are also grateful for helpful advice from Erik Jorgenson and Matthew LaBella. Strains N2 and FK312 were obtained from the Caenorhabditis Genetics Centre (University of Minnesota, Minneapolis, MN). The MH33 monoclonal antibody was obtained from the Developmental Studies Hybridoma Bank developed under the auspices of the NICHD and maintained by the University of Iowa, Department of Biology, Iowa City, IA. The work was supported by the German Research Council (LE566/14-1, 3) grant to R. E. Leube, and by the Netherlands Organization for Scientific Research (NWO)-VICI 016.VICI.170.165 grant to M. Boxem.

Funding

The work was supported by the German Research Council (LE566/14-1, 3) grant to R. E. Leube, and by the Netherlands Organization for Scientific Research (NWO)-VICI 016.VICI.170.165 grant to M. Boxem. The authors declare no competing financial interests.

Supplementary Figures

ATG | TCG | GCG | GTT | AGT | TAT | TCG | ATG | CAC | AGA | ACC | ACC | ACA | ACT | ACA | TCC | TCC |
 TCA | TCA | CAC | GGA | GGT | GTC | TCA | GCC | GGC | CAT | GCC | GCT | GAG | GAG | TTC | GTT | GCC |
 TCT | GCC | GAG | CGC | GAG | AAG | CAA | GAG | ATG | CAG | CAG | TTG | AAC | TCT | CGC | CTT | GAA |
 GTT | TAC | ATC | AGC | CGT | GTC | CGT | CAA | CTT | GAG | GAT | CGT | AAC | AAG | GAG | CTT | GTG |
 ATT | GAA | TTG | GAC | ACC | CTC | CGA | GGA | TCA | CTT | GGA | AAT | GAC | ATC | GGA | CAG | ATC |
 AAG | TTC | AAA | TTC | AAC | GAT | TCG | TTG | GTC | AAA | GTT | CGC | CGT | GAG | ATC | TCA | GAA |
 GCT | CAT | TCT | GGA | ACT | ATT | GGA | GTT | GAA | GTT | AAG | GTC | GAC | AGA | TTGAGAGATGAT
 TTGAATGACTACAGACACAGgtacaattttatttgcataattccattcttaattggcaaatatttcagATA
 TGAAGA | GGC | CCG | TCG | TGA | AGTTGAGCGTGAGAAGACCACTTGGGGAGGAGCTATTTACAAGC
 ACAAGCTGAGCTTGACACAACAAGTCCCGCTATGCCGCCATTTGGACGAGGAAAAGAGACTTTATG
 CTGAACAAGATCAACTCTATCTTCAATTGGCTGCCGCCAAGGATGAGCTTGACGCCGCAATTGTTGAT
 CGCCGCCGCTTCAAGCTGAGGAAGATGACCTCAAGATTGAGCTGGAATCTTTGGGAAGAAATCCACTC
 TCAAGAAATCACTGAGCTTCGCACTCTTCTTGCTCAAGCTCCAGCCGACACAAGAGAGTTCTTCAAGA
 ATGAATTGGCTCTTGCTATCAGAGAAAATCAAGGCTGAATACGACAAGATCATCAAACCACCAGAGTT
 GATCTTGAGACAATCTTCCAGAGCAAGATTAGCGCCGTCGAATCATCAATCGTCTCCAAGAACGAGGC
 TGCCGTTTTCCGTCAAGAGGAGATCAGAAAAGATGAACGAGAGCATCACCACATTGCGAGCCAAGCTCA
 GCGAGCTCGAAGCCCGTAACTCTGCTTTGGAGAGAGAAGCCAACACACTCCAGATTTCAACTCGGAGAA
 GATCAAAGAGCTTACGAATCAGAGCTTCAAGAGAGACAATGCCCTCCGATTTATGCGTGAAGACTG
 CCAGACTTTGATTGCTGAACTTCAAGCTCTTCTTAACACCAAACAACTTTGGATACTGAGATTGCCA
 TCTACAGAAAGCTTGTCGAGTCCGAGGAAGGAAGATTCACTCATGTTGGACAGGGGGTCTGTGTCGCC
 CAGCAGGAGACTACAAGATTGGTACCAGTCGAGCAAGATCACTGGGACTCTGGAGAGGTTCAAACCTCG
 TTCCTCATTCAAGAGACACGCTAAGGGAAATGTGAGCATCGTTGAGTGCGATCCACAAGGAAAGTACA
 TCATTCTGAAAACACCAGTGGATCAGTTGCCGAAGATGTAAGCAACTTTGAAATCCGTCGTGTTATT
 GATGGAGTTCAAGCCTTCGTTTTCCGTCTCCCATCTCACTTAGTTATTCAACAACACGGACATCTTAA
 GATCTACGGACGCAATTCAGGAGGAATTAACCTACCACCAGACTCAATTGTGATGGAATCTCACCCAT
 CATGGGGACAAGGAGGACAAGTTGAAACATTTCTTGACAATAGTCACGGAATTGAGAAGGCTTCGCAC
 ATCCAGACGACGGTCGCTTCTCCCGTTAA

Figure S1. Exon sequence of the *ifb-2(kc20)* allele. The depicted sequence shows the spliced gene model of isoform *ifb-2a*. The transcriptional start codon is highlighted in green. Exons are shown in alternating yellow/orange colors. The unmarked sequence represents the intron 3 that is deleted together with parts of adjacent exons 3 and 4 in the *ifb-2(kc20)* allele carrying an 83 base pair deletion (double cross out; position 5.751.812 - 5.751.893). The deletion induces a premature stop (highlighted in red) encoding only a truncated protein of 120 amino acids, 116 of which correspond to the native IFB-2 protein.

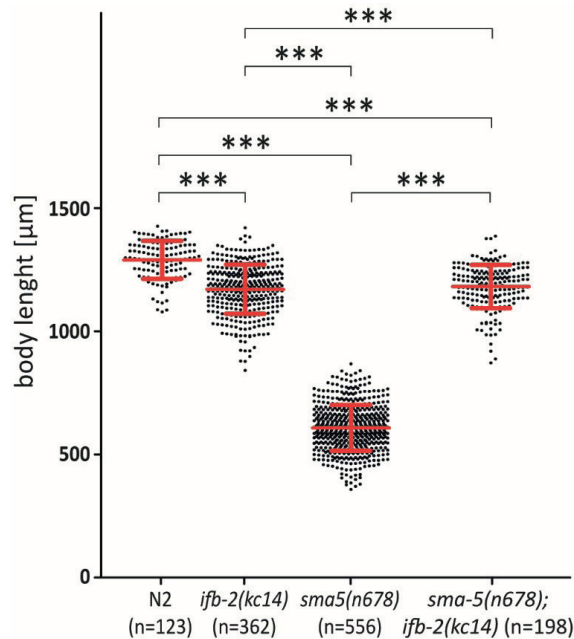
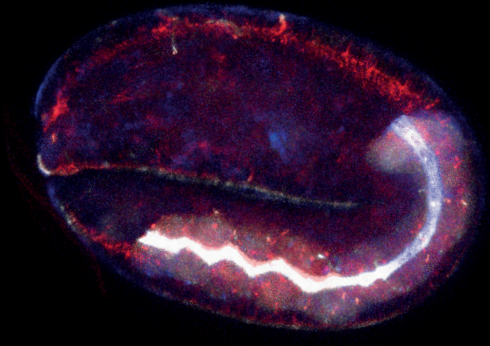
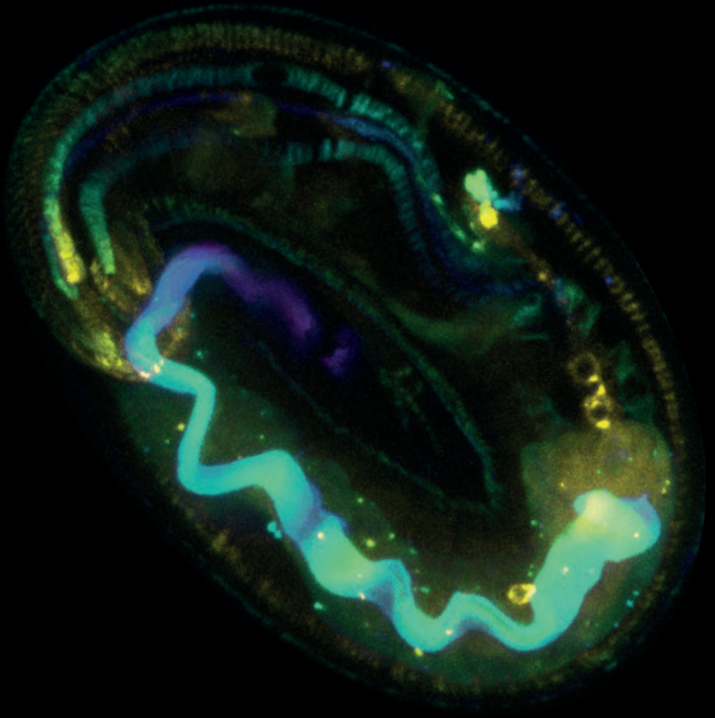
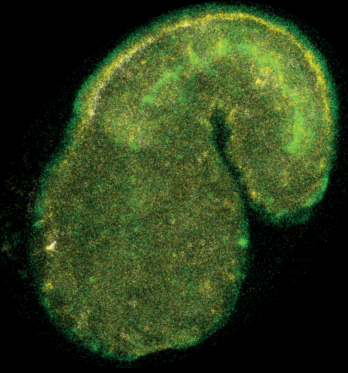
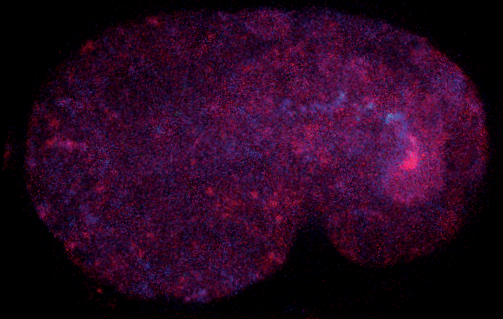


Figure S2. Comparison of body length 4 days after egg laying reveals efficient rescue of the *sma-5(n678)* phenotype by *ifb-2(kc14)*. The scatter dot blot summarizes the results of body length measurements in N2, *ifb-2(kc14)*, *sma-5(n678)* and *sma-5(n678);ifb-2(kc14)*. Note that loss of IFB-2 rescues the body length phenotype of *sma-5(n678)* to the level of *ifb-2(kc14)* single mutants (N2: 1287±76.75 μm; *ifb-2(kc14)*: 1168±99.49 μm; *sma-5(n678)*: 608.2±91.97 μm; *sma-5(n678);ifb-2(kc14)*: 1179±87.57 μm; *** p<0.0001).



Chapter 7

Optogenetically-controlled localization
of the apical polarity protein PAR-6

Sanne Remmelzwaal, Ruben Schmidt and Mike Boxem.

Developmental Biology, Institute of Biodynamics and Biocomplexity, Department of Biology,
Faculty of Science, Utrecht University, Padualaan 8, 3584 CH, Utrecht, The Netherlands.

Abstract

Cell polarity is fundamental for the morphology and functioning of epithelial tissues. Epithelial polarization is established by the interplay between conserved groups of cortical polarity proteins that define distinct cortical domains. Here, we use optogenetic manipulation of apical PAR polarity protein localization to investigate apical domain formation and maintenance in the *Caenorhabditis elegans* intestine. Using the ePDZ-LOV optogenetic system we localized PAR-3 and PAR-6 to the cortices of the intestinal cells by dimerization with a ubiquitous membrane anchor. Directed recruitment of PAR-6 to the basolateral membrane did not cause PAR-6 to lose its association with the apical domain, and its basolateral localization was lost over time. Long-term activation of the optogenetic machinery did not alter intestinal PAR-6 localization: PAR-6 did not localize basolaterally but retained its apical localization. Temporary optogenetic basolateral localization of PAR-6 did not alter apical-basal polarity of the intestinal cells. These experiments indicate that the ePDZ-LOV-based optogenetic approach used is not suitable to robustly and functionally manipulate polarized PAR-6 localization in the established epithelium of the *C. elegans* intestine, or requires substantial further optimization.

Introduction

Biological tubes are defined by epithelial sheets of interconnected, polarized cells wrapping around a hollow lumen. The apical sides of epithelial cells generate the luminal surface, while their basolateral domains connect to neighboring cells and the extracellular matrix. The lateral and apical domains are separated by cell-cell junctions, constructing a sheet of tightly-attached cells that provide a selective permeable barrier for the exterior environment.

Cell polarity is initiated upon cues from the inter- or extracellular environment and reinforced by conserved cortical polarity regulators. These proteins define opposing domains through a complex network of complementary and antagonistic interactions. The apical PAR complex proteins Par3, Par6, and aPKC constitute one of these highly conserved protein networks and play a central role in the establishment and maintenance of epithelial cell polarity in metazoans. The scaffold protein Par3 recruits another scaffold Par6, which binds to the kinase aPKC and localizes to the apical cortex interdependently. Here, aPKC phosphorylates the basolateral proteins Lgl and Par1 which excludes them from the apical domain. Together, mutual inhibition between the apical and basolateral polarity proteins defines membrane domain identities, while the cytoskeleton directs membrane components to build polarized cell architecture.

An essential structural characteristic of intestinal epithelial cells is the formation of an apical brush border: an array of finger-like protrusions called microvilli which increase surface area for enhanced absorption. Polarity establishment and brush border formation are both early events in intestine development that rely on cytoskeletal and trafficking pathways. The ERM (ezrin, radixin, moesin) family member ezrin is a PI(4,5)P₂ lipid- and actin-interacting protein that links filamentous actin to the membrane to form microvilli. Additionally, ezrin promotes apical localization and activation of the small GTPase Cdc42 to drive apical differentiation and brush border formation by the apical PAR complex.

Cdc42, ezrin and the apical PAR complex are mislocalized in Microvillus Inclusion Disease (Michaux et al., 2016), a condition in which microvilli form on the basal domain of enterocytes as a result of polarity inversion. Studies of the *Caenorhabditis elegans* intestine revealed that disruption of apical trafficking by loss of the V0 sector of the vacuolar ATPase leads to similar phenotypes, including the formation of cytoplasmic microvillus inclusions and mislocalization of PAR proteins (Bidaud-Meynard et al., 2019). Additionally, disruption of polarized trafficking by clathrin and its AP-1 adapter leads to *de novo* apical membrane formation on the lateral side of *C. elegans* intestinal cells (Shafaq-Zadah et al., 2012b; Zhang et al., 2012).

The *C. elegans* intestine comprises of a single layer of 20 polarized cells, that due to its simplicity and similarity to vertebrate intestinal cells has provided an appealing model for studying polarity and lumenogenesis during development. In the embryonic intestine, the apical PAR complex maintains apical and junctional continuity to build a functional tube (Sallee et al., 2021). Nevertheless,

the complex is non-essential during larval development of the tissue (Castiglioni et al., 2020). Disruption of epithelial polarity maintenance in the established intestine leads to mislocalization of the apical PAR proteins and the formation of ectopic lumens (Shafaq-Zadah et al., 2012b; Winter et al., 2012; Zhang et al., 2012), but their function in the established intestinal epithelium remains elusive. It additionally remains unknown if the apical PAR complex maintains its instructive role in established epithelia and how initial asymmetries in cortical polarity regulators are translated to the correct specification of apical domain structure.

In this chapter, we use optogenetic manipulation of PAR protein localization to investigate apical domain formation and maintenance in the *C. elegans* intestine. We show that PAR-3 and PAR-6 can be localized to the cortices of the intestinal cells by dimerization with a ubiquitous membrane anchor. Following directed recruitment of PAR-6 to the basolateral membrane, we observed that PAR-6 retains its localization at the apical domain and loses its basolateral localization over time. Long-term activation of light-controlled PAR-6 localization did not overcome the mechanisms that control cell polarity, and the protein returned to its baseline polarized location. We therefore conclude that temporary optogenetic basolateral localization of PAR-6 alone is insufficient to manipulate apical-basal polarity in the fully established epithelium of the *C. elegans* intestine.

Results

The ePDZ-LOV system enables protein recruitment to the cell membrane in the intestine of *C. elegans* larvae

We set out to investigate apical domain formation by PAR-3 and PAR-6 in an established epithelium, using optogenetic dimerization with engineered membrane anchors to allow for spatial and temporal control of the manipulation of polarity. Multiple light-inducible dimers have been developed, including tunable light-controlled interacting protein tags (TULIPs) (Strickland et al., 2012) and improved light-inducible dimers (iLID) (Guntas et al., 2015). Both use the photosensitive light-oxygen-voltage 2 (LOV2) domain from *Avena sativa* phototropin 1 for dimerization, combined with an engineered PDZ (ePDZ) domain in the case of TULIP, or the *E. coli* SspB protein in the case of iLID. In the absence of blue light, the peptide is caged by LOV2, but upon illumination, LOV2 undergoes a conformational change that makes the peptide available for dimerization (Figure 1A). TULIPs were shown to function in *C. elegans*, and TULIP tags can target fluorescent proteins to the membrane of embryos (Fielmich et al., 2018), seam cells and neurons (Harterink et al., 2016). However, TULIPs have not yet been implemented in the established intestinal epithelium of *C. elegans* larvae (Figure 1B).

To characterize the ePDZ-LOV system in the *C. elegans* intestine, we used strains with a membrane-bound LOV2 domain, expressed as a pleckstrin-homology domain (PH)-GFP protein fusion (PH::GFP::LOV), together with mCherry::ePDZ fusions of PAR-3 or PAR-6, extrachromosomally expressed under control of

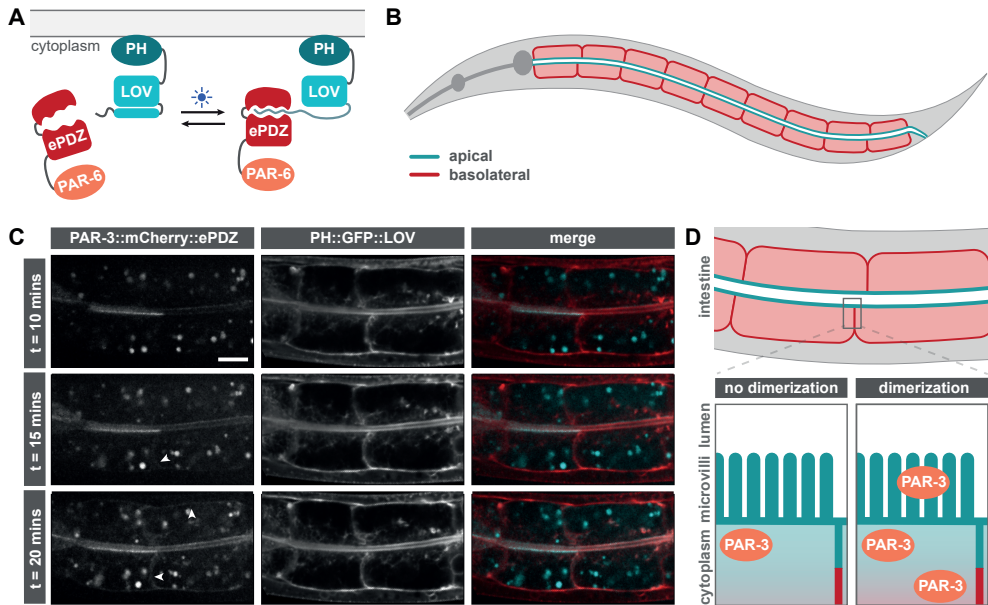


Figure 1. The ePDZ-LOV system enables protein recruitment to the intestinal plasma membrane. (A) Schematic representation of the ePDZ-LOV system experimental setup. The light-oxygen-voltage 2 (LOV) domain is attached to an anchor of choice—here the membrane-bound pleckstrin-homology (PH) domain. An engineered PDZ (ePDZ) domain is fused to a protein of choice (here PAR-6). Blue light induces a conformational change in the LOV that makes the peptide available for dimerization with ePDZ. (B) A schematic of the *C. elegans* intestine with the apical membrane in cyan and the basolateral membrane in red. (C) Activation of the ePDZ-LOV system by blue light recruits PAR-3::mCherry::ePDZ to PH::GFP::LOV in the *C. elegans* intestine. (D) Schematic overview of the experiment in C. Without dimerization PAR-3::mCherry::ePDZ localizes to the apical domain of the intestinal cells. Upon dimerization with PH::GFP::LOV, PAR-3::mCherry::ePDZ additionally localizes to the plasma membrane of the intestinal cells.

All microscopy images in this study are taken using a spinning disk confocal microscope and all scale bars represent 10 μm .

the intestine-specific *vha-6* promoter (Figure 1A). Since GFP is also excited with blue light, experiments that involve GFP imaging imply global and continuous induction of ePDZ-LOV dimerization. Shortly after illumination with a blue (491 nm) laser, PAR-3 localized at the apical domain (Figure 1C, 1D), resembling the wild-type situation (Castiglioni et al., 2020). Animals expressing PH::GFP::LOV and extrachromosomal PAR-6::mCherry::ePDZ often displayed irregular intestinal morphologies (Figure S1A), even though the extrachromosomal line was selected to have visibly low overexpression of PAR-6::mCherry::ePDZ. In a subset of PAR-6::mCherry::ePDZ expressing animals, PAR-6 decorated the lateral membrane, although never strongly and longer induction of dimerization rarely induced basal localization (Figure S1B). However, TULIP activation did induce global recruitment of PAR-3::mCherry::ePDZ to PH::GFP::LOV (Figure 1C, 1D). Basolateral localization of PAR-3 became visible as patches covering the cell membrane 15 minutes after exposure and reached near-homogenous cell membrane coverage 20 minutes after exposure in L3 and L4 stage larvae.

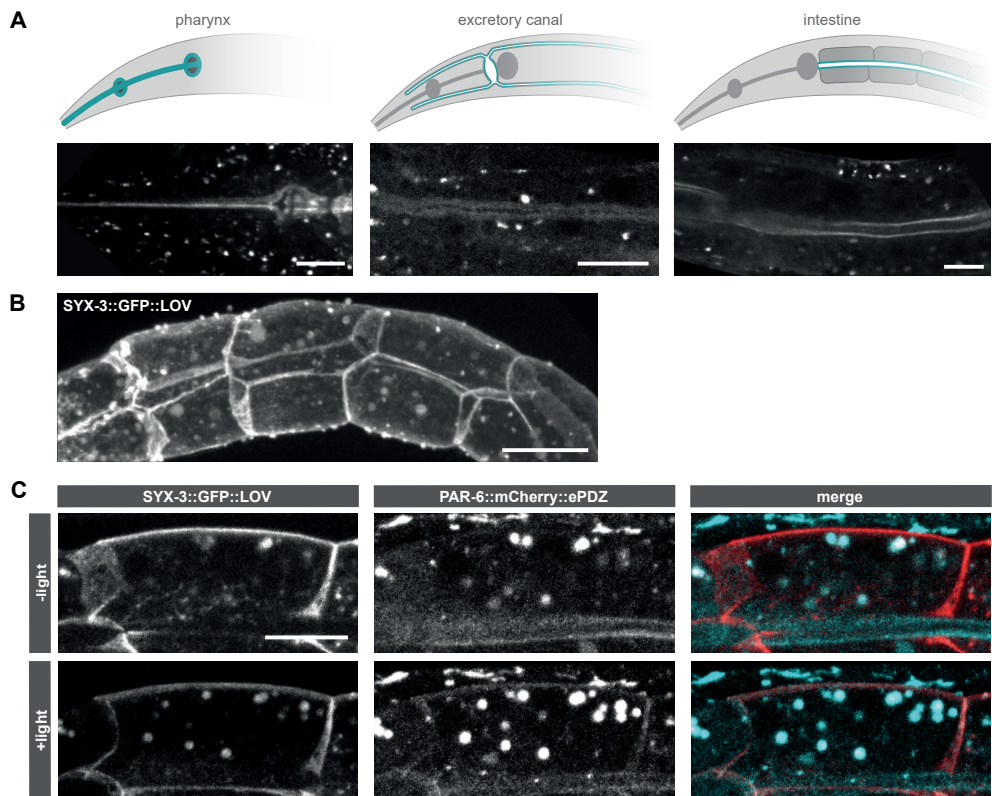


Figure 2. SYX-3::GFP::LOV serves as a suitable anchor to recruit endogenous PAR-6::mCherry::ePDZ to the basolateral domain. (A) Endogenous PAR-6::mCherry::ePDZ localizes apically in *C. elegans* epithelia. (B) SYX-3::GFP::LOV expression under control of the intestine-specific *vha-6* promoter. (C) Endogenous PAR-6::mCherry::ePDZ localizes to the apical domain of the *C. elegans* intestine. Activation of the ePDZ-LOV system by blue light additionally recruits PAR-6::mCherry::ePDZ to SYX-3::GFP::LOV at the basolateral membrane.

Together these data show that optogenetic control of protein dimerization by TULIPs can be induced in the established intestinal epithelium of *C. elegans* larvae.

SYX-3::LOV serves as an inducible anchor for basolateral recruitment of PAR-6::ePDZ

After this proof of principle experiment, we aimed to relocate not only excess polarity regulators that were introduced by extrachromosomal overexpression, but aspired to distribute endogenous PAR proteins to the basolateral membrane. Using CRISPR/Cas9, we generated an endogenous PAR-6::mCherry::ePDZ fusion, from here on referred to as PAR-6::ePDZ. As previously reported (Castiglioni et al., 2020), PAR-6 was expressed in epithelial tissues including the pharynx, excretory canal, intestine and epidermis (Figure 2A). Homozygous animals were viable and we did not observe any obvious developmental or growth defects, indicating that the PAR-6 protein is functional.

The relative size of the highly folded apical membrane, opposed to the smooth basolateral membrane, likely ensures high apical/basal membrane anchor ratios. This, in combination with the apical domain being the native location of the PAR complex, presumably favors dimerization at the apical rather than basolateral membrane. To further optimize basolateral localization of apical PAR proteins, we anticipated that a ubiquitous membrane anchor might not be effective in achieving adequate basolateral PAR-6 levels to manipulate cell polarity. To circumvent this problem, we aimed to induce endogenous PAR-6 dimerization with an anchor that exclusively localizes to the basolateral membrane. We selected three proteins that were reported to localize basolaterally in intestinal cells and are not strongly linked to the regulation of polarity: the pharynx- and intestine-specific aquaporin AQP-1 (Zhang et al., 2012), the *C. elegans* syntaxin family orthologue SYX-3 (previously known as SYN-1) (Yamashita et al., 2009) and an artificial truncation of the cell adhesion molecule and homologue of L1CAM, the SAX-7 basal peptide (Low et al., 2019). We generated plasmids encoding GFP::LOV fusion proteins of the proposed basolateral anchors under control of the intestine specific *vha-6* promoter and expressed the plasmids in animals carrying endogenous PAR-6::ePDZ from an extrachromosomal array. Spinning disk confocal imaging of transgenic animals revealed that AQP-1::LOV was not exclusively basolateral (data not shown), and will therefore not serve as a suitable basolateral anchor for the optogenetic experiments. The SAX-7 basal peptide localized primarily basolaterally and the anchor successfully dimerized with PAR-6::ePDZ at the basolateral membrane upon exposure to blue light (Figure S2A). Overexpression of the peptide regularly induced a ruffled basolateral membrane phenotype independent from its dimerization with PAR-6 (Figure S2B). Since mislocalization of PAR-6 can generate ectopic lumens (Zhang et al., 2012), we anticipated that basolateral localization of apical PAR-6 might lead to excess basolateral membrane formation. We therefore argued that the membrane ruffles marked by SAX-7 basal peptide overexpression might interfere with observing the hypothesized phenotype of prolonged basolateral PAR-6 localization. Animals overexpressing SYX-3::GFP::LOV (from here on referred to as SYX-3::LOV) showed normal basolateral organization (Figure 2B). We additionally observed PAR-6 localization at the basolateral domain 5 minutes after illumination (Figure 2C), demonstrating both more rapid and homogenous relocalization compared to the experiments with a ubiquitous membrane anchor and extrachromosomal PAR-6::ePDZ. We therefore consider SYX-3::LOV as a reliable basolateral anchor for optogenetic localization of PAR-6 and favor endogenously expressed PAR-6::ePDZ in combination with a basolateral membrane anchor over extrachromosomal PAR-6 in combination with an ubiquitous membrane anchor for light-controlled PAR-6 localization.

Continuous activation of the TULIP system does not alter intestinal PAR-6 localization

Temporary light-controlled localization of PAR-6 did not visibly alter intestinal organization. To examine the effect of prolonged PAR-6 localization to the basolateral membrane, we allowed larvae with endogenous PAR-6::ePDZ and extrachromosomal SYX-3::LOV expression to develop under continuous blue

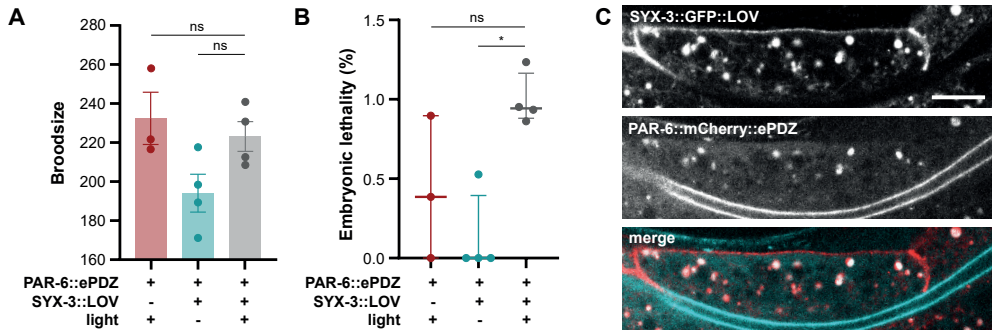


Figure 3. Continuous activation of the ePDZ-LOV system does not alter PAR-6::mCherry::ePDZ localization. (A) Broodsize assay of *par-6::mCherry::ePDZ* animals with and without extrachromosomal SYX-3::GFP::LOV expression, in the presence and absence of blue light. (B) Embryonic lethality scored as the percentage of unhatched eggs to total broodsize. Same animals were assessed as in experiment in A. (C) Endogenous PAR-6::mCherry::ePDZ fails to dimerize with SYX-3::GFP::LOV upon continuous illumination with blue light.

light exposure. We hypothesized that continuous induction of PAR-6::ePDZ-SYX-3::LOV dimerization would interfere with embryogenesis and intestine formation, and therefore would result in embryonic lethality. *par-6::ePDZ;syx-3::LOV* animals that were grown under blue light did not show reduced brood sizes (Figure 3A). In addition, we observed a slight significant change in embryonic lethality between animals with and without blue light exposure (Figure 3B). We did not observe a significant change in embryonic lethality between animals expressing *par-6::ePDZ* only and animals exposed to blue light with *par-6::ePDZ;syx-3::LOV* expression. Since *par-6* mutations lead to almost full embryonic lethality (Watts et al., 1996) and blue light exposure is toxic (Abdel-Rahman et al., 2017; De Magalhaes Filho et al., 2018), the small significant change in embryonic lethality can most probably be assigned to blue light toxicity. We argued that the minor toxicity of continuous PAR-6::ePDZ-SYX-3::LOV dimerization might technically be explained by residual apical PAR-6, late embryonic expression of the SYX-3::LOV transgene, or a combination of both.

To investigate if PAR-6 was retained at its native localization site, we performed spinning disk confocal microscopy. Surprisingly, PAR-6 was not found at the basolateral membrane and its expression pattern resembled that of control animals (Figure 3C). Animals were grown under light-emitting diodes (LED), that might not produce light with sufficient intensity to ensure light-induced dimerization. If this is the case, illumination with a blue laser would initiate PAR-6 recruitment to the basolateral domain. However, after 1 hour of repeated laser exposure, PAR-6 still retained its localization at the apical domain and was not observed at the basolateral cortex (Figure S3A).

We also investigated if optogenetic recruitment of PAR-6 to the basolateral domain would bring about transfer of its interaction partners. We used an existing CRISPR knock-in line expressing PKC-3 (aPKC) fused to GFP (GFP::PKC-3)

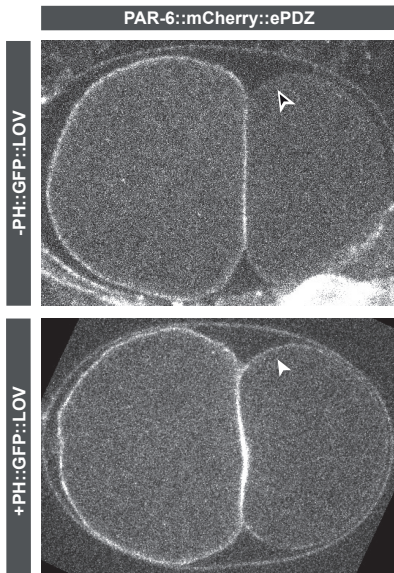


Figure 4. Optogenetic relocation of PAR-6::mCherry::ePDZ in the *C. elegans* zygote. Global activation of the ePDZ-LOV system in an one-cell embryo expressing endogenous PAR-6::mCherry::ePDZ with (+) or without (-) expression of PH::GFP::LOV.

laser. In control two-cell embryos, PAR-6 exclusively localized to the anterior cell, but by global activation of dimerization we were able to expand PAR-6 cortical localization posteriorly (Figure 4). TULIPs have previously been used to manipulate localization of various proteins in the *C. elegans* embryo and was proven to work both rapidly (instantly upon blue light activation) and robust (Fielmich et al., 2018), resulting in near homogeneous redistribution of optogenetically-controlled proteins. PAR-6 relocation to the posterior cell was relatively slow (order of seconds after blue light induction) and did not visibly approach anterior localization levels. Additionally, we did not observe defects in cellular division. Anterior-posterior segregation of the PAR polarity proteins drives asymmetric cell division (Kemphues, 2000), suggesting that optogenetic dimerization at the posterior membrane did not alter anterior/posterior PAR-6 ratios sufficiently to interfere with this highly controlled and essential process. All in all, our data imply that cortical PAR-6 is too stable in both developing embryos and the established intestinal epithelium to manipulate with the TULIP optogenetic machinery.

(Castiglioni et al., 2021), constructed a SYX-3::BFP::LOV plasmid and expressed it together with PAR-6::ePDZ in the GFP::PKC-3 background. Global activation of PAR-6::ePDZ/SYX-3::BFP::LOV dimerization did not result in robust localization of PAR-6 to the basolateral domain and we consequently failed to observe translocation of PKC-3 (Figure S3B). Together, these data suggest that PAR-6 localization at the apical domain and retention from the basolateral domain of the *C. elegans* intestine is remarkably robust.

The TULIP system is not suitable to homogeneously alter PAR-6 localization in the *C. elegans* embryo

The highly controlled nature of PAR-6 localization could be attributed to the fully established and non-dynamic character of the intestinal epithelium in *C. elegans* larvae. We therefore aimed to control PAR-6 localization in the early embryo. We used embryos that expressed PH::GFP::LOV and endogenously labelled PAR-6::ePDZ, and induced global cortical enrichment by illuminating the embryo with a blue

Discussion

Recent findings demonstrated that the apical PAR complex is non-essential for postembryonic development of the *C. elegans* intestine (Castiglioni et al., 2020). Since the PAR proteins are mislocalized upon disruption of epithelial polarity maintenance (Shafaq-Zadah et al., 2012b; Winter et al., 2012; Zhang et al., 2012), we wondered if their instructive role in apicobasal polarity is retained in established tissues. We exploited the optogenetic TULIP system to systematically control the localization of endogenous PAR polarity proteins in the fully established epithelium of the *C. elegans* intestine. Using light-induced ePDZ–LOV heterodimerization we aimed to relocate PAR-6 to the basolateral domain to determine if the PAR complex maintains its instructive properties in established epithelia. We aspired to exploit the reestablishment of apical polarity to discover how initial asymmetries in cortical polarity regulators are translated to the correct specification of apical membrane domains. However, our experiments demonstrated that the TULIPs optogenetic system is not suitable to robustly and functionally manipulate polarized PAR-6 localization in intestinal cells. TULIP-mediated PAR-6 relocalization was not nearly as effective as previous results of the system in *C. elegans* (Fielmich et al., 2018; Harterink et al., 2016). We did not accomplish stable basolateral PAR-6 localization, nor induction of ectopic apical domain identity. It is difficult to speculate what makes PAR-6 difficult to relocate, since multiple mechanisms may keep PAR-6 at its native apical domain. Additionally, the exact position relative to the membrane and cytoskeleton of relocalized PAR-6 may not mimic the normal situation, affecting the ability of PAR-6 to promote apical domain identity.

In the proof-of-principle experiment, we aimed to localize both extrachromosomal PAR-3 and PAR-6 to the membrane of the intestinal cells using an ubiquitous PH::LOV membrane anchor. Even though PAR-3 was easily relocated, PAR-6 relocalization appeared to be less feasible. Nevertheless, PAR-6 was readily relocalized using a strictly basolateral anchor. Differences between PAR-3 and PAR-6 relocalization can be explained based on their slightly diverging molecular roles and their integration in protein complexes. PAR-6 is considered to be a protein-protein interaction hub (Pires and Boxem, 2017; Riga et al., 2020), while such a role has not been assigned for PAR-3. Furthermore, the PAR-3 *Drosophila* orthologue Bazooka is known to establish transient interactions (Krahn et al., 2010). This suggests that there might be a cytoplasmic PAR-3 pool readily available for ePDZ/LOV-heterodimerization, while PAR-6 is favorably retained in its native protein complex structure.

The main function of the apical membrane is the absorption of nutrients – facilitated by its large surface area through the formation of many membrane covered microvilli. The surface of the apical membrane therefore easily surpasses the surface area of the smooth basolateral membrane, leading to a higher density of membrane anchors at the apical domain in the initial experiment. The myriad PH::LOV anchors are thus largely positioned in the native location of the apical polarity proteins, further favoring their retention at the apical rather than basolateral domain. This might additionally explain why

we observed only a nominal reduction in apical PAR-6 intensity upon basolateral PAR-6 relocalization.

Additional PAR-6 specific characteristics could be responsible for the incomplete relocation. The affinity of PAR-6 for CDC-42 or any of its many, apically localized, interaction partners might outweigh the affinity of PAR-6::ePDZ for the LOV peptide. These competing interactions could be circumvented by decreasing the affinity of PAR-6 for its apically localized interaction partners via the disruption of binding domain functions using CRISPR/Cas9-mediated genome editing. However, since this induces a permanent change in the genome, it will likely interfere with essential embryonic polarity processes, causing unintended side effects and presumably early embryonic lethality. Additionally, since PAR-6 serves as an apical protein interaction hub, many proteins might need to be altered to reach this goal. Alternatively, it is plausible that TULIP uncaging is hindered upon fusion to the PAR-6 protein. Even though PAR-6 and the ePDZ domain are separated by a linker and mCherry protein, we do not have any insight on the conformation of said proteins. Hence, it would be an interesting avenue to explore whether other apical polarity proteins are more susceptible to TULIP-mediated protein relocalization.

Even though we were able to relocate PAR-6 basolaterally, it proved to be challenging to stably maintain basolateral PAR-6 expression. Additional activation of the TULIP system by blue laser, after continuous activation by blue LED light did no longer attain PAR-6 localization at the basolateral membrane. It appears that PAR-6 can only be recruited to the basolateral membrane once. Suggesting that a mechanism is in place to maintain proper polarity protein distribution. Other polarity proteins might be activated upon initial PAR-6 relocalization to maintain polarity. This suggest that maintenance of polarity in the *C. elegans* intestine is stronger than the cue to reinduce apical polarity where it does not belong. Future experiments should elucidate if relocalization of PAR-6 to the basolateral membrane induces upregulation of its antagonistic interactors and therefore shine light on how polarity is maintained in the established epithelium of the *C. elegans* intestine.

Materials and Methods

***C. elegans* strains and maintenance**

Caenorhabditis elegans strains were cultured under standard conditions (Brenner, 1974). Strains expressing both ePDZ and LOV protein motifs were regarded as light-sensitive and cultured in the dark. All experiments were performed with animals grown on nematode growth medium (NGM) agar plates at 15 or 20 °C. Table S1 contains a list of all the strains used.

Molecular cloning

SapTrap assembly was done as described (Schwartz and Jorgensen, 2016) using existing SEC donor modules (Dickinson et al., 2018) or new donor modules generated by cloning PCR fragments or custom gBlocks (IDT) into Eco53kl-digested

vector pHSG298 (Takara Biosciences). For the *Pvha-6::par-3::mCherry::ePDZ::tbb-2 3'UTR* and *Pvha-6::par-6::mCherry::ePDZ::tbb-2 3'UTR* constructs, *Pvha-6*, *par-3* and *par-6* were amplified from genomic N2 DNA, *mCherry*, *BFP* and the *tbb-2 3'UTR* were amplified from prior plasmids, and *ePDZ* was ordered as a gBlock (IDT). A list of all used oligonucleotides (IDT) and gBlocks (IDT) is included in Table S2 and used plasmids are listed in Table S3. PCR fragments were generated using Q5 Hot Start High-Fidelity DNA Polymerase (New England Biolabs) and gel purified using the Nucleospin kit (Machery-Nagel). DNA concentrations were measured using a BioPhotometer D30 (Eppendorf). DNA vectors used for genome editing were purified from DH5a *E. coli* using a Qiagen midiprep kit and sequence-verified by Sanger sequencing (Macrogen).

CRISPR/Cas9 genome engineering

The *par-6::ePDZ::mCherry* endogenous gene fusion was generated in an N2 background by homology-directed repair of CRISPR/Cas9-induced DNA double-strand breaks (DSBs), using the SEC method and a plasmid-based repair template. The repair template was assembled into pMLS257 (Addgene #73716) using SapTrap with custom and SEC modules as follows (from 5' to 3'): left homology arm, a C-terminal linker (pMLS287), *mCherry*, SEC (pDD363), *ePDZ*, and right homology arm. Homology arms of ~600 bp upstream and downstream of the DSB were amplified from N2 genomic DNA and included mutations of the sgRNA recognition sites to prevent re-cutting after repair. The injection mix contained: 60 ng/μl *Peft-3::Cas9* (Addgene #46168), 15 ng/μl repair template, 100 ng/μl sgRNA, and 2.5 ng/μl *Pmyo-2::mCherry* (Addgene #19327). Microinjection of young adult hermaphrodite germlines was done using an inverted microinjection setup (Eppendorf FemtoJet 4x mounted on a Zeiss Axio Observer A.1 equipped with an Eppendorf Transferman 4r). Injected animals were singled and incubated for 3 days at 20 °C before adding 250 ng/μl of hygromycin per plate. Rol animals lacking visible *mCherry* expression were selected after 4–5 days. To eliminate the selection cassette through Cre-Lox recombination, L1 progeny of selected homozygous Rol animals were heat-shocked in a water bath at 34 °C for 1 hour. Correct excision was confirmed by selection of non-Rol animals and subsequent Sanger sequencing (Macrogen). A list of all DNA- and RNA-based reagents is included as Table S2 and sequence files of the final gene fusion is included in Supplemental DNA files.

Light microscopy

Imaging of *C. elegans* was done by mounting embryos or larvae on a 5% agarose pad in a 10 mM Tetramisole solution in M9 buffer to induce paralysis. Spinning disk confocal imaging was performed using a Nikon Ti-U microscope equipped with a Yokogawa CSU-X1-M1 confocal head and an Andor iXon DU-885 camera, using a 60x 1.4 NA objective. Directed PAR-6 recruitment in embryos was performed using a Nikon Eclipse Ti with Perfect Focus System, Yokogawa CSU-X1-A1 spinning disk confocal head, Plan Apo VC 60x N.A. 1.40 oil objective, Photometrics Evolve 512 EMCCD camera and DV2 two-channel beam-splitter for simultaneous dual-color imaging. For both microscopes, microscopy data was acquired using MetaMorph Microscopy Automation & Image Analysis Software.

All stacks along the z-axis were obtained at 0.25 μm intervals. Laser power and exposure times were kept constant within experiments.

Dark state experiments and local recruitment of ePDZ-tagged proteins to membrane LOV

Dark state experiments were performed on the spinning disk setup described above. For local photoactivation of LOV2 in *C. elegans* embryos, light was applied in a region of variable size depending on each individual experiment using a 491 nm laser controlled with the ILas system (Roper Scientific France/PICT IBI SA, Institut Curie). During both global and local photoactivation assays animals were kept away from blue light as much as practically feasible. To this end, aluminum foil was used to cover the microscope setup, and optical filters were inserted in the light path to remove LOV2-activating wavelengths from the transmitted light used to locate animals on slides.

Quantification of brood size and lethality

Starting at the L4 stage, individual P0 animals were cultured at 20 °C and transferred to a fresh plate every 24 hours for 6 days in the dark or under blue light emitting diodes (LEDs). Hatched and unhatched progeny were scored 24 hours after removal of the P0, and larval lethality was scored 48 hours after removal of the P0.

Image analysis

All images were analyzed and processed using ImageJ (Fiji).

Statistical analysis

All statistical analyses were performed using GraphPad Prism 8. For population comparisons, a D'Agostino & Pearson test of normality was first performed to determine if the data was sampled from a Gaussian distribution. All data were drawn from a Gaussian distribution, comparisons between populations were done using a one-way ANOVA if the SDs of the populations differ significantly. For data not drawn from a Gaussian distribution, a non-parametric test was used (Mann-Whitney for 2 populations and Kruskal-Wallis for > 2 populations). ANOVA and non-parametric tests were followed up with multiple comparison tests of significance (Dunnnett's, Tukey's, Dunnnett's T3 or Dunn's). Tests of significance used and sample sizes are indicated in the figure legends. No statistical method was used to pre-determine sample sizes. No samples or animals were excluded from analysis. The experiments were not randomized, and the investigators were not blinded to allocation during experiments and outcome assessment.

Acknowledgments

We thank J. Kerver for technical assistance. Some strains were provided by the *Caenorhabditis* Genetics Center.

Supplemental information

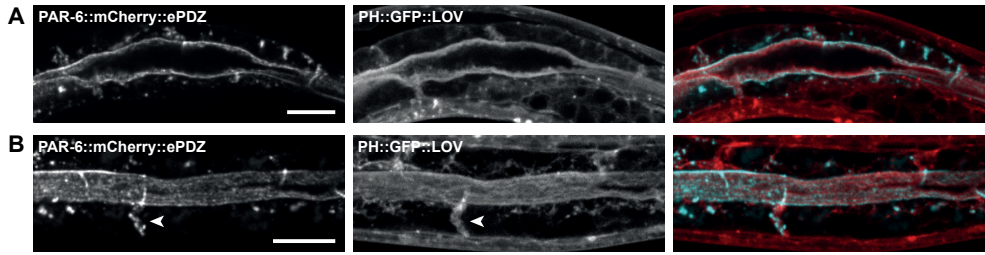


Figure S1. Intestines of animals with transgenic expression of *par-6::mCherry::ePDZ* and *PH::GFP::LOV*. (A) Animals expressing PAR-6::mCherry::ePDZ and PH::GFP::LOV display disrupted intestinal morphologies. (B) PAR-6::mCherry::ePDZ localizes basolaterally upon illumination with blue light. Arrowhead indicates lateral membrane.

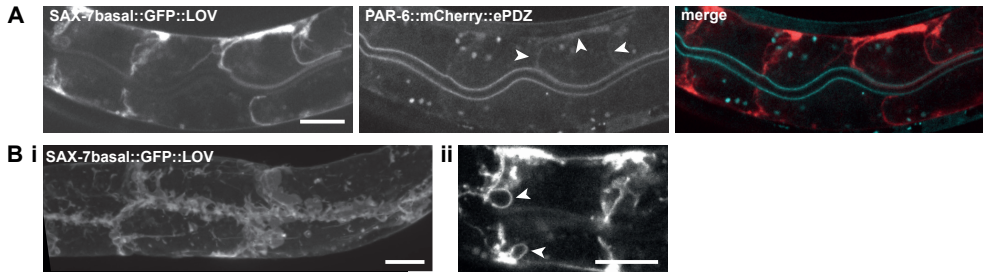


Figure S2. The SAX-7 basal peptide fused to GFP::LOV works as an anchor to recruit PAR-6::mCherry::ePDZ to the basolateral membrane. (A) Upon illumination with blue light, animals expressing PAR-6::mCherry::ePDZ and SAX-7basal::GFP::LOV show basolateral localization of PAR-6::mCherry::ePDZ. Arrowheads indicate basolateral PAR-6::mCherry::ePDZ. (B) Animals expressing SAX-7basal::GFP::LOV show irregular basolateral membrane morphologies. Arrowheads indicate bubble-shaped membrane structures at the basolateral domain.

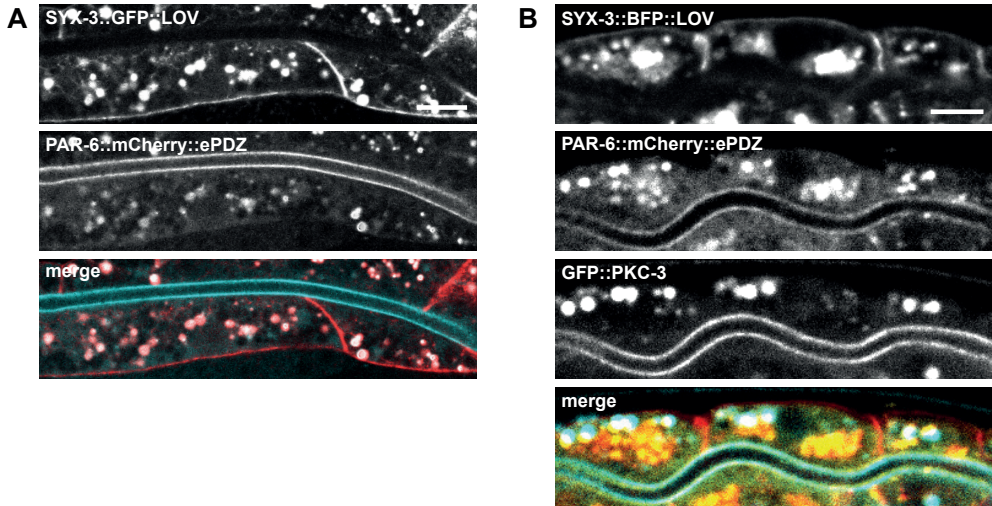


Figure S3. Exposing animals to a blue laser after continuous illumination with blue LED light failed to localize PAR-6::mCherry::ePDZ basolaterally. (A) Animals expressing endogenous *par-6::mCherry::ePDZ* and extrachromosomal *syx-3::GFP::LOV* developed under continuous blue LED light exposure before being exposed to a high-intensity blue-light laser. PAR-6::mCherry::ePDZ failed to localize basolaterally. (B) Upon exposure to a high-intensity blue laser, PAR-6::mCherry::ePDZ and GFP::PKC-3 retained their localization at the apical domain.

Table S1. List of strains used.

Name	Genotype	Source
N2	Wild type	CGC
BOX392	<i>par-6(mib57[par-6::mCherry-LoxP::ePDZ])I</i>	This study
BOX405	<i>par-6(mib57[par-6::mCherry-LoxP::ePDZ])I</i> ; <i>pkc-3(it309[GFP::pkc-3])II</i>	This study
SV2204	<i>par-6(mib57[par-6::mCherry::epdz] I</i> ; <i>cxTi10816(he259[Peft-3::ph(co)::egfp::lov::tbb-2UTR]) IV</i>	This study

Table S2. DNA reagents used.

Name		Sequence
<u>To generate <i>Pelt-2</i> SapTrap fragment</u>		
oSMR1	<i>Pelt-2</i> forward	ctGCTCTTCgTGGTAATTTTCGAAATGTATGAACTCCAATT
oSMR2	<i>Pelt-2</i> reverse	ctGCTCTTCgCATtctataatctatcttttagtttctatttattagaatgcc
Template: <i>C. elegans</i> genomic DNA		
<u>To generate <i>Pvha-6</i> SapTrap fragment</u>		
oSMR3	<i>Pvha-6</i> forward	ctGCTCTTCgTGGTTGCCAGTGATGAATCCAA GCAC
oSMR4	<i>Pvha-6</i> reverse	ctGCTCTTCgCATtttttatgggttttgtaggttttagtcg
Template: <i>C. elegans</i> genomic DNA		
<u>To generate <i>par-3b</i> SapTrap fragment</u>		
oSMR5	<i>par-3b</i> forward	ctGCTCTTCgATGTCGGCTTCATCCACGTCATC
oSMR6	<i>par-3b</i> reverse	ctGCTCTTCgCTTGTA CTGGGAAAACGATGAGGCG
Template: <i>C. elegans</i> genomic DNA		
<u>To generate <i>par-6a</i> SapTrap fragment</u>		
oSMR7	<i>par-6a</i> forward	ctGCTCTTCgATGTCCTACAACGGCTCCTACCA TC
oSMR8	<i>par-6a</i> reverse	ctGCTCTTCgCTTGTCCTCTCCACTGTCCGAAT CATTG
Template: <i>C. elegans</i> genomic DNA		
<u>To generate <i>mCherry</i> SapTrap fragment</u>		
oSMR9	<i>mCherry</i> forward	ctGCTCTTCgAAGTCCAAGGGAGAGGAGGAC AACATG
oSMR10	<i>mCherry</i> reverse	ctGCTCTTCgACCGTAGAGCTCGTCCATTCCCTC CG
Template: pJIR83 (Addgene #75028)		

To generate *tbb-2* 3'UTR SapTrap fragment

oSMR11 *tbb-2* 3'UTR forward ctGCTCTTCgTACTgagactttttcttggcggc
tbb-2 3'UTR reverse ctGCTCTTCgACGTAAgataaatgcaaaatcctttc
aag

Template: *C. elegans* genomic DNA

ePDZ (germline optimized) SapTrap fragment

gBlock *ePDZ gBlock* aaaactGCTCTTCgGGTagcggcagcggtagcAT
GCCAGAGCTCGGATTCTCGATCTCCGGAGGT
GTCGGAGGCCGTGGAAATCCATTCCGTCCTG
ACGATGATGGAATTTTTGTTACTCGGGTCCA
ACCAGAAGGACCAGCTAGCAAATCTTCAA
CCTGGAGACAAGgtaagTTAATTAAtttcatcga
gagatcgtgcaatttctcattcatgaagacttttcagAT
CATCCAAGCCAACGGTACTCTTTCATTAATA
TTGAGCACGGTCAGGCTGTCAGCCTTCTCAA
GACCTTCCAGAACACAGTCGAGCTCATCATC
GTCCGAGAGGTAGGAAACGGAGCTAAGCAG
GAGATCCGTGTCCCGTTCGAAAAGGACGGA
GGATCCGGAGGAGTTTCCAGTGTTCCAACCA
ACCTTGAGGTCGTTGCTGCCACACCAACAAG
CCTTCTCATCTCCTGGGATGCTTACCGTGAAC
TTCCAGTCTCCTACTATAGGATCACCTACGGA
GAGACCGGAGGAAATTCTCCAGTCCAAGAA
TTCACGGTCCCAGgtaagTTAATTAAttttatga
gaatctaaaagtaatttggagagtacaatattttcagG
AAGCAAGTCGACCGCCACAATTTCCGGATTG
AAGCCAGGAGTCGACTACACCATCACTGTCT
ATGCTCATTACAATATCATTACTACTCATCA
CCAATCTCCATCAATTATAGAACGAGTAGAT
TGGAGCTCAAGCTCCGTATTTGCAATCGAC
AGTGCCACGCGCCCGTGATCCACCCGTCGCG
ACGcGAAGAGCagaaaa

To generate *aqp-1* SapTrap fragment

oSMR15 *aqp-1b* forward ctGCTCTTCgATGACGGCCGAGGAAGATACTT
TGC
oSMR16 *aqp-1b* reverse ctGCTCTTCgCTTAGCTTGAAGCAATTTTTGTT
GCTC

Template: *C. elegans* genomic DNA

To generate *eGFP* SapTrap fragment

oSMR19 *eGFP forward* ctGCTCTTCgAAGTCCAAGGGAGAGGAACTC
TTCAC

oSMR20 *eGFP reverse* ctGCTCTTCgACCGTAGAGCTCGTCCATTCCG
TGGG

Template: pJIR82 (Addgene #75027)

To generate *LOV* SapTrap fragment

oSMR21 *LOVpep forward* ctGCTCTTCgGGTggaggcggtgggGGAGGATC

oSMR22 *LOVpep reverse* ctGCTCTTCgCGTTTAGACCCAGGTGTCGACG
GC

Template: pLF068 (Fielmich *et al.* 2018)

To generate *par-6* homology arms SapTrap fragments for CRISPR

oSMR25 *F_RHA_PAR6cterm* GGCTGCTCTTCgACGTGAaaaactcttttcagcca

oSMR26 *R_RHA_PAR6cterm* GGGTGCTCTTCgTACcccgaaattatgtcatttctg
gg

oSMR27 *F_LHA_PAR6cterm* GGCTGCTCTTCgTGGctaggcgagcgaagtgtg

oSMR28 *R_LHA_PAR6cterm* GGGTGCTCTTCgCGCGTCTCTCCACTATCAC
TG

Template: *C. elegans* genomic DNA

To generate *syx-3* SapTrap fragment

oSMR35 *SYX-3 forward* ctGCTCTTCgATGCCTAGGGATCGGTTAAAGG

oSMR36 *SYX-3 reverse* ctGCTCTTCgCTTACAAATAGGAGTAAAGTGG
CAAACG

Template: *C. elegans* genomic DNA

To generate *sax-7* basal peptide SapTrap fragment
(including silent mutation to remove internal SapI recognition site)

oSMR37 *SAX-7basal forward* ctGCTCTTCgATGGGGTTACGAGAGACGATG

oSMR38 *SAX-7basal reverse* ctGCTCTTCgCTTCTCGGGCCGTTGCGCCGGC

oSMR39 *SAX-7 mut forward* GTTCGTGTTGCTGCTCTaCAAGTTGATCCAGA
AG

oSMR40 *SAX-7 mut reverse* CTTCTGGATCAACTTGtAGAGCAGCAACACG
AAC

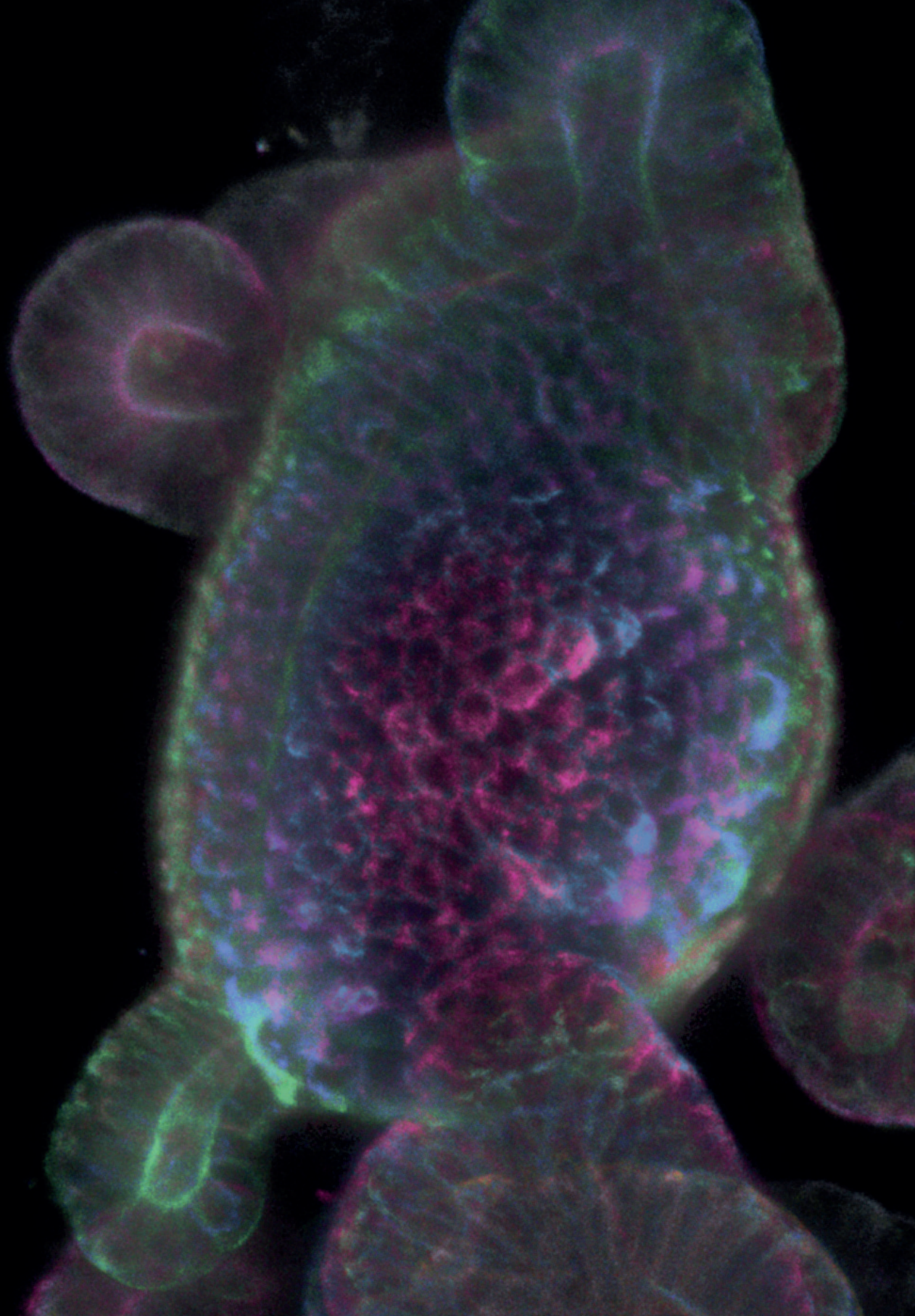
Template: pMH516

To generate *bfp* SapTrap fragment

oSMR47 *BFP forward* ctGCTCTTCGAAGTCCGAACTCATCAAGGAG
AAC

oSMR48 *BFP reverse* ctGCTCTTCgACCGTTGAGCTTGTGTCCGAGC

Template: HR023



Chapter 8

General discussion

Sanne Remmelzwaal

Small protein, big impact

Analyzing the maintenance of biological tube architecture is pivotal in understanding general principles of tissue morphology and to combat diseases with compromised tubular structure, like polycystic kidney disease and inflammatory bowel disorders. In this thesis I have used the *Caenorhabditis elegans* intestine as a model to understand the maintenance of tube morphogenesis. By combining cutting edge techniques such as CRISPR/Cas9-mediated genetic modification, advanced microscopy and *in vivo* protein-protein interaction assays we have established new principles in the maintenance of *C. elegans* intestinal lumen morphology.

Proteins interact with other proteins in an intricate network of interactions that determines most biological processes, thus the behavior of the biological system. Mapping these interactions has been a joint endeavor spanning most model organisms, and *C. elegans* research has contributed significantly (Chapter 2). Methods identifying protein-protein interactions are continuously developed and improved to answer changing needs and to overcome current challenges. In chapter 3 we developed CeLINC, an optical binary protein-protein interaction assay to determine whether two proteins interact *in vivo*. Most protein interactions in *C. elegans* have been mapped using the yeast two-hybrid system (Chapter 2; Walkout et al., 2000), but this technique does not allow interaction identification in the protein's native environment and excludes any post-translational modifications. It additionally requires cloning or the purchase of expensive libraries. CeLINC uses plasmids from a provided toolkit to identify interactions *in vivo* and does so tissue-specifically. Besides yeast two-hybrid studies, significant contributions to the *C. elegans* interactome came from using mass-spectrometry based approaches (Chapter 2). A drawback of these techniques is that they require extensive planning, expertise, and the use of expensive reagents and equipment. CeLINC is easy to implement and produces clear results using material generally available in any *C. elegans* laboratory. CeLINC therefore provides many advantages over the most-commonly used protein-protein interaction techniques. However, as with any interaction technique, CeLINC also has drawbacks. CeLINC identifies interactions between two fluorescently-tagged proteins and can therefore not easily be applied in bulk or identify interactions beyond the chosen pair. The attachment of the fluorescent protein could furthermore affect the folding and structure of the tagged protein and thus interfere with its interactions. However, the simple nature and implementation of CeLINC makes it a powerful, "off-the-shelf" technique readily available for the *C. elegans* community.

In chapter 4 we identified the small coiled-coil protein BBLN-1 as a novel regulator of intermediate filament (IF) network integrity and apical membrane morphology. Loss of *bbln-1* resulted in plasma membrane invaginations into the cytoplasm of the intestinal cells and the collapse of the IF network into cables surrounding these protrusions. We have shown that BBLN-1 localizes to, interacts with, and depends on IFs at the electron-dense endotube (Chapter 4). This IF-rich structure lies just below the apical membrane to provide physical

support and acts as a barrier against pathogens and physiological stresses (Chapter 6; Geisler and Leube, 2016; Geisler et al., 2019; Toivola et al., 2010).

The structure of the IF network needs to be maintained to ensure proper function. This is illustrated by over 80 different “IF-pathies”, in which disrupted IF organization contributes to diseases ranging from skin fragility to neurological disorders. Changes in phosphorylation, sumoylation, and other post-translational modifications modulate IF organization (Snider and Omary, 2014), but few potential cofactors are known to effect such changes. Besides BBLN-1, *C. elegans* research has identified two other IF organizers: SMA-5 (Geisler et al., 2016) and IFO-1 (Carberry et al., 2012). SMA-5 is a stress-activated MAP kinase that, when lost, paradoxically leads to increased IF phosphorylation (Geisler et al., 2016). IFO-1 is thought to attach IFs to cell junctions and other cytoskeletal components to maintain epithelial integrity (Carberry et al., 2012). Loss of *sma-5* or *ifo-1* induces similar phenotypes to *bbln-1* mutants and depletion of the intestinal IF *ifb-2* rescued the invagination phenotypes from loss of *bbln-1*, *sma-5*, or *ifo-1* function—albeit the latter not fully (Chapter 4 and 6). Although an interaction between IFs and BBLN-1 was confirmed, it is not known whether SMA-5 and IFO-1 interact with IFs. Moreover, the exact IF-affecting roles of IFO-1, SMA-5, and BBLN-1 are all speculative.

Similarities between IFO-1 and fragments of the IF organizer filaggrin have been noted (Carberry et al., 2012), but evidence for similar function is lacking and the partial rescue of *ifo-1* mutant animals by *ifb-2* loss suggests an additional role beyond IF network structuring. It was suggested that the protective effect of IFs against stress is mediated by reduced IF phosphorylation, resulting in a more resilient IF network (Geisler et al., 2016). If SMA-5 indeed suppresses IFB-2 function, it would be interesting to explore if IFB-2 overexpression can phenocopy the *sma-5* mutants, or if phosphomimicking *ifb-2* mutants can similarly suppress invagination formation.

In chapter 4 we proposed several mechanisms explaining BBLN-1 function, how BBLN-1 affects the IF network and what causes invagination formation. One possible hypothesis is that BBLN-1 directly anchors IFs to the terminal web or cell junctions, but we noted that the dynamic nature of its association with the IF network suggests that BBLN-1 has a more indirect effect on IF network structure. We also consider BBLN-1 as a general protector against protein aggregation, since its mammalian homologue bublin (BBLN) was identified as a heat-resistant protector against protein aggregation (Tsuboyama et al., 2020) and is differentially expressed in neurodegenerative diseases that are characterized by protein aggregation (Kim et al., 2020; Kong et al., 2009; Nijssen et al., 2018). Abnormal IF aggregation was found to drive cytoplasmic invaginations (Chapter 4) and we suggested that the intact IF network possibly compensates for luminal pressure, which forces the plasma membrane through weak spots in the IF network in *bbln-1* mutants. Alternative hypotheses regard IFs with a more instructive role in controlling lumen width and possibly coordinate the transport of membrane promoting vesicles.

Interestingly, we revealed a putative interaction between BBLN-1 and members of the cytoplasmic V_1 unit of the vacuolar H^+ -ATPase (V-ATPase), providing an interesting potential avenue linking membrane biogenesis and BBLN-1 function (Chapter 4). In chapter 5 we applied CeLINC (Chapter 3) to confirm their interaction. In particular, BBLN-1 interacted with the rotary stalk subunits of the multiprotein-complex and loss of these subunits reduced cytoplasmic BBLN-1, while loss of general cytoplasmic V_1 -ATPase subunits diminished BBLN-1 levels at the apical membrane (Chapter 5, Figure 5B). Interestingly, loss of V_1 -ATPase function induced bubble-shaped membrane structures at the apical domain. We hypothesized that BBLN-1 aids V-ATPase stalk assembly in the cytoplasm upon which it exploits its interaction with V-ATPases for trafficking to the apical domain on RAB-11 coated vesicles (Chapter 5, Discussion). Nevertheless, we were unable to dissect BBLN-1 and V-ATPase function in apical membrane morphogenesis.

Taking into consideration previous literature, and the data and hypotheses presented in this thesis, I propose a hypothetical model in which the small coiled-coil protein BBLN-1 collaborates with V-ATPases and IFs to structure the apical membrane of the *C. elegans* intestine. This speculative model does not disregard the hypotheses described above and could well coexist or be integrated with the stated theories. It mostly integrates data from chapter 4 and 5, and is set up as several consecutive stages:

- (i) **BBLN-1 aids V-ATPase stalk assembly in the cytoplasm.** This is based on the data identifying BBLN-1 as a high confidence interactor of the F and D subunits of the rotary stalk of the V-ATPase, and its effect on V-ATPase apical localization levels. It should be noted that V-ATPases are still able to assemble in absence of BBLN-1, although possibly less efficiently, since loss of *bbln-1* only reduces V-ATPase levels and is not lethal, while loss of V-ATPases is.
- (ii) **BBLN-1 exploits its interaction with the V-ATPase stalk for integration in RAB-11 coated vesicles.** Loss of V_1 -ATPases lead to diminished BBLN-1 levels at the apical domain, suggesting that BBLN-1 depends on V-ATPases for its localization. Preliminary data show that loss of the small GTPase *rab-11.1* induces invagination phenotypes (data not shown), which suggests that RAB-11 might be involved in the proposed BBLN-1/V-ATPase pathway.
- (iii) **RAB-11/V-ATPase/BBLN-1-coated vesicles are transported to the apical domain where a physical barrier in the form of the IF-rich endotube hinders membrane vesicle passage for their incorporation in the plasma membrane.** It has repeatedly been proposed that IFs physically separate the cell into compartments to coordinate cytoskeletal activities (Chang and Goldman, 2004; Potokar et al., 2007), organize organelles (Quiroz et al., 2020; Schwarz and Leube, 2016), or direct vesicle trafficking (as hypothesized by Carberry et al., 2009; Hüsken et al., 2008). Studies revealed that indeed, vimentin and nestin IFs form a physical barrier against intracellular vesicle trafficking (Jiu, 2018) and in the excretory canal of *C. elegans* IFs restrain lateral vesicle access to the lumen (Khan et al., 2019). Small holes in the

dense *C. elegans* intestinal IF network were observed, but argued to be too small to allow vesicle passage (Carberry et al., 2009), vesicles therefore need another means to penetrate the IF barrier.

- (iv) A V-ATPase-dependent factor induces a conformational change in IFs to open up the network for vesicle passage.** Vesicles themselves might provide molecular activities to restructure the IF network. This is seen in the mammalian urothelium where a dense Keratin 20 IF meshwork localizes beneath the plasma membrane (Wankel et al., 2016). Well-defined pores in the mesh have been proposed to function as exchange sites between the plasma membrane and intracellular Rab8/Rab11-coated vesicles for surface area enlargement (Veranič and Jezernik, 2002; Wankel et al., 2016). Interestingly, Rab8 and Rab11 did not cross this barrier (Wankel et al., 2016). Various regulators of vesicle trafficking like the Rabs have been shown to interact with IFs (Margiotta and Bucci, 2016; Styers et al., 2005). Vesicle passage may therefore occur via a direct interaction with the IF network. I propose that a V-ATPase-dependent factor opens the IF network based on several structural dissimilarities between the membrane protrusions induced by IF network disorganization (Chapter 4, Figure 5; Chapter 6) and V-ATPase loss-of-function (Chapter 5, Figure 5C and S3B). In contrast to mutants with gross IF network defects, the bubble-shaped structures in V-ATPase mutants were not specified by the apical membrane marker ERM-1 and appeared to accumulate subapical of the IF network. These preliminary data suggest that loss of V-ATPase function hinders vesicle access to the apical domain leading to their accumulation before the endotube, implying that V-ATPases provide the factor for opening the IF network. Accordingly, vesicles can no longer overcome the IF barrier in absence of V-ATPases, causing accumulation of vesicle material subapical of the endotube; while upon IF disorganization, V-ATPase-decorated vesicles can cross the endotube region, but is uncontrolled in areas of diminished IF network integrity.
- (v) BBLN-1 establishes an interaction with the head or tail domains of IFs.** The IF network is built as a complex structure of molecular interactions between the acidic rod and the basic head domain (Chapter 1, Figure 3; Herrmann and Aebi, 2016). These interactions hinder IFs solubility *in vitro*, but phosphorylation by protein kinases dissolves IFs very effectively (Herrmann and Aebi, 2016). In cells, various posttranslational modifications are known to remodel IF networks dynamically (Snider and Omary, 2014). IF reorganization is typically accomplished by phosphorylation of one or more Ser/Thr residues in the head and tail domains of IFs. The head and tail domains therefore facilitate IF network formation and regulate the mechanical integrity of the network (Herrmann and Aebi, 2016; Lin et al., 2010; Zhou et al., 2021). IF-network altering interactions like that of *sma-5* (Chapter 6), *ifo-1* (Chapter 6), and *bbln-1* (Chapter 4), therefore most likely work through their head and tail domains and their loss-of-function leads to overall similar effects: insoluble IFs resulting in their aggregation.
- (vi) BBLN-1 action recloses the IF network and maintains its barrier function.** BBLN-1 proved to be associated with the IF network in a highly

dynamic fashion (Chapter 4, Figure 2E and 2F). This implies that BBLN-1 is not structurally embedded in the network, but likely performs repeated functions that require constant supply of new protein. Besides, BBLN-1 is continuously needed to maintain IF network structure; loss of BBLN-1 later in development still induced bubble-shaped membrane protrusions and loss of IF network integrity (Chapter 4, Figure S5). Vesicular membrane trafficking is a continuous process that occurs at any point in an animal's lifetime. From the moment that the IF network has developed its barrier-like properties, vesicles need to overcome the barrier and loss of *bbln-1* would leave openings in the IF network that accumulate in severity over time.

The model is further supported by several lines of evidence presented in this thesis in the context of previous literature. First, *bbln-1* loss has a dramatic effect on the IF network, but this phenotype remains restricted to the intestine (Chapter 4). In this tissue, IFs form a unique circumferential sheet-like barrier, a characteristic consistent with a role in restricting vesicle access to the membrane (Carberry et al., 2009; Hüsken et al., 2008). A similar structure is observed in the nematode's excretory canal, but here specialized membrane structures protrude through the IF barrier to connect to the lumen to form canaliculi (Buechner et al., 2020). The intestine lacks such membrane structures and vesicles therefore need an alternative means to overcome the dense IF network. Since the intestine is the only tissue in *C. elegans* in which we find such a continuous IF barrier, this is likely an intestine-specific process and loss of the integrity-maintaining mechanism through BBLN-1 therefore leads to an intestine-restricted phenotype.

Second, membrane invaginations preferentially developed in proximity to cell junctions (Chapter 4, Figure S2A-S2D). Cell junctions are hypothesized to be favored landmarks for apical vesicle trafficking (Köhler and Zahraoui, 2005; Zahraoui et al., 2000). Given the trafficking-dependent model for membrane protrusion formation in *bbln-1* mutants, invaginations should preferentially occur at the junctions.

Last, loss of the entire IF network by *ifb-2* depletion induced luminal widening and suppressed the bubble-shaped membrane invagination phenotype in *bbln-1* (Chapter 4, Figure 3A and S6C), *ifo-1* (Chapter 6), and *sma-5* (Chapter 6) mutants. When IF network integrity is lost, as in *sma-5*, *ifo-1*, and *bbln-1* mutants, apical vesicle access will be hindered in areas with aggregated IF material and rather favored in areas of the IF network with diminished structural integrity. These "hotspots" of excess vesicle fusion drive the formation of bubble-shaped membrane protrusions. Upon loss of the IF network, vesicle access is no longer controlled by the IF barrier nor restricted to hotspots, but is distributed over the entire apical domain, leading to overall luminal widening.

In relation to this model, many open questions remain. If vesicle trafficking is indeed disrupted upon *bbln-1* loss, other trafficking mutants should induce plasma membrane protrusions as well. The preliminary data showing that loss of the small GTPase RAB-11.1 can cause bubble-shaped membrane protrusions

at the apical domain therefore needs to be confirmed. Furthermore, it would be interesting to investigate if trafficking is indeed disrupted in *bbln-1* mutants. Future studies should strengthen the claim that BBLN-1 is directed to the endotube by V-ATPase-decorated vesicles, elucidate if BBLN-1 associates with the IF network to maintain its integrity upon vesicle passage, and demonstrate if vesicle passage is favored in areas with less IFs. Imaging with increased resolution, for example using stimulation emission depletion microscopy, could describe whether the collapsed IF network favors vesicle fusion in regions of low IF network integrity. Using fluorescent markers of trafficking components in *bbln-1* mutants one could observe preferred vesicle fusion at weak regions of the IF network and hindrance of vesicle access to the apical membrane at IF cables in confirmation of the model. This will aid in concluding if disorganized IFs affect the translocation of membrane-promoting vesicles to the apical membrane. Furthermore, by resolving the subcellular localization of BBLN-1 in the *C. elegans* embryo in a temporal manner, we could observe when BBLN-1 starts to decorate the apical domain in respect to IFs and apical trafficking markers. Together, these experiments could broaden our understanding of the mechanism behind the *bbln-1* phenotype and reveal if BBLN-1, V-ATPases and IFs collaborate in a linear pathway to maintain lumen morphology.

In order to propose a mechanistic role of IFs in vesicular trafficking, the factor responsible for IF network opening should be elucidated. Interestingly, there is a growing significance for the role of IFs in vesicular transport (Margiotta and Bucci, 2016; Styers et al., 2005) that has uncovered many potential ways in which restructuring of the IF network is involved in vesicle trafficking and vice versa. For example, the vesicular protein Rab7 interacts with the mammalian IF Vimentin to alter its phosphorylated state to determine its incorporation in the IF network (Cogli et al., 2013). In astrocytes, vesicle trafficking has been shown to be strongly affected by depolymerization of IFs (Potokar et al., 2007). A link between vesicle trafficking and IFs was additionally found through a direct interaction between IFs and the adaptor protein AP-3, by which IFs are proposed to recruit AP-3 for vesicle formation and uncoating (Styers et al., 2005). However, it remains elusive what mechanism is responsible for vesicle passage through the IF network in the *C. elegans* intestine.

The molecular and structural effect of the IF modulators on IFs remains largely unknown. *In vitro* IF assembly assays with *sma-5*, *ifo-1*, or *bbln-1* could elucidate their effect on overall IF network structure. Furthermore, post-translational modification techniques could reveal if IFs are differently modified in the absence and presence of BBLN-1, elucidating if the interaction between BBLN-1 and IFs infers a covalent change to IFs or that its change is entirely structural. Preliminary data indicates that, unlike *sma-5* but similar to *ifo-1* (Geisler et al., 2016), *bbln-1* mutations do not alter phosphorylation status of IFs (F. Geisler, unpublished results). Interestingly, BBLN-1 harbors a phosphorylation site (PhosphoPep (Bodenmiller et al., 2008)) and preliminary experiments performed during the writing of this thesis revealed a shift in BBLN-1 phosphorylation in a *sma-5* mutant background (F. Geisler, unpublished preliminary result), suggesting that

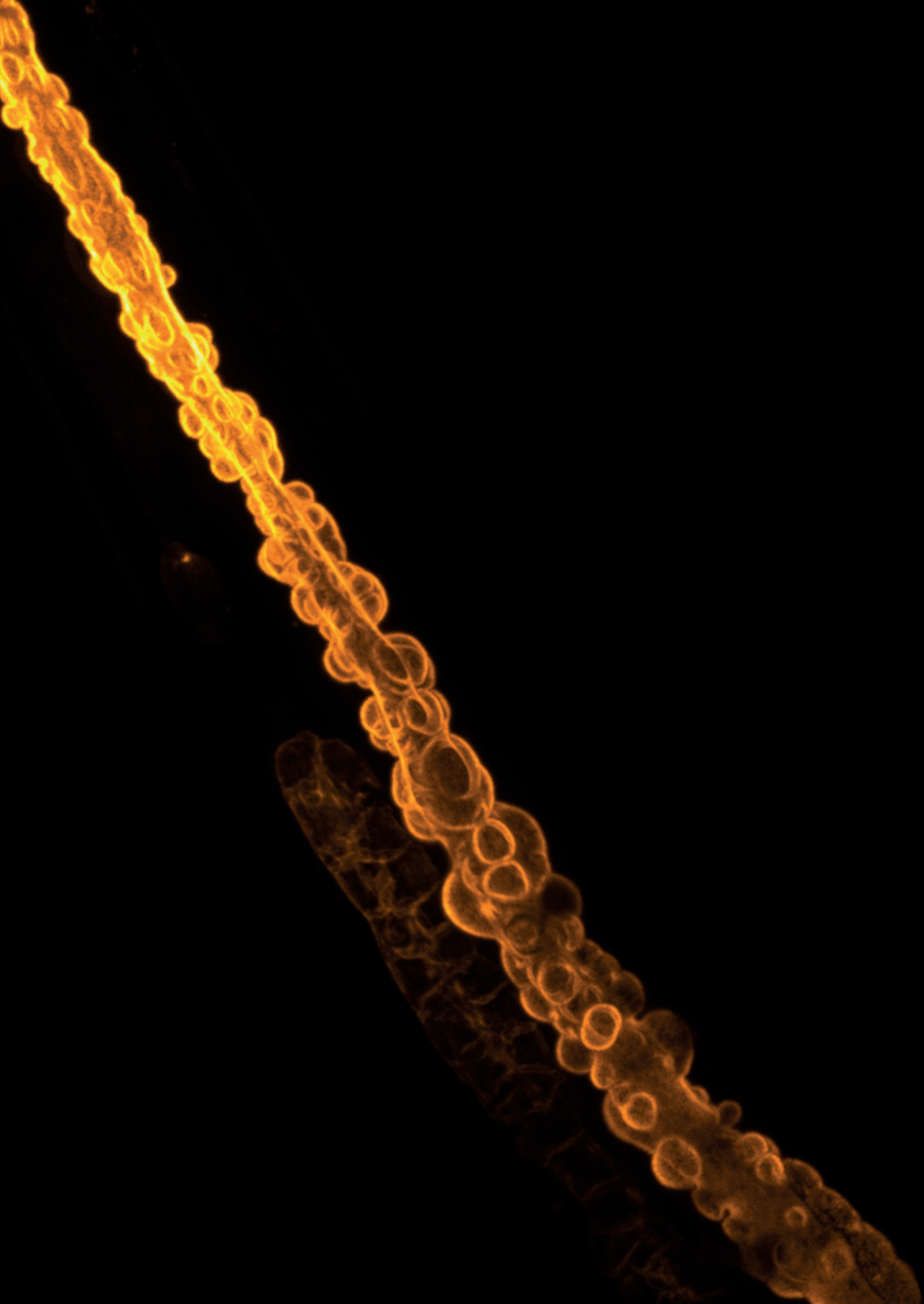
BBLN-1 acts downstream of the kinase to alter the IF network. Future efforts should reveal if SMA-5 indeed modifies the phosphorylated state of BBLN-1 and if this shift is responsible for altering IF network structure. However, additional mechanisms of IF network restructuring must be at work since phosphorylation states of the IFs differ between the *sma-5* and *bbln-1* mutants. Moreover, BBLN-1 and SMA-5 do not act in a simple linear pathway as double *bbln-1* and *sma-5* loss resulted in increased phenotype severity (Chapter 4). Future endeavors should broaden our understanding of the interplay between SMA-5, IFO-1, BBLN-1 and the IF network and reveal possible collaborative functions for the IF modulators.

Although the BBLN-1/V-ATPase/IFs model described here focusses on membrane trafficking, it should be noted that the *bbln-1* loss-of-function phenotype might arise as a result of mechanical alterations—in which luminal flow drives the protrusions through regions of weak IF network structure (as suggested in Chapter 4)—or follows from a combination of mechanical forces and the model described above. Additionally, the model describes an intestine-specific phenotype and therefore omits BBLN-1 function at the IF network in other tissues. One can speculate that BBLN-1 is a broad regulator of IF network organization, but that the protein performs essential functions in other tissues only upon stresses, or that changes in the IF network in other tissues are so minimal that loss of *bbln-1* and other losses in IF network integrity result in mild phenotypes that go unnoticed with the used experimental techniques. In any case, the function of BBLN-1 in other tissues and the nature of its loss-of-function phenotype remains for now unknown.

The common conclusion of many lines of research thus far, is that—from *C. elegans* to human—cells and tissues with irregular or missing IFs exhibit structural defects, in particular following stress. In the studies presented in this thesis we have regarded IFs not only as a network providing structural support, but have opened up new functional prospects for the IF system in cell signaling and vesicular trafficking. With that, we provide possible ways in which tissues maintain barrier properties of surface covering epithelia, while preserving intracellular communication mechanisms.

As a last remark—by performing the experimental and literature research for this thesis it became increasingly clear that, of the three cytoskeletal filaments, IFs remain by far the least understood in terms of their assembly, cellular organization, and function. A quick Google Scholar search yielded me 3 million hits for “actin”, 1 million for “microtubule” and only 200 000 for “intermediate filaments”. Given their implications in a diverse range of diseases and cellular processes, I would therefore like to emphasize the need and importance to study these underdogs of the cytoskeleton.

Sanne Remmelzwaal



Addendum

References

Nederlandse samenvatting

Curriculum vitae

List of publications

Acknowledgments (Dankwoord)

References

- Abdel-Rahman, F., Okeremgbo, B., Alhamadah, F., Jamadar, S., Anthony, K., and Saleh, M.A. (2017). *Caenorhabditis elegans* as a model to study the impact of exposure to light emitting diode (LED) domestic lighting. *Journal of Environmental Science and Health, Part A* 52, 433–439.
- Achilleos, A., Wehman, A.M., and Nance, J. (2010). PAR-3 mediates the initial clustering and apical localization of junction and polarity proteins during *C. elegans* intestinal epithelial cell polarization. *Development* 137, 1833–1842.
- Aher, A., and Akhmanova, A. (2018). Tipping microtubule dynamics, one protofilament at a time. *Current Opinion in Cell Biology* 50, 86–93.
- Ahier, A., and Jarriault, S. (2014). Simultaneous Expression of Multiple Proteins Under a Single Promoter in *Caenorhabditis elegans* via a Versatile 2A-Based Toolkit. *Genetics* 196, 605–613.
- Al-Hashimi, H., Hall, D.H., Ackley, B.D., Lundquist, E.A., and Buechner, M. (2018). Tubular Excretory Canal Structure Depends on Intermediate Filaments EXC-2 and IFA-4 in *Caenorhabditis elegans*. *Genetics* genetics.301078.2018.
- Andrew, D.J., and Ewald, A.J. (2010). Morphogenesis of epithelial tubes: Insights into tube formation, elongation, and elaboration. *Developmental Biology* 341, 34–55.
- Arabidopsis* Interactome Mapping Consortium (2011). Evidence for network evolution in an *Arabidopsis* interactome map. *Science* 333, 601–607.
- Armenti, S.T., and Nance, J. (2012). Adherens junctions in *C. elegans* embryonic morphogenesis. *Subcell Biochem* 60, 279–299.
- Armenti, S.T., Chan, E., and Nance, J. (2014). Polarized exocyst-mediated vesicle fusion directs intracellular lumenogenesis within the *C. elegans* excretory cell. *Developmental Biology* 394, 110–121.
- Arribere, J.A., Bell, R.T., Fu, B.X.H., Artiles, K.L., Hartman, P.S., and Fire, A.Z. (2014). Efficient Marker-Free Recovery of Custom Genetic Modifications with CRISPR/Cas9 in *Caenorhabditis elegans*. *Genetics* 198, 837–846.
- Asakawa, K., Handa, H., and Kawakami, K. (2020). Optogenetic modulation of TDP-43 oligomerization accelerates ALS-related pathologies in the spinal motor neurons. *Nat Commun* 11.
- Asghar, M.N., Silvander, J.S.G., Helenius, T.O., Lähdeniemi, I.A.K., Alam, C., Fortelius, L.E., Holmsten, R.O., and Toivola, D.M. (2015). The Amount of Keratins Matters for Stress Protection of the Colonic Epithelium. *PLOS ONE* 10, e0127436.

Barrios-Rodiles, M., Brown, K.R., Ozdamar, B., Bose, R., Liu, Z., Donovan, R.S., Shinjo, F., Liu, Y., Dembowy, J., Taylor, I.W., et al. (2005). High-throughput mapping of a dynamic signaling network in mammalian cells. *Science* 307, 1621–1625.

Beatty, A., Morton, D., and Kemphues, K. (2010). The *C. elegans* homolog of *Drosophila* Lethal giant larvae functions redundantly with PAR-2 to maintain polarity in the early embryo. *Development* 137, 3995–4004.

Bergmann, C., Guay-Woodford, L.M., Harris, P.C., Horie, S., Peters, D.J.M., and Torres, V.E. (2018). Polycystic kidney disease. *Nat Rev Dis Primers* 4, 50.

Bernadskaya, Y.Y., Patel, F.B., Hsu, H.-T., and Soto, M.C. (2011). Arp2/3 promotes junction formation and maintenance in the *Caenorhabditis elegans* intestine by regulating membrane association of apical proteins. *Mol. Biol. Cell* 22, 2886–2899.

Bidaud-Meynard, A., Nicolle, O., Heck, M., Le Cunff, Y., and Michaux, G. (2019). A V0-ATPase-dependent apical trafficking pathway maintains the polarity of the intestinal absorptive membrane. *Development* 146.

Bilder, D. (2000). Cooperative Regulation of Cell Polarity and Growth by *Drosophila* Tumor Suppressors. *Science* 289, 113–116.

Bilder, D., Schober, M., and Perrimon, N. (2003). Integrated activity of PDZ protein complexes regulates epithelial polarity. *Nat. Cell Biol.* 5, 53–58.

Bischof, J., Duffraisse, M., Furger, E., Ajuria, L., Giraud, G., Vanderperre, S., Paul, R., Björklund, M., Ahr, D., Ahmed, A.W., et al. (2018). Generation of a versatile BiFC ORFeome library for analyzing protein–protein interactions in live *Drosophila*. *ELife* 7, e38853.

Bodenmiller, B., Campbell, D., Gerrits, B., Lam, H., Jovanovic, M., Picotti, P., Schlapbach, R., and Aebersold, R. (2008). PhosphoPep—a database of protein phosphorylation sites in model organisms. *Nat Biotechnol* 26, 1339–1340.

de Boer, E., Rodriguez, P., Bonte, E., Krijgsveld, J., Katsantoni, E., Heck, A., Grosveld, F., and Strouboulis, J. (2003). Efficient biotinylation and single-step purification of tagged transcription factors in mammalian cells and transgenic mice. *Proc. Natl. Acad. Sci. U.S.A.* 100, 7480–7485.

Bossinger, O., Fukushige, T., Claeys, M., Borgonie, G., and McGhee, J.D. (2004). The apical disposition of the *Caenorhabditis elegans* intestinal terminal web is maintained by LET-413. *Dev. Biol.* 268, 448–456.

Bott, C.J., and Winckler, B. (2020). Intermediate filaments in developing neurons: Beyond structure. *Cytoskeleton (Hoboken)* 77, 110–128.

Boulton, S.J., Gartner, A., Reboul, J., Vaglio, P., Dyson, N., Hill, D.E., and Vidal, M. (2002). Combined functional genomic maps of the *C. elegans* DNA damage response. *Science* 295, 127–131.



- Boxem, M., Maliga, Z., Klitgord, N., Li, N., Lemmens, I., Mana, M., de Lichtervelde, L., Mul, J.D., van de Peut, D., Devos, M., et al. (2008). A protein domain-based interactome network for *C. elegans* early embryogenesis. *Cell* 134, 534–545.
- Branon, T.C., Bosch, J.A., Sanchez, A.D., Udeshi, N.D., Svinkina, T., Carr, S.A., Feldman, J.L., Perrimon, N., and Ting, A.Y. (2017). Directed evolution of TurboID for efficient proximity labeling in living cells and organisms. *BioRxiv*.
- Braun, P., Tasan, M., Dreze, M., Barrios-Rodiles, M., Lemmens, I., Yu, H., Sahalie, J.M., Murray, R.R., Roncari, L., de Smet, A.-S., et al. (2009). An experimentally derived confidence score for binary protein-protein interactions. *Nat. Methods* 6, 91–97.
- Brenner, S. (1974). The genetics of *Caenorhabditis elegans*. *Genetics* 77, 71–94.
- Brückner, A., Polge, C., Lentze, N., Auerbach, D., and Schlattner, U. (2009). Yeast Two-Hybrid, a Powerful Tool for Systems Biology. *Int J Mol Sci* 10, 2763–2788.
- Bryant, D.M., Datta, A., Rodríguez-Fraticelli, A.E., Peränen, J., Martín-Belmonte, F., and Mostov, K.E. (2010). A molecular network for de novo generation of the apical surface and lumen. *Nat Cell Biol* 12, 1035–1045.
- Bryant, D.M., Rognot, J., Datta, A., Overeem, A.W., Kim, M., Yu, W., Peng, X., Eastburn, D.J., Ewald, A.J., Werb, Z., et al. (2014). A Molecular Switch for the Orientation of Epithelial Cell Polarization. *Developmental Cell* 31, 171–187.
- Buechner, M., Yang, Z., and Al-Hashimi, H. (2020). A Series of Tubes: The *C. elegans* Excretory Canal Cell as a Model for Tubule Development. *Journal of Developmental Biology* 8, 17.
- Bugaj, L.J., Choksi, A.T., Mesuda, C.K., Kane, R.S., and Schaffer, D.V. (2013). Optogenetic protein clustering and signaling activation in mammalian cells. *Nature Methods* 10, 249–252.
- C. elegans* Sequencing Consortium (1998). Genome sequence of the nematode *C. elegans*: a platform for investigating biology. *Science (New York, N.Y.)* 282, 2012–2018.
- Campanale, J.P., Sun, T.Y., and Montell, D.J. (2017). Development and dynamics of cell polarity at a glance. *J Cell Sci* 130, 1201–1207.
- Carberry, K., Wiesenfahrt, T., Windoffer, R., Bossinger, O., and Leube, R.E. (2009). Intermediate filaments in *Caenorhabditis elegans*. *Cell Motility* 66, 852–864.
- Carberry, K., Wiesenfahrt, T., Geisler, F., Stöcker, S., Gerhardus, H., Überbach, D., Davis, W., Jorgensen, E., Leube, R.E., and Bossinger, O. (2012). The novel intestinal filament organizer IFO-1 contributes to epithelial integrity in concert with ERM-1 and DLG-1. *Development* 139, 1851–1862.

Caria, S., Magtoto, C.M., Samiei, T., Portela, M., Lim, K.Y.B., How, J.Y., Stewart, B.Z., Humbert, P.O., Richardson, H.E., and Kvansakul, M. (2018). *Drosophila melanogaster* Guk-holder interacts with the Scribbled PDZ1 domain and regulates epithelial development with Scribbled and Discs Large. *J. Biol. Chem.* 293, 4519–4531.

Castiglioni, V.G., Pires, H.R., Rosas Bertolini, R., Riga, A., Kerver, J., and Boxem, M. (2020). Epidermal PAR-6 and PKC-3 are essential for larval development of *C. elegans* and organize non-centrosomal microtubules. *ELife* 9, e62067.

Caufield, J.H., Sakhawalkar, N., and Uetz, P. (2012). A comparison and optimization of yeast two-hybrid systems. *Methods* 58, 317–324.

Chamcheu, J.C., Siddiqui, I.A., Syed, D.N., Adhami, V.M., Liovic, M., and Mukhtar, H. (2011). Keratin gene mutations in disorders of human skin and its appendages. *Arch Biochem Biophys* 508, 123–137.

Chan, C.J., and Hiiragi, T. (2020). Integration of luminal pressure and signalling in tissue self-organization. *Development* 147.

Chan, R.C., Chan, A., Jeon, M., Wu, T.F., Pasqualone, D., Rougvie, A.E., and Meyer, B.J. (2003). Chromosome cohesion is regulated by a clock gene paralogue TIM-1. *Nature* 423, 1002–1009.

Chang, L., and Goldman, R.D. (2004). Intermediate filaments mediate cytoskeletal crosstalk. *Nat Rev Mol Cell Biol* 5, 601–613.

Chatr-Aryamontri, A., Oughtred, R., Boucher, L., Rust, J., Chang, C., Kolas, N.K., O'Donnell, L., Oster, S., Theesfeld, C., Sellam, A., et al. (2017). The BioGRID interaction database: 2017 update. *Nucleic Acids Res.* 45, D369–D379.

Che, D.L., Duan, L., Zhang, K., and Cui, B. (2015). The Dual Characteristics of Light-Induced Cryptochrome 2, Homo-oligomerization and Heterodimerization, for Optogenetic Manipulation in Mammalian Cells. *ACS Synth. Biol.* 4, 1124–1135.

Cheeseman, I.M., and Desai, A. (2005). A combined approach for the localization and tandem affinity purification of protein complexes from metazoans. *Sci. STKE* 2005, pl1.

Cheeseman, I.M., Niessen, S., Anderson, S., Hyndman, F., Yates, J.R., Oegema, K., and Desai, A. (2004). A conserved protein network controls assembly of the outer kinetochore and its ability to sustain tension. *Genes Dev.* 18, 2255–2268.

Choi, H., Larsen, B., Lin, Z.-Y., Breitkreutz, A., Mellacheruvu, D., Fermin, D., Qin, Z.S., Tyers, M., Gingras, A.-C., and Nesvizhskii, A.I. (2011). SAINT: probabilistic scoring of affinity purification–mass spectrometry data. *Nature Methods* 8, 70–73.

Choi, J., Troyanovsky, R.B., Indra, I., Mitchell, B.J., and Troyanovsky, S.M. (2019). Scribble, Erbin, and Lano redundantly regulate epithelial polarity and apical adhesion complex. *J Cell Biol* 218, 2277–2293.



Chu, A., Zirngibl, R.A., and Manolson, M.F. (2021). The V-ATPase $\alpha 3$ Subunit: Structure, Function and Therapeutic Potential of an Essential Biomolecule in Osteoclastic Bone Resorption. *Int J Mol Sci* 22, 6934.

Chung, C., Mader, C.C., Schmitz, J.C., Atladottir, J., Fitchev, P., Cornwell, M.L., Kolecke, A.J., Crawford, S.E., and Gorelick, F. (2011). The vacuolar-ATPase modulates matrix metalloproteinase isoforms in human pancreatic cancer. *Lab Invest* 91, 732–743.

Clemen, C.S., Herrmann, H., Strelkov, S.V., and Schröder, R. (2013). Desminopathies: pathology and mechanisms. *Acta Neuropathol* 125, 47–75.

Coch, R.A., and Leube, R.E. (2016). Intermediate Filaments and Polarization in the Intestinal Epithelium. *Cells* 5, 32.

Coch, R.A., Geisler, F., Annibal, A., Antebi, A., and Leube, R.E. (2020). Identification of a Novel Link between the Intermediate Filament Organizer IFO-1 and Cholesterol Metabolism in the *Caenorhabditis elegans* Intestine. *Int J Mol Sci* 21, E8219.

Cogli, L., Progida, C., Bramato, R., and Bucci, C. (2013). Vimentin phosphorylation and assembly are regulated by the small GTPase Rab7a. *Biochim Biophys Acta* 1833, 1283–1293.

Cooper, J.F., and Van Raamsdonk, J.M. (2018). Modeling Parkinson's Disease in *C. elegans*. *Journal of Parkinson's Disease* 8, 17–32.

Corsi, A.K. (2015). A Transparent window into biology: A primer on *Caenorhabditis elegans*. *WormBook* 1–31.

Coskun, M. (2014). Intestinal Epithelium in Inflammatory Bowel Disease. *Frontiers in Medicine* 1, 24.

Cotter, K., Stransky, L., McGuire, C., and Forgac, M. (2015). Recent Insights into the Structure, Regulation, and Function of the V-ATPases. *Trends in Biochemical Sciences* 40, 611–622.

Coulombe, P.A., and Omary, M.B. (2002). "Hard" and "soft" principles defining the structure, function and regulation of keratin intermediate filaments. *Curr Opin Cell Biol* 14, 110–122.

Coulombe, P.A., and Wong, P. (2004). Cytoplasmic intermediate filaments revealed as dynamic and multipurpose scaffolds. *Nature Cell Biology* 6, 699–706.

Coulombe, P.A., Kerns, M.L., and Fuchs, E. (2009). Epidermolysis bullosa simplex: a paradigm for disorders of tissue fragility. *J Clin Invest* 119, 1784–1793.

Croce, A., Cassata, G., Disanza, A., Gagliani, M.C., Tacchetti, C., Malabarba, M.G., Carlier, M.-F., Scita, G., Baumeister, R., and Di Fiore, P.P. (2004). A novel actin barbed-end-capping activity in EPS-8 regulates apical morphogenesis in intestinal cells of *Caenorhabditis elegans*. *Nat Cell Biol* 6, 1173–1179.

Cutting, G.R. (2015). Cystic fibrosis genetics: from molecular understanding to clinical application. *Nat Rev Genet* 16, 45–56.

Datta, A., Bryant, D.M., and Mostov, K.E. (2011). Molecular Regulation of Lumen Morphogenesis. *Current Biology* 21, R126–R136.

Davis, M.W., Hammarlund, M., Harrach, T., Hullett, P., Olsen, S., and Jorgensen, E.M. (2005). Rapid single nucleotide polymorphism mapping in *C. elegans*. *BMC Genomics* 6, 118.

De Magalhaes Filho, C.D., Henriquez, B., Seah, N.E., Evans, R.M., Lapierre, L.R., and Dillin, A. (2018). Visible light reduces *C. elegans* longevity. *Nat Commun* 9, 927.

Desai, A., Rybina, S., Müller-Reichert, T., Shevchenko, A., Shevchenko, A., Hyman, A., and Oegema, K. (2003). KNL-1 directs assembly of the microtubule-binding interface of the kinetochore in *C. elegans*. *Genes Dev.* 17, 2421–2435.

Dickinson, D.J., Slabodnick, M.M., Chen, A.H., and Goldstein, B. (2018). SapTrap assembly of repair templates for Cas9-triggered homologous recombination with a self-excising cassette. *Micropublication: Biology* 3.

Didonna, A., and Opal, P. (2019). The role of neurofilament aggregation in neurodegeneration: lessons from rare inherited neurological disorders. *Mol Neurodegener* 14, 19.

Dong, X., Kheiri, S., Lu, Y., Xu, Z., Zhen, M., and Liu, X. (2021). Toward a living soft microrobot through optogenetic locomotion control of *Caenorhabditis elegans*. *Sci. Robot.* 6, eabe3950.

Drew, K., Lee, C., Huizar, R.L., Tu, F., Borgeson, B., McWhite, C.D., Ma, Y., Wallingford, J.B., and Marcotte, E.M. (2017). Integration of over 9,000 mass spectrometry experiments builds a global map of human protein complexes. *Mol. Syst. Biol.* 13, 932.

Dreze, M., Monachello, D., Lurin, C., Cusick, M.E., Hill, D.E., Vidal, M., and Braun, P. (2010). High-quality binary interactome mapping. *Meth. Enzymol.* 470, 281–315.

Duchaine, T.F., Wohlschlegel, J.A., Kennedy, S., Bei, Y., Conte, D., Pang, K., Brownell, D.R., Harding, S., Mitani, S., Ruvkun, G., et al. (2006). Functional proteomics reveals the biochemical niche of *C. elegans* DCR-1 in multiple small-RNA-mediated pathways. *Cell* 124, 343–354.

Dunham, W.H., Mullin, M., and Gingras, A.-C. (2012). Affinity-purification coupled to mass spectrometry: basic principles and strategies. *Proteomics* 12, 1576–1590.

Endo, M., Hattori, M., Toriyabe, H., Ohno, H., Kamiguchi, H., Iino, Y., and Ozawa, T. (2016). Optogenetic activation of axon guidance receptors controls direction of neurite outgrowth. *Scientific Reports* 6, 23976.



- Erber, A., Riemer, D., Bovenschulte, M., and Weber, K. (1998). Molecular Phylogeny of Metazoan Intermediate Filament Proteins. *J Mol Evol* 47, 751–762.
- Estes, K.A., Szumowski, S.C., and Troemel, E.R. (2011). Non-Lytic, Actin-Based Exit of Intracellular Parasites from *C. elegans* Intestinal Cells. *PLOS Pathogens* 7, e1002227.
- Etienne-Manneville, S. (2018). Cytoplasmic Intermediate Filaments in Cell Biology. *Annual Review of Cell and Developmental Biology* 34, 1–28.
- Feldman, J.L., and Priess, J.R. (2012). A Role for the Centrosome and PAR-3 in the Hand-Off of MTOC Function during Epithelial Polarization. *Current Biology* 22, 575–582.
- Ferrari, A., Veligodskiy, A., Berge, U., Lucas, M.S., and Kroschewski, R. (2008). ROCK-mediated contractility, tight junctions and channels contribute to the conversion of a preapical patch into apical surface during isochoric lumen initiation. *Journal of Cell Science* 121, 3649–3663.
- Fields, S., and Song, O. (1989). A novel genetic system to detect protein-protein interactions. *Nature* 340, 245–246.
- Fielmich, L.-E., Schmidt, R., Dickinson, D.J., Goldstein, B., Akhmanova, A., and van den Heuvel, S. (2018). Optogenetic dissection of mitotic spindle positioning in vivo. *ELife* 7, e38198.
- Futai, M., Sun-Wada, G.-H., Wada, Y., Matsumoto, N., and Nakanishi-Matsui, M. (2019). Vacuolar-type ATPase: A proton pump to lysosomal trafficking. *Proceedings of the Japan Academy, Series B* 95, 261–277.
- Geisler, F., and Leube, R.E. (2016). Epithelial Intermediate Filaments: Guardians against Microbial Infection? *Cells* 5, 29.
- Geisler, F., Gerhardus, H., Carberry, K., Davis, W., Jorgensen, E., Richardson, C., Bossinger, O., and Leube, R.E. (2016). A novel function for the MAP kinase SMA-5 in intestinal tube stability. *MBoC* 27, 3855–3868.
- Geisler, F., Coch, R.A., Richardson, C., Goldberg, M., Denecke, B., Bossinger, O., and Leube, R.E. (2019). The intestinal intermediate filament network responds to and protects against microbial insults and toxins. *Development* 146, dev169482.
- Geisler, F., Coch, R.A., Richardson, C., Goldberg, M., Bevilacqua, C., Prevedel, R., and Leube, R.E. (2020). Intestinal intermediate filament polypeptides in *C. elegans*: Common and isotype-specific contributions to intestinal ultrastructure and function. *Scientific Reports* 10, 1–18.
- Gentil, B.J., Tibshirani, M., and Durham, H.D. (2015). Neurofilament dynamics and involvement in neurological disorders. *Cell Tissue Res* 360, 609–620.
- Ghanta, K.S., and Mello, C.C. (2020). Melting dsDNA donor molecules potentiates precision genome editing in *C. elegans*. *BioRxiv* 2020.08.03.235036.

Giot, L., Bader, J.S., Brouwer, C., Chaudhuri, A., Kuang, B., Li, Y., Hao, Y.L., Ooi, C.E., Godwin, B., Vitols, E., et al. (2003). A protein interaction map of *Drosophila melanogaster*. *Science* 302, 1727–1736.

Göbel, V., Barrett, P.L., Hall, D.H., and Fleming, J.T. (2004). Lumen Morphogenesis in *C. elegans* Requires the Membrane-Cytoskeleton Linker erm-1. *Developmental Cell* 6, 865–873.

Goldstein, B., and Hird, S.N. (1996). Specification of the anteroposterior axis in *Caenorhabditis elegans*. *Development* 122, 1467–1474.

Goryachev, A.B., and Leda, M. (2017). Many roads to symmetry breaking: molecular mechanisms and theoretical models of yeast cell polarity. *MBoC* 28, 370–380.

Goudeau, J., Sharp, C.S., Paw, J., Savy, L., Leonetti, M.D., York, A.G., Updike, D.L., Kenyon, C., and Ingaramo, M. (2021). Split-wrmScarlet and split-sfGFP: tools for faster, easier fluorescent labeling of endogenous proteins in *Caenorhabditis elegans*. *Genetics* 217.

Graham, L.A., Hill, K.J., and Stevens, T.H. (1994). VMA7 encodes a novel 14-kDa subunit of the *Saccharomyces cerevisiae* vacuolar H(+)-ATPase complex. *Journal of Biological Chemistry* 269, 25974–25977.

Graham, L.A., Powell, B., and Stevens, T.H. (2000). Composition and assembly of the yeast vacuolar H(+)-ATPase complex. *Journal of Experimental Biology* 203, 61–70.

Gunsalus, K.C., Ge, H., Schetter, A.J., Goldberg, D.S., Han, J.-D.J., Hao, T., Berriz, G.F., Bertin, N., Huang, J., Chuang, L.-S., et al. (2005). Predictive models of molecular machines involved in *Caenorhabditis elegans* early embryogenesis. *Nature* 436, 861–865.

Guntas, G., Hallett, R.A., Zimmerman, S.P., Williams, T., Yumerefendi, H., Bear, J.E., and Kuhlman, B. (2015). Engineering an improved light-induced dimer (iLID) for controlling the localization and activity of signaling proteins. *PNAS* 112, 112–117.

Hahn-Windgassen, A., and Gilst, M.R.V. (2009). The *Caenorhabditis elegans* HN-F4 α Homolog, NHR-31, Mediates Excretory Tube Growth and Function through Coordinate Regulation of the Vacuolar ATPase. *PLOS Genetics* 5, e1000553.

Hapiak, V., Hresko, M.C., Schriefer, L.A., Saiyasisongkham, K., Bercher, M., and Plenefisch, J. (2003). *Mua-6*, a gene required for tissue integrity in *Caenorhabditis elegans*, encodes a cytoplasmic intermediate filament. *Developmental Biology* 263, 330–342.

Harris, T.W., Arnaboldi, V., Cain, S., Chan, J., Chen, W.J., Cho, J., Davis, P., Gao, S., Grove, C.A., Kishore, R., et al. (2020). WormBase: a modern Model Organism Information Resource. *Nucleic Acids Research* 48, D762–D767.



Harterink, M., van Bergeijk, P., Allier, C., de Haan, B., van den Heuvel, S., Hoo-genraad, C.C., and Kapitein, L.C. (2016). Light-controlled intracellular transport in *Caenorhabditis elegans*. *Current Biology* 26, R153–R154.

Hartley, J.L., Temple, G.F., and Brasch, M.A. (2000). DNA Cloning Using In Vitro Site-Specific Recombination. *Genome Res.* 10, 1788–1795.

Havugimana, P.C., Hart, G.T., Nepusz, T., Yang, H., Turinsky, A.L., Li, Z., Wang, P.I., Boutz, D.R., Fong, V., Phanse, S., et al. (2012). A census of human soluble protein complexes. *Cell* 150, 1068–1081.

Herrmann, H., and Aebi, U. (2016). Intermediate Filaments: Structure and Assembly. *Cold Spring Harb Perspect Biol* 8, a018242.

Herrmann, H., Kreplak, L., and Aebi, U. (2004). Isolation, Characterization, and In Vitro Assembly of Intermediate Filaments. In *Methods in Cell Biology*, (Academic Press), pp. 3–24.

Hiemstra, P.S., McCray, P.B., and Bals, R. (2015). The innate immune function of airway epithelial cells in inflammatory lung disease. *European Respiratory Journal* 45, 1150–1162.

Hoege, C., Constantinescu, A.-T., Schwager, A., Goehring, N.W., Kumar, P., and Hyman, A.A. (2010). LGL Can Partition the Cortex of One-Cell *Caenorhabditis elegans* Embryos into Two Domains. *Current Biology* 20, 1296–1303.

Hu, Y., Flockhart, I., Vinayagam, A., Bergwitz, C., Berger, B., Perrimon, N., and Mohr, S.E. (2011). An integrative approach to ortholog prediction for disease-focused and other functional studies. *BMC Bioinformatics* 12, 357.

Hudry, B., Viala, S., Graba, Y., and Merabet, S. (2011). Visualization of protein interactions in living *Drosophila* embryos by the bimolecular fluorescence complementation assay. *BMC Biol* 9, 5.

Hüsken, K., Wiesenfahrt, T., Abraham, C., Windoffer, R., Bossinger, O., and Leube, R.E. (2008). Maintenance of the intestinal tube in *Caenorhabditis elegans*: the role of the intermediate filament protein IFC-2. *Differentiation* 76, 881–s3.

Hutchins, J.R.A., Toyoda, Y., Hegemann, B., Poser, I., Hériché, J.-K., Sykora, M.M., Augsburg, M., Hudecz, O., Buschhorn, B.A., Bulkescher, J., et al. (2010). Systematic analysis of human protein complexes identifies chromosome segregation proteins. *Science* 328, 593–599.

van Ineveld, R.L., Ariese, H.C.R., Wehrens, E.J., Dekkers, J.F., and Rios, A.C. (2020). Single-Cell Resolution Three-Dimensional Imaging of Intact Organoids. *J Vis Exp*.

Iruela-Arispe, M.L., and Beitel, G.J. (2013). Tubulogenesis. *Development* 140, 2851–2855.

Iruela-Arispe, M.L., and Davis, G.E. (2009). Cellular and Molecular Mechanisms of Vascular Lumen Formation. *Developmental Cell* 16, 222–231.

Jacob, J.T., Coulombe, P.A., Kwan, R., and Omary, M.B. (2018). Types I and II Keratin Intermediate Filaments. *Cold Spring Harb Perspect Biol* 10, a018275.

Jahnel, O., Hoffmann, B., Merkel, R., Bossinger, O., and Leube, R.E. (2016). Mechanical Probing of the Intermediate Filament-Rich Caenorhabditis Elegans Intestine. *Methods Enzymol* 568, 681–706.

Jewett, C.E., and Prekeris, R. (2018). Insane in the apical membrane: Trafficking events mediating apicobasal epithelial polarity during tube morphogenesis. *Traffic* 10.1111/tra.12579.

Ji, Y.J., Choi, K.Y., Song, H.-O., Park, B.-J., Yu, J.-R., Kagawa, H., Song, W.K., and Ahnn, J. (2006). VHA-8, the E subunit of V-ATPase, is essential for pH homeostasis and larval development in *C. elegans*. *FEBS Lett* 580, 3161–3166.

Jiu, Y. (2018). Vimentin intermediate filaments function as a physical barrier during intracellular trafficking of caveolin-1. *Biochem Biophys Res Commun* 507, 161–167.

Joseph, B.B., Blouin, N.A., and Fay, D.S. (2018). Use of a Sibling Subtraction Method for Identifying Causal Mutations in *Caenorhabditis elegans* by Whole-Genome Sequencing. *G3 (Bethesda)* 8, 669–678.

Julien, C., Tomberlin, C., Roberts, C.M., Akram, A., Stein, G.H., Silverman, M.A., and Link, C.D. (2018). In vivo induction of membrane damage by β -amyloid peptide oligomers. *Acta Neuropathologica Communications* 6, 131.

Kallay, L.M., McNickle, A., Brennwald, P.J., Hubbard, A.L., and Braiterman, L.T. (2006). Scribble associates with two polarity proteins, Lgl2 and Vangl2, via distinct molecular domains. *J. Cell. Biochem.* 99, 647–664.

Kamath, R.S., Fraser, A.G., Dong, Y., Poulin, G., Durbin, R., Gotta, M., Kanapin, A., Le Bot, N., Moreno, S., Sohrmann, M., et al. (2003). Systematic functional analysis of the *Caenorhabditis elegans* genome using RNAi. *Nature* 421, 231–237.

Kaminsky, R., Denison, C., Bening-Abu-Shach, U., Chisholm, A.D., Gygi, S.P., and Broday, L. (2009). SUMO Regulates the Assembly and Function of a Cytoplasmic Intermediate Filament Protein in *C. elegans*. *Developmental Cell* 17, 724–735.

Kao, C.-Y., Los, F.C.O., Huffman, D.L., Wachi, S., Kloft, N., Husmann, M., Karabrahimi, V., Schwartz, J.-L., Bellier, A., Ha, C., et al. (2011). Global functional analyses of cellular responses to pore-forming toxins. *PLoS Pathog* 7, e1001314.

Karabinos, A., Schulze, E., Klisch, T., Wang, J., and Weber, K. (2002). Expression profiles of the essential intermediate filament (IF) protein A2 and the IF protein C2 in the nematode *Caenorhabditis elegans*. *Mechanisms of Development* 117, 311–314.



- Karabinos, A., Schulze, E., Schünemann, J., Parry, D.A.D., and Weber, K. (2003). In Vivo and in Vitro Evidence that the Four Essential Intermediate Filament (IF) Proteins A1, A2, A3 and B1 of the Nematode *Caenorhabditis elegans* Form an Obligate Heteropolymeric IF System. *Journal of Molecular Biology* 333, 307–319.
- Karabinos, A., Schünemann, J., and Weber, K. (2004). Most genes encoding cytoplasmic intermediate filament (IF) proteins of the nematode *Caenorhabditis elegans* are required in late embryogenesis. *European Journal of Cell Biology* 83, 457–468.
- Karabinos, A., Schünemann, J., and Parry, D.A.D. (2017). Assembly studies of six intestinal intermediate filament (IF) proteins B2, C1, C2, D1, D2, and E1 in the nematode *C. elegans*. *Cytoskeleton* 74, 107–113.
- Kemphues, K. (2000). PARsing embryonic polarity. *Cell* 101, 345–348.
- Kennedy, M.J., Hughes, R.M., Peteya, L.A., Schwartz, J.W., Ehlers, M.D., and Tucker, C.L. (2010). Rapid blue-light-mediated induction of protein interactions in living cells. *Nat Methods* 7, 973–975.
- Khan, L.A., Zhang, H., Abraham, N., Sun, L., Fleming, J.T., Buechner, M., Hall, D.H., and Gobel, V. (2013). Intracellular lumen extension requires ERM-1-dependent apical membrane expansion and AQP-8-mediated flux. *Nat Cell Biol* 15, 143–156.
- Khan, L.A., Jafari, G., Zhang, N., Membreno, E., Yan, S., Zhang, H., and Gobel, V. (2019). A tensile trilayered cytoskeletal endotube drives capillary-like lumenogenesis. *J Cell Biol* 218, 2403–2424.
- Khoury, M.J., and Bilder, D. (2020). Distinct activities of Scrib module proteins organize epithelial polarity. *PNAS* 117, 11531–11540.
- Kim, D.I., and Roux, K.J. (2016). Filling the Void: Proximity-Based Labeling of Proteins in Living Cells. *Trends Cell Biol.* 26, 804–817.
- Kim, N.Y., Lee, S., Yu, J., Kim, N., Won, S.S., Park, H., and Heo, W.D. (2020a). Optogenetic control of mRNA localization and translation in live cells. *Nature Cell Biology* 22, 341–352.
- Kim, S.M., Cho, S.Y., Kim, M.W., Roh, S.R., Shin, H.S., Suh, Y.H., Geum, D., and Lee, M.A. (2020b). Genome-Wide Analysis Identifies NURR1-Controlled Network of New Synapse Formation and Cell Cycle Arrest in Human Neural Stem Cells. *Mol Cells* 43, 551–571.
- Kirkwood, K.J., Ahmad, Y., Larance, M., and Lamond, A.I. (2013). Characterization of native protein complexes and protein isoform variation using size-fractionation-based quantitative proteomics. *Mol. Cell Proteomics* 12, 3851–3873.
- Köhler, K., and Zahraoui, A. (2005). Tight junction: a co-ordinator of cell signalling and membrane trafficking. *Biology of the Cell* 97, 659–665.

Kolotuev, I., Hyenne, V., Schwab, Y., Rodriguez, D., and Labouesse, M. (2013). A pathway for unicellular tube extension depending on the lymphatic vessel determinant Prox1 and on osmoregulation. *Nat Cell Biol* 15, 157–168.

Kong, W., Mou, X., Liu, Q., Chen, Z., Vanderburg, C.R., Rogers, J.T., and Huang, X. (2009). Independent component analysis of Alzheimer's DNA microarray gene expression data. *Mol Neurodegeneration* 4, 5.

Kontani, K., Moskowitz, I.P.G., and Rothman, J.H. (2005). Repression of Cell-Cell Fusion by Components of the *C. elegans* Vacuolar ATPase Complex. *Developmental Cell* 8, 787–794.

Koorman, T., Klompstra, D., van der Voet, M., Lemmens, I., Ramalho, J.J., Nieuwenhuize, S., van den Heuvel, S., Tavernier, J., Nance, J., and Boxem, M. (2016). A combined binary interaction and phenotypic map of *C. elegans* cell polarity proteins. *Nat. Cell Biol.* 18, 337–346.

Köppen, M., Simske, J.S., Sims, P.A., Firestein, B.L., Hall, D.H., Radice, A.D., Rongo, C., and Hardin, J.D. (2001). Cooperative regulation of AJM-1 controls junctional integrity in *Caenorhabditis elegans* epithelia. *Nat Cell Biol* 3, 983–991.

Krahn, M.P., Bückers, J., Kastrup, L., and Wodarz, A. (2010). Formation of a Bazooka-Stardust complex is essential for plasma membrane polarity in epithelia. *Journal of Cell Biology* 190, 751–760.

Kristensen, A.R., Gsponer, J., and Foster, L.J. (2012). A high-throughput approach for measuring temporal changes in the interactome. *Nat. Methods* 9, 907–909.

Kroll, J.R., Rimmelzwaal, S., and Boxem, M. (2021). CeLINC, a fluorescence-based protein-protein interaction assay in *C. elegans*. *Genetics*.

Ku, N.-O., and Omary, M.B. (2006). A disease- and phosphorylation-related non-mechanical function for keratin 8. *Journal of Cell Biology* 174, 115–125.

Kumar, A., Baruah, A., Tomioka, M., Iino, Y., Kalita, M.C., and Khan, M. (2020). *Caenorhabditis elegans*: a model to understand host-microbe interactions. *Cell. Mol. Life Sci.* 77, 1229–1249.

Kutscher, L.M., and Shaham, S. (2014). Forward and reverse mutagenesis in *C. elegans*. *WormBook : The Online Review of C. Elegans Biology* 1–26.

Lamesch, P., Milstein, S., Hao, T., Rosenberg, J., Li, N., Sequerra, R., Bosak, S., Doucette-Stamm, L., Vandenhaute, J., Hill, D.E., et al. (2004). *C. elegans* ORFeome version 3.1: increasing the coverage of ORFeome resources with improved gene predictions. *Genome Res.* 14, 2064–2069.

Lee, S., Park, H., Kyung, T., Kim, N.Y., Kim, S., Kim, J., and Heo, W.D. (2014). Reversible protein inactivation by optogenetic trapping in cells. *Nature Methods* 11, 633–636.



- Lee, S.-K., Li, W., Ryu, S.-E., Rhim, T., and Ahnn, J. (2010). Vacuolar (H⁺)-ATPases in *Caenorhabditis elegans*: What can we learn about giant H⁺ pumps from tiny worms? *Biochimica et Biophysica Acta (BBA) - Bioenergetics* 1797, 1687–1695.
- Lenfant, N., Polanowska, J., Bamps, S., Omi, S., Borg, J.-P., and Reboul, J. (2010). A genome-wide study of PDZ-domain interactions in *C. elegans* reveals a high frequency of non-canonical binding. *BMC Genomics* 11, 671.
- Leung, B., Hermann, G.J., and Priess, J.R. (1999). Organogenesis of the *Caenorhabditis elegans* Intestine. *Developmental Biology* 216, 114–134.
- Li, J., and Le, W. (2013). Modeling neurodegenerative diseases in *Caenorhabditis elegans*. *Experimental Neurology* 250, 94–103.
- Li, B., Kim, H., Beers, M., and Kempthues, K. (2010a). Different domains of *C. elegans* PAR-3 are required at different times in development. *Developmental Biology* 344, 745–757.
- Li, J., Kim, H., Aceto, D.G., Hung, J., Aono, S., and Kempthues, K.J. (2010b). Binding to PKC-3, but not to PAR-3 or to a conventional PDZ domain ligand, is required for PAR-6 function in *C. elegans*. *Developmental Biology* 340, 88–98.
- Li, S., Armstrong, C.M., Bertin, N., Ge, H., Milstein, S., Boxem, M., Vidalain, P.-O., Han, J.-D.J., Chesneau, A., Hao, T., et al. (2004). A map of the interactome network of the metazoan *C. elegans*. *Science* 303, 540–543.
- Li, Y.-P., Chen, W., Liang, Y., Li, E., and Stashenko, P. (1999). Atp6i-deficient mice exhibit severe osteopetrosis due to loss of osteoclast-mediated extracellular acidification. *Nat Genet* 23, 447–451.
- Licata, L., and Orchard, S. (2016). The MIntAct Project and Molecular Interaction Databases. *Methods Mol. Biol.* 1415, 55–69.
- Liégeois, S., Benedetto, A., Garnier, J.-M., Schwab, Y., and Labouesse, M. (2006). The V0-ATPase mediates apical secretion of exosomes containing Hedgehog-related proteins in *Caenorhabditis elegans*. *J. Cell Biol.* 173, 949–961.
- Lievens, S., Van der Heyden, J., Masschaele, D., De Ceuninck, L., Petta, I., Gupta, S., De Puysseleir, V., Vauthier, V., Lemmens, I., De Clercq, D.J.H., et al. (2016). Proteome-scale Binary Interactomics in Human Cells. *Mol. Cell Proteomics* 15, 3624–3639.
- Lim, C.H., Kaur, P., Teo, E., Lam, V.Y.M., Zhu, F., Kibat, C., Gruber, J., Mathuru, A.S., and Tolwinski, N.S. (2020). Application of optogenetic Amyloid- β distinguishes between metabolic and physical damages in neurodegeneration. *ELife* 9, e52589.
- Lin, Y.-C., Broedersz, C.P., Rowat, A.C., Wedig, T., Herrmann, H., MacKintosh, F.C., and Weitz, D.A. (2010). Divalent Cations Crosslink Vimentin Intermediate Filament Tail Domains to Regulate Network Mechanics. *Journal of Molecular Biology* 399, 637–644.

Liu, F., and Heck, A.J.R. (2015). Interrogating the architecture of protein assemblies and protein interaction networks by cross-linking mass spectrometry. *Curr. Opin. Struct. Biol.* 35, 100–108.

Lockwood, C.A., Lynch, A.M., and Hardin, J. (2008). Dynamic analysis identifies novel roles for DLG-1 subdomains in AJM-1 recruitment and LET-413-dependent apical focusing. *Journal of Cell Science* 121, 1477–1487.

Low, I.I.C., Williams, C.R., Chong, M.K., McLachlan, I.G., Wierbowski, B.M., Kolotuev, I., and Heiman, M.G. (2019). Morphogenesis of neurons and glia within an epithelium. *Development* 146.

Lubarsky, B., and Krasnow, M.A. (2003). Tube Morphogenesis: Making and Shaping Biological Tubes. *Cell* 112, 19–28.

Luck, K., Kim, D.-K., Lambourne, L., Spirohn, K., Begg, B.E., Bian, W., Brignall, R., Cafarelli, T., Campos-Laborie, F.J., Charlotteaux, B., et al. (2020). A reference map of the human binary protein interactome. *Nature* 580, 402–408.

Luschnig, S., and Uv, A. (2014). Luminal matrices: An inside view on organ morphogenesis. *Experimental Cell Research* 321, 64–70.

Lynley, A.M., and Dale, B.A. (1983). The characterization of human epidermal filaggrin: A histidine-rich, keratin filament-aggregating protein. *Biochimica et Biophysica Acta (BBA) - Protein Structure and Molecular Enzymology* 744, 28–35.

MacQueen, A.J., Baggett, J.J., Perumov, N., Bauer, R.A., Januszewski, T., Schrieffer, L., and Waddle, J.A. (2005). ACT-5 is an essential *Caenorhabditis elegans* actin required for intestinal microvilli formation. *Molecular Biology of the Cell* 16, 3247–3259.

Magin, T.M., Vijayaraj, P., and Leube, R.E. (2007). Structural and regulatory functions of keratins. *Exp Cell Res* 313, 2021–2032.

Mailleux, A.A., Overholtzer, M., and Brugge, J.S. (2008). Lumen formation during mammary epithelial morphogenesis: insights from in vitro and in vivo models. *Cell Cycle* 7, 57–62.

Marcello, M.R., Druzhinina, M., and Singson, A. (2018). *Caenorhabditis elegans* sperm membrane protein interactome. *Biol. Reprod.* 98, 776–783.

Margiotta, A., and Bucci, C. (2016). Role of Intermediate Filaments in Vesicular Traffic. *Cells* 5, 20.

Markaki, M., and Tavernarakis, N. (2020). *Caenorhabditis elegans* as a model system for human diseases. *Current Opinion in Biotechnology* 63, 118–125.

Martín-Belmonte, F., Yu, W., Rodríguez-Fraticelli, A.E., Ewald, A., Werb, Z., Alonso, M.A., and Mostov, K. (2008). Cell-Polarity Dynamics Controls the Mechanism of Lumen Formation in Epithelial Morphogenesis. *Current Biology* 18, 507–513.



- Mathew, D., Gramates, L.S., Packard, M., Thomas, U., Bilder, D., Perrimon, N., Gorczyca, M., and Budnik, V. (2002). Recruitment of scribble to the synaptic scaffolding complex requires GUK-holder, a novel DLG binding protein. *Curr. Biol.* *12*, 531–539.
- Maxson, M.E., and Grinstein, S. (2014). The vacuolar-type H⁺-ATPase at a glance – more than a proton pump. *Journal of Cell Science* *127*, 4987–4993.
- McDonald, K.L. (2014). Rapid embedding methods into epoxy and LR White resins for morphological and immunological analysis of cryofixed biological specimens. *Microsc Microanal* *20*, 152–163.
- McGhee, J.D. (2007). The *C. elegans* intestine. *WormBook* 1–36.
- Mehta, V., and Trinkle-Mulcahy, L. (2016). Recent advances in large-scale protein interactome mapping. *F1000Res* *5*.
- Mellacheruvu, D., Wright, Z., Couzens, A.L., Lambert, J.-P., St-Denis, N.A., Li, T., Miteva, Y.V., Hauri, S., Sardi, M.E., Low, T.Y., et al. (2013). The CRAPome: a contaminant repository for affinity purification–mass spectrometry data. *Nature Methods* *10*, 730–736.
- M. Friedrich, B., and A. Safran, S. (2012). How cells feel their substrate: spontaneous symmetry breaking of active surface stresses. *Soft Matter* *8*, 3223–3230.
- Michaux, G., Massey-Harroche, D., Nicolle, O., Rabant, M., Brousse, N., Goulet, O., Bivic, A.L., and Ruettemle, F.M. (2016). The localisation of the apical Par/Cdc42 polarity module is specifically affected in microvillus inclusion disease. *Biology of the Cell* *108*, 19–28.
- Miller, K.E., Kim, Y., Huh, W.-K., and Park, H.-O. (2015). Bimolecular Fluorescence Complementation (BiFC) Analysis: Advances and Recent Applications for Genome-Wide Interaction Studies. *J. Mol. Biol.* *427*, 2039–2055.
- Munn, E.A., and Greenwood, C. a. (1984). The occurrence of submicrovillar endotube (modified terminal web) and associated cytoskeletal structures in the intestinal epithelia of nematodes. *Philosophical Transactions of the Royal Society of London. B, Biological Sciences* *306*, 1–18.
- Muñoz-Jiménez, C., Ayuso, C., Dobrzynska, A., Torres-Mendéz, A., Ruiz, P. de la C., and Askjaer, P. (2017). An Efficient FLP-Based Toolkit for Spatiotemporal Control of Gene Expression in *Caenorhabditis elegans*. *Genetics* *206*, 1763–1778.
- Munro, E., Nance, J., and Priess, J.R. (2004). Cortical Flows Powered by Asymmetrical Contraction Transport PAR Proteins to Establish and Maintain Anterior-Posterior Polarity in the Early *C. elegans* Embryo. *Developmental Cell* *7*, 413–424.
- Müsch, A. (2004). Microtubule Organization and Function in Epithelial Cells. *Traffic* *5*, 1–9.

Myllymäki, S.M., Teräväinen, T.P., and Manninen, A. (2011). Two Distinct Integrin-Mediated Mechanisms Contribute to Apical Lumen Formation in Epithelial Cells. *PLOS ONE* 6, e19453.

Nance, J., Munro, E.M., and Priess, J.R. (2003). *C. elegans* PAR-3 and PAR-6 are required for apicobasal asymmetries associated with cell adhesion and gastrulation. *Development* 130, 5339–5350.

Nguyen, M.K., Kim, C.Y., Kim, J.M., Park, B.O., Lee, S., Park, H., and Heo, W.D. (2016). Optogenetic oligomerization of Rab GTPases regulates intracellular membrane trafficking. *Nature Chemical Biology* 12, 431–436.

Nijssen, J., Aguila, J., Hoogstraaten, R., Kee, N., and Hedlund, E. (2018). Axon-Seq Decodes the Motor Axon Transcriptome and Its Modulation in Response to ALS. *Stem Cell Reports* 11, 1565–1578.

Nishimura, K., Fukagawa, T., Takisawa, H., Kakimoto, T., and Kanemaki, M. (2009). An auxin-based degron system for the rapid depletion of proteins in nonplant cells. *Nat. Methods* 6, 917–922.

Oeffinger, M. (2012). Two steps forward--one step back: advances in affinity purification mass spectrometry of macromolecular complexes. *Proteomics* 12, 1591–1608.

Omary, M.B. (2009). “IF-pathies”: a broad spectrum of intermediate filament-associated diseases. *J Clin Invest* 119, 1756–1762.

Omary, M.B., Coulombe, P.A., and McLean, W.H.I. (2004). Intermediate Filament Proteins and Their Associated Diseases. *New England Journal of Medicine* 351, 2087–2100.

Oot, R.A., Kane, P.M., Berry, E.A., and Wilkens, S. (2016). Crystal structure of yeast V1-ATPase in the autoinhibited state. *EMBO J* 35, 1694–1706.

Osswald, M., Santos, A.F., and Morais-de-Sá, E. (2019). Light-Induced Protein Clustering for Optogenetic Interference and Protein Interaction Analysis in *Drosophila* S2 Cells. *Biomolecules* 9.

Overeem, A.W., Bryant, D.M., and van IJzendoorn, S.C.D. (2015). Mechanisms of apical-basal axis orientation and epithelial lumen positioning. *Trends in Cell Biology* 25, 476–485.

Pasti, G., and Labouesse, M. (2014). Epithelial junctions, cytoskeleton, and polarity. *WormBook* 1–35.

Paulson, C.C. (2009). Analysis of *C. elegans* genes required for maintaining intestinal lumen morphology and ingested drug resistance. Southern Methodist University.



- Perez-Riverol, Y., Csordas, A., Bai, J., Bernal-Llinares, M., Hewapathirana, S., Kundu, D.J., Inuganti, A., Griss, J., Mayer, G., Eisenacher, M., et al. (2019). The PRIDE database and related tools and resources in 2019: improving support for quantification data. *Nucleic Acids Research* *47*, D442–D450.
- Pir, G.J., Choudhary, B., and Mandelkow, E. (2017). Caenorhabditis elegans models of tauopathy. *The FASEB Journal* *31*, 5137–5148.
- Pires, H.R., and Boxem, M. (2017). Mapping the Polarity Interactome. *J. Mol. Biol.*
- Pohl, C. (2017). The Midbody and its Remnant in Cell Polarization and Asymmetric Cell Division. In *Asymmetric Cell Division in Development, Differentiation and Cancer*, J.-P. Tassan, and J.Z. Kubiak, eds. (Cham: Springer International Publishing), pp. 165–182.
- Pollard, T.D. (2016). Actin and Actin-Binding Proteins. *Cold Spring Harbor Perspectives in Biology* *8*, a018226.
- Potokar, M., Kreft, M., Li, L., Daniel Andersson, J., Pangršič, T., Chowdhury, H.H., Pekny, M., and Zorec, R. (2007). Cytoskeleton and Vesicle Mobility in Astrocytes. *Traffic* *8*, 12–20.
- Potter, S.C., Luciani, A., Eddy, S.R., Park, Y., Lopez, R., and Finn, R.D. (2018). HMMER web server: 2018 update. *Nucleic Acids Res* *46*, W200–W204.
- Qin, X., Park, B.O., Liu, J., Chen, B., Choessel-Cadamuro, V., Belguise, K., Heo, W.D., and Wang, X. (2017). Cell-matrix adhesion and cell-cell adhesion differentially control basal myosin oscillation and Drosophila egg chamber elongation. *Nature Communications* *8*, 14708.
- Qin, X., Hannezo, E., Mangeat, T., Liu, C., Majumder, P., Liu, J., Choessel-Cadamuro, V., McDonald, J.A., Liu, Y., Yi, B., et al. (2018). A biochemical network controlling basal myosin oscillation. *Nature Communications* *9*, 1210.
- Quinlan, R.A., Schwarz, N., Windoffer, R., Richardson, C., Hawkins, T., Broussard, J.A., Green, K.J., and Leube, R.E. (2017). A rim-and-spoke hypothesis to explain the biomechanical roles for cytoplasmic intermediate filament networks. *Journal of Cell Science* *130*, 3437–3445.
- Quiroz, F.G., Fiore, V.F., Levorse, J., Polak, L., Wong, E., Pasolli, H.A., and Fuchs, E. (2020). Liquid-liquid phase separation drives skin barrier formation. *Science* *367*, eaax9554.
- Ramalho, J.J., Sepers, J.J., Nicolle, O., Schmidt, R., Cravo, J., Michaux, G., and Boxem, M. (2020). C-terminal phosphorylation modulates ERM-1 localization and dynamics to control cortical actin organization and support lumen formation during C. elegans development. *Development*.
- Ramos, G.P., and Papadakis, K.A. (2019). Mechanisms of Disease: Inflammatory Bowel Diseases. *Mayo Clin Proc* *94*, 155–165.

Reboul, J., Vaglio, P., Rual, J.-F., Lamesch, P., Martinez, M., Armstrong, C.M., Li, S., Jacotot, L., Bertin, N., Moore, T., et al. (2003). *C. elegans* ORFeome version 1.1: experimental verification of the genome annotation and resource for proteome-scale protein expression. *Nature Genetics* 34.

Redemann, S., Schloissnig, S., Ernst, S., Pozniakowsky, A., Ayloo, S., Hyman, A.A., and Bringmann, H. (2011). Codon adaptation-based control of protein expression in *C. elegans*. *Nat Methods* 8, 250–252.

Reece-Hoyes, J.S., Pons, C., Diallo, A., Mori, A., Shrestha, S., Kadreppa, S., Nelson, J., Diprima, S., Dricot, A., Lajoie, B.R., et al. (2013). Extensive rewiring and complex evolutionary dynamics in a *C. elegans* multiparameter transcription factor network. *Mol. Cell* 51, 116–127.

Reipert, S., Goldammer, H., Richardson, C., Goldberg, M.W., Hawkins, T.J., Hollerschwandtner, E., Kaufmann, W.A., Antreich, S., and Stierhof, Y.-D. (2018). Agitation Modules: Flexible Means to Accelerate Automated Freeze Substitution. *J Histochem Cytochem* 66, 903–921.

Remmelzwaal, S., Geisler, F., Stucchi, R., van der Horst, S., Pasolli, M., Kroll, J.R., Jarosinska, O.D., Akhmanova, A., Richardson, C.A., Altelaar, M., et al. (2021). BBLN-1 is essential for intermediate filament organization and apical membrane morphology. *Current Biology* 31, 2334–2346.e9.

Riga, A., Castiglioni, V.G., and Boxem, M. (2020). New insights into apical-basal polarization in epithelia. *Current Opinion in Cell Biology* 62, 1–8.

Rigaut, G., Shevchenko, A., Rutz, B., Wilm, M., Mann, M., and Séraphin, B. (1999). A generic protein purification method for protein complex characterization and proteome exploration. *Nat. Biotechnol.* 17, 1030–1032.

Rodriguez, J., Peglion, F., Martin, J., Hubatsch, L., Reich, J., Hirani, N., Gubieda, A.G., Roffey, J., Fernandes, A.R., St Johnston, D., et al. (2017). aPKC Cycles between Functionally Distinct PAR Protein Assemblies to Drive Cell Polarity. *Developmental Cell* 42, 400–415.e9.

Rodriguez-Boulan, E., and Macara, I.G. (2014). Organization and execution of the epithelial polarity programme. *Nat Rev Mol Cell Biol* 15, 225–242.

Roignot, J., Peng, X., and Mostov, K. (2013). Polarity in Mammalian Epithelial Morphogenesis. *Cold Spring Harb Perspect Biol* 5, a013789.

Rolland, T., Taşan, M., Charlotteaux, B., Pevzner, S.J., Zhong, Q., Sahni, N., Yi, S., Lemmens, I., Fontanillo, C., Mosca, R., et al. (2014). A proteome-scale map of the human interactome network. *Cell* 159, 1212–1226.

Rual, J.-F., Ceron, J., Koreth, J., Hao, T., Nicot, A.-S., Hirozane-Kishikawa, T., Vandenhaute, J., Orkin, S.H., Hill, D.E., Heuvel, S. van den, et al. (2004). Toward Improving *Caenorhabditis elegans* Phenome Mapping With an ORFeome-Based RNAi Library. *Genome Res.* 14, 2162–2168.



Rual, J.-F., Venkatesan, K., Hao, T., Hirozane-Kishikawa, T., Dricot, A., Li, N., Berriz, G.F., Gibbons, F.D., Dreze, M., Ayivi-Guedehoussou, N., et al. (2005). Towards a proteome-scale map of the human protein-protein interaction network. *Nature* *437*, 1173–1178.

Sacharidou, A., Stratman, A.N., and Davis, G.E. (2012). Molecular mechanisms controlling vascular lumen formation in three-dimensional extracellular matrices. *Cells Tissues Organs* *195*, 122–143.

Salas, P.J., Forteza, R., and Mashukova, A. (2016). Multiple roles for keratin intermediate filaments in the regulation of epithelial barrier function and apico-basal polarity. *Tissue Barriers* *4*, e1178368.

Sallee, M.D., Pickett, M.A., and Feldman, J.L. (2021). Apical PAR complex proteins protect against programmed epithelial assaults to create a continuous and functional intestinal lumen. *ELife* *10*, e64437.

Sandilands, A., Sutherland, C., Irvine, A.D., and McLean, W.H.I. (2009). Filaggrin in the frontline: role in skin barrier function and disease. *J Cell Sci* *122*, 1285–1294.

Sanghvi-Shah, R., and Weber, G.F. (2017). Intermediate Filaments at the Junction of Mechanotransduction, Migration, and Development. *Frontiers in Cell and Developmental Biology* *5*, 81.

Santos-Pereira, C., Rodrigues, L.R., and Côrte-Real, M. (2021). Emerging insights on the role of V-ATPase in human diseases: Therapeutic challenges and opportunities. *Med Res Rev* *41*, 1927–1964.

Sauvanet, C., Wayt, J., Pelaseyed, T., and Bretscher, A. (2015). Structure, Regulation, and Functional Diversity of Microvilli on the Apical Domain of Epithelial Cells. *Annu. Rev. Cell Dev. Biol.* *31*, 593–621.

Sayers, E.W., Beck, J., Bolton, E.E., Bourexis, D., Brister, J.R., Canese, K., Comeau, D.C., Funk, K., Kim, S., Klimke, W., et al. (2020). Database resources of the National Center for Biotechnology Information. *Nucleic Acids Res* *49*, D10–D17.

Schäffer, U., Schlosser, A., Müller, K.M., Schäfer, A., Katava, N., Baumeister, R., and Schulze, E. (2010). SnAvi--a new tandem tag for high-affinity protein-complex purification. *Nucleic Acids Res.* *38*, e91.

Schatz, P.J. (1993). Use of peptide libraries to map the substrate specificity of a peptide-modifying enzyme: a 13 residue consensus peptide specifies biotinylation in *Escherichia coli*. *Biotech.* *11*, 1138–1143.

Schelling, J.R. (2016). Tubular atrophy in the pathogenesis of chronic kidney disease progression. *Pediatr Nephrol* *31*, 693–706.

Schindelin, J., Arganda-Carreras, I., Frise, E., Kaynig, V., Longair, M., Pietzsch, T., Preibisch, S., Rueden, C., Saalfeld, S., Schmid, B., et al. (2012). Fiji: an open-source platform for biological-image analysis. *Nature Methods* *9*, 676–682.

Schwartz, M.L., and Jorgensen, E.M. (2016). SapTrap, a Toolkit for High-Throughput CRISPR/Cas9 Gene Modification in *Caenorhabditis elegans*. *Genetics* 202, 1277–1288.

Schwarz, N., and Leube, R.E. (2016). Intermediate Filaments as Organizers of Cellular Space: How They Affect Mitochondrial Structure and Function. *Cells* 5, E30.

Schwarz, N., Windoffer, R., Magin, T.M., and Leube, R.E. (2015). Dissection of keratin network formation, turnover and reorganization in living murine embryos. *Scientific Reports* 5, 9007.

Shafaq-Zadah, M., Brocard, L., Solari, F., and Michaux, G. (2012). AP-1 is required for the maintenance of apico-basal polarity in the *C. elegans* intestine. *Development* 139, 2061–2070.

Shyu, Y.J., Hiatt, S.M., Duren, H.M., Ellis, R.E., Kerppola, T.K., and Hu, C.-D. (2008). Visualization of protein interactions in living *Caenorhabditis elegans* using bimolecular fluorescence complementation analysis. *Nature Protocols* 3, 588–596.

Sigurbjörnsdóttir, S., Mathew, R., and Leptin, M. (2014). Molecular mechanisms of de novo lumen formation. *Nat Rev Mol Cell Biol* 15, 665–676.

Silverman, G.A., Luke, C.J., Bhatia, S.R., Long, O.S., Vetica, A.C., Perlmutter, D.H., and Pak, S.C. (2009). Modeling Molecular and Cellular Aspects of Human Disease Using the Nematode *Caenorhabditis elegans*. *Pediatr Res* 65, 10–18.

Simonis, N., Rual, J.-F., Carvunis, A.-R., Tasan, M., Lemmens, I., Hirozane-Kishikawa, T., Hao, T., Sahalie, J.M., Venkatesan, K., Gebreab, F., et al. (2009). Empirically controlled mapping of the *Caenorhabditis elegans* protein-protein interactome network. *Nat. Methods* 6, 47–54.

Smits, A.H., and Vermeulen, M. (2016). Characterizing Protein-Protein Interactions Using Mass Spectrometry: Challenges and Opportunities. *Trends Biotechnol.* 34, 825–834.

Snider, N.T., and Omary, M.B. (2014). Post-translational modifications of intermediate filament proteins: mechanisms and functions. *Nat Rev Mol Cell Biol* 15, 163–177.

Snider, J., Kittanakom, S., Damjanovic, D., Curak, J., Wong, V., and Stagljar, I. (2010). Detecting interactions with membrane proteins using a membrane two-hybrid assay in yeast. *Nat Protoc* 5, 1281–1293.

Srinivasan, D.G., Fisk, R.M., Xu, H., and van den Heuvel, S. (2003). A complex of LIN-5 and GPR proteins regulates G protein signaling and spindle function in *C. elegans*. *Genes Dev.* 17, 1225–1239.

Stagljar, I., Korostensky, C., Johnsson, N., and te Heesen, S. (1998). A genetic system based on split-ubiquitin for the analysis of interactions between membrane proteins in vivo. *Proc. Natl. Acad. Sci. U.S.A.* 95, 5187–5192.



- Stephens, R., Lim, K., Portela, M., Kvensakul, M., Humbert, P.O., and Richardson, H.E. (2018). The Scribble Cell Polarity Module in the Regulation of Cell Signaling in Tissue Development and Tumorigenesis. *J. Mol. Biol.* *430*, 3585–3612.
- Strickland, D., Lin, Y., Wagner, E., Hope, C.M., Zayner, J., Antoniou, C., Sosnick, T.R., Weiss, E.L., and Glotzer, M. (2012). TULIPs: tunable, light-controlled interacting protein tags for cell biology. *Nat Methods* *9*, 379–384.
- Strilić, B., Eglinger, J., Krieg, M., Zeeb, M., Axnick, J., Babál, P., Müller, D.J., and Lammert, E. (2010). Electrostatic Cell-Surface Repulsion Initiates Lumen Formation in Developing Blood Vessels. *Current Biology* *20*, 2003–2009.
- Stumpf, M.P.H., Thorne, T., de Silva, E., Stewart, R., An, H.J., Lappe, M., and Wiuf, C. (2008). Estimating the size of the human interactome. *Proc. Natl. Acad. Sci. U.S.A.* *105*, 6959–6964.
- Stutz, K., Kaech, A., Aebi, M., Künzler, M., and Hengartner, M.O. (2015). Disruption of the *C. elegans* Intestinal Brush Border by the Fungal Lectin CCL2 Phenocopies Dietary Lectin Toxicity in Mammals. *PLoS ONE* *10*, e0129381.
- Styers, M.L., Kowalczyk, A.P., and Faundez, V. (2005). Intermediate Filaments and Vesicular Membrane Traffic: The Odd Couple's First Dance? *Traffic* *6*, 359–365.
- Su, W.-H., Mruk, D.D., Wong, E.W.P., Lui, W.-Y., and Cheng, C.Y. (2012). Polarity Protein Complex Scribble/Lgl/Dlg and Epithelial Cell Barriers. *Adv Exp Med Biol* *763*, 149–170.
- Sulston, J.E., Schierenberg, E., White, J.G., and Thomson, J.N. (1983). The embryonic cell lineage of the nematode *Caenorhabditis elegans*. *Developmental Biology* *100*, 64–119.
- Sundaram, M.V., and Buechner, M. (2016). The *Caenorhabditis elegans* Excretory System: A Model for Tubulogenesis, Cell Fate Specification, and Plasticity. *Genetics* *203*, 35–63.
- Sun-Wada, G.-H., Murata, Y., Namba, M., Yamamoto, A., Wada, Y., and Futai, M. (2003). Mouse proton pump ATPase C subunit isoforms (C2-a and C2-b) specifically expressed in kidney and lung. *J Biol Chem* *278*, 44843–44851.
- Szklarczyk, D., Morris, J.H., Cook, H., Kuhn, M., Wyder, S., Simonovic, M., Santos, A., Doncheva, N.T., Roth, A., Bork, P., et al. (2017). The STRING database in 2017: quality-controlled protein-protein association networks, made broadly accessible. *Nucleic Acids Res.* *45*, D362–D368.
- Taipale, M., Tucker, G., Peng, J., Krykbaeva, I., Lin, Z.-Y., Larsen, B., Choi, H., Berger, B., Gingras, A.-C., and Lindquist, S. (2014). A quantitative chaperone interaction network reveals the architecture of cellular protein homeostasis pathways. *Cell* *158*, 434–448.

Taslimi, A., Vrana, J.D., Chen, D., Borinskaya, S., Mayer, B.J., Kennedy, M.J., and Tucker, C.L. (2014). An optimized optogenetic clustering tool for probing protein interaction and function. *Nature Communications* 5, 4925.

Teitelbaum, S.L. (2007). Osteoclasts: What Do They Do and How Do They Do It? *Am J Pathol* 170, 427–435.

Tewari, M., Hu, P.J., Ahn, J.S., Ayivi-Guedehoussou, N., Vidalain, P.-O., Li, S., Milstein, S., Armstrong, C.M., Boxem, M., Butler, M.D., et al. (2004). Systematic interactome mapping and genetic perturbation analysis of a *C. elegans* TGF-beta signaling network. *Mol. Cell* 13, 469–482.

Therrien, M., and Parker, J.A. (2014). Worming forward: amyotrophic lateral sclerosis toxicity mechanisms and genetic interactions in *Caenorhabditis elegans*. *Frontiers in Genetics* 5, 85.

Timmons, L., and Fire, A. (1998). Specific interference by ingested dsRNA. *Nature* 395, 854.

Toivola, D.M., Strnad, P., Habtezion, A., and Omary, M.B. (2010). Intermediate filaments take the heat as stress proteins. *Trends in Cell Biology* 20, 79–91.

Tomashek, J.J., Garrison, B.S., and Klionsky, D.J. (1997a). Reconstitution in Vitro of the V1 Complex from the Yeast Vacuolar Proton-translocating ATPase: assembly recapitulates mechanism. *Journal of Biological Chemistry* 272, 16618–16623.

Tomashek, J.J., Graham, L.A., Hutchins, M.U., Stevens, T.H., and Klionsky, D.J. (1997b). V1-situated Stalk Subunits of the Yeast Vacuolar Proton-translocating ATPase. *Journal of Biological Chemistry* 272, 26787–26793.

Toyomura, T., Murata, Y., Yamamoto, A., Oka, T., Sun-Wada, G.-H., Wada, Y., and Futai, M. (2003). From Lysosomes to the Plasma Membrane: localization of vacuolar type H⁺-ATPase with the $\alpha 3$ isoform during osteoclast differentiation. *Journal of Biological Chemistry* 278, 22023–22030.

Troemel, E.R., Félix, M.-A., Whiteman, N.K., Barrière, A., and Ausubel, F.M. (2008). Microsporidia Are Natural Intracellular Parasites of the Nematode *Caenorhabditis elegans*. *PLOS Biology* 6, e309.

Tsuboyama, K., Osaki, T., Matsuura-Suzuki, E., Kozuka-Hata, H., Okada, Y., Oyama, M., Ikeuchi, Y., Iwasaki, S., and Tomari, Y. (2020). A widespread family of heat-resistant obscure (Hero) proteins protect against protein instability and aggregation. *PLOS Biology* 18, e3000632.

Vaart, A. van der, Godfrey, M., Portegijs, V., and Heuvel, S. van den (2020). Dose-dependent functions of SWI/SNF BAF in permitting and inhibiting cell proliferation in vivo. *Science Advances* 6, eaay3823.

Ventura, G., Moreira, S., Barros-Carvalho, A., Osswald, M., and Morais-de-Sá, E. (2020). Lgl cortical dynamics are independent of binding to the Scrib-Dlg complex but require Dlg-dependent restriction of aPKC. *Development* 147.



- Veranič, P., and Jezernik, K. (2002). Trajectorial organisation of cytokeratins within the subapical region of umbrella cells. *Cell Motility* 53, 317–325.
- Vicencio, J., Martínez-Fernández, C., Serrat, X., and Cerón, J. (2019). Efficient Generation of Endogenous Fluorescent Reporters by Nested CRISPR in *Caenorhabditis elegans*. *Genetics* 211, 1143–1154.
- Voss, M., Vitavska, O., Walz, B., Wieczorek, H., and Baumann, O. (2007). Stimulus-induced phosphorylation of vacuolar H(+)-ATPase by protein kinase A. *J Biol Chem* 282, 33735–33742.
- Waaijers, S., and Boxem, M. (2014). Engineering the *Caenorhabditis elegans* genome with CRISPR/Cas9. *Methods* 68, 381–388.
- Waaijers, S., Koorman, T., Kerver, J., and Boxem, M. (2013). Identification of human protein interaction domains using an ORFeome-based yeast two-hybrid fragment library. *J. Proteome Res.* 12, 3181–3192.
- Waaijers, S., Muñoz, J., Berends, C., Ramalho, J.J., Goerdayal, S.S., Low, T.Y., Zoumaro-Djayoon, A.D., Hoffmann, M., Koorman, T., Tas, R.P., et al. (2016). A tissue-specific protein purification approach in *Caenorhabditis elegans* identifies novel interaction partners of DLG-1/Discs large. *BMC Biol.* 14, 66.
- Walhout, A.J., Sordella, R., Lu, X., Hartley, J.L., Temple, G.F., Brasch, M.A., Thierry-Mieg, N., and Vidal, M. (2000a). Protein interaction mapping in *C. elegans* using proteins involved in vulval development. *Science* 287, 116–122.
- Walhout, A.J., Boulton, S.J., and Vidal, M. (2000b). Yeast two-hybrid systems and protein interaction mapping projects for yeast and worm. *Yeast* 17, 88–94.
- Walhout, A.J.M., Reboul, J., Shtanko, O., Bertin, N., Vaglio, P., Ge, H., Lee, H., Doucette-Stamm, L., Gunsalus, K.C., Schetter, A.J., et al. (2002). Integrating Interactome, Phenome, and Transcriptome Mapping Data for the *C. elegans* Germline. *Current Biology* 12, 1952–1958.
- Wan, C., Borgeson, B., Phanse, S., Tu, F., Drew, K., Clark, G., Xiong, X., Kagan, O., Kwan, J., Bezginov, A., et al. (2015). Panorama of ancient metazoan macromolecular complexes. *Nature* 525, 339–344.
- Wang, L., Wu, D., Robinson, C.V., Wu, H., and Fu, T.-M. (2020). Structures of a Complete Human V-ATPase Reveal Mechanisms of Its Assembly. *Molecular Cell* 80, 501-511.e3.
- Wang, S., Tang, N.H., Lara-Gonzalez, P., Zhao, Z., Cheerambathur, D.K., Prevo, B., Chisholm, A.D., Desai, A., and Oegema, K. (2017). A toolkit for GFP-mediated tissue-specific protein degradation in *C. elegans*. *Development* 144, 2694–2701.
- Wang, T., Yanger, K., Stanger, B.Z., Cassio, D., and Bi, E. (2014). Cytokinesis defines a spatial landmark for hepatocyte polarization and apical lumen formation. *Journal of Cell Science* 127, 2483–2492.

Wankel, B., Ouyang, J., Guo, X., Hadjiolova, K., Miller, J., Liao, Y., Tham, D.K.L., Romih, R., Andrade, L.R., Gumper, I., et al. (2016). Sequential and compartmentalized action of Rabs, SNAREs, and MAL in the apical delivery of fusiform vesicles in urothelial umbrella cells. *MBoC* 27, 1621–1634.

Watanabe, N., Nagamatsu, Y., Gengyo-Ando, K., Mitani, S., and Ohshima, Y. (2005). Control of body size by SMA-5, a homolog of MAP kinase BMK1/ERK5, in *C. elegans*. *Development* 132, 3175–3184.

Watts, J.L., Etemad-Moghadam, B., Guo, S., Boyd, L., Draper, B.W., Mello, C.C., Priess, J.R., and Kempthues, K.J. (1996). *par-6*, a gene involved in the establishment of asymmetry in early *C. elegans* embryos, mediates the asymmetric localization of PAR-3. *Development* 122, 3133–3140.

Weber, K., Plessmann, U., and Ulrich, W. (1989). Cytoplasmic intermediate filament proteins of invertebrates are closer to nuclear lamins than are vertebrate intermediate filament proteins; sequence characterization of two muscle proteins of a nematode. *The EMBO Journal* 8, 3221–3227.

Weimann, M., Grossmann, A., Woodsmith, J., Özkan, Z., Birth, P., Meierhofer, D., Benlasfer, N., Valovka, T., Timmermann, B., Wanker, E.E., et al. (2013). A Y2H-seq approach defines the human protein methyltransferase interactome. *Nat. Methods* 10, 339–342.

Welchman, D.P., Mathies, L., and Ahringer, J. (2007). Similar requirements for CDC-42 and the PAR-3/PAR-6/PKC-3 complex in diverse cell types. *Dev Biol* 305, 347–357.

Wen, W., and Zhang, M. (2018). Protein Complex Assemblies in Epithelial Cell Polarity and Asymmetric Cell Division. *J. Mol. Biol.* 430, 3504–3520.

Williams, K., Williams, K., Baucher, H.M., and Plenefisch, J. (2015). The Tail Domain Is Essential but the Head Domain Dispensable for *C. elegans* Intermediate Filament IFA-2 Function. *PLOS ONE* 10, e0119282.

Winter, J.F., Höpfner, S., Korn, K., Farnung, B.O., Bradshaw, C.R., Marsico, G., Volkmer, M., Habermann, B., and Zerial, M. (2012). *Caenorhabditis elegans* screen reveals role of PAR-5 in RAB-11-recycling endosome positioning and apicobasal cell polarity. *Nat Cell Biol* 14, 666–676.

Woo, W.-M., Goncharov, A., Jin, Y., and Chisholm, A.D. (2004). Intermediate filaments are required for *C. elegans* epidermal elongation. *Dev. Biol.* 267, 216–229.

Xin, X., Gfeller, D., Cheng, J., Tonikian, R., Sun, L., Guo, A., Lopez, L., Pavlenco, A., Akintobi, A., Zhang, Y., et al. (2013). SH3 interactome conserves general function over specific form. *Mol. Syst. Biol.* 9, 652.

Yachie, N., Petsalaki, E., Mellor, J.C., Weile, J., Jacob, Y., Verby, M., Ozturk, S.B., Li, S., Cote, A.G., Mosca, R., et al. (2016). Pooled-matrix protein interaction screens using Barcode Fusion Genetics. *Mol. Syst. Biol.* 12, 863.



- Yamagata, M., and Sanes, J.R. (2018). Reporter–nanobody fusions (RANbodies) as versatile, small, sensitive immunohistochemical reagents. *PNAS* *115*, 2126–2131.
- Yamakawa, T., Okamatsu, N., Ishikawa, K., Kiyohara, S., Handa, K., Hayashi, E., Sakai, N., Karakawa, A., Chatani, M., Tsuji, M., et al. (2020). Novel gene Merlot inhibits differentiation and promotes apoptosis of osteoclasts. *Bone* *138*, 115494.
- Yamashita, M., Iwasaki, K., and Doi, M. (2009). The non-neuronal syntaxin SYN-1 regulates defecation behavior and neural activity in *C. elegans* through interaction with the Munc13-like protein AEX-1. *Biochemical and Biophysical Research Communications* *378*, 404–408.
- Yang, X., Coulombe-Huntington, J., Kang, S., Sheynkman, G.M., Hao, T., Richardson, A., Sun, S., Yang, F., Shen, Y.A., Murray, R.R., et al. (2016). Widespread Expansion of Protein Interaction Capabilities by Alternative Splicing. *Cell* *164*, 805–817.
- Yao, Z., Aboualizadeh, F., Kroll, J., Akula, I., Snider, J., Lyakisheva, A., Tang, P., Kotlyar, M., Jurisica, I., Boxem, M., et al. (2020). Split Intein-Mediated Protein Ligation for detecting protein-protein interactions and their inhibition. *Nature Communications* *11*, 2440.
- Yoon, S., and Leube, R.E. (2019). Keratin intermediate filaments: intermediaries of epithelial cell migration. *Essays Biochem* *63*, 521–533.
- Yoshida, T., and Nakagawa, M. (2012). Clinical aspects and pathology of Alexander disease, and morphological and functional alteration of astrocytes induced by GFAP mutation. *Neuropathology* *32*, 440–446.
- Yoshimori, T., Yamamoto, A., Moriyama, Y., Futai, M., and Tashiro, Y. (1991). Bafilomycin A1, a specific inhibitor of vacuolar-type H(+)-ATPase, inhibits acidification and protein degradation in lysosomes of cultured cells. *J Biol Chem* *266*, 17707–17712.
- Yu, H., Tardivo, L., Tam, S., Weiner, E., Gebreab, F., Fan, C., Svrikapa, N., Hirozane-Kishikawa, T., Rietman, E., Yang, X., et al. (2011). Next-generation sequencing to generate interactome datasets. *Nat. Methods* *8*, 478–480.
- Zahraoui, A., Louvard, D., and Galli, T. (2000). Tight Junction, a Platform for Trafficking and Signaling Protein Complexes. *J Cell Biol* *151*, 31–36.
- Zdobnov, E.M., Tegenfeldt, F., Kuznetsov, D., Waterhouse, R.M., Simão, F.A., Ioannidis, P., Seppey, M., Loetscher, A., and Kriventseva, E.V. (2017). OrthoDB v9.1: cataloging evolutionary and functional annotations for animal, fungal, plant, archaeal, bacterial and viral orthologs. *Nucleic Acids Res* *45*, D744–D749.
- Zhang, H., Kim, A., Abraham, N., Khan, L.A., Hall, D.H., Fleming, J.T., and Gobel, V. (2012). Clathrin and AP-1 regulate apical polarity and lumen formation during *C. elegans* tubulogenesis. *Development* *139*, 2071–2083.

Zhang, J.W., Parra, K.J., Liu, J., and Kane, P.M. (1998). Characterization of a Temperature-sensitive Yeast Vacuolar ATPase Mutant with Defects in Actin Distribution and Bud Morphology*. *Journal of Biological Chemistry* 273, 18470–18480.

Zhang, L., Ward, J.D., Cheng, Z., and Dernburg, A.F. (2015). The auxin-inducible degradation (AID) system enables versatile conditional protein depletion in *C. elegans*. *Development* 142, 4374–4384.

Zhong, Q., Pevzner, S.J., Hao, T., Wang, Y., Mosca, R., Menche, J., Taipale, M., Taşan, M., Fan, C., Yang, X., et al. (2016). An inter-species protein-protein interaction network across vast evolutionary distance. *Mol Syst Biol* 12, 865.

Zhou, X., Lin, Y., Kato, M., Mori, E., Liszczak, G., Sutherland, L., Sysoev, V.O., Murray, D.T., Tycko, R., and McKnight, S.L. (2021). Transiently structured head domains control intermediate filament assembly. *PNAS* 118.

Zhu, J., Shang, Y., Wan, Q., Xia, Y., Chen, J., Du, Q., and Zhang, M. (2014). Phosphorylation-dependent interaction between tumor suppressors Dlg and Lgl. *Cell Res.* 24, 451–463.

Samenvatting

Biologische buizen (Hoofdstuk 1)

De meeste dierlijke organen, zoals de longen, nieren en het bloedvatstelsel, zijn opgebouwd uit biologische buizen. Deze buizen verzorgen het transport van moleculen en vormen daarmee een essentieel onderdeel van het dierlijk lichaam. De inhoud van deze buizen vloeit door een holte, of lumen, die wordt gedefinieerd door het membraan van gespecialiseerde epitheelcellen. Deze cellen vormen een laag die de binnenkant van het lichaam scheidt van de buitenwereld. Epitheelcellen zijn daarom tegelijkertijd verantwoordelijk voor de uitwisseling van moleculen (zoals zuurstof en nutriënten) en het vormen van een barrière tegen het externe milieu (zoals bacteriën en giftige stoffen). Om zulke tegenstrijdige functies uit te voeren, verdeelt de cel zich in verschillende membraandomeinen. Het apicale membraan omhult het lumen en het basolaterale membraan staat in contact met de buurcellen. De vorm en grootte van het apicale membraan is daarmee direct verantwoordelijk voor de grootte en vorm van het lumen, die weer bepaalt hoe snel vloeistoffen en moleculen door de buizen stroomt. Dat laatste is onder andere belangrijk voor de efficiëntie waarmee moleculen worden uitgewisseld, maar bepaalt ook of weefsels niet kapot gaan. Het is daarom essentieel voor de goede werking van organen en weefsels om de juiste structuur en grootte van het lumen te bewaken, maar hoe dat precies gebeurt is nog grotendeels onbekend.

***Caenorhabditis elegans* als modelorganisme (Hoofdstuk 1)**

In dit proefschrift heb ik de kleine rondworm *Caenorhabditis elegans* (afgekort: *C. elegans*) gebruikt om te onderzoeken hoe de juiste structuur van biologische buizen wordt onderhouden. *C. elegans* leent zich goed voor biologisch onderzoek en wordt daarom al bijna 60 jaar gebruikt als modelorganisme. Een volwassen rondworm bestaat uit enkel 959 cellen en is ongeveer 1 millimeter lang. In het wild leeft *C. elegans* in de vochtige aarde, maar in het lab groeien ze op een petrischaal gevuld met een gel met daarop bacteriën als voedsel. De wormen zijn hermafrodit, ze hebben daarom zowel mannelijke als vrouwelijke geslachtsorganen en kunnen zichzelf bevruchten. Het grote voordeel hiervan is dat alle nakomelingen hetzelfde DNA hebben als de ouder. Daarnaast kan één ouder in een week wel meer dan 300 nakomelingen krijgen, die binnen enkele dagen uitgroeien tot een volwassen worm.

Bovendien is *C. elegans* grotendeels doorzichtig, deze kwaliteit maakt het dier uitermate geschikt voor microscopie. Alle cellen en weefsels kunnen zichtbaar worden gemaakt onder een eenvoudige microscoop. Door middel van een techniek genaamd CRISPR/Cas9 kunnen echter ook fluorescente eiwitten in cellen en weefsels worden ingebracht. Deze kleurstoffen worden verbonden aan eiwitten van interesse om cellulaire structuren zichtbaar te maken en moleculaire processen te kunnen volgen.

Eiwit-eiwitinteracties (Hoofdstuk 2)

Eiwitten zijn de biologische moleculen die aan de basis staan van alle cellulaire processen. Een groot onderdeel van hun functie komt tot stand door fysieke

en chemische interacties met andere eiwitten. Het in kaart brengen van eiwit-eiwitinteracties is daarom essentieel om achter de functie van een eiwit en het daarbij behorende cellulaire proces te komen. Onderzoek in *C. elegans* staat al jaren voorop als het gaat om het identificeren van alle eiwit-eiwitinteracties die plaats vinden in één organisme. De interacties worden onderzocht met behulp van klassieke technieken zoals “yeast two-hybrid” en eiwitpurificatie gevolgd door massa spectrometrie, maar in het onderzoeksveld worden constant technieken ontwikkeld of verbeterd om zo bij te dragen aan het streven om alle eiwit-eiwitinteracties van *C. elegans* in kaart te brengen.

CeLINC (Hoofdstuk 3)

Om bij te dragen aan het identificeren van alle eiwit-eiwitinteracties die plaats vinden in *C. elegans*, hebben wij een nieuwe techniek ontwikkeld. Met deze techniek wordt een fluorescent eiwit van interesse (bijv. het groen fluorescerende eiwit GFP) gevangen in bundels in de cel. Zo wordt de fluorescentie geconcentreerd in die bundels, wat de detectie van het groene licht vergemakkelijkt. Indien het eiwit interacteert met een eiwit die verbonden is aan een andere kleur fluorescent eiwit (bijv. het rode eiwit mCherry), zal op de plekken van die bundels overlap ontstaan tussen groen en rood licht. Als de eiwitten geen interactiepaar vormen zal het rode eiwit niet naar de bundels getrokken worden en zijn de bundels enkel groen fluorescerend. Met deze techniek kunnen we weefsel- en cel-specifiek eiwit-eiwitinteracties in *C. elegans* blootleggen.

BBLN-1/Bublin (Hoofdstuk 4)

Weten wat een gen doet is essentieel om ziektes te begrijpen en hun behandelingen te ontwikkelen. De makkelijkste manier om achter de functie van een gen te komen is om een gen te verwijderen of inactiveren en te zien welke functie daarmee verloren gaat. In hoofdstuk 4 hebben wij deze aanpak gebruikt om genen te ontdekken die de structuur van een lumen onderhouden. We gebruikte hiervoor de darm van *C. elegans* als modelweefsel. Deze dient als een uitstekend model omdat de darm op celniveau veel op de darmcellen van mensen lijkt, maar uit enkel 20 cellen bestaat die in één cellaag een buis vormen, wat onderzoek zeer vergemakkelijkt. Na het muteren van een groot aantal *C. elegans* om willekeurig genen te inactiveren, hebben we gezocht naar wormen met een misvormde darm. Eén van de wormen die we vonden ontwikkelde bubbels van het apicale, naar het lumen gerichte, membraan. Deze bubbels werden veroorzaakt door het verlies van een gen met tot dan toe onbekende functie. Wij hebben het gen en daarbij behorende eiwit BBLN-1 (zeg: bublin) genoemd. In gezonde wormen zorgt BBLN-1 ervoor dat het lumen van de darm zijn goede, gladde structuur behoudt. Dit doet BBLN-1 door middel van een interactie met intermediaire filamenten; eiwitten die onderdeel zijn van het skelet van de cel. Intermediaire filamenten zijn flexibel, maar sterk, en vormen een netwerk onder het apicale membraan. In afwezigheid van BBLN-1 valt het netwerk uiteen en vormen de intermediaire filamenten een soort kabels onder het membraan. Tussen die kabels ontwikkelen zich vervolgens de apicale-membraanbubbels.

Om onze bevindingen te vertalen naar dieren van een hogere orde, hebben wij vervolgens onderzocht of BBLN-1 nog steeds bestaat in mensen, dat wilt zeggen, dat het gen nagenoeg hetzelfde is gebleven na miljoenen jaren van evolutie die ons scheidt van de rondwormen. Met behulp van een database heb ik alle menselijke genen vergeleken met *C. elegans* BBLN-1 en gevonden dat mensen ook een versie van BBLN-1 hebben, die wij Bublin (BBLN) hebben genoemd. In mensen is Bublin's functie echter nog grotendeels onbekend en vervolgonderzoek moet uitwijzen of menselijke darmcellen ook bubbels zouden ontwikkelen als Bublin inactief is.

Moleculaire zuurpompen en BBLN-1 (Hoofdstuk 5)

In hoofdstuk 4 hebben we laten zien dat BBLN-1 met intermediaire filamenten samenwerkt om de structuur van het darmlumen te onderhouden. Het is echter niet uit te sluiten dat BBLN-1 via de samenwerking met andere eiwitten ook deze functie uitvoert. In hoofdstuk 4 hebben we naast de interactie tussen BBLN-1 en intermediaire filament ook gevonden dat BBLN-1 een interactie aangaat met onderdelen van vacuolar H⁺-ATPases (V-ATPases). Dit zijn ionenpompen die bestaan uit meerdere eiwitten en onder andere zorgen voor de verzuring van compartimenten in de cel. Ze zijn betrokken bij de ontwikkeling van veel verschillende soorten ziektes zoals botziekten en kanker, maar ook bij virale infecties. Daarnaast zijn V-ATPases belangrijk voor het transport en de opname van membraan onderdelen in het plasmamembraan van de cel. Dat laatste maakt ze een aantrekkelijke kandidaat voor het aanleveren van extra membraan in de bubbelmutant.

In hoofdstuk 5 hebben we de eiwit-eiwitinteractie tussen V-ATPase onderdelen en BBLN-1 bevestigd. Daarnaast hebben we ontdekt dat niet elk weefsel in de worm de verzuringsfunctie van V-ATPases gebruikt. Als laatste hebben we gevonden dat door het inactiveren van V-ATPase onderdelen apicale-membraanbubbels in de darm ontstaan die erg lijken op die wanneer BBLN-1 mist. Deze bevindingen bieden interessante invalshoeken voor toekomstig onderzoek naar deze belangrijke ionenpompen.

Intermediaire filamenten en celcommunicatie (Hoofdstuk 6)

Door de jaren heen heeft onderzoek naar intermediaire filamenten steeds overtuigender bewijs geleverd dat deze eiwitten voor structuur en ondersteuning zorgen. In een recent onderzoek en in hoofdstuk 4 is ontdekt dat de afwezigheid van een eiwit genaamd SMA-5 structurele verandering in de darm aanbrengt die zich uitend als apicale-membraanbubbels. Deze bubbels gaan samen met veranderingen in de elektrische lading van intermediaire filamenten. SMA-5 is een eiwit die de lading van eiwitten kan veranderen en wordt geactiveerd onder invloed van stress. Hiermee is het eiwit onderdeel van een celcommunicatie netwerk die reacties op gang brengt om de cel te beschermen tegen gevaarlijke situaties. In hoofdstuk 6 hebben we laten zien dat het effect van de afwezigheid van SMA-5 teniet kan worden gedaan door een intermediair filament te inactiveren. Dit resultaat koppelt structurele aan communicerende onderdelen van de cel en biedt mogelijke toepassingen voor verbindingen tussen andere onderdelen van het celskelet en celcommunicatie.

Het sturen van eiwitlokalisatie met behulp van licht (Hoofdstuk 7)

De ongelijke verdeling van onderdelen en functies in een cel heet celpolariteit. Polariteit komt tot stand door de onderlinge interacties tussen polariteitseiwwitten. Zo zijn er de PAR-eiwitten die het apicale membraan in de darm van *C. elegans* definiëren. In hoofdstuk 7 was ons doel om deze PAR-eiwitten te verplaatsen van het apicale naar het basolaterale membraan van de darm, in de hoop om typische apicale structuren basolateraal te laten vormen. Het verplaatsen van de PAR-eiwitten hebben we gedaan met behulp van een techniek waarin twee eiwwitten (LOV en ePDZ) aan elkaar binden onder invloed van blauw licht. Met behulp van CRISPR/Cas9 hebben wij ePDZ verbonden aan een PAR-eiwit en LOV aan het membraan. Zo konden wij door op de cellen met blauw licht te schijnen de PAR-eiwitten naar het (basolaterale) membraan verplaatsen. Echter bracht de verplaatsing van de PAR-eiwitten niks teweeg. We hebben uit deze experimenten daarom moeten concluderen dat het verplaatsen van de PAR-eiwitten alleen niet genoeg is om polariteit te induceren in een volgroeid weefsel zoals de *C. elegans* darm.

Klein eiwit, grote gevolgen (Hoofdstuk 8)

Wanneer we beter begrijpen hoe biologische buizen hun goede structuur behouden, kan deze kennis bijdragen aan een algemeen begrip van weefsel- en orgaanopbouw. Dit kan waardevol zijn voor het identificeren van oorzaken van aandoeningen waarin deze integriteit verloren is gegaan (zoals inflammatoire darmziekten en cystenieren) en voor de behandeling hiervan. Door een combinatie van nieuwe technieken voor genetische manipulatie, microscopie en het identificeren van eiwit-eiwitinteracties hebben we met het onderzoek in dit proefschrift bijgedragen aan de algemene kennis over weefselstructuur en openen we deuren voor vervolgonderzoek. Zo kan de ontdekking van het kleine eiwit BBLN-1/Bublin en de daaraan gerelateerde bubbel mutant zomaar ten grondslag liggen aan grootse openbaringen in de toekomst.

Curriculum vitae

Sanne Remmelzwaal was born on Valentine's day 1994 in Velp, the Netherlands, as the first born daughter of Bram and Ellen Remmelzwaal. She finished her pre-university education in 2012 at Corlaer College in Nijkerk and started studying Biology at Utrecht University. With the experimental research thesis "Understanding the role of LL5 β in cytokinesis" and internship at the Akhmanova lab she finished her Bachelor's in 2015, to continue her scientific education with the master Molecular and Cellular Life Sciences at the Graduate School of Life Sciences at Utrecht University. Proceeding with this master offered the opportunity to continue her internship at the Akhmanova lab and to be involved with three research papers concerning protein-protein interactions. She finalized her major internship with the report "The multifaceted MICAL3 and its midbody associated interaction partners: Using a cross-linking and mass spectrometry based approach to identify protein interaction domains". With over a year of experimental experience during her University education, she switched gears to focus on the theory. She started her minor internship at the Theory of Biomolecular Matter group led by prof. dr. Bela Mulder at AMOLF, Amsterdam. Here, she learned the coding languages C++ and Python to mathematically model the dynamics of the cytoskeletal protein actin. She concluded her Master's with a literature thesis at the Heck lab at Utrecht University entitled "Lifting a corner of the veil: Identifying lysosomal acid hydrolases directed by mannose-6-phosphate receptors". During her Master's she served as a committee member in the Molecular and Cellular Life Sciences Response Group to form a link between the students and coordinators of the Master's program. In November 2017, Sanne started her PhD at Utrecht University in the lab of prof. dr. Mike Boxem where she investigated the molecular requirements to build a functioning epithelial tissue. Her PhD education was part of the Cancer, Stem Cells and Developmental Biology graduate school for which she served as a PhD students committee member from September 2019 to September 2021. The results of her research are presented in this thesis.

List of publications

Kroll, J.R., Remmelzwaal, S. & Boxem, M. (2021). CeLINC, a fluorescence-based protein-protein interaction assay in *C. elegans*. *Genetics*.

Remmelzwaal, S., Geisler, F., Stucchi, R., van der Horst, S., Pasolli, M., Kroll, J. R., ... & Boxem, M. (2021). BBLN-1 is essential for intermediate filament organization and apical membrane morphology. *Current Biology*, 31, 2334–2346.

Remmelzwaal, S., & Boxem, M. (2019). Protein interactome mapping in *Caenorhabditis elegans*. *Current Opinion in Systems Biology*, 13, 1-9.

Čaval, T., Zhu, J., Tian, W., Remmelzwaal, S., Yang, Z., Clausen, H., & Heck, A. J. (2019). Targeted analysis of lysosomal directed proteins and their sites of mannose-6-phosphate modification. *Molecular & Cellular Proteomics*, 18(1), 16-27.

Liu, Q., Remmelzwaal, S., Heck, A. J., Akhmanova, A., & Liu, F. (2017). Facilitating identification of minimal protein binding domains by cross-linking mass spectrometry. *Scientific reports*, 7(1), 1-11.

Liu, Q., Liu, F., Yu, K. L., Tas, R., Grigoriev, I., Remmelzwaal, S., ... & Akhmanova, A. (2016). MICAL3 Flavoprotein Monooxygenase Forms a Complex with Centralspindlin and Regulates Cytokinesis. *Journal of Biological Chemistry*, 291(39), 20617-20629.

Noordstra, I., Liu, Q., Nijenhuis, W., Hua, S., Jiang, K., Baars, M., Remmelzwaal, S., ... & Akhmanova, A. (2016). Control of apico-basal epithelial polarity by the microtubule minus-end-binding protein CAMSAP3 and spectraplakine ACF7. *Journal of cell science*, 129(22), 4278-4288.

Acknowledgments (Dankwoord)

Get ready for some Dungleish!

Allereerst **Mike**; hier is 'ie dan. Je bent van me af: geen discussies meer over onconventionele kleurschema's en woordgrapjes (blijf van mijn titel af!). In mijn ogen was deze PhD echt een smooth-ride en ik wil je daarvoor super bedanken. Je hebt mij vanaf het begin af aan vrij laten voelen om de projecten te doen waar ik enthousiast voor was en ik voelde mij vanaf het eerste moment dat ik je kantoor in kwam al enorm op m'n gemak. Ik weet nog dat je zei: "aan het einde van jouw PhD ben ik hopelijk niet meer jouw co-promotor, maar promotor" en dat is je ook mooi gelukt! Je zet doelen en die haal je ook en het maakt me super benieuwd naar jouw volgende grote doel! Dankjewel voor de chille begeleiding en ik wens je het allerbeste! (Also: take good care of my F1!)

Mijn tweede promotor **Sander**; het is bewonderingswaardig hoe jij een gevoel van familie over de groep laat vallen. Niet alleen voor expats, maar ook voor Nederlanders als ik voelde de groep direct als thuiskomen en daar heb jij een grote hand in. De Thanksgiving dinners en Sinterklaas vieringen zijn een super fijne traditie en ik zal ze zeker missen! Dankjewel voor al jouw kritische vragen en de steun de afgelopen jaren.

Thanks a lot to those who directly contributed to the work in this thesis. **Rudolf** and **Florian**, thank you for introducing me to the intermediate filament community, welcoming me in Aachen, and for the wonderful collaboration and discussions. **Riccardo**, our collaboration started when I was just a bachelor student and I'm very happy you stayed until almost the end of my PhD. Thank you for always making time to help and for all the fun talks. **Cell bio group**, thank you for letting me invade your precious cell culture room, for sharing your very limited space and time, and for all your help and suggestions. I would also like to thank the reading and doctoral **committee** for taking time to read about worms and bubbles!

Ruben, jojojjojooooo! Van pittige (science) discussies tot depressief-katerig slenteren door Barcelona (nog thanks voor de M&M's hè!): we went places. Het was altijd een feestje om op het lab aan te komen en te zien dat m'n boi er ook was—oké niet altijd, na-je-ochtend-koffie-altijd. I count myself lucky dat ik op het lab begon, jou leerde kennen en dacht: deze langharige ginger dude is oké. Het duurde even tot ik een Iron Maiden karaoke sessie inzette om jou dat ook te laten realiseren, maar hier zijn we dan, het punt dat ik niet meer zeg "dat is Ruben, een collega", maar "Ruben, an acquaintance" *wuhp-TSSCH*. Dat er nog maar vele winter-BBQs, band-roadtrips en internetgekkies-sessies mogen plaatsvinden. Laterrrrrr! **Vincent**, lab-papa. Altijd, écht altijd, aanwezig voor een luisterend oor of oplossing en een zeer welkome balans in de ietwat eenzijdige muziekkeuze van mijn overbuurman (al is het maar een kleine verschuiving in de balans). Dankjewel voor al je advies en steun—wetenschappelijk en sociaal—en voor je onuitputtende betrokkenheid. Je bent en blijft de basis op het lab en ik zal flink moeten wennen dat ik niet voor antwoorden op de random vragen in het leven jou als buurman kan raadplegen. (Ik heb voor jou extra m'n best

gedaan om er geen Engelse verbasteringen tussendoor te laten slippen.) **Jorian**, geen politieke pesterijen meer en misschien voor het eerst wel niemand op het lab die je plaatjes steelt. Moeilijke dingen om aan te wennen neem ik aan. Ik vond het heerlijk om bij je bench te hangen en dat als ik jou tegenkwam op het lab ik erop kon rekenen om een uur later naar huis te gaan. Vergeet me niet te bellen als jouw gossip-uitlaadklep en we gaan binnenkort écht samen klimmen, beloofd! **Vic**, girl, I miss you already. Thanks for initiating almost every social colleague-event I can remember, for introducing me to the Bonitas, for bringing people together. I miss your honest opinion, fierce discussions and even your cheating at boardgames. Best of luck with your new career in science and I can't wait to visit your self-designed/-made home! **Amalia**, your energy, humor, and support made my time in the lab so much fun! I'm so glad that—despite the weather—my country stole your heart and you're here to stay. Let's have many many more G&Ts together! **Helena**, my lab mom. The lab really wasn't the same when you left. I can't begin to thank you enough for all your support, laughs, and the warm welcome in the lab and your lovely home. Keep sharing your love like you do, you're an amazing woman! **Jason**, thank you for letting me in on an incredibly smooth collaboration for the CeLINC paper and for answering all my grammar/vocabulary-questions. You brought a welcome type of structure into our meetings and the lovely American atmosphere to parties (keep up the amazing beer brewing!), thanks for that! **Tessa**, wat word ik blij van jouw energie en Hollandse eerlijkheid. Dankjewel voor je adviezen, relativering en de super leuke Zumba les natuurlijk! Je bent een topper en ik zie je hopelijk snel op de dansvloer! DJ **Ben**! Wat voelde het heerlijk en bijzonder om op het kantoor aan te komen en begroet te worden met jou: "Wat fijn dat je er bent!" Jouw betrokkenheid, fotografie skills en manieren om een feestje te maken ga ik zeker missen! **Janine**, our photography and explosion expert! Thank you for listening to all my complaints but also for sharing so many happy moments together, from here to Florence. **Elise**, niet lang waren we elkaars buurtjes op kantoor en in het lab, maar jouw enthousiasme en interesse zorgde ervoor dat ik je direct waardeerde en vertrouwde als betrokken collega. Ik was gelijk onder de indruk van jouw science skills; heel veel succes met jouw PhD, dat wordt een makkie! **Suzan**, de komst van jouw lab zorgde voor een heerlijke verfrissing op de werkvloer. Wat een bijzondere gave is jouw mensenkennis: ik verbaasde me elke keer over hoe leuk, geïnteresseerd en getalenteerd de studenten en werknemers waren die je had gevonden. Dankjewel voor al jouw betrokkenheid en heerlijk nuchtere Hollandse gesprekken. **Suzanne**, we zijn maar even kantoorbuddies geweest, maar wat was dat gezellig! Onze (iets te luide) gesprekken, gelach en geklaag is precies waar ik energie van krijg. Gelukkig konden we nadat je weg was nog even samenwerken en shinen je prachtige organoids nu onder andere als chapter images in mijn proefschrift! Dankjewel voor de gezelligheid en jouw samenwerking! **Inge**, dankjewel voor al de gezellige gesprekken en het creëren van een warme sfeer in de groep! **Juliane**, 'cool people office' member! Altijd daar voor een koffietje of fashion mening. Dankjewel voor je steun en betrokkenheid als kantoor buurvrouw! **Molly**, your drive, positive attitude, and scientific gift are truly inspiring! I wish you all the success in your current adventures! **Alex**, you entered the lab during the most crazy time I can imagine, but it didn't stop you from worming your way into the research and fitting right in with the group. Best of luck combining al your crazy coding, lab work & parenting, you're doing

amazing! **Loes**, wat heerlijk dat je kon blijven. Ik denk dat je een enorme aanwinst bent voor het lab, super veel succes tijdens jouw PhD! **João**, thanks for handing me over the most beautiful and amazing mutant, it made my PhD so much fun!

Olga: BEST. STUDENT. EVER. From lab fashion to sing-a-longs and being my rock in the lab. I only had to ask and you delivered (often even literally: hello neighbor!). I feel so incredibly #BLESSED to have found an immediate connection with you from the first time we spoke and that we could collaborate for a (despite covid) crazy fun year. You made my PhD extra extra fun, thanks so so much! Best of luck with taking care of our babies and making Bublin famous! And don't forget we still need to get our matching tattoos!

Bonitas! Thanks for all the laughs and cries together. For taking me into your fashionable, loving, gorgeous group of women who miraculously always brought the sun out on your birthdays in my rainy country. I loved our journey to Florence, fun at masterclasses, retreats, parties and the introduction to the wonderful world of the Eurovision Song contest. **CSND committee 2020/2021/...** as with most committees, we didn't meet on an entirely voluntary basis, but I was so happy and surprised to find so much fun and laughter with you! After every one of our "meetings" I felt like the only thing we had done was crying of laughter. Thanks for all the lovely dinners, BBQs and karaoke nights! I'm super excited to see all of you defending, let's celebrate with neuronal cell death expert Dr. Disa Ronno!

Rick&Morty/Rick&Corona&Elections/something German/"**The crew**" we don't do nice so let's just say: HA FIRST! Loserrss. And for Maurice and the Philler: invaginations, invaginations, invaginations. B7 vriendjes/**Arne & Co./ BIOLOGENNNN!** Hoe saai we *C. elegans* ook vonden, ik denk dat ik na vier jaar echt moet accepteren dat ik een wormen-mens ben geworden. Ik heb voor jullie extra hard m'n best gedaan om het onderzoek nog meer op te leuken! Lies, thanks voor al de heerlijke vrijmibo's en je altijd nuchtere blik. Arie bedankt voor je super lieve interesse en betrokkenheid. Het voelt altijd als thuiskomen bij jullie (ook zonder de oneindige kaas- en wijnsupply). **Jorrit**, bruh! Het einde van een tijdperk: geen koffie, biertjes/rosétjes en wandelingen meer op de Uithof. Wat een mooie tijden hebben we daar gehad. Thanks voor jouw voortdurende enthousiasme! **Liekkk**, sinds 2006 altijd aanwezig voor de beste uitlaadkles-sessies, daydrinking en vreetbuien. Dankjewel dat je er echt altijd voor me bent. Geen PhD gezeik meer van mijn kant! Al duurt het misschien even voordat ik over bubbels kan praten zonder aan mijn onderzoek te denken... **Jolien**, jouw interesse voor mijn wormpjes gaven mij nieuwe energie. Super leuk dat je zelfs mee kwam naar het lab om mijn lichtgevende baby's te bekijken. Dankjewel voor al jouw vragen en het herinneren van zelfs de allerkleinste details.

Lieve **puntkooybaxzwaal-fam**, ik ben elke keer weer zo verbaasd hoe betrokken jullie zijn met mij en mijn wormpjes. Van de wimpermassage tot wormpjes in de vriezer, jullie interesse en enthousiasme geven mij echt een gevoel van thuiskomen en ik vind het heerlijk dat jullie mij laten gaan (of zelfs aanmoedigen) in mijn wormen-gekte. Super super bedankt voor jullie interesse en betrokkenheid de afgelopen jaren! **Tommietoet!** De transport expert. Mensen verbazen zich altijd over het grote verschil tussen onze banen, maar bij het

schrijven van mijn proefschrift realiseerde ik me dat we allebei een liefde hebben voor wegen (die van jou van asfalt en die van mij in het lichaam)! Thanks voor al jouw enthousiasme en nuchterheid. De dagelijkse telefoongesprekken op weg naar werk/huis waren een perfect begin/einde van mijn werkdag! **Amber**; ik wilde altijd iets met sterrenkunde doen en jij iets biologisch/medisch, and look at us know! Ik vind het super fijn om met jou een onderzoekende wetenschappelijke interesse te delen en ik geniet er heel erg van dat we elkaars vragen over de wetenschap kunnen beantwoorden. Ik ben trots om je zo te zien groeien en vind het super bijzonder dat jij naast me wilt staan op deze belangrijke dag! **Paps en mams**, jullie zijn de reden dat ik hier nu sta. Jullie hebben de basis gelegd voor mijn onderzoekend vermogen en mij geleerd dat er altijd een oplossing is, die ik zelf kan vinden. Ik heb nooit het gevoel gehad dat jullie vonden dat ik harder moest werken of dat er een druk op mij lag om een bepaald doel te bereiken. Het gaat bij jullie niet om status of hoe goed iemand het doet, als je maar plezier hebt en gelukkig bent. Ik ben super blij en trots op die houding en dat jullie die op mij hebben overgedragen. Ik ben dankbaar dat ik hier daarom sta omdat het mij leuk leek om een PhD te doen, om bij te dragen aan de wetenschap en niet voor het krijgen van een titel of papiertje. Jullie hebben mij altijd vrij gelaten om het pad te begaan dat ik wilde en daar ben ik jullie super dankbaar voor—en paps, natuurlijk ook super bedankt voor al de proofreading en adviezen.

Liefste **Daniël**, wat hebben we goed van onze PhD gebruik gemaakt met al die prachtige (last-minute) reizen. Zoals je weet is vakantie-Dani één van mijn favorieten, maar ik had nooit gedacht dat ik zo zou genieten van het afgelopen 1,5 jaar samen met jou opgesloten te zitten in ons kleine koude Kanaleneiland appartementje. De uitgebreide diners, hapjes en proeverijen maakte het zo'n bijzondere tijd waarin we elkaar en onszelf nog beter leerden kennen. Je steunde me met mijn vroege ritme en zag het zelfs als vanzelfsprekend om samen met mij om 4 uur uit bed te gaan. Dit is één van de voorbeelden waarom supportieve bij jou echt een understatement is. Van een complete verzorging tijdens een hectische schrijfweek tot een luisterend oor tijdens mijn emotionele ups-en-downs ("microscopie is echt mijn passie"—"the injectionmicroscope is a place for crying"). Ik vind het zo fijn om iemand gevonden te hebben waarmee ik zo op één lijn zit. Ik kan niet wachten om te zien wat ons volgende avontuur zal zijn en ben benieuwd waar we samen terecht gaan komen.

Voor al mijn andere lieve vrienden en familie die ik niet heb genoemd: ik heb jullie ongetwijfeld een keer meegenomen in mijn eeuwige emotioneel rollercoaster tussen oneindig geklaag en (waarschijnlijk voor jullie) onbegrijpelijk enthousiasme voor mijn wormpjes en onderzoek. Dankjulliewel voor het aanhoren.

Het is nu echt klaar! Tijd om enorm enthousiast te zijn en te klagen over het volgende avontuur!

